2013

Characterisation and application of the MOSkin radiation dosimeter at clinical kilovoltage x-ray energies

Cheryl Pei Ling Lian
University of Wollongong, pll098@uow.edu.au

CHARACTERISATION AND APPLICATION OF THE MOSKIN RADIATION DOSIMETER AT CLINICAL KILOVOLTAGE X-RAY ENERGIES

A thesis submitted in fulfilment of the
requirements for the award of the degree

DOCTOR OF PHILOSOPHY

from

UNIVERSITY OF WOLLONGONG

by

CHERYL LIAN PEI LING
M.MED.RAD.PHYS (DISTINCTION)
PG DIP.ED (CREDIT)
B.ENG (ELECTRICAL, HONS)

SCHOOL OF ENGINEERING PHYSICS
2013

CERTIFICATION

I, Cheryl Lian Pei Ling, declare that this thesis, submitted in fulfilment of the requirements for the award of Doctor of Philosophy, in the school of Engineering Physics, University of Wollongong, is wholly my own work unless otherwise referenced or acknowledged. The document has not been submitted for qualifications at any other academic institution.

_____

Cheryl Lian
Sept 5, 2013

ACKNOWLEDGEMENTS

First and foremost, I wish to thank Professor Anatoly Rosenfeld, Director of the Centre for Medical Radiation Physics at the School of Engineering Physics, University of Wollongong, for his unwavering belief and commitment to the completion of this project. Thanks to Dr Dean Cutajar for your friendship and practical advice at all times. I am grateful to Dr Jeannie Wong who played an instrumental role with her knowledge and expertise on the Dose Magnifying Glass (DMG) without which Chapter 6 would not have been possible. I wish to express heartfelt gratitude to Dr Martin Butson at the Illawarra Cancer Care Centre, Wollongong Hospital, and Mr Andy Young at St Vincent's Public Hospital, for their commitment to this project and time spent with me, contributing to the completion of this work. In particular, thanks to Dr Nigel Freeman for access to the anthropomorphic phantom at the Department of Radiation Oncology at St Vincent's Hospital without which the measurements performed in Chapter 7 and 8 would not have been possible.

I wish to express my deepest love to my parents who have been my constant source of inspiration in life. Thank you Dad for your constant words of wisdom and encouragement. This thesis is dedicated to you. I would like to believe that my scientific contribution in the form of this thesis has advanced the current state of scientific knowledge in some way.

I wish to thank the Australian government for financial support in the form of an Australian Postgraduate Award. Thank you for believing in the value of research for a better tomorrow.

Finally, I wish to conclude this section by quoting from Sir Isaac Newton, perhaps the most influential scientist of all time. As clichéd as this quote may be, it continues to ring true, loud and clear in the never-ending pursuit of good science by layman and scientists alike.

"If I have been able to see further, it was only because I stood on the shoulders of giants."
-Sir Isaac Newton
Scientist and Mathematician
1642 - 1727

ABSTRACT

X-ray Computed Tomography (CT) is an invaluable diagnostic imaging tool in clinical practice. However in recent years due to the widespread availability and burgeoning use of Multi-Slice CT (MSCT) scanners, cumulative lifetime radiation dose has increasingly become an issue of public concern. Currently, no real-time radiation dosimeter exists in the diagnostic radiology clinic to directly verify patient skin doses. Moreover, existing CT dose measures such as the Computed Tomography Dose Index (CTDI) and Dose Length Product (DLP) as displayed on the MSCT scanner console do not directly relate to patient dose.

The objective of the following thesis is to investigate if the MOS*kin* dosimeter, based on real-time MOSFET technology, developed at the Centre for Medical Radiation Physics (CMRP) at the University of Wollongong, Australia, may be applied in clinical diagnostic x-ray CT photon beams as a CT radiation dosimeter.

The main contributions of this thesis were firstly, the use of Monte Carlo simulations with the GEANT4 Toolkit to characterise the energy response of a prototype MOS*kin* dosimeter at clinical kilovoltage x-ray photon energies. Further simulation studies with the GEANT4 Toolkit found that the addition of a composite metallic foil or a change in the thickness of the overlying polyamide layer from the initial MOS*kin* design resulted in an energy independent radiation sensor. Secondly, a comprehensive experimental characterisation of the MOS*kin* dosimeter was performed in this work which led to the application of the MOS*kin* in three separate experimental studies in diagnostic CT radiology. The first experimental application was the acquisition of CT beam profiles through the combined use of the MOS*kin* dosimeter and the CMRP Dose Magnifying Glass (DMG). The second study applied the MOS*kin* dosimeter to radiation protection verification for the female breast. The third study was the application of the MOS*kin* dosimeter for point organ dose measurements in a tissue-equivalent adult anthropomorphic phantom leading to the derivation of effective dose.

The MOS*kin* has been shown to be a reliable and robust quality assurance tool for the measurement of the range of doses normally associated with x-ray CT scans. It is

recommended, based on the results of this thesis, that the MOS*kin* is used as a dosimetry tool in the radiology clinic for CT quality assurance and organ point dose measurements. In addition, the potential for real-time patient skin dose monitoring in the radiology clinic, not previously possible with the existing generation of dosimeters, is now possible with the MOS*kin* dosimeter.

Table of Contents

List of Tables....viii
List of Figures....ix
List of Publications....xii
1 Introduction....1
1.1 Radiation Exposure and Health Risk....4
1.2 Research Aims and Thesis Organization....5
2 Background and Literature Review....7
2.1 Structure and function of the skin....7
2.2 Biological response to radiation....9
2.3 Indirect damage....10
2.4 Effective dose....11
2.4.1 Risk of radiation-induced cancer....16
2.5 Skin dose....22
2.6 Radiological Dose Quantities and Units....23
2.6.1 Exposure....23
2.6.2 Kerma....25
2.6.3 Absorbed Dose....27
2.6.4 Cavity Theory....28
2.6.5 CT Dose Indices....31
2.7 Properties of an ideal dosimeter....35
2.8 Dosimeters for clinical radiological dose monitoring....41
2.8.1 Overview of commercial dosimeters available....41
2.9 MOSFET Characterisation studies....42
2.10 Summary....48
3 Physics of MOSFET Dosimetry....49
3.1 Structure and Basic Physics of the MOSFET....49
3.2 Principle and operation of a single MOSFET radiation dosimeter....50
3.3 Post-exposure drift....53
3.4 Sensitivity change with accumulated dose....53
3.5 Creep-up effect....54
3.6 Effects of temperature variation on MOSFETs....54
3.7 Summary....55
4 Monte Carlo characterisation of MOSFET dosimeters in clinical kilovoltage x-ray photon beams....56

4.1 Introduction 56
4.2 GEANT4 Simulations 61
4.3 Elements of a GEANT4 Simulation 63
4.3.1 The World Volume 64
4.3.2 The Primary Beam Source 64
4.3.3 The Water Phantom 64
4.3.4 Detector Geometry 64
4.3.5 The Sensitive Volume 64
4.3.6 Physics Processes 65
4.3.7 Data Acquisition and data output 65
4.3.8 Simulation time 65
4.4 Materials and Methods 67
4.4.1 Software generated x-ray spectra 67
4.4.2 Geometrical description of the simulated MOSFET dosimeters 70
4.4.3 Dosimeter Response Factor 73
4.5 Results and Discussion 74
4.5.1 Simulated energy response of the conventional MOSFET with epoxy bubble 74
4.5.2 Simulated energy response of the MO*Skin* 74
4.5.3 Optimisation of MO*Skin* energy response with thin metallic foil 79
4.5.4 Simulated depth dose response 81
4.5.5 Simulated angular response 84
4.6 Conclusions and Recommendations 85
5 Experimental characterisation of the MO*Skin* radiation dosimeter at clinical kilovoltage photon energies 87
5.1 Introduction 87
5.2 Materials 88
5.2.1 Source Beam 88
5.2.2 Phantoms 88
5.2.3 The MO*Skin* Dosimetry System 89
5.2.4 Ionisation chambers 90
5.3 Methods 90
5.3.1 Experimental setup for surface dose measurements 90
5.3.2 Effect of gate voltage on surface dose measurements 91
5.3.3 Individual Reproducibility and Batch Homogeneity 91
5.3.4 Short-term Signal Fading 92

5.3.5 Dose Linearity 92
5.3.6 MO*Skin* sensitivity change as a function of radiation history 92
5.3.7 Energy dependence 93
5.3.8 Angular dependence 93
5.3.9 Depth dose water (tissue) equivalence 94
5.4 Results and Discussion 94
5.4.1 Effect of gate voltage on surface dose measurements 94
5.4.2 Individual Reproducibility and Batch Homogeneity 95
5.4.3 Short-term Signal fading 95
5.4.4 Dose Linearity 96
5.4.5 Effect of accumulated dose on *MOSkin* sensitivity 96
5.4.6 Energy Dependence 97
5.4.7 Angular Dependence 98
5.4.8 Depth dose water equivalence 100
5.5 Conclusions 103
6 Multi-Slice Computed Tomography Dose Profile Assessment 105
6.1 Introduction 105
6.2 Materials 107
6.2.1 CT scanner 107
6.2.2 Phantoms 108
6.2.3 Dose Magnifying Glass (DMG) System 108
6.2.4 Gafchromic XR-QA2 film 110
6.3 Methods 111
6.3.1 CT Beam Characterisation 111
6.3.2 Experimental Setup of the DMG data acquisition system 112
6.3.3 Calibration of the dosimeters 113
6.3.4 CT Beam Profile Measurements 119
6.4 Results and Discussion 120
6.4.1 Reproducibility of CT scans with the DMG 120
6.4.2 Beam Profile Assessment 121
6.5 Conclusion 127
7 Assessment of Breast Dose in Clinical MSCT Pulmonary Imaging with the MO*Skin* Radiation Dosimeter 128
7.1 Introduction 128
7.2 Materials 129
7.2.1 The Alderson Radiation Therapy (ART) Anthropomorphic Phantom 129

7.2.2 The AttenuRad CT Breast Shield System 130
7.3 Methods 131
7.3.1 Scan protocols 131
7.3.2 Dosimetry 132
7.3.3 Quantitative image quality evaluation 133
7.4 Results and Discussion 133
7.4.1 Evaluation of breast dose 133
7.4.2 Quantitative image quality evaluation 138
7.5 Conclusions 140
8 Application of the MOS*kin* dosimeter in the assessment of effective dose in clinical MSCT scans 142
8.1 Introduction 142
8.2 Materials and Methods 143
8.2.1 MSCT scanner and anthropomorphic phantom inserts 143
8.2.2 Dosimeters 144
8.2.3 MSCT Scan protocols 145
8.2.4 NRPB-SR250 ImPACT CT Patient Dosimetry Calculator 148
8.2.5 Calculation of Effective dose 149
8.3 Results and Discussion 150
8.3.1 Measured organ doses 150
8.3.2 Evaluation of Effective Dose 155
8.4 Conclusions 158
9 Overall Findings and Conclusions 160
References 164
Appendix A: Source Code for the computational model of the MOS*kin* 182
Appendix B: X-ray spectra generated by XCOMP5R and SpekCalc at beam qualities 50 kVp to 250 kVp 202
Appendix C: Calibration and Measurement Protocols for the application of radiation dosimeters in clinical kilovoltage x-ray photon beams 206
Appendix D: NRPB-SR250 Calculation of Effective Dose 208

List of Tables

Table 2.1: Typical average effective doses for various imaging modalities. These values can be compared with the average U.S. annual effective dose equivalent from all sources of approximately 3.6 mSv (Adapted from [12,47,48]). 12
Table 2.2: Tissue-Weighting Factors for ICRP Reports 26, 60 and 103 (Reproduced from [47]) 13
Table 2.3: Published k coefficients[a] (Reproduced from McCollough *et al* 2010 [47]) ... 15
Table 2.4: Advantages and disadvantages associated with the MOSFET, diode, radiochromic film, TLD and OSL radiation dosimeter. 38
Table 2.5: Summary of characteristics of the MOSFET, diode, radiochromic film, TLD and OSL radiation dosimeter 39
Table 4.1: Summary of known MOSFET energy response factors from existing literature 58
Table 4.2: Tube potential and filter combinations of the Gulmay D3300 orthovoltage unit used in this investigation. 67
Table 4.3: Composition of materials in the simulated MOSFETs. 70
Table 4.4: Summary of the results of the maximum energy response factors in a monoenergetic photon beam, derived from this simulation study 78
Table 5.1: Effect of different gate voltages on MOSkin Dose Sensitivity for a tube potential of 150 kVp and an applied dose of 20 cGy. 95
Table 5.2: Comparison of the Monte-Carlo predicted DRF with that of the measured DRFs. DRFs were normalized to 150 kVp. 98
Table 5.3: Measured and predicted PDD (a) 100 kVp spectrum (b) 150 kVp spectrum 103
Table 6.1: Scan parameters of this study with a typical clinical tube potential of 120 kVp tube current of 300 mAs and a total scan range of 120 mm. 108
Table 7.1: Scan Parameters for CT Pulmonary Embolus (PE) imaging protocols 132
Table 8.1: Imaging parameters for 16-slice MDCT of the abdominal-pelvic region for a renal calculus protocol; and of the chest for a pulmonary embolus (PE) protocol 146
Table 8.2: Comparison of CT anthropomorphic phantom organ point dose measurements between the MO*Skin* and Gafchromic XR-QA2 radiochromic film for the renal calculus scan. Organ locations were derived from references [51,212]. The primary scan field ranged from slab 25 to 34. 151
Table 8.3: Comparison of CT anthropomorphic phantom organ point dose measurements between the MO*Skin* and Gafchromic XR-QA2 radiochromic film for the pulmonary embolus scan. Organ locations were derived from references [51,212]. The primary scan field ranged from slab number 10 to 21. 153
Table 8.4: Comparison of effective dose calculated by direct and indirect means 155

List of Figures

Figure 2.1: Schematic representation of normal skin. The epidermis houses both basal cells and squamous cells, the source cells for basal cell cancers (BCC) and squamous cell cancers (SCC), respectively. Melanocytes are also present in normal skin, and are the source cells for melanoma. The basement membrane separates the avascular epidermis and the vascular dermis, and is located just inferior to the basal cells. Reproduced from [43]. 7
Figure 2.2: Chain of events following exposure to ionizing radiation (Reproduced from [45] 9
Figure.2.3: Radiation induced DNA damages. For illustration purposes, the DNA double helix is represented as a flat, ladder-like structure. Reproduced from [46]. 11
Figure 2.4: Calculation of effective dose 13
Figure 2.5: Population size needed to detect risk. The size of the population necessary to detect risk is very large and inversely related to the square of the dose (Pg 68, [74]). 17
Figure 2.6: Low dose response curves in risk assessment (a) linear, no-threshold (b) sublinear (c) supralinear (d) hormesis (e) threshold. Figure from Pg.30, [74]. 18
Figure 2.7: The BEIR VII Lifetime Risk Model. In a lifetime, approximately 42 (represented by solid circles) of 100 people will be diagnosed with solid cancer or leukaemia from causes unrelated to radiation. For a single exposure to 100 mSv of low LET radiation, 1 cancer (solid cancer or leukaemia, represented by a star) per 100 people could result (Figure reproduced from [73]). 19
Figure 2.8: Graph shows the lifetime attributable risk of radiation-induced cancer incidence as a function of age at exposure for males and females. The graph is based on data from the atomic bomb survivors as analysed by the BEIR VII committee. Graph reproduced from [9] based on data from [41]. 20
Figure 2.9: Graph shows the comparison of excess relative risk (ERR) at age 70 years for exposure at age 10 or 40 years for specific solid cancers for the atomic bomb survivors. Graph reproduced from [9], based on results from [82]. 21
Figure 2.10: The components of the charge included in exposure according to its definition (Reproduced from Pg 57, [92]) 23
Figure 2.11: Schematic diagram of a free-air chamber used for the measurement of exposure (Reproduced from Pg 59, [92]) 25
Figure 2.12: Energy transfer and absorption is a two-stage process. A photon with energy hν interacts with an atom of the medium, transferring all (photoelectric effect) or some of its energy (Compton scatter) to an electron. The kinetic energy of the electrons is deposited in the medium mostly by ionisation, although some may be lost as bremsstrahlung and other radiative processes. Kerma, or the transfer of energy, occurs at the point of interaction. Absorbed dose, however, is along the path of recoiling electrons determined by their range R_e in the medium. (Reproduced from Martin 2000) 28
Figure 2.13: Gas in cavity v enclosed by a wall to illustrate the Bragg-Gray principle (Reproduced from Pg 368, [93]) 29
Figure 2.14: The radiation dose profile along a line perpendicular to the plane of a single axial CT scan shows a peak where the primary beam slices through the CTDI phantom. The tails of the dose profile are caused by scattered radiation. The integral of the area under the curve is normalized to the nominal beam width NT to determine

CTDI. A $CTDI_{100}$ value is obtained if integration limits of ±50mm are used. (Reproduced from [48]). 32
Figure 2.15: The radiation dose profiles from nine adjacent axial CT scans along a line perpendicular to the axial scans, when summed, produce the MSAD profile. The MSAD is measured with the use of point detectors such as TLDs and solid state dosimeters or film (Reproduced from [48]). The limits of integration determine how much dose from the scatter tails is included. 33
Figure 2.16: Schematic representation of the radiation beam and a typical cylindrical phantom used for CT dosimetry (Reproduced from [72]) 34
Figure 3.1: P-channel enhancement MOSFET(also known as a pMOSFET) (Reproduced from [160]) 50
Figure 3.2: Physical model of ionizing radiation induced effects in MOS structures, with a positive gate bias applied. Upon irradiation, 3 major processes dominate in the MOSFET; namely, (1) the accumulation of trapped charge in the SiO_2, (2) the transport of holes through the oxide and and (3) the increase in the number of bulk oxide and interface traps. Reproduced from [161]. 51
Figure 3.3: Graph of shift in V_{TH} before and after radiation exposure for n-MOSFET , for p-MOSFET shift is in opposite direction. (Reproduced from[162]). 52
Figure 4.1: Mass attenuation absorption curves of silicon ($\mu en\rho)_{Si}$ over that of water ($\mu en\rho)_{water}$ 57
Figure 4.2: Hierarchical Class Diagram of the MOSFET GEANT4 application. The open circle on the lines represents a using relationship; the class at the circle end uses the adjoined category 66
Figure 4.3: Graph showing the relationship between HVL and equivalent photon energy, calculated from the total attenuation coefficients by Johns and Cunningham [96] To obtain the equivalent photon energy of a known measured HVL from these graphs, the method of linear interpolation was used. 68
Figure 4.4: X-ray photon spectra produced by the Xcomp5r software for 50, 75, 100, 125, 150kVp and by the SpekCalc software for 200kVp and 250kVp with input machine parameters as specified in Table 4.1. Only the 100 and 150 kVp spectra are shown here. Binning of each datum point in the spectrum was set at 1 keV intervals. These photon spectra were input into the GEANT4 code. Appendix B shows the generated spectra at tube potentials of 50, 75, 100, 125, 150, 200, 250 kVp for the filter combinations listed in Table 4.2. 69
Figure 4.5 a) Cross sectional view of the simulated MOSFET structure with hemispherical epoxy bubble. The 0^o orientation of the MOSFET refers to the beam normally incident on the epoxy bubble, while the 180^o orientation refers to the beam normally incident on the flat kapton surface b) Top view of commercial MOSFET structure (not to-scale) 71
Figure 4.6: MOSFET setup geometry for an on-surface irradiation with the upside down MOSFET (i.e. at a 180^o orientation) 71
Figure 4.7: Cross sectional view of the MOS*kin* structure. The 0^o orientation refers to the beam normally incident on the kapton polyamide surface of the MOS*kin*. b) Top view of MOS*kin* structure (not to-scale) 72
Figure 4.8: Diagram showing the use of the DRF at beam quality Q. With the MOS*kin* positioned face-up on the surface of the water phantom and irradiated by an incident photon beam of beam quality Q, the DRF is defined as the ratio of the absorbed dose in the micron-thick SiO2 sensitive volume to the absorbed dose in the micron-thick water

volume at 70 µm depth in the water phantom.....73
Figure 4.9: MOSFET energy response (DRF) for monoenergetic photon energies from 15 keV to 300 keV plotted alongside the mass energy absorption coefficient ratio of silicon to water. 75
Figure 4.10: MOS*kin* energy response (DRF) for monoenergetic photon energies from 15 keV to 300 keV plotted alongside the mass anergy absorption coefficient ratio of silicon to water. 75
Figure 4.11: Monte Carlo simulated DRF with the faceup MOS*kin* on phantom surface. Different thicknesses of polyamide film were simulated; 20 µm polyamide film (♦) and 70 µm polyamide film (Δ).....77
Figure 4.12: Comparison of the simulated energy response of the MOS*kin* with the simulated energy response of the conventional MOSFET with epoxy bubble. 78
Figure 4.13: Comparison of the simulated energy response of the MOS*kin* in a monoenergetic beam and a spectral beam. Effective energy of the spectral beam was derived from the interpolation of values from the HVL curve in Appendix B. 79
Figure 4.14: Comparison of the energy response of the face-up MOS*kin* (no metallic foil) with the energy-optimised MOS*kin* (with metallic foil) on the surface of the water phantom.....80
Figure 4.15: Schematic design of the energy-optimised MO*Skin* dosimeter, with the placement of a metallic filter, to correct the energy dependence of the MO*Skin* by flattening its dose response across a desired energy range. 80
Figure 4.16: Depth dose response of the MOS*kin* dosimeter at various depths ranging from on surface (0 mm) to 60 mm depth in a 30 cm x 30 cm x 20cm homogeneous water phantom for incident x-ray photon spectra (a) 50 kVp (b) 100 kVp (c) 150 kVp (d) 250 kVp. Responses were normalized to 1 at a depth of 20 mm in water.....83
Figure 4.17: Simulated angular response of the MOSkin (a) 50 kVp (b) 200 kVp in free air geometry for single and dual MO*Skin* configurations. 85
Figure 5.1: Custom manufactured cylindrical PMMA phantom insert for angular response characterisations.....89
Figure 5.2: Photograph of the MO*Skin* dosimeter designed and developed by the Centre for Medical Radiation Physics (CMRP) at the University of Wollongong.....89
Figure 5.3: The Clinical Semiconductor Dosimetry System (CSDS) designed and developed by the Centre for Medical Radiation Physics (CMRP) at the University of Wollongong (Picture reproduced from [191]).....90
Figure 5.4: Experimental setup for the *MOSkin* placed on the surface of the 30 cm × 30 cm × 15 cm RMI 457 solid water phantom (Gammex RMI, Middleton, WI) during dose delivery at superficial and orthovoltage energies.....91
Figure 5.5: The custom manufactured phantom insert consisting of 2 longitudinally sliced PMMA halves were placed into the slot in the polystyrene phantom at a depth of 1 cm in polystyrene. 94
Figure 5.6: *MOSkin* surface dose linearity for 50 kVp, 100 kVp and 150 kVp beams...96
Figure 5.7: Measured *MOSkin* energy response normalized to 1 at 250kVp.....98
Figure 5.8: Angular response of the MO*Skin* with a (a) 100 kVp (b)150 kVp incident photon beam normalized to its response at 0^o (face up).....100
Figure 5.9: Measured depth dose response in RMI 457 solid water for the (a) 100 kVp beam (b) 150 kVp beam.....102
Figure 6.1: Oblique view of a CT gantry with an x-ray tube, an x-ray fan and detectors for (a) single slice CT scan (b) 4-slice CT scan (Reproduced from [2]).....106

Figure 6.2: a) The CMRP Dose Magnifying Glass (DMG) mounted on a ceramic substrate. (Photograph reproduced from [197] (b) The isocentre of the sensitive detector is denoted by the intersection of the lines which corresponds approximately to channel 64 of the 128-channel DMG. 109
Figure 6.3: Control circuitry of the DMG system. 110
Figure 6.4: Structure of Gafchromic film, type XR-QA2 (Reproduced from [200]) ... 110
Figure 6.5: Photograph of the setup for the measurement of CT beam HVL with an ion chamber 111
Figure 6.6: Experimental setup of the CMRP DMG system. a: Photograph showing the DMG aligned to the isocentre of the CT scanner using the laser positioning reference markers. b: Cross sectional profile (Not-to-scale). The sensitive detector array of the DMG is shaded in black for clarity. 112
Figure 6.7: Schematic of the experimental setup a) solid water phantom and DMG positioned in the scanner room b) control circuitry with associated electronics positioned in the scanner room c) CPU for data acquisition at the operator's console for instantaneous data acquisition 112
Figure 6.8: Sensitivity profile of the 25.4 mm length Dose Magnifying Glass (DMG) in a 120 kVp x-ray CT beam. Outlying points greater than 20% of the mean were not considered, indicating dead channels. 114
Figure 6.9: Each 3 cm x 3 cm Gafchromic XR-QA2 film piece was irradiated to a known dose using the Gulmay superficial orthovoltage unit. 115
Figure 6.10: Calibration plot of Gafchromic XR-QA2 film at 150 kVp 117
Figure 6.11: Energy response of Gafchromic XR-QA2 film at 75 kVp, 100 kVp and 150 kVp. 117
Figure 6.12: Low dose depth dose response of XR-QA2 film compared to the MOSkin dosimeter and Markus IC. 20 mGy was delivered on the phantom surface. 118
Figure 6.13: Gafchromic XR-QA2 film after CT irradiation 119
Figure 6.14: Reproducibility of CT beam measurements with the DMG. Measurements with the DMG were repeated three times in axial mode, nominal beam collimation=1.25 mm. The average COV across all channels was 7%. Maximum COV= 23%, Minimum COV=1%. 121
Figure 6.15: Single tube rotation with 10 mm nominal beam collimation. (Scan protocol 1, Table 6.1) FWHM (DMG) = 14.5 mm, FWHM (film) = 17.1 mm, % difference (Film-DMG) = 15%. MO*Skin* point dose measurement at CT beam isocentre = 13.0 mGy 122
Figure 6.16: Single tube rotation with 20 mm nominal beam collimation (Scan protocol 2, Table 6.1) FWHM (DMG) = 22.6 mm, FWHM (film)= 33.3 mm, % difference (film-DMG)= 32%. MO*Skin* point dose measurement at CT beam isocentre=18.8 mGy 122
Figure 6.17: Axial scan mode with 1.25 mm nominal beam collimation (Scan protocol 3, Table 6.1). FWHM (DMG)=31.2 mm, FWHM (film)= 37.3 mm, % difference (film-DMG)= 16%. MO*Skin* point dose measurement at CT beam isocentre= 55.1 mGy 123
Figure 6.18: Axial scan mode with 5 mm beam collimation (Scan protocol 4, Table 6.1) FWHM (DMG)= 44.0mm, FWHM (film)=55.9 mm, % difference (film- DMG)= 21%. MO*Skin* point dose measurement at CT beam isocentre= 36.2 mGy 124
Figure 6.19: Axial scan mode with 20 mm beam collimation (Scan protocol 5, Table 6.1) FWHM (DMG)= 43.0 mm, FWHM (film)= 47.8 mm, % difference (film-DMG)=10.0%. MO*Skin* point dose measurement at CT beam isocentre= 30.4 mGy . 124
Figure 6.20: Helical scan mode at 20 mm nominal beam collimation, pitch 0.625 (Scan

protocol 6, Table 6.1) FWHM (DMG)= 61.4 mm, FWHM (film)= 70.7 mm, % difference (film-DMG)=13.0%. MO*Skin* point dose measurement at CT beam isocentre = 55.1 mGy. 126
Figure 6.21: Helical scan mode at 20 mm nominal beam collimation, pitch 0.875 (Scan protocol 7, Table 6.1) FWHM (DMG)= 70.0 mm, FWHM (film)= 74.6 mm, % difference (film-DMG)=6.0%. MO*Skin* point dose measurement at CT beam isocentre= 34.8 mGy 126
Figure 6.22: Helical scan mode at 20 mm nominal beam collimation, pitch 1.35 (Scan protocol 8, Table 6.1) FWHM (DMG)= 61.3 mm, FWHM (film)= 78.5 mm, % difference (film-DMG)=22.0%. MO*Skin* point dose measurement at CT beam isocentre = 27.5 mGy 126
Figure 7.1: The chest anthropomorphic phantom showing one MO*Skin* on the superficial surface of the breast representing superficial breast skin dose and another MO*Skin* at the base of the breast representing deep breast dose 129
Figure 7.2: Bismuth breast shield placement (AttenuRad CT Breast Shield System, F&L Medical Products, Vandergrift, PA) for breast dose measurements 131
Figure 7.3: The effect of various dose reduction strategies on superficial breast dose measured by the MO*Skin* dosimeter (☐) and Gafchromic XR-QA2 film (■). Error bars show the range of point dose measurements obtained by both dosimeters. 134
Figure 7.4: The effect of various dose reduction strategies on deep breast dose measured by the MOSkin dosimeter(☐) and Gafchromic XR-QA2 film(■). Error bars show the range of point dose measurements obtained by both dosimeter 135
Figure 7.5: Average breast dose measured by both dosimeters in 4 different scan conditions. Error bars show the average spread of point dose measurements obtained by both dosimeters. 137
Figure 8.1: Schematic of the custom-milled solid water holder designed to fit into the anthropomorphic phantom for dosimeter point organ dose assessment 143
Figure 8.2: Photograph of a single slab of the anthropomorphic phantom with a piece of Gafchromic film placed in the custom made solid water holder 144
Figure 8.3: Application of the MOS*kin* (■) and film (☐) dosimeters for CT organ point dose measurement in the anthropomorphic phantom. The dotted line demarcates the anatomical position of the heart. 145
Figure 8.4: Characterisation of the depth dose response of the MOSkin dosimeter and film with 10 cGy (100 mGy) delivered dose to the surface of the phantom 145
Figure 8.5: Scout scan (120 kVp, 10 mA) of the tissue-equivalent anthromorphic phantom used in this study. The total scan range of this phantom was 800.7 mm. Slab numbers 10 to 34 are depicted as shown. Each slab is 25 mm. 147
Figure 8.6: The mathematical software model applied in the NRPB-SR250 CT Dosimetry calculator used for the computation of effective dose. A scan range of 260 mm and 300 mm was specified in the renal calculus scan (shown on left) and the pulmonary embolus scan (shown on right) respectively. 149
Figure 8.7: Renal calculus CT imaging scan. Point organ dose measurements obtained with the MO*Skin* dosimeter and Gafchromic XR-QA2 film (a) 18 organ locations of interest as specified in ICRP 60 (b) 20 organ locations of interest as specified in ICRP 103. Error bars refer to the range of doses obtained with 3 individual point dosimeter readouts. 153
Figure 8.8: Pulmonary embolus CT imaging scan. Point organ dose measurements obtained with the MOSkin dosimeter and Gafchromic XQ-QA2 film (a) 19 organs of

interest, ICRP 60 (b) 21 organs of interest, ICRP 103. Error bars refer to the range of doses obtained with 3 individual point dosimeter readouts. 155
Figure 8.9: Comparison of effective dose (E) estimates by 3 methods for the (a) renal calculus (b) pulmonary embolus protocol.....156

Glossary

Automatic Tube Current Modulation (ATCM): Is a machine-triggered feature whereby the tube current changes (modulates) according to patient size and shape in order to maintain image quality and optimise the use of the x-ray beam. ATCM is preceded by a scan projection radiograph (SPR) which acquires attenuation information of the individual patient.

Multiple Scan Average Dose (MSAD): In a multiple scan examination where the table is incremented between successive tube rotations, the MSAD is the integral dose averaged over one scan interval in the central region of the dose profile.

Low kilovoltage photon energies: photon energies under 100 keV

Clinical kilovoltage x-ray energies: energy range of photons from 50 kVp (29.8 keV) to 250 kVp (120.3 keV)

Computed Tomography Dose Index (CTDI): CTDI is a volume-averaged measure of scanner output defined as the integral under the radiation dose profile from a single axial scan, including the dose tails, divided by the nominal beam width *NT*. It represents the average dose to a homogeneous cylindrical PMMA phantom volume with dedicated holes parallel to the longitudinal (z-) axis, and is usually measured with a 10 mm long pencil ionisation chamber as the quantity $CTDI_{100}$, with integration limits of ±50 mm Centreed over the dose profile. Typical CTDI values for diagnostic CT range from 3 mGy (low dose and pediatric protocols) to 60 mGy (adult head examinations).

Pitch: A term used in helical CT that represents the gaps or overlaps between the radiation dose profiles from consecutive rotations of the x-ray source. It is defined as the ratio of table travel distance per rotation (I) to the nominal beam width or beam collimation (NT). A pitch < 1 indicates overlapping dose profiles, while a pitch > 1 indicates gaps between dose profiles. When pitch= 1, MSAD is the same as CTDI.

$$\text{Pitch} = \frac{\text{Table travel (mm) per gantry rotation}}{\text{beam collimation (mm)}}$$

Overranging effect: Overscan is a phenomenon associated with helical MSCT scanners where the irradiated length is longer than the imaged length due to the need to obtain the necessary projection data for image reconstruction at the beginning and end of the scanned volume. Depending on protocol, the overscan on a 16-slice MSCT scanner can range from 1 cm to 10 cm [1]. Figure a illustrates.

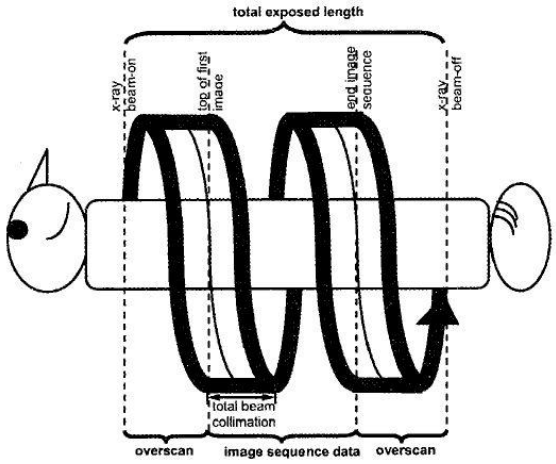

Figure a: Overscanning phenomena (Reproduced from [1])

Slice Thickness: In MSCT scanners, the slice thickness is determined by the width of the detectors. Slice width is changed by electronically binning different numbers of individual detector elements together. Figure b illustrates this concept. Slices are acquired simultaneously in MSCT. This is in contrast to Single Slice CT (SSCT) scanners where slice thickness is changed by mechanically changing the collimator position.

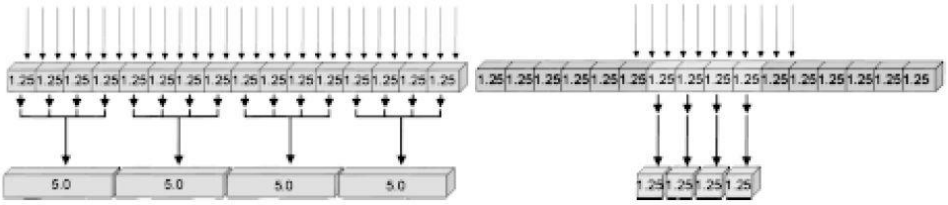
Figure b: Reproduced from [2]

Z-axis geometric efficiency: the percentage of the x-ray beam width in the z-direction that is seen by the detectors. Figure c illustrates.

$$\text{z-axis geometric efficiency} = \frac{\text{area under z-axis dose profile falling within active detectors}}{\text{area under total z-axis dose profile}}$$

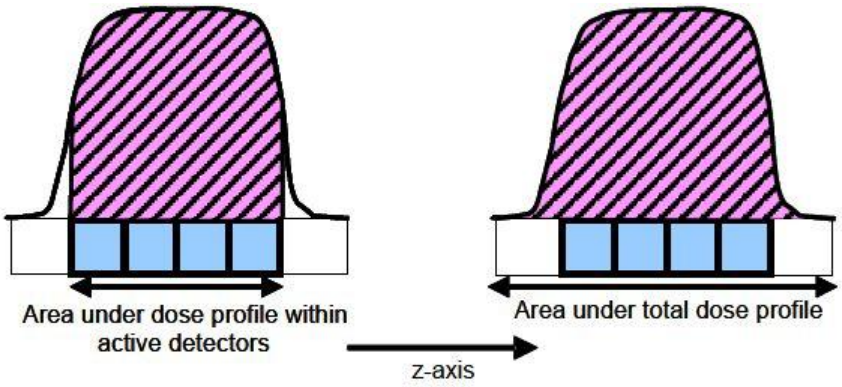

Figure c: Reproduced from [3].

List of Publications

Refereed publications

1. C.P.L. Lian, J.H.D. Wong, A. Young, D. Cutajar, M. Petasecca, M.L.F. Lerch, A.B. Rosenfeld, "Measurement of Multi-Slice Computed Tomography (MSCT) Dose Profile with the Dose Magnifying Glass (DMG) and the MOS*kin* Radiation Dosimeter", *Radiation Measurements,* vol 55, pages 51-5 (2013).

2. C.P.L. Lian, A. Young, D. Cutajar, N. Freeman, A.B. Rosenfeld, "Organ Point Dose Measurements in Clinical Multi-Slice Computed Tomography (MSCT) examinations with the MOS*kin*^{TM} Radiation Dosimeter", *Radiation Measurements*, vol 55, pages 56-9 (2013).

3. C.P.L. Lian, M.A.R. Othman, D. Cutajar, M. Butson, S. Guatelli, A.B. Rosenfeld, "Monte Carlo study of the energy response and depth dose water equivalence of the MO*Skin* radiation dosimeter at clinical kilovoltage photon energies", *Australasian Physical & Engineering Sciences in Medicine*, vol 34(2), pages 273-9 (2011).

4. Chuamsaamarkkee, K., Fuduli, I., Cutajar, D., Lian, C., Harvey, S. & Rosenfeld, A. B., "Skin dosimetry of thyroid radioiodine with MOS*kin* detector: A phantom study". *2011 IEEE Nuclear Science Symposium and Medical Imaging Conference, NSS/MIC 2011* pages. 258-260, 2012.

Conferences Presented

1. Cheryl PL Lian, Andy Young, Dean Cutajar, Michael Lerch, Anatoly B. Rosenfeld, "MO*Skin* Dosimetry for Real-time Breast Dose Assessment in CT Pulmonary Embolus Imaging", *17th International Conference on Solid State Dosimetry*, Poster Presentation, September 2013, Recife, Brazil.

2. C.Lian, M.A.R. Othman, D. Cutajar, M. Butson, S. Guatelli, A. Rosenfeld, "Monte Carlo Modeling and Experimental Characterisation of the MO*Skin*^{TM} Radiation Sensor for Application in Kilovoltage Dosimetry", *Engineering and Physical Sciences in Medicine (EPSM)*, Oral Presentation, November 2009, Canberra, Australia.

3. C. Lian, M.A.R. Othman, D. Cutajar, M. Petasecca, M. Butson, S. Guatelli, M. Lerch, A. Rosenfeld, "Characterisation Of The MO*Skin*^{TM} Radiation Dosimeter At Clinical Kilovoltage Energies", *16th International Conference on Solid State Dosimetry*, Oral Presentation, September 2010, Sydney, Australia.

4. C. Lian, M.A.R. Othman, D. Cutajar, M. Petasecca, M. Butson, S. Guatelli, M. Lerch, A. Rosenfeld, "Characterisation of the MO*Skin*^{TM} Radiation Dosimeter At Clinical Kilovoltage Energies: GEANT4 Simulations and Experiments", *16th International Conference on Solid State Dosimetry*, Poster Presentation, September 2010, Sydney, Australia.

1 Introduction

The Australian Radiation Protection & Nuclear Safety Agency (ARPANSA) estimates that the growth in x-ray multi-slice CT scans (MSCT) is increasing at a rate of approximately 9% per annum, with over 2 million MSCT scans done in the year 2009 alone [4]. Indeed, medical x-rays are by far the largest, single man-made source of radiation exposure to the UK and the US population, with CT scanning accounting for about 68% of the UK medical x-ray dose [5] and almost 50% of the US collective medical x-ray dose [6]. The UNSCEAR 2008 report estimated that although CT scanning constitutes just 7.9% of diagnostic radiology examinations in level 1 healthcare countries (with 1 or more physicians per 1000 people), it contributes substantially at 47% to the overall collective effective dose from diagnostic radiology procedures [7].

With the widespread use of medical radiation for the diagnosis and treatment of disease, Brenner and Hall (2008)[8] have postulated that medical radiation will potentially become a major public health threat if current levels of usage remain unchecked. In other words, even though individual patient health risk due to CT exposure may be small when weighted against the benefit of early medical diagnosis, when viewed at a national level, a significant public health issue could potentially result at current rates of usage and without the use of proper dose management strategies aimed at maximizing the patient benefit-risk ratio. Several authors have noted that MSCT is a nontrivial source of radiation exposure [6,8-12].

What follows is that it is necessary to control patient doses by optimising and monitoring the use of x-ray imaging systems, in particular, MSCT scanners. In the case of MSCT imaging, the amount of radiation dose a patient receives depends on two factors; on the design of the CT scanner (x-ray tube filtration, beam shaping filters, collimator design, focus-to-axis distance) and the way the CT scanner is used (user selected scanning parameters such as tube kilovoltage, exposure time and scan length)[13].

Several manufacturers, particularly CT equipment manufacturers such as GE, Philips, Toshiba and Siemens, have devised machine dose reduction capabilities, for example, tube current modulation which adapts the incoming energy of the x-ray beam to patient width and thickness, thus lowering delivered radiation dose while not compromising patient image quality [14]. However, for clinics with older CT equipment, more stringent dose checks should be conducted regularly to ensure that the CT system is operating within safe dose limits.

To this end, regular quality assurance (QA) performed by a trained medical physicist is necessary to monitor drifts in medical equipment performance over time in a medical clinic. A trained medical physicist typically performs dose measurements periodically to assess beam quality output.

Diagnostic reference levels (DRLs) serve as radiation trigger levels for dose optimisation [15]. They are not dose limits; they are essentially indicators of common practice and are expected to change over time as new acquisition protocols and various clinical applications evolve [4]. Thus, DRLs provide a useful means for institutions to evaluate machine output as part of annual QA by comparing previous dose records. With the use of DRLs, existing machine performance can be evaluated and actions be taken to keep radiation exposure as low as reasonably achievable (according to the ALARA principle) for radiation protection. DRLs are typically set at the 75^{th} percentile of the dose distribution from a dose survey conducted across a broad user base, using a specified dose measurement protocol and phantom.

The use of DRLs as a dose optimisation tool is recognised by many professional bodies and organizations worldwide, such as the International Commission of Radiation Protection (ICRP), American College of Radiology (ACR), American Association of Physicists in Medicine (AAPM), United Kingdom Health Protection Agency (UK HPA), International Atomic Energy Agency (IAEA), European Commission (EC) [15] and more recently, the Australasian College of Physical and Engineering Sciences in Medicine (ACPSEM)[16]. With the increasing use of MSCT scanning in diagnostic radiology, combined with the fact that MSCT contributes the largest amount of man-made radiation dose to the population, the Australian Radiation Protection and Nuclear

Safety Agency (ARPANSA) has currently prioritized CT as a key imaging modality for establishing national DRLs [4]. To-date, ongoing web-based surveys allow the periodic update of DRLs to reflect changes in technology and imaging technique in the Australian context [17].

There is ongoing interest in the medical physics community to verify doses delivered during routine diagnostic examinations, particularly for high-dose examinations such as x-ray CT [18,19]. Recent research in medical imaging dosimetry is largely focused on skin and organ dose determination via both direct measurement methods with radiation sensors and Monte Carlo simulations to the radiosensitive breast tissues of women [14,20-23], pregnant women and their unborn foetuses [1,23-25] and very young children [26-30]. Various ongoing clinical evaluation attempts are currently being conducted in major medical institutions to determine the effectiveness of bismuth breast shields [22,31] and eye goggles [32,33] for radiation protection in x-ray CT [34], since the human gonads (uterus and ovaries for the female and prostate for the male), thyroid and the eye lens are particularly radiosensitive organs. A combined approach of experimental measurements verified by Monte Carlo simulations is helpful in individual patient dose evaluation as several studies have shown [24,35,36].

The major advantage of MOSFETs over conventional thermo-luminescent dosimeter (TLD) measurements is that MOSFETs give real-time dose readouts, which is particularly useful in the clinical setting, where time constraint, usability and convenience are factors that hugely affect their successful adoption. Real-time dosimetry measurements using MOSFETs is useful since the current generation of multi-slice CT scanners requires the rapid development of appropriate CT scan protocols to keep up to pace with the pressure of clinical deployment upon machine arrival in a typically high workload city hospital. Using MOSFETs overcomes the tedious pre-calibration, annealing, and post-irradiation readout processes associated with the conventional method of using TLD chips for organ dosimetry. The tedious processes of preparing the TLD chips pre- and post- irradiation is possibly one of the reasons why patient skin or organ dosimetry is not as common practice in clinical radiology as it should be.

With advances in imaging technology, comes the need for greater dose surveillance in radiological imaging. The need for radiological dose monitoring is exemplified by recent medical lawsuits on overdosing of patients in radiology, particularly in CT. The U.S Food and Drug Administration (FDA) has very recently (since October 8, 2009) issued a notification to hospitals and practitioners performing CT scans to review their CT scan protocols [37] and called for greater vigilance regarding dose indices normally displayed on the machine console, following reported patient overdose from imaging CT at the Cedars-Sinai Medical Centre [38]. If real-time dosimetry had been in place, timely interventions during dose delivery would have prevented patient overdose.

From the recent overdosing incidents that have occurred, it is clear that regular equipment quality control and online patient dose assessment is necessary for two main reasons. Firstly, regular QA/ patient dose survey provides the patient, practitioner and researcher the much needed assurance that the imaging procedure is safe. Secondly, in the case of legal lawsuits involving the hospital or clinic, a data record of regular machine QA can mean the avoidance of a hefty fine and loss of institution reputation. Indeed, an updated quality control record is to be expected of a socially responsible radiation administering institution.

1.1 Radiation Exposure and Health Risk

There are many confounding factors when dealing with stochastic risk as a result of low-dose medical radiation exposures. These confounding factors are firstly, the long, variable latent period (about 5 to 30 years or more) between low dose radiation exposure and the onset of radiation-induced carcinogenesis; secondly that cancer due to radiation is primarily indistinguishable from spontaneous cancers; thirdly, that the effects of radiation may differ from individual to individual; and fourthly, that the background incidence of cancer is relatively high. In Australia alone, it is expected that 50% of Australians will be diagnosed with cancer by the age of 85 [39] as a result of lifestyle factors that may or may not be confounded by low-dose medical radiation exposure.

It has been estimated that 0.4% of all cancers in the United States may be attributable to

the radiation from CT [40]. At the current rate of CT usage, Brenner and Hall postulate that this estimate may be in the range of 1.5% to 2% of cancers arising as a result of radiation from medical diagnostic CT exposure. The BEIR VII Report [41] provides age-, sex- and site-specific Lifetime Attributable Risk (LAR) estimates as a result of low levels of low LET ionizing radiation such as medical diagnostic x-rays.

1.2 Research Aims and Thesis Organization

It has been recognised that with the increasing availability and widespread use of MSCT multi-phase scanning, cumulative dose to CT patients is not negligible. There is a need for greater patient dose surveillance in CT scan scenarios in the face of fast-changing MSCT technology. In the case of kilovoltage treatment scenarios in clinical radiotherapy, real-time patient monitoring of doses is helpful to avoid radiation-related skin injury.

The MOS*kin* dosimeter, built on real-time MOSFET technology and designed by the Centre for Medical Radiation Physics (CMRP) at the University of Wollongong, has previously been shown to be suitable for the measurement of skin doses in radiation therapy applications. The aim of the following thesis was firstly, to characterise the response of the MOS*kin* dosimeter in clinical kilovoltage beams so as to evaluate its suitability for future radiological applications. Secondly, following its characterisation, the MOS*kin* dosimeter was applied in 3 separate experimental studies involving clinical diagnostic x-ray CT beams.

Chapter 2 describes the necessary radiobiological background leading up to a review of radiation risk in low dose studies. Following which, essential radiological dose terminology is introduced. Previous characterisation attempts of the more commonly known radiation dosimeters such as the MOSFET, radiochromic film and the TLD are also outlined in this chapter.

In Chapter 3, the basic physics of the radiation MOSFET is presented. The purpose of this chapter is to provide an overview of how a radiation MOSFET works, so that future clinical applications with the MOSFET can be better understood from a physical viewpoint.

Chapter 4 details the theoretical aspects of the project; Monte Carlo simulations were performed to address the issue of MOS*kin* energy dependence at low energies. Two design solutions are proposed to improve the energy response of this dosimeter. In addition, depth dose simulations were performed to assess how well the MOS*kin* functions as a possible in-phantom dosimeter in clinical radiological beams.

Chapter 5 presents a series of experimental characterisation tests conducted on the MOS*kin* in a clinical kilovoltage x-ray photon beam. In particular, MOS*kin* properties such as individual readout reproducibility, batch homogeneity, signal fading, dose linearity, change in MOS*kin* sensitivity with accumulated dose, energy response, angular response and depth dose characterization tests were performed using a clinical superficial/orthovoltage therapy unit.

Chapter 6 illustrates the use of the MOS*kin* dosimeter as a point dosimeter for the absolute dose calibration of the Dose Magnifying Glass (DMG), another of the CMRP developed dosimeters based on silicon strip detector technology. Applied together with the MOS*kin* dosimeter, the DMG was shown to be a novel quality assurance tool in the assessment of the x-ray CT beam profile in a water phantom in this study.

In Chapter 7, the MOS*kin* was applied to a CT x-ray beam to determine average breast dose on the basis of superficial and deep breast dose point measurements. Our measurements showed that the combined use of automatic tube current modulation and bismuth breast shields reduced breast dose by as much as 64% in a typical clinical pulmonary embolus scan.

Chapter 8 presents the application of the MOS*kin* dosimeter in the measurement of organ doses in an anthropomorphic phantom in a clinical MSCT photon beam. Measured organ doses then led to the derivation of effective dose pertaining to each imaging protocol. Radiochromic film (Gafchromic XR-QA film) was used as an alternative dosimeter.

Chapter 9 summarises our overall research findings from this work.

2 Background and Literature Review

2.1 Structure and function of the skin

The skin consists of two compartments, namely the outermost epidermis (an average of 70 μm thickness) and the underlying dermis (3 to 4 mm thickness). The epidermis protects the skin from UV radiation and other environmental stressors. The dermis, which is a much thicker, more vascularised tissue, contains the sensory receptors, nerve fibres, sweat glands, sebaceous glands and provides mechanical support and supplies the epidermis with nutrients [42]. Figure 2.1 illustrates.

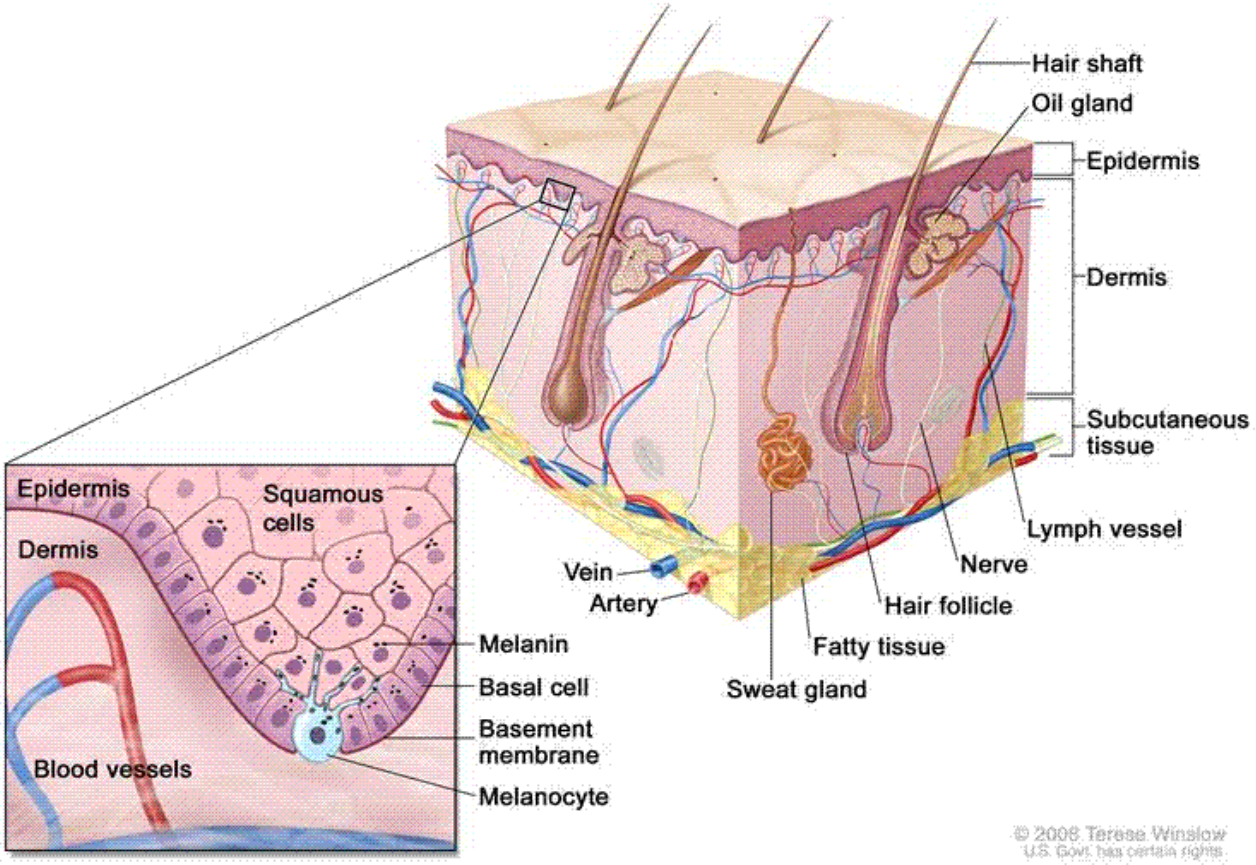

Figure 2.1: Schematic representation of normal skin. The epidermis houses both basal cells and squamous cells, the source cells for basal cell cancers (BCC) and squamous cell cancers (SCC), respectively. Melanocytes are also present in normal skin, and are the source cells for melanoma. The basement membrane separates the avascular epidermis and the vascular dermis, and is located just inferior to the basal cells. Reproduced from [43].

The epidermis varies in thickness according to its location on the body. On the adult face, for example, it is just 20 μm in thickness [44], and about 50 μm thick at the

eyelids. The epidermis is up to 1.5 mm thick at the palms and soles [42]. The deepest layer of the epidermis is the basal layer which ranges from 20 to 100 μm thickness in Man. The basal layer is the region where most cell division takes place. In a short span of 15 to 30 days, the epidermis regenerates itself when keratinocytes from the basal layer differentiate to form spinous granular layer and finally the surface layer of the skin.

As the basal layer is a rapidly dividing region, it has been conservatively established by previous research to be the target cell layer for carcinogenesis. For the purpose of cancer risk evaluation and skin exposure contribution to the calculation of effective dose, the ICRP assumes the basal layer (target cell layer) of the epidermis to be positioned at a nominal depth of 70 μm (7 mg cm^{-2}) [44].

Radiation biologists have identified 3 main factors that affect the skin reaction when exposed to x-rays. The 3 factors that determine the type and severity of skin reaction are namely, exposure-related factors, biological factors and ethnic background.

Exposure-related factors include that of dose rate, fractionation, size of the exposed area and the specific site of exposure. Generally speaking, the higher the dose rate and the larger the exposed area, the more severe the skin reaction is expected to be. Fractionation is associated with a less severe skin reaction as tissue has had time to repair. The most sensitive region of the skin is that of the anterior portion of the neck, with the trunk and surfaces of the extremities, and back of the neck and scalp being less sensitive. Least sensitive to radiation are the skin of the palms of the hands and soles. It is interesting to note that while the skin of the scalp is relatively resistant to skin effects, it is also most severely affected by epilation, otherwise known as radiation induced hair loss.

Biological factors include the age at the time of exposure, oxygen status of the irradiated tissue, hormonal status and genetic factors. Pediatric patients are at greater risk of the stochastic effects of radiation (i.e. probability of radiation-induced cancer) due to their more rapidly dividing cells and their longer latent period due to longer life expectancy at time of exposure. Patients with a predisposition to a DNA repair gene

defect such as ataxia telangectasia may also be more severely affected by radiation.

Finally, ethnic factors also account for differences in skin reaction; with the fair hair and fair skin population being more radiosensitive, while the black African and Carribean races having the most radio-resistant skin types.

2.2 Biological response to radiation

When ionizing radiation passes through matter, cellular damage results when radiation is absorbed. Immediate chemical changes occur when the free radical OH• interacts with solute molecules, followed by molecular damage (to the DNA, RNA and enzymes) within seconds to minutes after radiation exposure, and biological damage (which may be temporary or irreparable) which may occur within hours or over decades (Figure 2.2). At a cellular level, permanent cell death occurs if a radiation threshold is exceeded (thereby known as the deterministic effect of radiation), or stochastic effects may result which is essentially a state whereby cells undergo transformation, rendering them abnormal, for example, where cell growth becomes inhibited or cells multiply uncontrollably (become malignant) as a result of radiation exposure. It is the individual's capacity for cell repair that regulates the onset of permanent cellular transformation.

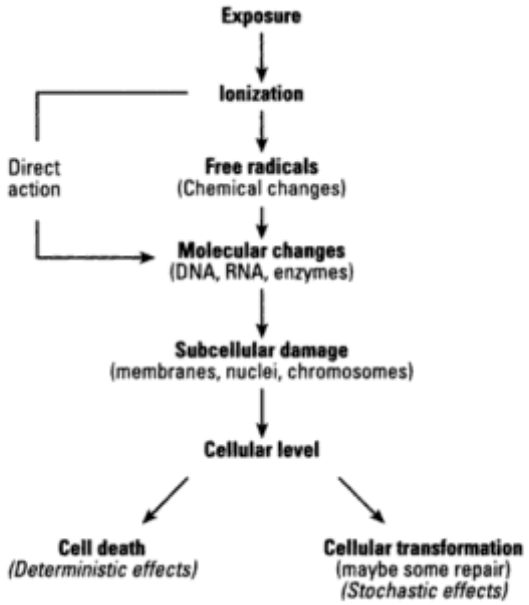

Figure 2.2: Chain of events following exposure to ionizing radiation (Reproduced from [45]

2.3 Indirect damage

When radiation exposure occurs, the immediate chemical changes that occur are caused by the ionisation process. The molecules that are affected by radiation include proteins (such as enzymes) and nucleic acid (DNA).

Direct damage results when a covalent bond in a solute molecule is broken directly by the incoming ionizing radiation.

In indirect damage, when a water molecule is subjected to radiation, it decomposes to form a positively charged water ion and a free electron. (Eq 2.1). The water ion immediately decomposes to a free radical known as the hydroxyl ion (OH•) (Eq 2.2).

Ionisation:

H_2O + radiation $\rightarrow$ $H_2O^+ + e^-$ Eq. 2.1

Decomposition of positively charged water ion:

H_2O^+ decomposes$\rightarrow$ $H^+ + OH\bullet$ Eq. 2.2

The $OH^\bullet$ free radical is responsible for the chemical changes in solute molecules which occur instantaneously upon radiation exposure. It is this initial chemical event that sets off a whole series of subsequent damaging chain reactions in tissue. Indirect damage as described commonly occurs since living tissue is composed of more than 70% to 90% water.

Figure 2.3 illustrates the major types of DNA damage induced by ionizing radiation, whether by the direct or indirect action of ionizing radiation introduced earlier. A DNA strand is represented as a ladder-like structure; information that is contained on both sides of a DNA double helix (ladder) is complementary to each other. Hence, whenever a lesion occurs on one side of the DNA (known as a single strand break), the DNA can be easily repaired since the intact strand provides the necessary reproducible information.

Double strand breaks (DSB) are thus considered more critical as they can result in irreversible damage to the cell since there is a loss of the necessary template information. When such a disrepair occasionally occurs, point mutations, chromosomal translocations and gene fusions result, all of which are associated with cancer induction [10]. It is estimated that there is a 3-4% chance of DSB for every 1 Gy per cell [46].

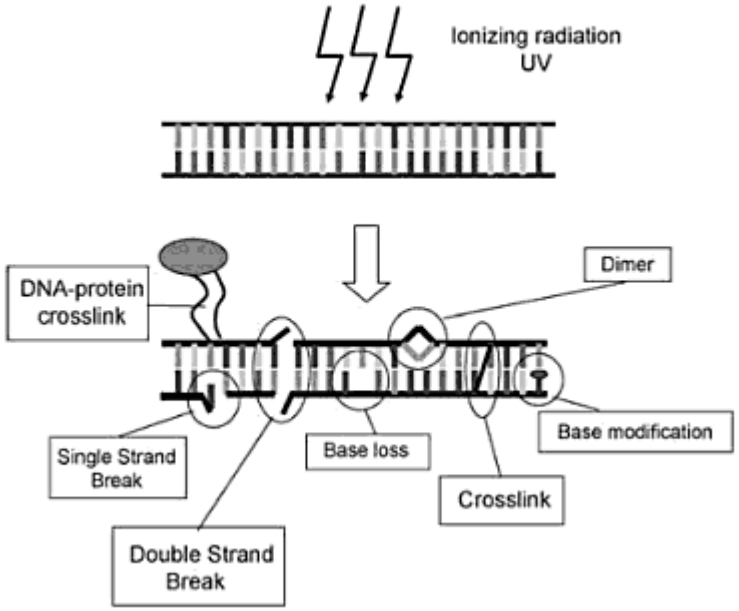

Figure.2.3: Radiation induced DNA damages. For illustration purposes, the DNA double helix is represented as a flat, ladder-like structure. Reproduced from [46].

2.4 Effective dose

Patients and practitioners want to know the risk of an imaging procedure. Effective dose is a useful parameter that allows the comparison of risks from different imaging procedures as well as between different imaging techniques. Effective dose allows the risk of the non-uniform dose exposure received by the patient to be quantified in terms of a uniform, whole-body exposure, also known as the "whole-body equivalent" dose value [47]. It is expressed in units of milliSieverts (mSv).

Effective dose is formally defined as the weighted sum of the products of absorbed dose to each organ and the ICRP determined organ/tissue weighting factors for that particular organ. Equation 2.3 illustrates.

$$\text{Effective Dose} = \sum_{\text{all organs}} (\text{Dose}_{\text{organ}} \times \text{ICRP Weighting factor}_{\text{organ}}) \qquad \text{Eq. 2.3}$$

Table 2.1 shows the typical effective dose values for various imaging modalities including that for general radiography, nuclear medicine and CT adapted from McCollough et al 2010 [47], Bauhs et al 2008 [48] and Mettler et al 2008 [12].

From Table 2.1, it can be seen that average effective doses in radiological imaging vary over a range of values, depending on the imaging protocol used and the anatomic region scanned. Combined abdominal-pelvic CT imaging contributes a large effective dose, of between 8 to 14 mSv. This may be explained by the fact that the radiosensitive gonads (uterus and testis) lie in the scan region. Myocardial perfusion in nuclear medicine (9-41 mSv) and CT coronary angiography (1-18 mSv) are interventional procedures with the female breast being a radiosensitive tissue, in the irradiated scan region. Doses vary within a large range mainly because of differences in techniques used by different interventional radiologists and the time taken to perform the scan depending on the complexity of each interventional procedure.

Table 2.1: Typical average effective doses for various imaging modalities. These values can be compared with the average U.S. annual effective dose equivalent from all sources of approximately 3.6 mSv (Adapted from [12,47,48]).

Examination	Effective Dose (mSv)
Radiography/Fluoroscopy	
Hand radiograph	<0.1
Dental bitewing radiograph	<0.1
Chest radiograph	0.1-0.2
Mammogram	0.3-0.6
Lumbar spine radiograph	0.5-1.5
Barium enema examination	3-6
Diagnostic coronary angiogram	5-10
Nuclear Medicine	
Lung scan	2-3
Bone scan	3-5
Myocardial perfusion (sestamibi)	9-16
Myocardial perfusion (thallium)	35-41
Myocardial perfusion (^{18}F-FDG)	14
CT	
Head CT	1-2

Chest CT	5-8
Abdomen CT	5-8
Pelvis CT	3-6
Abdomen and pelvis CT	8-14
Coronary artery calcium CT	0.1-3
Coronary CT angiogram	1-18

Effective dose cannot be determined directly. Effective dose is commonly derived by one of the three methods illustrated in Figure 2.4. The first method is by directly measuring organ doses in anthropomorphic phantoms using dosimeters such as traditional TLDs [28,49,50] , real-time MOSFETs [32,36,51-53] or photodiodes [54-56]. The measured organ doses are then multiplied by an established ICRP weighting factor (Table 1.2) to determine the effective dose. The second method, as illustrated, uses Monte Carlo simulations in anthropomorphic phantoms[57-60] or cylindrical phantoms [61]. The third method simply applies a pre-defined k coefficient (Table 2.3) to the CT scanner console displayed dose-length-product (DLP).

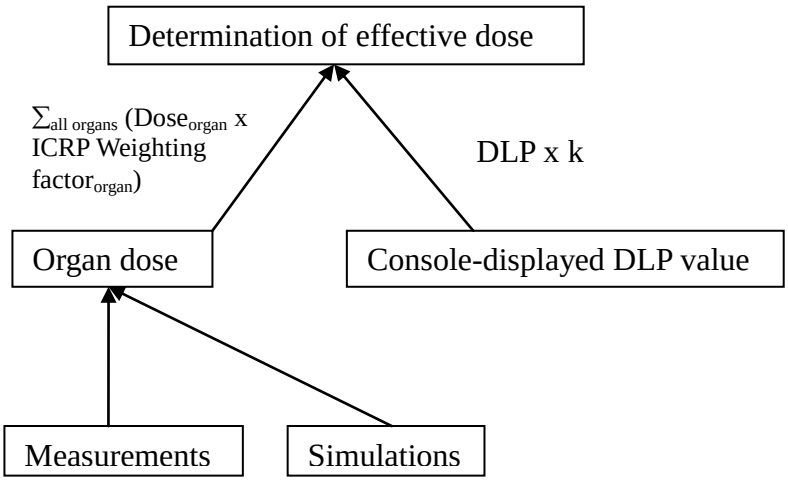

Figure 2.4: Calculation of effective dose

Table 2.2: Tissue-Weighting Factors for ICRP Reports 26, 60 and 103 (Reproduced from [47])

	Tissue-weighting factor		
Tissue or Organ	ICRP 26 [62]	ICRP 60 [63]	ICRP 103 [64]
Gonads	0.25	0.20	0.08
Red bone marrow	0.12	0.12	0.12
Lung	0.12	0.12	0.12
Colon		0.12	0.12

Stomach		0.12	0.12
Breast	0.15	0.05	0.12
Bladder		0.05	0.04
Liver		0.05	0.04
Oesophagus		0.05	0.04
Thyroid	0.03	0.05	0.04
Skin		0.01	0.01
Bone surface	0.03	0.01	0.01
Brain			0.01
Salivary glands			0.01
Remainder	0.30	0.05	0.12
Total	1.00	1.00	1.00

The Monte Carlo (MC) method of calculating organ doses is based upon the established datasets of MC based organ dose coefficients, such as those from the UK National Radiological Protection Board (NRPB) [65]. The Institute for Radiation Protection (GSF) also provides similar data [66]. More recently, various research groups have modelled scanner geometry (including that of bow tie filters) [35,67,68] as well as voxel phantoms [24,35,68,69].

Difficulties with the Monte Carlo method include the need for detailed scanner geometry and the expensive computational time frequently associated with Monte Carlo simulations. Scanner geometry can be difficult to obtain as scanner design is often manufacturer-specific proprietary information. However, in the work done by Gu *et al*. 2009 [35], they successfully used an iterative trial-and-error approach to model a GE Lightspeed CT scanner. Results from their CT model were subsequently validated with measured CTDI values and dose profiles reported in the available literature.

The disadvantages associated with experimental dose measurements include (1) the need to understand the type of radiation dosimeter best suited for the measurement of low doses, (2) the tedious task of dosimeter characterisation, and (3) the subsequent placement of dosimeters into the anthropomorphic phantom for the direct measurement of organ doses. Experimental uncertainties can also be huge at low doses; a guideline provided by a recent IAEA report [70] states that a 20% measurement accuracy is

considered acceptable in diagnostic radiology dosimetry where organ doses are low and where the uncertainty for an absolute risk for a stochastic effect is high. In practice, it is probably reasonable to expect up to a 40% difference for out-of-field dose measurements with MOSFETs compared to Monte Carlo simulations in a CT cone beam as previously reported [36].

Another way to derive effective dose involves the use of a pre-established DLP -to-effective dose conversion coefficient k, depending on the anatomic region scanned (Table 2.3).

DLP is defined as DLP = $CTDI_{vol}$ x irradiated length; with modern helical scanners, the irradiated length is often longer than the prescribed scan range [28] so care must be taken when calculating DLP from $CTDI_{vol}$. However, most modern helical CT scanners also display the value of the DLP on the scanner console. The effective dose can then be calculated as follows:

Effective dose= DLP x k Eq. 2.4

Where k is a known coefficient, with units of mSv/[mGy-cm]).
However, as Frush and Yoshizumi (2006) [71] have stated, the DLP method is not useful for deriving individual patient doses as the DLP is derived from acrylic phantoms available in only two sizes. This is not representative of the range of human patient shapes and sizes. Indeed, using the DLP method to calculate individual patient effective doses has been reported to underestimate the actual radiation exposure for adult cardiac and pulmonary 64-detector CT angiography protocols [53]. Moreover, DLP does not provide any information about specific organ doses [53].

Table 2.3: Published k coefficients[a] (Reproduced from McCollough *et al* 2010 [47])

	k Coefficients (mSv/[mGy-cm])				
Anatomic region	Jessen et al., 1999 [72]	EC 2000	EC 2004, Appendix B	EC 2004, Appendix C and NRPB-W67	Phantom (cm)
Head	0.0021	0.0023	0.0023	0.0021	16
Head and neck				0.0031	16

Neck	0.0048	0.0054		0.0059	32
Chest	0.014	0.017	0.018	0.014	32
Abdomen	0.012	0.015	0.017	0.015	32
Pelvis	0.019	0.019	0.017	0.015	32
Chest, abdomen and pelvis				0.015	32

[a]Effective Dose=k*DLP, where DLP=console displayed dose-length product.

Radiation risk may be described using the following broad categories: negligible <0.1 mSv; minimal 0.1-1 mSv; very low 1-10 mSv, and low 10-100 mSv [47]. Differences of several mSv do not, in principle, imply any true differences in biologic detriment due to the many uncertainties used to derive the effective dose, such as differences in age, sex and body habitus. For the purpose of epidemiologic studies and/or individual risk estimates, McCollough et al 2010 [47] recommends the precise modelling of doses to specific tissues and organs in order to account for differences in individual patient body size and shape. Age- and sex- specific risk coefficients from the BEIR VII Report [73] should then be applied for individual patient risk estimates.

2.4.1 Risk of radiation-induced cancer

Radiation risk, whether perceived, potential or known [9], needs to be clarified when discussing the likelihood of developing cancer from ionizing radiation exposure from medical imaging.

For low dose risk to be detected and properly evaluated, a large population sample size needs to be considered. Figure 2.5 shows the relationship between average population dose and the population size required for detectable risk. The diagonal line demarcates the regions where risk is detectable. Of the nuclear incidents that have taken place in history, only the 1945 atomic bomb survivor study provides a large enough dataset for the evaluation of dose risks. However, below 200 mSv, due to population size constraints, the dose risk to the Japanese survivors cannot be reliably evaluated. Similarly, the exposed populations in the 1979 Three Mile Island (TMI) incident and the 1986 Chernobyl recovery worker group are too small for any conclusive relationship between low radiation doses and cancer induction [74].

As a general rule, the population size required to detect risk with 95% confidence is inversely related to the square of the average population dose [74]. As shown in Figure 2.5, in order to assess risk at 10 mSv (typical of a single phase abdomen-pelvic CT imaging scan), a sample size of 10 million (10^7) people is required. When the average population dose is increased tenfold to 100 mSv (typically of doses in CT perfusion imaging), the population size needed to detect risk is reduced by a factor of 100; a sample size of 10^5 people is required when the average population dose is 100 mSv.

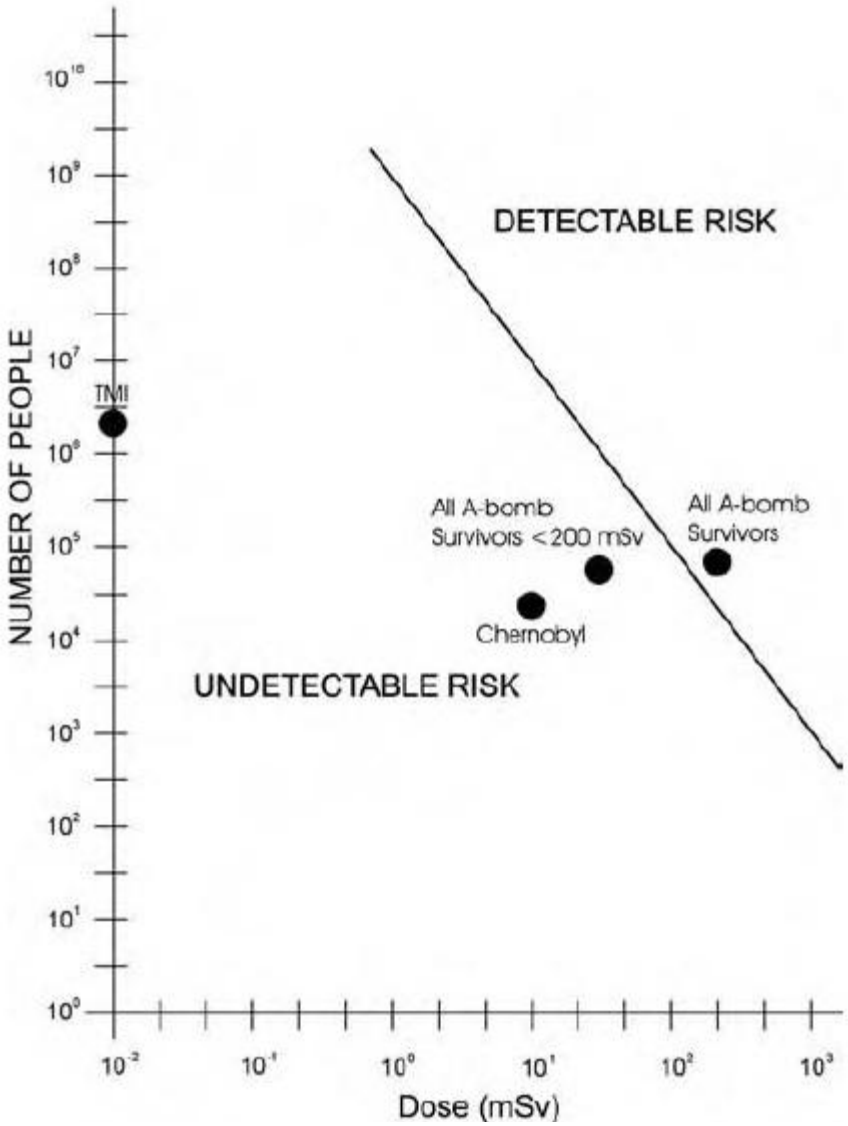

Figure 2.5: Population size needed to detect risk. The size of the population necessary to detect risk is very large and inversely related to the square of the dose (Pg 68, [74]).

As can be seen, it is not an easy task to estimate risk at low doses due to the absence of a sufficiently large population sample size. The BEIR VII report [73] adopts the stance of the linear no threshold (LNT) low dose response relationship (Figure 2.6) between exposure to ionizing radiation and the development of solid cancers in humans. This model is used for radiation protection purposes, where for doses < 100 mSv, the risk of stochastic effects (ie. cancer induction) is assumed to decrease linearly with decreasing dose with no threshold.

The LNT low dose response model is currently the most widely accepted model amongst organizations both at the international and at the national level, such as the ICRP and the UNSCEAR at the international level, and the UK HPA, US NCRP and the US BEIR committees at the national level. A more extensive discussion of existing low dose response relationships can be found in references [46,74,75] amongst many others. Figure 2.6 shows the LNT dose response relationship pictorially in relation to other known theories on low dose responses.

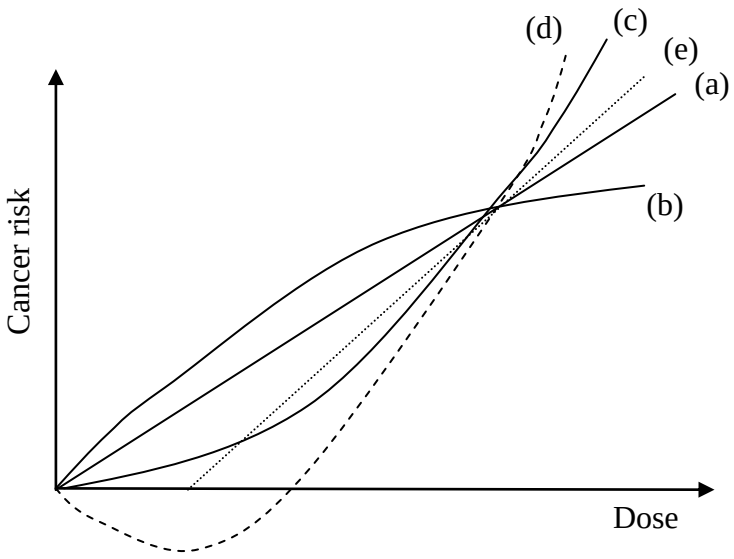

Figure 2.6: Low dose response curves in risk assessment (a) linear, no-threshold (b) sublinear (c) supralinear (d) hormesis (e) threshold. Figure from Pg.30, [74].

The BEIR VII lifetime risk model is shown in Figure 2.7. The Japanese survivors of the atomic bombings were the primary source of data in the BEIR VII report, used for estimating risks of solid cancers and leukaemia following low dose radiation exposure. In the BEIR VII model, for every 100 people exposed to 100 mSv of radiation, 1 person will likely develop a radiation-induced solid cancer or leukaemia. Incorporating the

LNT low dose response model, risk is extrapolated to lower doses. For example, for 10 mSv of radiation received, out of 1000 people, 1 individual would be expected to develop a radiation-induced solid cancer or leukaemia. It should be emphasized again, that below doses of 100 mSv, statistical limitations make it difficult to truly verify and/or assess risk in humans.

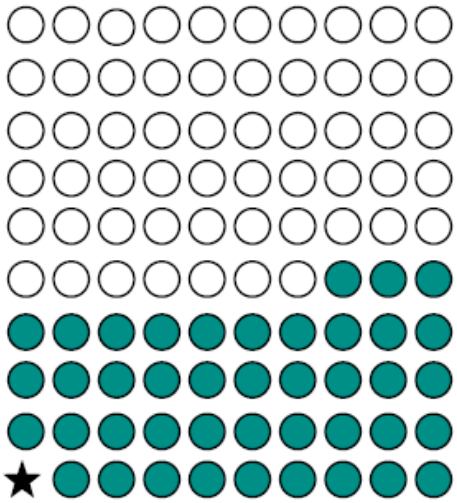

Figure 2.7: The BEIR VII Lifetime Risk Model. In a lifetime, approximately 42 (represented by solid circles) of 100 people will be diagnosed with solid cancer or leukaemia from causes unrelated to radiation. For a single exposure to 100 mSv of low LET radiation, 1 cancer (solid cancer or leukaemia, represented by a star) per 100 people could result (Figure reproduced from [73]).

The 4 dominant factors that influence the cancer risk after ionizing radiation are: (1) genetic considerations, (2) age at exposure, (3) sex and (4) fractionation and protraction of exposure [9]. Each of these factors is discussed as follows:

(1) Genetic considerations: genetic predisposition as well as the presence of gene mutations such as the ATM, BRCA1 and other repair pathway genes appears to account for why certain subpopulations are more radiosensitive than others.

(2) Age at exposure: Figure 2.8 shows the relationship between the lifetime attributable risk of cancer incidence and the age at exposure, with children being more radiosensitive than adults. The data fitted in the graph illustrates the decline in risk with age. However, it must be emphasized that while some solid

cancers show a decrease in risk with age, for many solid cancers, there is little difference in risk between 10 and 40 years of age (Figure 2.9). In particular, there appears to be an increase of lung cancer with increasing age as Figure 2.9 shows.

(3) Gender differences: From Figure 2.8, it can be seen that females have a higher lifetime attributable risk of cancer incidence compared to males. In particular, excess relative risk (ERR) for breast cancer is dominant since female breast glandular tissue is radiosensitive. It has been reported that when the breasts are directly irradiated during coronary CT angiography, a 0.2 to 2.2% increased lifetime relative risk for breast cancer results [10,76,77]. It has also been found that female paediatric patients are more susceptible to thyroid cancers. For a chest CT scan, risk estimates were 11 thyroid cancers per 10 000 scans at age 10 years for females, while that for males was 2 thyroid cancers per 10 000 scans at age 10 [78].

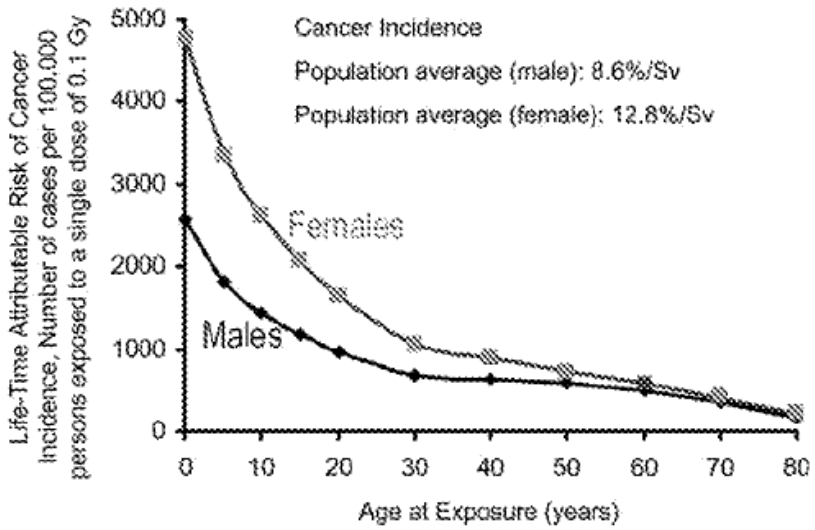

Figure 2.8: Graph shows the lifetime attributable risk of radiation-induced cancer incidence as a function of age at exposure for males and females. The graph is based on data from the atomic bomb survivors as analysed by the BEIR VII committee. Graph reproduced from [9] based on data from [41].

(4) Fractionation and total time of exposure: In general, the lower the absorbed doses and dose rate, the less the ERR due to the time lag for damaged DNA repair. A more extensive discussion of the effects of fractionation and

protraction of exposure may be found in other useful references[9,73,79-81]

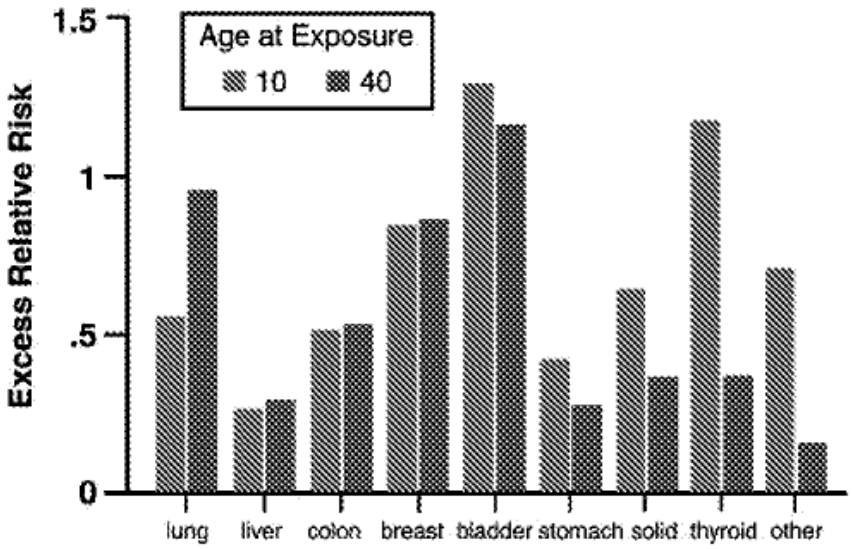

Figure 2.9: Graph shows the comparison of excess relative risk (ERR) at age 70 years for exposure at age 10 or 40 years for specific solid cancers for the atomic bomb survivors. Graph reproduced from [9], based on results from [82].

Of most concern is that the use of CT imaging is increasing, driven by the fact that CT is a fast and accurate diagnostic tool. In most cases, a CT scan is weighted in the patient's favour as individual risk is very small. However, seemingly small individual risks applied to an increasingly large population is what makes CT a potential public health issue in the coming decades [10], particularly in children.

Several authors have comprehensively analysed the risk of CT scanning on radiation induced carcinogenesis based on available epidemiological evidence [8,10,11,40,78,83], and concluded that for a typical CT study involving 2 or 3 scans, cancer risk can be directly assessed from epidemiological data without the need to extrapolate risks to lower doses [8]. For radiology usage for the years 1991-96, it was estimated that the cumulative cancer risk in the UK, US and Japan population up to 75 years old that could be attributable to diagnostic x-rays to be 0.6%, 0.9% and 3% respectively [40]. It is estimated that these proportions are now larger due to the rapid growth in the use of CT since 1996 [8]. In a separate report, it is estimated that the lifetime risk of fatal cancer following radiation exposure is approximately 12×10^{-2} Sv^{-1} (1.2% per 100 mSv) and 15×10^{-2} Sv^{-1} (1.5% per 100 mSv) in boys and girls younger than 10 years,

respectively[26,73].

Even as early as 2002, the ICRP commented that "the absorbed dose to tissue from CT can often approach or exceed the levels known to increase the probability of cancer"[84]. The BEIR VII report recommends that follow-up epidemiological studies be continued on patient cohorts undergoing CT scanning [73].

A recent study has noted a positive association between radiation dose from CT scans and the incidence of leukaemia and brain tumours [85]. In addition, a recent Australian epidemiological study also provides direct evidence that CT scans during childhood and adolescence result in an increase in overall cancer incidence and for many individual types of cancer, such as that of the digestive organs, skin, soft tissue, female genital, urinary tract, brain and thyroid [86].

2.5 Skin dose

Larger patients often receive larger skin dose because they require more energetic radiation to reach the tissues in their bodies for imaging, while smaller patients will receive a relatively larger dose to their internal organs for the same exposure settings.

Since internal organs are more radiosensitive than the skin, this usually results in the smaller patients (children or adults with a smaller build) incurring a higher effective dose for the same CT settings and, hence, have a larger stochastic risk of cancer.

Children have been estimated to be up to ten times more radiosensitive than adults undergoing CT [26]. Moreover, there is a tendency in a CT setting for a lack of size-based adjustments and for adult CT scanning protocols to be simply taken from adult CT procedures [18]. This exposes the pediatric patient to higher doses than is necessary for an accurate diagnosis.

As mentioned earlier in section 1.1, in recent years, leading CT manufacturers, such as Toshiba, Siemens, GE and Phillips have incorporated automatic tube current modulation into their CT scanning systems which adjusts tube current according to patient body size

and thickness for dose reduction. The intensity of the photon beam in this case also affects patient skin dose.

The IAEA has recently reviewed the use of lifetime dose monitors to track an individual's lifetime dose as part of the effort for dose traceability [87].

2.6 Radiological Dose Quantities and Units

The most commonly encountered radiological dose quantities include: exposure, kerma and absorbed dose. The formal definitions of these dose quantities are useful in that they lead to the formal understanding of the interaction of x-ray photons with matter.

2.6.1 Exposure

Exposure is defined as the ionisation of x-ray photons in air. It is equivalent to air kerma. The old unit Roentgen R is now obsolete and has been replaced by the SI unit C kg^{-1}. Nonetheless, a conversion between units exists and is as follows:

$$1\ R = 2.58 \times 10^{-4}\ C\ kg^{-1} \qquad \text{Eq. 2.5}$$

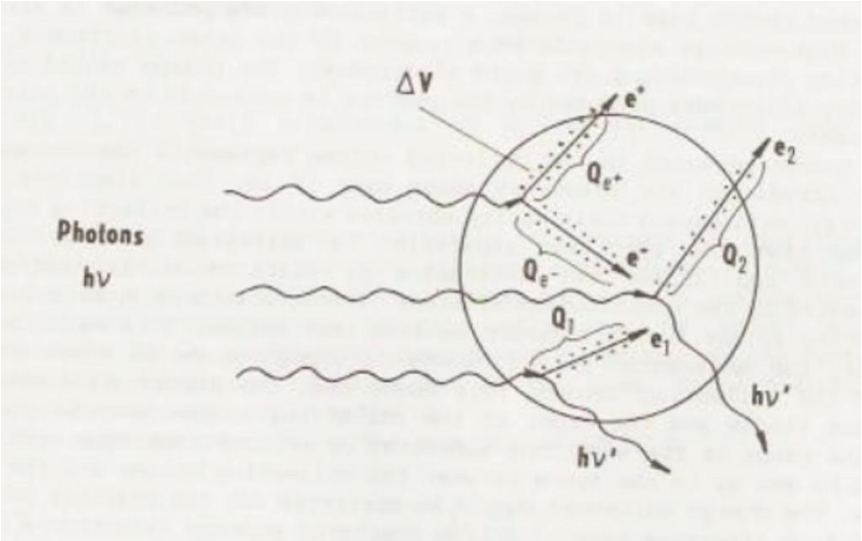

Figure 2.10: The components of the charge included in exposure according to its definition (Reproduced from Pg 57, [92])

Figure 2.10 illustrates exposure X, defined by the International Commission on Radiation Units and Measurements (ICRU) as:

$$X = \frac{dQ}{dm} \qquad \text{Eq. 2.6}$$

where dQ is the absolute value of the total charge of the ions of one sign produced in air when all the electrons liberated by photons in air of mass dm are completely stopped in air. dQ does not include ionisation due to the photons emitted by electrons.

In terms of the photon spectral energy fluence Ψ_E, exposure X may similarly be defined as:

$$X = \frac{e}{W} \int \Psi_E \frac{\mu_{en}(E)}{\rho} dE \qquad \text{Eq. 2.7}$$

where $\mu_{en}(E)/\rho$ is the mass energy absorption coefficient for air at energy E,

e is the elementary charge,

W is the mean energy deposited in air per ion pair formed

It is assumed that electronic equilibrium exists at a given point of interest where the number of electrons entering a small volume V is the same as the number of electrons leaving it. The principle of electronic equilibrium in air is applied in the use of the free-air ionisation chamber as shown in Figure 2.11.

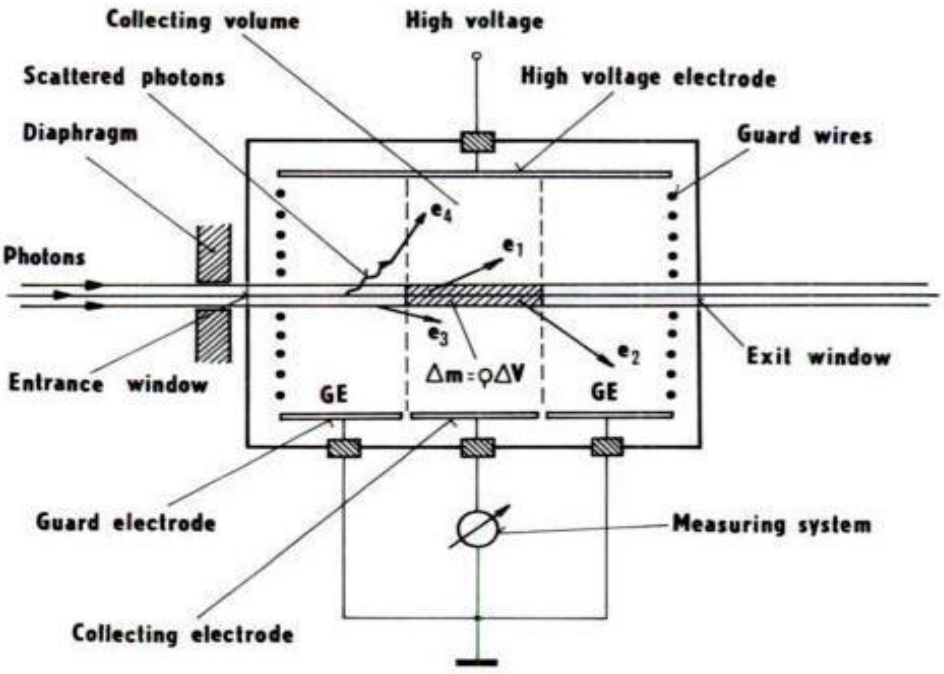

Figure 2.11: Schematic diagram of a free-air chamber used for the measurement of exposure (Reproduced from Pg 59, [92])

A free-air ionisation chamber is an absolute dosimeter used primarily in standard laboratories for the calibration of other dosimetric devices. It provides an accurate measurement of the exposure unit.

This instrument consists of a radiation shielded container which houses electrodes, to which a photon beam passes from the entrance window to the exit window. When a voltage is applied at the high voltage electrode with respect to the other electrodes (guard and collecting electrode), ionisation of the incoming photon beam results. The secondary electrons are then collected on the electrodes.

The measured charge in collecting volume V with mass M therefore represents the ionisation in that volume. Referring to Figure 2.12, electrons such as e_1 expend all of their energy within volume V provided the electrode separation is large enough. Under electronic equilibrium, the ionisation by outgoing electron e_2 is completely matched by the contribution by incoming electron e_3. For this to occur, the distance between the entrance window of the ionisation chamber and the front of the collecting volume must be larger than the range of the secondary electrons. The same principle applies for the exit window of the ionisation chamber and the rear end of the collecting volume. For accurate measurements, the collected charge is corrected for contributions from electrons resulting from scattered primary photons such as in the case of e_4. Additional corrections such as ambient temperature, humidity, pressure, photon attenuation effects between the diaphragm and the centre of the collecting electrode, beam collimation, field distortion, ion recombination and stray radiation ensure the most accurate experimental measurements obtainable [92]. In addition, guard wires connected to a resistance divider are used to ensure a uniform electric field throughout the voume between the electrodes.

2.6.2 Kerma

Kerma, K, stands for Kinetic energy released per unit mass. In equation form,

$$K = \frac{d\overline{E_{tr}}}{dm} \qquad \text{Eq. 2.8}$$

SI unit: J kg^{-1} or Gy

where dE_{tr} refers to the sum of the initial kinetic energies of all produced charged particles in a mass m of a particular material.

Kerma is applicable to all types of uncharged particles in any material, unlike exposure which only applies to photon radiation in air. Kerma essentially refers to the 2-stage process that takes place when uncharged particles interact with matter. In Stage 1, uncharged particles transfer their energy to the kinetic energy of the produced charged particles. Stage 2 involves processes concerned with the energy deposited by these charged particles.

For polyenergetic photons, kerma K can be written as follows:

$$K = \int_E \Psi_E \frac{\mu_{tr}(E)}{\rho} dE$$

where Ψ_E is the spectral energy fluence of uncharged particles

and μ_{tr}/ρ is the mass energy transfer coefficient of the uncharged particles in the specified material.

As mentioned in the previous section, air kerma K_{air} replaces the obsolete quantity exposure X. To sum up, the quantities K_{air} and X, positioned at a point of interest in air with an energy fluence of Ψ, are related as follows [92]:

$$X = \frac{e}{W_{air}} \left(\frac{\mu_{en}}{\rho}\right)_{air} \Psi \qquad \text{Eq. 2.9}$$

$$K_{air} = \left(\frac{\mu_{tr}}{\rho}\right)_{air} \Psi \qquad \text{Eq. 2.10}$$

Therefore, K_{air} expressed in X is:

$$K_{air} = \frac{1}{1-g} \frac{W_{air}}{e} X \qquad \text{Eq. 2.11}$$

where g is the fraction of the initial kinetic energy of the electrons lost in

bremsstrahlung production.

2.6.3 Absorbed Dose

The primary physical quantity used in radiation dosimetry is absorbed dose, often simply referred to as dose [93]. Absorbed dose D is defined as the expectation value of the energy ε (a stochastic quantity) imparted to matter per unit mass at a point P in some finite volume V, to produce any effect attributable to radiation [94]. This means that, if D = 0, there is no radiation effect. While some kinds of radiation effects are proportional to D, other effects depend on D in a less straightforward manner [94]. For diagnostic energies, absorbed dose and kerma are equal.

Unlike exposure which is only defined for air (as described in section 2.1.1), absorbed dose is defined for any type of radiation (including both ionizing and non-ionizing), as well as for any kind of material. Symbolically, absorbed dose D at any point P in volume V is expressed as:

$$D = \frac{d\varepsilon}{dm} \qquad \text{Eq. 2.12}$$

SI unit: J kg^{-1} or Gy

where dε is the mean energy imparted in an infinitesimal volume dv at a point P during a certain time interval, and dm is the mass in dv.

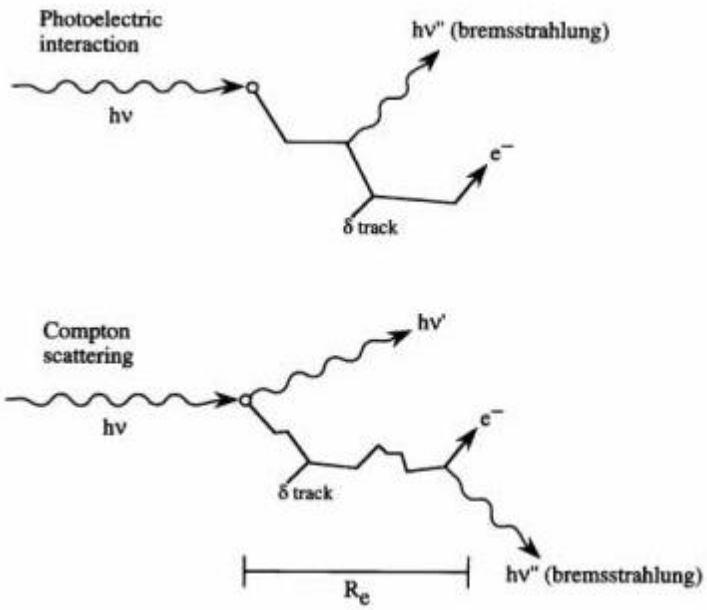

Figure 2.12: Energy transfer and absorption is a two-stage process. A photon with energy hν interacts with an atom of the medium, transferring all (photoelectric effect) or some of its energy (Compton scatter) to an electron. The kinetic energy of the electrons is deposited in the medium mostly by ionisation, although some may be lost as bremsstrahlung and other radiative processes. Kerma, or the transfer of energy, occurs at the point of interaction. Absorbed dose, however, is along the path of recoiling electrons determined by their range R_e in the medium. (Reproduced from Martin 2000)

At kilovoltage energies, the range of electrons is normally so short that kerma (energy transferred E_{tr}) can be sufficiently approximated to absorbed dose (energy absorbed E_{ab}). Note that the illustration of bremstrahlung, which is the result of very highly energetic incoming radiation, is also not relevant to kilovoltage energies (up to 300kVp) considered in this thesis.

The basis for the design of accurate dosimeters is most often referred to as the Bragg-Gray Cavity Theory, illustrated in Figure 2.13.

2.6.4 Cavity Theory

To measure dose deposited in a medium in the presence of ionizing radiation, a dosimeter (known as a cavity) is often placed within the material medium itself. Cavity theory, in effect, relates the dose absorbed in the medium to that absorbed by the cavity (dosimeter placed in the medium).
The following equation summarizes:

$$D_{med} = D_{cav} f_{med,cav} \qquad \text{Eq. 2.13}$$

where D_{med} is the dose to the medium of interest, D_{cav} is the average dose measured by the cavity (dosimeter placed within the medium) and $f_{med,cav}$ is the factor that corrects for variation in beam quality, radiation type, medium, size and composition of the cavity. ([95],[96]).

For a small cavity compared to the range of electrons incident on the cavity, the Bragg-Gray relation applies as follows:

$$f_{med,cav} = s_{med,cav} \qquad \text{Eq. 2.14}$$

where $s_{med,cav}$ is the average mass stopping power ratio of the electrons in the medium to

the cavity.

For a large cavity on the other hand, where "large" cavity refers to the range of electrons incident on it, the dose in the medium is more accurately described by the ratio of the mass energy absorption coefficent of the medium to the cavity material, averaged over the photon energy fluence spectrum present in the medium, neglecting any perturbation effects resulting from the introduction of the cavity into the medium:

$$f_{\text{med,cav}}=\left(\frac{\mu_{en}}{\rho}\right)_{med,cav} \qquad \text{Eq. 2.15}$$

A more general cavity theory proposed by Burlin (1966) takes into consideration that in practice, many of the dosimeters used are classified more as intermediate-sized cavities, whereby the dose registered by the dosimeter is due to the combined contribution of electrons generated both in the medium as well as within the cavity itself. The equation as follows

$$f_{\text{med,cav}}= ds_{\text{med,cav}} + (1\text{-}d)\left(\frac{\mu_{en}}{\rho}\right)_{med,cav} \qquad \text{Eq. 2.16}$$

where d is a weighting factor that describes how much of the dose contribution is due to the photon interactions in the medium compared to the dose contribution within the cavity. For d=0, a large cavity is represented where dose (from electrons) is solely the result of photon interactions in the cavity. For d=1, a small cavity is described where dose from electrons is produced by photon interactions in the medium only. An intermediate cavity has weighting factor d which lies between 0 and 1.

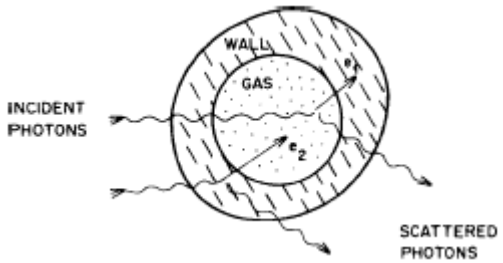

Figure 2.13: Gas in cavity v enclosed by a wall to illustrate the Bragg-Gray principle (Reproduced from Pg 368, [93])

Two assumptions are adopted when applying the Bragg-Gray Cavity Theory [94] to determine the dose to the material medium of interest.

Firstly, it is assumed that the material volume is small enough such that its presence will not perturb the existing radiation field. Secondly, the assumption is that this material volume is large enough to ensure electronic equilibrium within the volume, where each electron e_1 carrying a certain amount of energy out of v is compensated by another electron e_2 carrying the same energy in. In other words, the same ionisation occurs in v as if all electrons remained.

With these assumptions, it now becomes possible to mathematically describe how a photon detector works.

A photon detector is one that responds only to photons in its environment. Assuming electronic equilibrium and negligible photon attenuation in the detector, the ratio of dose to the medium of interest to dose in the detector is equal to that of the ratio of mass energy absorption coefficients of the medium to the detector (equation 2.17) that will valid for most used solid state detectors in low energy photon radiation field .

$$\frac{D_{med}}{D_{det}} = \frac{(\frac{\mu_{en}}{\rho})_{med}}{(\frac{\mu_{en}}{\rho})_{det}} \qquad \text{Eq. 2.17}$$

Likewise, an electron detector is defined as a detector that only responds to electrons. In such a situation, the ratio of dose to the detector D_{det} to dose in the medium D_{med} is equivalent to the ratio of the restricted mass collision stopping power $\frac{\bar{L}_{col}}{\rho}$ of the detector to the medium, expressed by the following equation:

$$\frac{\bar{D}_{det}}{D_{med}} = (\frac{\bar{L}_{col}}{\rho})^{det}_{med} \qquad \text{Eq. 2.18}$$

In medical physics, absorbed dose in human tissue is mostly the medium of interest. It follows that the ideal detector is tissue equivalent for accurate dose measurements. While LiF TLDs are tissue equivalent, they do not offer the many advantages that silicon detectors typically provide such as real-time dosimetry (where time constraint is a priority in the clinical scenario). The use of silicon based detectors will be described in section 2.3.

2.6.5 CT Dose Indices

The Computed Tomography Dose Index (CTDI) was developed more than 20 years ago for the purpose of quality assurance (QA) and dose optimisation (DO)[72]. It is a standardized measure of the dose output of a CT scanner that is often used to compare different scan protocols on a single scanner, monitor scanner drift with time or measure different dose outputs across different scanners. Comparison of $CTDI_{vol}$ values against known DRLs offers reassurance to both patient and medical provider that the equipment is operated in a manner consistent with the current standard of care.

Both regular QA and periodic DO is particularly important in CT, since CT delivers considerably more dose to the patient due to multiple rotations of the CT x-ray tube about the patient as compared to conventional screen-film projection radiography. It has been well documented that CT also lacks the visual cues to alert the operator of excessive radiation dose delivered [48]. In fact, overexposure often leads to a better image in CT, which works against the risk-benefit objective of radiological imaging in the first place.

The CTDI was first introduced by Shope et al (1981) [97] as the integral of the single slice dose profile for a single axial scan (i.e. one rotation of the x-ray tube) along the z-axis, normalized to the nominal beam width, also known as the slice thickness. The CTDI concept is illustrated in Figure 2.14.

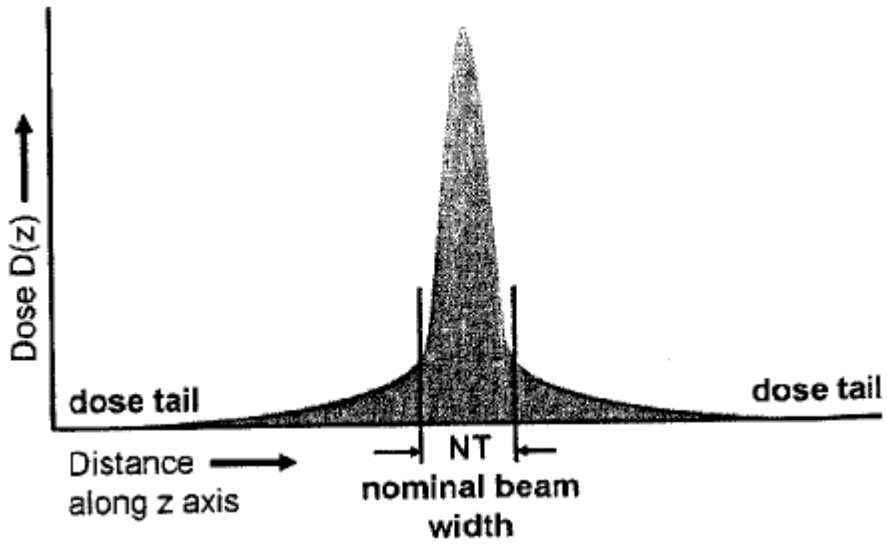

Figure 2.14: The radiation dose profile along a line perpendicular to the plane of a single axial CT scan shows a peak where the primary beam slices through the CTDI phantom. The tails of the dose profile are caused by scattered radiation. The integral of the area under the curve is normalized to the nominal beam width NT to determine CTDI. A $CTDI_{100}$ value is obtained if integration limits of ±50mm are used. (Reproduced from [48]).

Figure 2.15 illustrates the Multiple Scan Average Dose (MSAD) profile; as can be seen, the CTDI is used to estimate MSAD. MSAD is defined as the average dose over one scan interval in the central portion of a multiple scan dose profile. In this case, the CTDI includes the multiple rotational motion of the x-ray tube at the centre of a series of axial scans. With corrections for scan spacing, the CTDI estimates MSAD in a convenient manner.

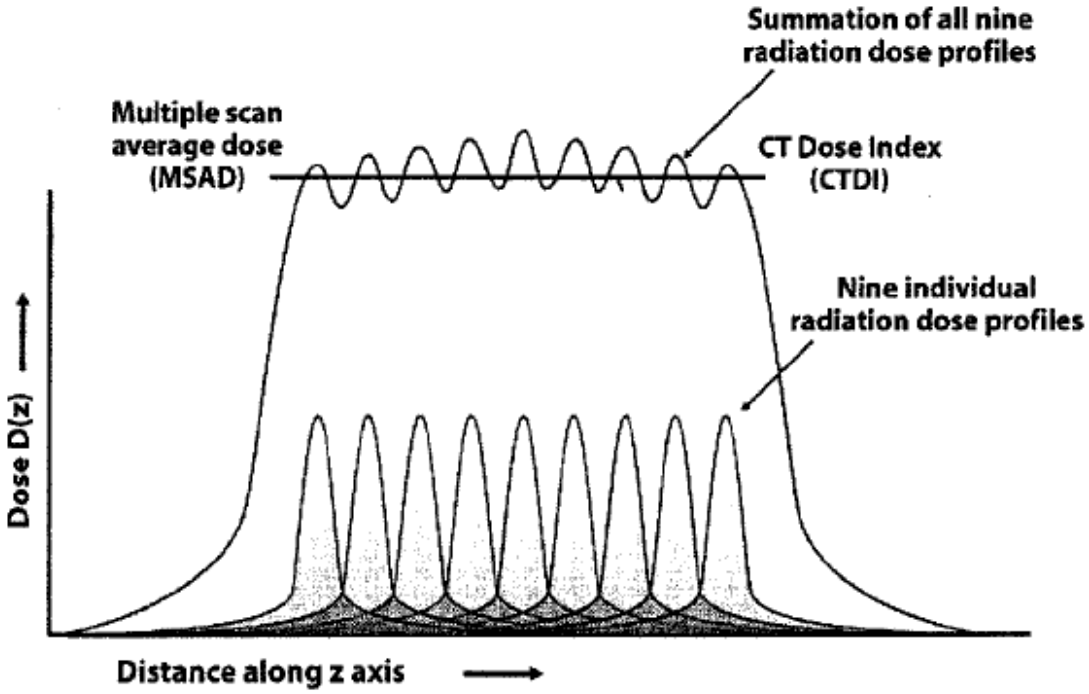

Figure 2.15: The radiation dose profiles from nine adjacent axial CT scans along a line perpendicular to the axial scans, when summed, produce the MSAD profile. The MSAD is measured with the use of point detectors such as TLDs and solid state dosimeters or film (Reproduced from [48]). The limits of integration determine how much dose from the scatter tails is included.

In theory , the ideal CTDI at a point (x,y) in the scan plane is given by

$$CTDI_{ideal} = \frac{1}{T}\int_{-\infty}^{+\infty} \mathrm{D(z)dz} \qquad \text{Eq. 2.19}$$

where D(z) is the longitudinal (z-axis) single scan dose profile at a point and T is the nominal slice width, also known as the full-width at half-maximum (FWHM) of the image sensitivity profile [98,99].

Dose indices used routinely to characterise CT exposure include the $CTDI_{100}$, $CTDI_{w}$ and $CTDI_{vol}$.

Figure 2.16 illustrates the typical setup for the practical measurement of CTDI. Measurements are done in either a homogeneous PMMA cylindrical phantom ($CTDI_{PMMA}$) as shown in the figure, or in air ($CTDI_{air}$). The 10 cm active length of the CT pencil ionisation chamber sums the total area under a single slice dose profile which also includes the effect of scatter.

For measurements of $CTDI_{PMMA}$, a 16 cm or a 32 cm diameter phantom is used. The 16 cm diameter standard head phantom represents an adult CT head or pediatric CT body

scan, while the 32 cm diameter standard body phantom represents an adult CT body scan.

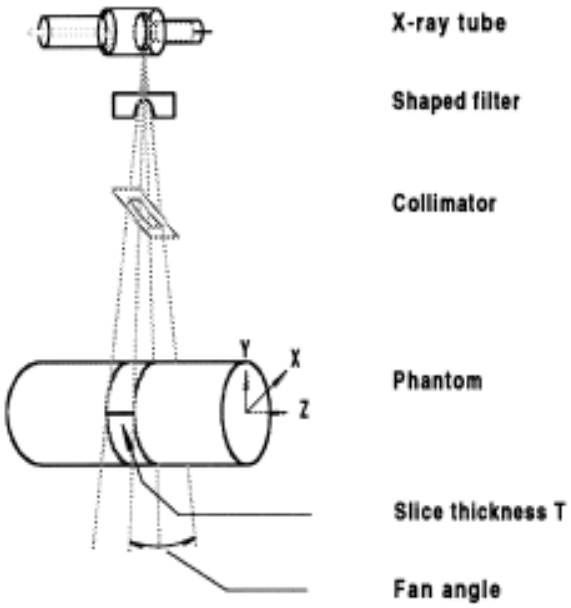

Figure 2.16: Schematic representation of the radiation beam and a typical cylindrical phantom used for CT dosimetry (Reproduced from [72])

The International Electrotechnical Commission (IEC) [100] defines $CTDI_{100,\,j}$ as:

$$CTDI_{100,j} = \frac{1}{NT}\int_{-50mm}^{+50mm} D(z)dz \qquad \text{Eq. 2.20}$$

where NT refers to the nominal collimated slice thickness (also approximately equal to the total beam width) in multislice scanners, j refers to the air kerma measurement at the phantom centre (as in $CTDI_{100,c}$) or periphery (as in $CTDI_{100,p}$). By definition, $CTDI_{100}$ refers to the average air kerma at the centre of the scan length z = 0 accumulated over a total scan length of 100 mm with contiguous slices.

It follows that the weighted CTDI ($CTDI_w$) is a measure of the average dose, a weighted combination of the central and peripheral doses as described by equation 2.21, on the basis of the assumption that dose decreases linearly with radial position from the surface to the centre of the phantom [101].

$$\mathrm{CTDI}_w = \frac{1}{3} CTDI_{100,c} + \frac{2}{3} CTDI_{100,p} \qquad \text{Eq. 2.21}$$

Finally, the volume CTDI (CTDI_{vol}) is the quantity that is displayed on the operator's console for modern helical MSCT scanners.

$$CTDI_{vol} = \frac{CTDI_w}{p} \qquad \text{Eq. 2.22}$$

where p is the pitch, otherwise known as the ratio of table feed per gantry rotation and total beam collimation. CTDI_{vol} is given in units of mGy and describes the average local dose within the scanned volume[101].

In recent years with the introduction of multislice helical CT scanners, total beam widths have exceeded 10 cm and tube rotation times are now less than 1 s. The prototype Toshiba 256-section system and the C-arm based cone beam systems have a nominal beam width of 12 cm [48], and the problem with using a pencil ionisation chamber with an active length of 100 mm is that much of the scatter tails are not collected which leads to a possible underestimate of the true dose [102]. This requires alternative ways of assessing dose. To address the issue of dose measurement in wide beam widths towards a more accurate approximation of individual patient dose, Brenner et al [103] suggests replacing the CTDI concept with more direct measurements of organ dose in realistic anthropomorphic phantoms on modern helical CT scanners, with the use of real-time MOSFET readouts or TLD measurements.

2.7 Properties of an ideal dosimeter

An "ideal" dosimeter does not exist in practice, and depending on the measurement situation, desirable dosimeter characteristics may vary accordingly. It is suggested that an ideal dosimeter demonstrates the following properties [94,104]:

- High accuracy and precision
- Linear response with dose
- Dose rate independence
- Energy independence
- Angular independence
- Good spatial resolution and small physical size
- Readout convenience

- Convenience of use

The description of each of the following properties closely follows that of reference [104]:

- Accuracy and precision

  Accuracy refers to how close the measured result is to the "true value". In practice, the parameter "uncertainty" characterises the inaccuracy of the result. Standard uncertainty u_c is expressed as:

$$u_c = \sqrt{{u_A}^2 + {u_B}^2}$$

  Where u_A refers to Type A uncertainties and u_B refers to Type B uncertainties [105].

  Precision refers to the reproducibility of repeated measurements obtained under similar conditions. A small standard deviation of results distribution indicates a high precision.

- Linearity

  A dosimeter should exhibit a linear dose response. Any non-linear behavior beyond a certain dose range should be corrected for.

- Dose rate dependence

  A dosimeter should have a dose response that is independent of dose rate, else this quantity needs to be corrected for.

- Energy dependence

  Energy dependence is broadly defined as the variation of the response of a dosimetry system with beam quality. When dosimetry systems are calibrated in a narrow radiation beam quality and subsequently used over a much wider energy range, this results in an energy dependent response. This energy response requires correction, by means of an appropriate scaling coefficient. The energy response of an ideal dosimeter is flat. Correction of the energy dependent response is necessary in the case of non-tissue (water) equivalent

dosimeters, since dose to tissue (water) is the medium of interest in medical physics.

- Angular dependence

  Angular dependence is defined as the variation in response of a dosimeter with the angle of incidence of radiation. In the ideal situation, dose response is independent of dosimeter orientation. However, angular dependence is an inherent property of practical dosimeters as a result of their construction, packaging or physical size. In-vivo dosimetry, in particular, requires that angular response corrections be applied.

- Spatial resolution and physical size

  Dose, as defined earlier, is essentially a point quality. Therefore, it is appropriate for a dosimeter to measure dose in a very small volume (point dosimeter) within a known spatial location.

- Readout convenience

  It is preferable to use a dosimeter that gives an instantaneous reading (such as ionisation chambers and solid state dosimeters) rather than a dosimeter that requires processing (such as film and TLDs).

- Convenience of use

  Some dosimeters are reusable (TLDs, semiconductor-based, OSL) while some are not reusable (film). Some dosimeters are more rugged and can withstand shocks (such as the ionisation chamber, whose sensitivity is not easily affected by mechanical pressure for example) as compared to others that are more sensitive to handling (TLDs).

Table 2.4 summarizes the advantages and disadvantages associated with the more traditional dosimeters, such as the diode and TLD and the more recently clinically applied dosimeters such as the MOSFET, radiochromic film and OSL. Table 2.5 summarises the basic characteristics associated with each type of dosimeter.

Table 2.4: Advantages and disadvantages associated with the MOSFET, diode, radiochromic film, TLD and OSL radiation dosimeter.

Dosimeter	Advantages	Disadvantages
MOSFET	• thin active area and small size • high sensitivity • near real-time dose readout • use of a small power source • immediate reuse • retention of dose history • simple instrumentation	• Sensitivity changes with accumulated dose • limited lifespan • precision in measurement is reduced at lower doses • temperature dependence
Diode	• small size • high sensitivity • instant readout • simple instrumentation	• Sensitivity changes with accumulated dose • Requires connecting cables • temperature dependence
Radiochromic film	• 2D spatial resolution • high sensitivity over a broad dose range • self development • easy to use	• Some period of development time is needed (6 hours at best between measurements and dose readout, although the current recommendation is at least a day) • Not reusable
TLD	• small size; point dose measurements possible • reasonably tissue equivalent • offline mode possible since they do not require electrical connections • ability to store accumulated dose • reusable	• no instant readout; readout and calibration is time consuming • signal erased during readout • accurate readout requires specialized technical training and extra care
OSL	• Minimal signal loss for repeated readout measurements • Simpler readout process using light instead of heat • Stable signal after 8 minutes post-irradiation • Reusable	• tends to accumulate a residual signal even after optical bleaching with fluorescent light

Table 2.5: Summary of characteristics of the MOSFET, diode, radiochromic film, TLD and OSL radiation dosimeter

Dosimeter / Property	Diode	MOSFET				TLD	Radiochromic film	OSL
Sensitivity	0.3 nC/cGy	1 mV/cGy		2.7 mV/cGy				
Reproducibility	>1 cGy < 0.5%	20 cGy 100 cGy 200 cGy	< 8% < 3% < 2%	20 cGy 100 cGy 200 cGy	< 3% < 1.2% < 0.8%			3% at an air kerma of 4.5 mGy
Lifetime	>10 000 Gy	200 Gy		70 Gy		reusable	Single use only	
Lower limit of detection		0.15 cGy with 25% uncertainty at 68.3% confidence level (TN model 1002 RD)				0.005 cGy (TLD-100)[1] <0.0006 cGy (TLD-100H)[2]	4 mGy (10% uncertainty) at an effective energy of 44 keV	
Creep-up effect	N/A	Up to 4 mV 4% for 100 cGy, 20% for 20 cGy				NA	NA	NA
Signal fading	N/A	Up to 2% for 200 cGy at 15 minutes, possibly greater for lower doses				< 10% per year	Best readout after 24 hours	
Detector size	0.8 mm x 0.8 mm	0.2 mm x 0.2 mm				1 mm x 1 mm crystals; may be smaller depending on physical form; powder, rods, ribbons	Available in sheets of 8”x10” or 14”x 17” and cut to preferred size depending on user needs.	
Effective atomic number at kilovoltage energies Z_{eff}(tissue)=7.64	Z_{eff}(silicon)=14	Z_{eff}(silicon)=14				Z_{eff}(LiF)=8.2	Z_{eff}(EBT)=6.98 Z_{eff}(EBT2)=6.84 Z_{eff}(MD55)=6.5	Z_{eff}(Al_2O_3)=11.2
Energy dependence	6% to 39% between Co-60 and 15 MV depends on packaging	Up to 3.2 at 75 kVp relative to 6 MV photon beam (TN model 1002 RD)				Energy response 30keV/1.25MeV 1.7 (TLD-100) 1.25 (TLD-100H)	EBT2 film 6.5±1% (50kVp to 10 MV)	• 20 to 30 % energy dependence in the kVp range from 80 to 140

					kVp. • About 3.2 at 50 kVp relative to Co60 gamma rays.
Angular dependence	±12% in commercially available diodes	< 3 % angular dependence at 70 kVp tube potential in a soft tissue equivalent phantom	None		No angular dependence when irradiated within a tissue equivalent cylindrical phantom
Depth dose tissue equivalence	Overestimation of 7% at 10 cm depth at 6 MV	Tissue equivalent in a homogeneous soft tissue equivalent phantom at a tube potential of 70 kVp. Depending on MOSFET directional orientation at depth, the epoxy attenuation effect may result in up to a 21% under-response at shallow depths of 1 cm.[106]	NIL		
Temperature dependence		By selecting a thermostable point on the current-voltage (I-V) curve, temperature dependence is minimized.	NIL	Stable at temperatures up to 60^{o}C	Within the temperature range 21^{o}C to 36^{o}C, the temperature dependence was not statistically significant within an uncertainty of 0.7%
Selected references	[107-111]	[23,106,112-114]	[115,116]	[117-121]	[122-125]

1. TLD-100 is LiF:Mg, Ti
2. TLD-100H is LiF:Mg, Cu, P

2.8 Dosimeters for clinical radiological dose monitoring

2.8.1 Overview of commercial dosimeters available

The assessment of skin dose is particularly useful in interventional radiology and CT perfusion imaging where maximum skin dose is known to approach deterministic levels. [126-128]. With timely dose information in the clinic, it can be expected that radiation-induced skin injuries will be avoided and this will further allow the optimisation of standard imaging protocols for individual patients in an interventional radiology setting.

The Unfors Patient Skin Dosimeter (PSD) is a commercially available product that is available for use in CT and fluoroscopy procedures to prevent excessive dose exposures and to avoid skin lesions. It works to decrease patient dose by sounding an alarm at intervals of 50 cGy as doses approach the deterministic dose limit of biological injury of 2 Gy [129]. This system uses a silicon sensor to monitor skin doses. A recent study has demonstrated the practical use of such a dosimeter to ensure occupational safety in interventional cardiology [130].

Another commercial radiation dosimeter that is the subject of many clinical investigations is the Thomson Nielson MOSFET (currently Best Medical,Canada[131]). This dosimeter has an epoxy bubble which provides protection of the chip and the necessary build-up for electronic equilibrium in kVp X-ray beams. It is designed to be used with the epoxy bubble facing the beam. This MOSFET has been the subject of numerous dose investigations in clinical radiological applications [32,71,126]. The next section outlines previous literature on MOSFET characterisation in a range of different quality radiation beams.

Landauer (Glenwood, Ill) makes an Optically Stimulated Luminescence (OSL) CTDI probe to measure the CT dose profile which is then integrated to determine the $CTDI_{100}$ [132]. The OSL probe is essentially an OSL-coated film substrate that is placed within a light-tight plastic cylinder. The probe is subsequently exposed in a CTDI phantom and can be readout on-site with a precision scanning laser. OSL dosimeters have been used in preliminary investigations to monitor surface and thyroid doses in multi-slice scanning [133] and skin doses during cerebral CT perfusion [133,134].

RTI Electronics (Gothenburg, Sweden) makes a solid-state real time dosimeter (Model CT-SD16) [135] . The probe is shaped like a CT pencil ionisation chamber, and consists of a thin-walled aluminium tube filled with plastic and containing 2 sub-millimetre thick solid state detectors located 16 cm apart. One detector is near the tip of the probe while the second is near the middle. The probe is coupled to an electrometer which records the dose measured in milli-second to micro-second time intervals from the start of the measurement, from which the dose profile is subsequently derived. More details can be found in [136].

2.9 MOSFET Characterisation studies

Dosimeter characterisation is necessary so that the behaviour and corresponding physical characteristics of the dosimetry system can be fully understood. This is a necessary first step to ensure that patient or phantom measurements that are subsequently obtained are reliable. In the following section, we summarize previous characterisation attempts, focusing particularly on the MOSFET radiation dosimeter.

Perhaps the most extensively characterised MOSFET dosimetry system to-date is the Thomson-Nielson MOSFET dosimetry system. Characterisation attempts are reflected in the experimental investigations of Bower & Hintenlang 1998 [137], Pomije *et al.* 2001[138] and Roshau & Hintelang 2003[114] among several others [21,113,139-142].

MOSFET dosimeter simulation models have been built to further study the physical characteristics and to better explain the reasons for MOSFET behavior. Wang *et al.(*2003, 2004, 2005) [143-145] gives greater insight into MOSFET geometry and materials that explain energy dependences due to interactions of radiation in the MOSFET structure.

Lavallee et al. (2006) [146] investigated the relationship of the integrated dose dependence and MOSFET sensitivity over an energy range relevant to radiotherapy and radiology applications. The radiation sources used were Co-60 with effective energy 1.25 MeV, Ir-192 with effective energy 380 keV and an orthovoltage unit providing X-ray spectra with tube potentials of 30 kVp and 150 kVp corresponding to effective

energies of 14.8 keV and 70.1 keV respectively. They found that the MOSFET sensitivity, expressed as a water calibration factor CF_w, which relates the threshold voltage shift V_T of the MOSFET to the dose it received, decreases with increasing V_T; the CF_w value is stable for Co-60 irradiations but decreased by 6%, 5% and 15% for beam energies of Ir-192, 150kVp and 30kVp. Moreover, it was also observed that the CF_w value drifts along the entire lifetime of the MOSFET for low x-ray energies such as that used for radiology, brachytherapy and surface therapy, and the decrease rate is higher for the first half of the device lifetime. Consequently, they recommended that the MOSFET is re-calibrated every 2500 mV. Doses should be reported as the average of several measurements since reproducibility is poor at low energy.

Attempts to ascertain the best type of dosimeter for monitoring dose in radiology has been performed by Dong et al. (2002) [140] with the characterisation of both MOSFET and TLD-100H. The authors found that with the TLD-100H, it was not necessary to correct for energy dependence over the range 40 kVp to 125 kVp, but this was not the case for MOSFETs. As the tube potential increased from 40 to 125 kVp, sensitivity was observed to decrease for MOSFETs. Therefore, this warrants the use of an energy correction factor within the tube potential 40 to 125 kVp, with an energy correction factor of 1.09 at 70kVp relative to 125kVp.

Benevides & Hintenlang (2006) [141] found that energy and angular response varied with the dosimeter model studied, typically increasing with tube potential through the mammography energy range (22-50 kVp). They attributed the variations in angular dependence to the asymmetrical MOSFET structure and the presence of packaging components. Also, in agreement with previous literature, the authors reported a decrease in angular dependence at 70 kVp when dosimeters were placed in a tissue equivalent phantom. However, it is noted that a free-in-air exposure measurement would be most useful for the subsequent conversion to average glandular dose in the breast. In contrast to Dong's study [21], which showed a flat energy dependence in the mammographic energy range, the energy response observed in the work done by Benevides & Hintenlang (2006) [141] showed a linear response to exposure for increasing tube potentials and tube mAs. The difference was due to the varying exposures recorded for the former [21], as opposed to the constant exposure by varying

mAs for each tube potential in the study by Benevides & Hintenlang (2006) [141].

In a more recent attempt to explore the use of TN-1002RD MOSFETs to measure tissue depth dose in heterogeneous phantoms in comparison with Monte Carlo simulations as the gold standard, Jones *et al.* (2005) [106] used TN-1002RD MOSFETs and cylindrical phantoms to perform interface measurements with an x-ray tube potential of 66 kVp at 200 mAs. Each cylindrical phantom measured was 7 cm in height, and was composed of a stack of 1 cm thick cylinders stacked upon each other. Soft tissue-equivalent material (S), bone-equivalent material (B) and lung tissue-equivalent material (L) formed individual cylindrical 1 cm slabs. The combinations used for the three phantoms were: SSSSSSS, SSBBSSS and SBLLBSS. It was found that at greater than 2 cm depth, experimental results matched Monte Carlo dose simulations regardless of dosimeter orientation. However, doses measured at the surface and at shallow depths up to 2 cm were consistently lower than the simulated doses with the epoxy bubble of the MOSFET facing the x-ray beam due to photon attenuation in the epoxy layer [106]. To avoid this under-response of dose at the surface/shallow depths less than 2 cm, Jones et al. (2005) [106] recommends that the flat side of the MOSFET face the x-ray beam when making surface dose measurements or at shallow depths less than 2cm.

For sensitivity measurements, Bower & Hintenlang (1998) [137] exposed the MOSFETs to approximately the same dose across various tube potentials ranging from 40 kVp to 150 kVp. It was found that when the flat kapton side of the MOSFET (opposite to epoxy bubble) faced the x-ray beam, surface sensitivity (mV response per unit of exposure) was 75% that of the average sensitivity when the epoxy (bubble) side faced the x-ray tube. In their work, they attributed the source of angular dependence to be the asymmetric construction of the MOSFET. Other authors who have conducted similar angular dependence studies attribute the decrease in MOSFET sensitivity in various orientations to the absorption of the lower energy portion of the x-ray spectrum by the MOSFET substrate, other reasons include the shielding effect of the packaging of the incident secondary electrons generated by x-ray[138,147].

When the MOSFET was placed in a tissue equivalent (TE) cylindrical phantom, sensitivity was found to be nearly independent of dosimeter orientation. [114,137,147].

Pomije et al. (2001) [138] reasons that the photons that are incident on the MOSFET when the sensor is placed in-phantom are more uniformly distributed compared to the case when dosimeter readings were measured free-in-air. Therefore, this explains the smaller variation in sensitivity of the in-phantom MOSFET compared to the in-air case.

With increasing tube potential, the severity of the MOSFET in-phantom angular dependence decreased [138]. The reason for this is due to less beam hardening at higher tube potentials resulting in a higher effective energy of the photons reaching the sensitive volume of the MOSFET in-phantom. Moreover, more Compton scattered electrons are produced at higher energies, resulting in a less directional radiation field and therefore less angular dependence at higher tube potentials.

Finally, Pomije's study [138] revealed that angular dependence in the axial plane was much less severe than that observed in the axial-normal plane. Again, the reasons for this difference in angular response is due to the device packaging and MOSFET geometrical structure. When rotating in the normal-axial plane, the amount of substrate (that acts as a shield) is more than in the case of an axial rotation. Moreover, the wire bonding leads attenuate the incident primary beam when rotating in the normal-axial plane, and this results in a less uniform photon flux reaching the active region of the MOSFET, which explains the greater angular dependence in the normal-axial orientation.

The application of MOSFETs for dose measurements in clinical radiology is relatively recent. In 1989, Peet and Pryor [148] first used MOSFET technology to measure patient skin entrance doses in diagnostic radiology. Subsequently in 2003, Yoshizumi *et al* [51] reported the first successful application of MOSFETs in CT dosimetry. For diagnostic CT examinations where risk to superficial organs such as the radiosensitive eye lens, thyroid gland, breast tissue and gonads is of concern, the direct application of the MOS*kin* dosimeter allows patient skin dose readings to be easily readout. Following which, dose records may be kept in a patient database and referenced to whenever required to avoid unjustified repeated CT scan examinations. The practical application of MOSFETs for skin and organ dose assessment has been proven in many radiological investigations [23,27,32,51,53] .

Commercial MOSFETs that are commonly used are the TN-502 series (standard-sensitivity also known as low-sensitivity models used for radiation therapy applications) and the TN-1002 series (high-sensitivity models suitable for diagnostic radiology applications), both from Best Medical, Canada. Within each of the MOSFET series, the RD and the RDI models represent the standard model with angular dependence and the isotropic model supposedly giving negligible directional dependence respectively.

Yoshizumi *et al.* (2007) [51] found good agreement between MOSFET measurements and TLD measurements in the group's recent attempt to assess organ dose using TLD-100 dosimeters and TN1002RD (Best Medical, Canada) MOSFETs in an adult female anthropomorphic phantom with a 4-slice MDCT scanner. By placing both MOSFETs and TLDs in 20 pre-selected organ locations within the phantom, the group determined organ dose for the institution's pulmonary embolus scan protocol. Apart from the MOSFET lower detection limit of 1.40 mGy at 25% uncertainty, the group concluded that MOSFETs were generally useful in assessing CT organ doses as long as the organ of interest was within the primary field of view of the beam. At lower than 1.40 mGy dose levels (for example, in measuring scattered radiation to organs lying outside the primary field of view), TLD dosimeters were found to be more suitable as they were able to register a more accurate reading since the TLD lower limit of detection is 0.10-0.20 mGy [19,23,51].

A study was performed by Hurwitz *et al.* (2006) [23] to determine radiation dose to the fetus in the uterus at 0 months and 3 months with the institution's chest (thoracic) pulmonary embolus, (abdominopelvic) appendicitis and (abdominopelvic) renal stone imaging protocols. This study used a modified pregnant adult female anthropomorphic phantom. TN1002RD MOSFETs were placed at 5 representative fetal locations in the uterus at 0 and at 3 months' gestation. Since MOSFET dosimeters had a less sensitive lower limit of detection, the MOSFETs were used exclusively for abdominopelvic (appendicitis and renal stone imaging) protocols for dose measurement within the primary beam. As for the case of measuring in-utero fetal dose in chest CT, TLD-100 dosimeters were used to measure the scatter radiation, or radiation that was outside of the primary beam, as low doses were accurately (and therefore preferably) measurable with TLD-100 dosimeters. The study revealed that imaging the mother for appendicitis

during the first trimester of pregnancy may theoretically double the fetal risk for developing childhood cancer. The risk was calculated based on extrapolation of risk using the linear-no threshold model in radiation protection.

In Peet & Pryor's (1999) evaluation of MOSFETs [148] for use in patient dosimetry in conventional film-screen radiography, the authors compared the use of standard MOSFETs and high-sensitivity MOSFETs connected to a high sensitivity-bias supply. The measurements were performed with a sample size of 195 to 1286 patients depending on the type of examination performed. They strongly favored the MOSFET measurement approach over the TLD approach for measuring entrance surface dose for common radiographic examinations, citing the fact that MOSFETs were able to give near-instantaneous readout, as opposed to TLDs with complex and lengthy pre-irradiation and post-irradiation annealing, batching and calibration procedures. It is recognized that apart from Chest PA views where the MOSFET's lower limit of detection restricts its application, all other projections such as abdomen AP, lumbar spine lateral, lumbar spine L5/S1 and pelvis AP gave MOSFET results with a total uncertainty of less than 25% at the 95% confidence level. Within the context of the study, the authors also noted that the energy response varies over the range of energies used clinically, and recommended that a calibration of the MOSFET dosimeter should be performed at each energy used for each type of examination. A similar conclusion was derived from Cheung et al. (2003)[149], who compared the performance of MOSFETs and TLDs in an orthovoltage beam with tube potential ranging from 50 kVp to 250 kVp. They found that MOSFETs tended to overrespond significantly (a relative response of 4.40 at 50 kVp normalized to 1 at 250 kVp) within the superficial to orthovoltage energy range. The authors attributed this to the TO-5 gold plate kovar substrate used in the particular MOSFET packaging.

An estimation of mean-glandular dose is a quantity of interest for radiology practitioners to assess the risk of radiation-induced carcinogenesis arising from mammographic examinations. Dong *et al.* (2002) [21] applied MOSFET technology to measure breast entrance skin air kerma (BESAK) in mammography. They found that MOSFETs were suitable for dose monitoring of BESAK in mammography. Among the 120 female patients surveyed using TN 1002RDI MOSFETs at 25-30 kV and a tube

current of 100mAs, the group found that energy dependence was less than 3% within this X-ray photon energy interval and the system displayed excellent dose response linearity. The mean glandular dose (MGD) which was subsequently obtained using conversion factors turned out to be 1.5 mGy, which was comparable to previously reported literature.

2.10 Summary

This chapter has provided the necessary background to understanding low dose risk as applied to radiological dose assessment. In addition, commonly encountered dose quantities in radiological physics have been described and the physical principles of dosimetry outlined. Literature on previous characterisation attempts with various MOSFET dosimetry systems has also been discussed and summarised.

3 Physics of MOSFET Dosimetry

Holmes-Siedle (1974) [150] first recognized the use of the MOSFET as a space-charge dosimeter. This so-named "space charge" essentially refers to the ionisation effect which occurs in the dielectric that causes a change in potential across the dielectric surface which can be measured non-destructively [151]. Following which, MOSFETs were successfully applied in space dosimetry for monitoring the effects of space radiation on orbiting satellites [152] and radiation monitoring in mixed gamma and neutron fields [153,154]. In more recent years, MOSFETs have been shown to be suitable dosimeters for dose verification and monitoring in radiation therapy [112,155-158] and radiology [32,51,159].

3.1 Structure and Basic Physics of the MOSFET

Figure 3.1 depicts the structure of the basic metal-oxide semiconductor field effect transistor (MOSFET). The p-channel enhancement MOSFET (also commonly referred to as the pMOSFET) as shown in the figure, is built on a negatively doped (n-type) silicon substrate. As its name aptly describes, the MOSFET is a sandwich type device made up of a metal (gate) layer, an insulating oxide (SiO_2) layer and a silicon semiconductor substrate, whose ability to function as a transistor device depends on the applied voltage V_G (creating a field effect).

The source and drain terminals sit directly on top of a positively doped (p-type) silicon region. Underneath the metal gate is an insulating SiO_2 layer, and the n-type silicon substrate then sits below the SiO_2 layer. The channel region is part of the silicon substrate, which lies directly below the oxide layer. When a sufficiently negative gate voltage V_G is applied relative to the silicon substrate, most of the minority carriers (in this case, the holes) are attracted from the bulk of the silicon substrate and the p+ source and drain regions and travel to the SiO_2-Si interface. Once a sufficient number of holes have gathered at this interface, a conduction channel forms. This conduction channel allows a significant amount of current to flow between the source and the drain (I_{ds}). The gate voltage required to allow conduction through the MOSFET is known as the threshold voltage V_{th}, to attain a constant current flow through the channel.

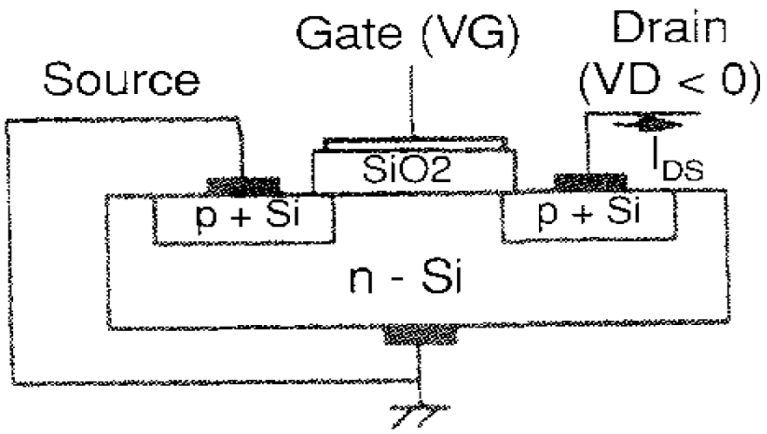

Figure 3.1: P-channel enhancement MOSFET(also known as a pMOSFET) (Reproduced from [160])

3.2 Principle and operation of a single MOSFET radiation dosimeter

The MOSFET is essentially a voltage-controlled device with 3 terminals; the source, gate and drain. The MOSFET as a radiation dosimeter works on the principle of the shift in threshold voltage ΔV_{TH} (with measurements taken before and after the MOSFET is irradiated). To reiterate, the threshold voltage V_{TH} is defined as the gate voltage needed to attain a predetermined current flow. The shift in threshold voltage ΔV_{TH} corresponds to the absorbed dose in the SiO_2. [161]

Figure 3.2 shows the physical model of ionizing radiation effects in MOSFETs, with a positive gate bias applied. Incident ionizing radiation creates electron-hole pairs within the SiO_2 layer. Typically, 18 eV is required to produce one electron-hole pair in the oxide [151] (shown by process 1 in Figure 3.2). The electrons, with much greater mobility than holes (up to 4 times at room temperature) move toward the p+ Si regions. Electron-hole pairs tend to recombine depending on the applied field, energy and type of incident radiation [162]. The holes that escape recombination remain behind near their point of generation. They are relatively immobile and result in negative voltage shifts of the MOSFET. Within a second at room temperature in response to the applied electric field, the holes undergo stochastic hopping through the oxide (process 2 in Figure 3.2), which gives rise to a transient recovery in the voltage shift. When the holes

are close to the Si-SiO_2 interface, some of them are captured in long term trapping sites (process 3 in Figure 3.2) which causes the negative voltage shift ΔV_{TH} that persists for years.

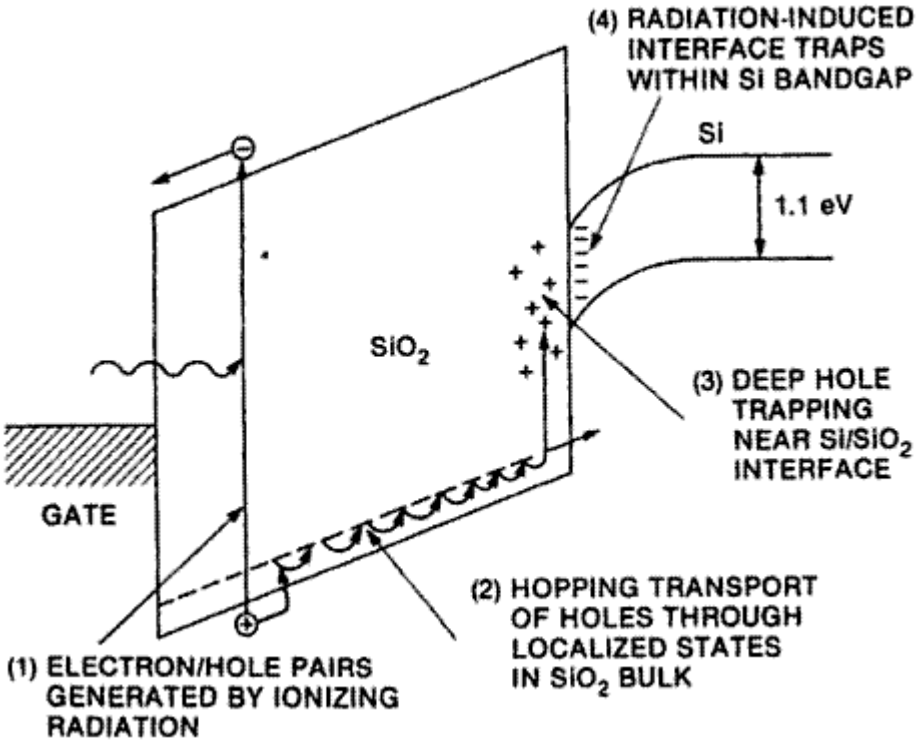

Figure 3.2: Physical model of ionizing radiation induced effects in MOS structures, with a positive gate bias applied. Upon irradiation, 3 major processes dominate in the MOSFET; namely, (1) the accumulation of trapped charge in the SiO_2, (2) the transport of holes through the oxide and and (3) the increase in the number of bulk oxide and interface traps. Reproduced from [161].

Figure 3.3 shows how the current that flows between the source and drain (I_{ds}) depends on the applied gate voltage V_{gs}. The threshold voltage shift ΔV_{TH} is proportional to the total quantity of trapped charges in the MOSFET, which is in turn linearly proportional to the absorbed dose in the SiO_2.

$$\Delta V_{TH} = V_s^{after} - V_s^{before} \qquad \text{Eq. 3.1}$$

where V_s^{before} and V_s^{after} is the measured output voltage before and after radiation exposure respectively.

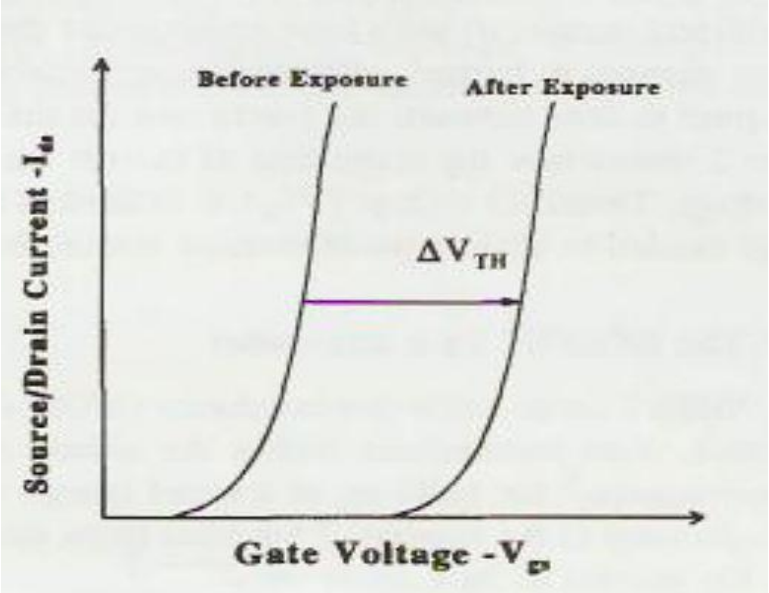

Figure 3.3: Graph of shift in V_{TH} before and after radiation exposure for n-MOSFET , for p-MOSFET shift is in opposite direction. (Reproduced from[162]).

MOSFETs can be used in either active or passive mode, with the former mode referring to an applied positive gate bias voltage, and the latter, in the absence of a gate voltage. The reason that the MOSFET is used in an active mode (with gate bias) is that the effect of electron-hole pair recombination is reduced. This means improved MOSFET linearity and sensitivity.

The response ΔV_{TH} for the passive mode of the pMOSFET can be predicted using simple electrostatic analysis [163,164] as:

$$\Delta V_{TH} \approx 0.0022 D^{0.4} t_{ox}^{2} \qquad \text{Eq. 3.2}$$

In the passive mode, due to the repulsion of the coulomb field produced by the trapped holes, the MOS*kin* exhibits a sublinear dose response and is modelled by the following equation[161]:

$$\Delta V_{th} = V_o[1 - \exp(-\beta D)] \qquad \text{Eq. 3.3}$$

The response of the MOSFET in the active mode may be predicted with the following equation:

$$\Delta V_{TH} = 0.04 D t_{ox}^{2} f \qquad \text{Eq. 3.4}$$

where D represents the dose in rad in the SiO_2 (1 rad=10 mGy), t_{ox} is the oxide

thickness in μm, and f is the fraction of holes created that escaped recombination. In the active mode, the dose response is linear over a wide dose range, compared to that operated in passive mode. With increasing positive bias, the parameter f approaches 1 [151]. As described by equation 3.4, the dose response of the MOSFET in the active mode depends on the oxide thickness and the electrical field in the oxide. The technology of oxide growth also contributes to the MOSFET dose response [165].

3.3 Post-exposure drift

Following radiation exposure, MOSFET fading (changing of the ΔVth in time) depends on the readout time interval. In some MOSFET positive fading was up to 14% during the first 26 hours after exposure, followed by a slow and steady decline.

This post-exposure drift effect, which affects measurement accuracy, is attributed to mechanisms such as positive ion diffusion, relaxation of charges residing in deep traps in the SiO_2, capacitance-voltage hysteresis, and thermal and non-thermal annealing of trapped charges ([166] cited in [167], p. 38). The enhanced f-noise is difficult to characterise since it depends on irradiation conditions (done in passive or active mode), technology of gate oxide growth, geometry of the device and the temperature [151]. Short term instability of the readout can be positive or negative (nonlinear in behaviour), and depends on accumulated dose.

It has been shown previously that with the use of online MOSFET dosimetry with a special microprocessor based V_{th} readout, the effect of slow traps on measurements can be reduced, thus improving readout accuracy [168].

3.4 Sensitivity change with accumulated dose

MOSFETs have a finite lifespan due to the saturation of the charge build-up effect in the gate oxide and the tolerance criterion of non-linearity of dose response [151]. After the prescribed dose limit is reached, MOSFETs should be removed from use or reset by means of UV or thermal annealing [169].

Lavallee [146] found that sensitivity change with integrated dose is only a function of short-term electron hole recombination, independent of irradiation type history. The

authors verified this by means of experiments involving cross-irradiations with Co-60 and 30 kV on the same MOSFET detector. Through a series of experiments, the authors recommend that frequent recalibration is performed (with every 2500 mV of accumulated dose) if accurate dosimetry is desired.

3.5 Creep-up effect

The creep-up effect, also known as the multiple query effect, is known to alter MOSFET post-irradiation readout accuracy. The phenomenon of "creep-up" is defined as the situation where the threshold voltage of the MOSFET increases when dose measurements are repeatedly taken, and depends on the time interval between successive readout cycles [170]. The physical explanation for this observed phenomenon is explained by a charge being injected by the measuring circuit to the MOSFET. This temporary perturbation in the charge distribution normally decays in a few minutes if no subsequent readout is performed. However, a premature re-read will no doubt result in an amplification of the signal. This phenomenon is most pronounced when accumulated dose exceeds 20 Gy [170].

3.6 Effects of temperature variation on MOSFETs

Temperature influences the mobility of the charge carriers in the channel which in turn affects the readout current. As reviewed by [151], by selecting a readout current corresponding to a thermostable point on a current-voltage characteristic drain current versus source gate voltage, such a temperature effect may be avoided [171]. Soubra *et al* [162] has also successfully used dual MOSFET sensors under different gate bias. When irradiated, the dual MOSFET sensor gives different threshold voltage shifts; subtracting these signals gives a resultant reading that is temperature independent.

Experiments by Cheung et al [172] examining the effects of temperature variation on MOSFET dosimetry found that the MOSFET produced a stable dose response for temperatures in the range 15 to 40^{o}C. A temperature correction function was found not to be necessary when comparing irradiations performed at room temperature and in-vivo at near body temperature. When performing patient skin measurements, the researchers recommend a 60 second wait before irradiation. This 60 s wait ensures that the device has gained thermal equilibrium, and that a 60 s post irradiation wait is also

necessary for measurement accuracy while the device is still attached to the patient. Alternatively, if the initial readout was performed at room temperature while not attached to the patient, the final reading should be performed 2 minutes after removal from the patient to allow thermal equilibrium to be established. As suggested by the authors, this latter method is recommended for dose analysis because this procedure minimizes any errors caused by fluctuations in the MOSFET probe temperature due to varying thermal contact with the patient, dependent upon the site of placement on the patient.

3.7 Summary

This chapter has provided an overview of the basic physics of MOSFETs as applied to radiation dosimetry. In particular, the physical working principles of MOSFETs, the post-exposure fading effect, the effect of accumulated dose, the creep-up phenomenon and MOSFET temperature dependence were described.

4 Monte Carlo characterisation of MOSFET dosimeters in clinical kilovoltage x-ray photon beams

4.1 Introduction

Metal Oxide Semiconductor Field Effect Transistors (MOSFETs) offer a solution to the need for real-time dosimetry in clinical environments. As noted previously in Chapter 2, the primary advantage of MOSFETs includes their simple instrumentation, quick setup and measurement readout associated with their use, an important consideration for potential clinical implementation.

MOSFETs, being semiconductor-based detectors, are known for their energy dependent response at low photon energies due to their increasing cross-section for the photoelectric effect due to their high atomic number ($Z_{silicon}$=14) relative to water (Z_{water}=7.4). This results in an overestimation of the absorbed dose in low energy beams when calibrated in megavoltage (MV) photon beams without energy response correction.

For incident photon energies lower than 100 keV, the mass energy absorption coefficient for silicon versus that of water is particularly pronounced. Figure 4.1 shows the plot of the ratio of the mass attenuation absorption curves of silicon $(\frac{\mu_{en}}{\rho})_{Si}$ over that of water $(\frac{\mu_{en}}{\rho})_{water}$ at kilovoltage photon energies, showing that at 15 keV photon energy, $(\frac{\mu_{en}}{\rho})_{Si}$ of silicon is up to 7 times higher than for $(\frac{\mu_{en}}{\rho})_{water}$ of water at 15 keV relative to 300 keV. This shows that silicon is not water equivalent at low kilovoltage photon energies.

For potential use as a clinical dosimeter where tissue (water) absorbed dose is the quantity of interest, it is essential for appropriate water correction factors to be implemented for accurate measurements.

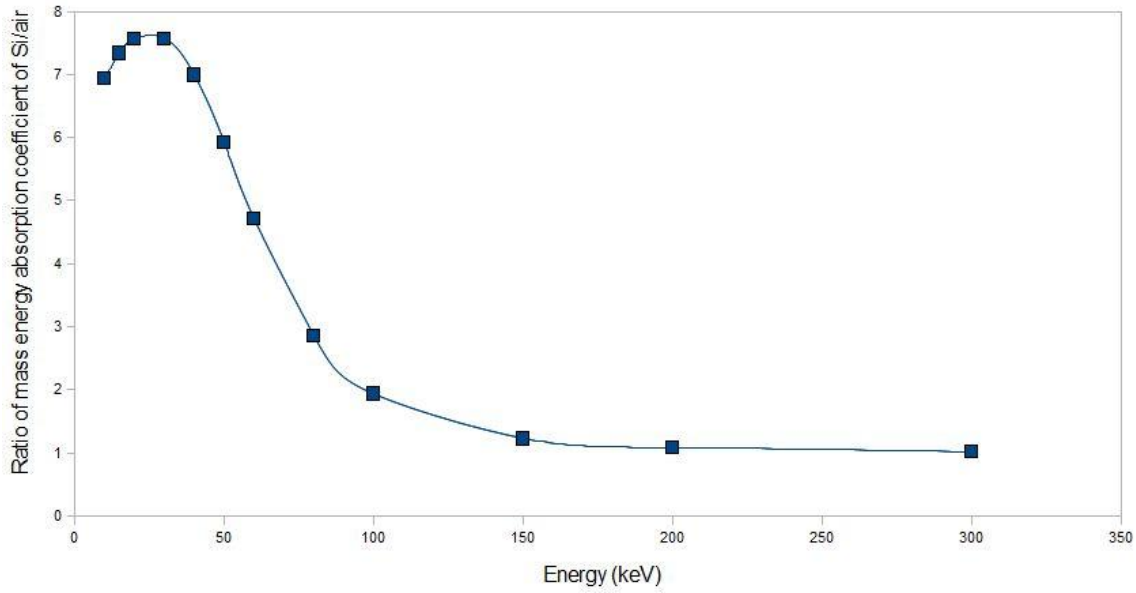

Figure 4.1: Mass attenuation absorption curves of silicon $(\frac{\mu_{en}}{\rho})_{Si}$ over that of water $(\frac{\mu_{en}}{\rho})_{water}$

This chapter examines the water equivalence of MOSFET detectors at clinical kilovoltage x-ray energies by means of Monte Carlo simulations and offers recommendations on how this energy dependence may be corrected for, particularly for dose measurements at the surface and at depth in a homogeneous water phantom. In addition, angular simulation response simulations were also performed to determine how the asymmetrical design of the MOSFET may potentially contribute to measurement uncertainties.

Previous literature indicates that detector packaging causes the energy response of the MOSFETs relative to water to vary dramatically from 2 to 30 in some cases [154,173-175]. In particular, first-generation MOSFET radiation dosimeters in their standard metallic package configurations were found to over-respond at low energies by a factor of up to 15 [173]. When replaced with a ceramic package, energy response improved; the detectors over-responded by only 4.0 to 5.0 times compared to that of tissue [154,173,175]. Table 4.1 summarizes previous literature on MOSFET energy response factors as a result of improvements in detector geometry and material housing. These energy response factors have been obtained by the researchers through a combination of both theoretical Monte Carlo simulations and practical experiments.

Table 4.1: Summary of known MOSFET energy response factors from existing literature

Maximum response	Reference Energy	Detector type	Details	Reference
4.19± 0.25 at 33keV in-air (MOSFET 1)	6 MV photons	TN-502-RD MOSFET	quasi monoenergetic beam	Edwards et al 1997[139]
4.44± 0.26 at 33keV in-air (MOSFET 2)	6 MV photons	TN-502-RD MOSFET	quasi monoenergetic beam	Edwards et al 1997 [139]
4.4 at 45keV in-air	incident energy greater than 200keV	TN-502-RD MOSFET	unknown	unpublished manufacturer's data[142]
3.2 at 53keV in-air with backscatter	6 MV photons	TN-502-RD MOSFET	spectral x-rays	Kron et al 1998[142]
5.9 at 25keV	6 MV photons	TN-1002-RD MOSFET	ideal monoenergetic photon beam	Wang et al 2005[145]
6.6 at 40keV	6 MV photons	TN-1002-RD MOSFET	ideal monoenergetic photon beam	Wang et al 2004[144]
6.5 at 36keV	6 MV photons	Wollongong nMOSFET	spectral x-rays	Kron et al 1998[142]
5.5 at 75kVp (mean 30keV) in free-air	6 MeV bremstrah-lung	unencapsulated Wollongong nMOSFET	spectral x-rays	Rosenfeld 1995[154]

5.0 at 75kVp (mean 30keV) in free-air	6 MeV bremstrah-lung	Wollongong nMOSFET with a polyethylene cap	spectral x-rays	Rosenfeld 1995[154]
8.2 at 125 kVp (54keV) in air	6 MeV bremstrah-lung	Wollongong nMOSFET with a TO-18 kovar package	spectral x-rays	Rosenfeld 1995[154]
7.0 at 100kVp (37keV) with backscatter	6 MeV bremstrah-lung	unencapsulated Wollongong nMOSFET	spectral x-rays	Rosenfeld 1995[154]
8.1 at 75kVp(30keV) with backscatter	6 MeV bremstrah-lung	Wollongong nMOSFET with a polyethylene cap	spectral x-rays	Rosenfeld 1995[154]
3.5 at 125kVp(54keV) with backscatter	6 MeV bremstrah-lung	Wollongong nMOSFET with a TO-18 kovar package	spectral x-rays	Rosenfeld 1995[154]
4.40 at 50kVp	250 kVp	Wollongong nMOSFET	spectral x-rays	Cheung et al 2003[149]
3.2 at 75kVp (mean 30keV) with backscatter	6 MV	CSDS MOSFET (CMRP)	spectral x-rays	Cheung 2009[113]

The MOS*kin* radiation dosimeter [176], recently developed at the Centre for Medical Radiation Physics (CMRP), University of Wollongong, Australia, has the unique feature of a thin, reproducible buildup layer to reliably measure skin doses and steep dose gradients at material interfaces to a high level of accuracy. The MOS*kin* dosimeter has been successfully applied in radiotherapy dose measurements; for example in high dose rate brachytherapy[156], intensity modulated radiation therapy (IMRT)[112] and tomotherapy [157].

As is the case with any radiation dosimeter prior to usage, it is necessary to characterise the MOS*kin* in the energy range of interest to achieve good measurement accuracy. In the case of diagnostic radiology in particular x-ray CT, the clinical kilovoltage energy range is of interest.

This chapter describes in detail the geometry of the CMRP MOS*kin* radiation dosimeter model and compares this with the geometrical modelling of a typical commercial MOSFET with a hemispherical epoxy bubble encapsulation. Section 4.5 provides a comprehensive description of the modelled dosimeter geometry. The GEANT4 Monte Carlo Toolkit was used for our numerical simulations to study how detector materials and geometry affects doses in the kilovoltage energy range. The dosimeters were evaluated for tissue equivalence in three different situations, namely in-air , on water phantom surface and at various depths in a homogeneous solid water phantom. A proposed optimised packaging design for the MOS*kin* was also investigated.

The correction factors derived from these simulations for absorbed-dose energy dependence should not be directly applied to individual MOSFETs in practice. This is because in the experimental situation, energy dependence is composed of 2 parts [177]: the absorbed-dose energy dependence at the point of measurements and the intrinsic energy dependence of the particular MO*Skin* .

As the results of previous simulations have indicated [116,178], Monte Carlo calculations do not accurately predict the relative response of detectors as a function of photon energy due to the physical processes that occur in the detector that are not incorporated into the simulation. This has also been extensively discussed in solid state literature, including TLDs.[178]

In other words, the numerical simulations only model absorbed-dose energy dependence within the framework and capabilities of the GEANT4 Simulation Toolkit. Absorbed-dose energy dependence D(Q) is essentially a ratio of the dose to the scoring volume of the dosimeter $D_{SiO2}(Q)$ to that of the dose to the medium $D_w(Q)$ in the absence of a detector at beam quality Q as seen in equation 4.1.

$$Absorbed\ dose\ energy\ dependence, D(Q) = \frac{D_{SiO2}(Q)}{D_w(Q)} \qquad \text{Eq. 4.1}$$

Intrinsic energy dependence $k_{bq}(Q)$ is a ratio of dose to the sensitive volume of the detector $D_{SiO2}(Q)$ to the detector reading at the same beam quality $M_{SiO2}(Q)$.

$$Intrinsic\ energy\ dependence\ k_{bq}(Q) = \frac{D_{SiO2}(Q)}{M_{SiO2}(Q)} \qquad \text{Eq. 4.2}$$

Intrinsic energy dependence arises as a result of a complex series of physical interaction processes that occur at an atomic level post-irradiation and readout as previously described in Chapter 3.

Taken together, the overall energy response of a detector is a product of the absorbed-dose energy dependence D(Q) and that of intrinsic energy dependence $k_{bq}(Q)$ [177].

$$Overall\ detector\ energy\ dependence = D(Q) \cdot k_{bq}(Q) \qquad \text{Eq. 4.3}$$

Nonetheless, with the GEANT Monte Carlo toolkit, our simulation studies on absorbed-dose energy dependence are helpful for understanding how modifications in MOSFET design and material composition affect dose measurements.

4.2 GEANT4 Simulations

GEANT, an acronym for **GE**ometry **AN**d **T**racking, is a Monte-Carlo software toolkit for the simulation of elementary particles through matter. GEANT was originally developed in the early 1990s at **C**onseil **E**uropéen pour la **R**echerche **N**ucléaire (CERN, European Council for Nuclear Research, Geneva, Switzerland) for high energy physics.

Today, the GEANT toolkit, GEANT4, is built upon C++ classes, with an object-oriented design. In recent years, GEANT4 has found wide applications in fields like nuclear and accelerator physics, space science, medical physics and radiation protection.

GEANT4 is a highly versatile toolkit which enables a user to model to precise detail any experimental setup in terms of detector geometry and materials, define the particles involved in the interaction and the corresponding physics processes associated with their interaction in matter. GEANT4's built-in graphical and analysis interfaces allow the user to visualize and store their results in histograms for further analysis. Visualization tools include OpenGL, HepRApp and VRMLView. Analysis tools include AIDA and OpenScientific.

For the following study, GEANT4 version 4.9.1.p02 was used with the low energy electromagnetic data libraries installed. At the energy ranges simulated, photon interactions include the photoelectric effect and the Compton effect while electron interactions include ionisation, bremsstrahlung and multiple scattering. The cut-off value represents the threshold for producing secondary particles, and this value was set to be 0.1 μm in the micron thin sensitive detector volume; this cut-off value corresponded to an energy of about 1 keV, below which no particles would be produced.

For in-air and surface dose simulations, a monoenergetic plane parallel source beam the size of the widest dimensional area of each dosimeter was used (ie. a 2.5 mm x 2.5 mm plane source was used for MOSFET simulations and a 2.5 mm x 0.8 mm plane source was used for MO*Skin* simulations), and each run emitted between a range of 10^7 to 10^9 primary photons in order to achieve <24% uncertainty at a 95% confidence interval throughout all simulation runs, and also for the simulations to complete in a reasonable amount of time of 70 hours; with completion within a reasonable time frame being a major criteria for our simulations. The reason for the use of monoenergetic photon beams is that it allowed for the study of how individual detector response changes with photon energy while eliminating the compounding effect of spectral x-rays [142]. Xcomp5R and SpekCalc was subsequently used to generate x-ray spectra as our input for an investigation of MOSFET response in a clinically realistic spectral beam. Section

4.4.1 illustrates. Appendix B shows the software generated spectra with clinical beam parameters.

It is expected that most of the dose contribution will be from the primary beam since the beam dimensions were set to be as large as the dosimeter dimensions. It follows that the majority of the backscatter contribution that is scored by the sensitive volume of the device is expected to originate from within the detector and its immediate packaging itself. Wang et al (2005)[145] found that in their simulations tracking regional dose contributions that most of the backscatter contribution originated from within the modelled MOSFET dosimeter itself. For example at 180 keV incident photon energies, 70% of dose contribution was from backscattered electrons originating from the epoxy bulb, 13% from the silicon substrate and the rest of the contributions from various parts of the device structure.

For the purpose of simulating detector surface dose and depth dose response, a 10 cm x 10 cm x 20 cm water phantom was simulated. The dimensions of the water phantom simulated are more than sufficient for adequate backscatter of the primary beam considering that the maximum electron range for 300 keV electrons is just 0.1 cm in water [96].

4.3 Elements of a GEANT4 Simulation

Figure 4.2 illustrates the hierarchical class diagram of the MOSFET GEANT4 application. As seen in the Figure, user-created concrete classes MOSFET DetectorConstruction(), MOSFETPhysicsList(), MOSFETPrimaryGeneratorAction(), are derived from GEANT4 base classes G4VUserDetectorConstruction(), G4VUserPhysicsList() and G4VUserPrimaryGeneratorAction() respectively. These are the three mandatory classes in any GEANT4 application, with the former 2 classes being initialization classes (i.e. invoked at program initialization, while the PrimaryGenerator Action class is invoked during program execution.

MOSFETDetectorConstruction() describes the simulation setup. This concrete class defines, constructs and places volumes, including the sensitive detector volume to be used in the simulation. MOSFETPrimaryGeneratorAction() generates primary events.

The G4GeneralParticleSource() was applied in our simulations. The MOSFETPhysicsList() class allowed the activation of the physics that was required in our simulations; primarily the photoelectric effect and the Compton effect. Figure 4.2 shows how the various classes of the GEANT4 application relate to each other.

4.3.1 The World Volume

The world volume was specified as a 40 cm x 40 cm x 30 cm cubic volume of air in our simulation setup.

4.3.2 The Primary Beam Source

A plane parallel photon beam was generated from a 5 mm diameter circular source field. The source was set 1 cm above the surface of the water phantom for the simulations.

4.3.3 The Water Phantom

A water phantom of dimensions 30 cm x 30 cm x 20 cm was specified. The dimensions of the water phantom used are more than sufficient for adequate backscatter of the primary beam considering that the maximum electron range for 300 keV electrons is just 0.1 cm in water [96].

4.3.4 Detector Geometry

The dimensions of the dosimeters were modelled to specifications after the schematics of the MOSFET and the MOSkin (Figure 4.5 and 4.7 respectively). This class required the specification of the materials to be used, as well as the identification of the sensitive scoring region.

4.3.5 The Sensitive Volume

The sensitive volume of SiO_2 sensitive volume was modeled according to the specifications in the schematic with a thickness of 1 μm. It is this region that dose scoring takes place, where the absorbed dose is computed alongside the RunAction () class.

4.3.6 Physics Processes

By default, GEANT4 sets the range cut value to 1.0 mm. This means that a particle will not be produced if the expected range in the current material is less than 1.0 mm. Depending on the application of interest, the user may choose different range cut values for various particles or geometrical regions to speed up CPU processing time. This user-specified range cut value does not mean the distance a particle travels; rather, the cut value is converted into threshold energies internally by a simple formula in GEANT4 for each unique material and for each particle type (be it an electron, positron and gamma) [179].

For the MOSFET application, we have set different range cut values for each geometrical region to speed up computation time at no loss to computational accuracy. A 1 cm cut value in the surrounding water medium in the water phantom corresponded to a production threshold energy of keV in water. A 0.1 μm cut value within the sensitive region of the micron thin scoring volume of the MOSFET device corresponded to a production threshold energy of 990 eV.

4.3.7 Data Acquisition and data output

Dose was scored in the sensitive volume and two quantities, namely the incident photon energy and dose deposited in the sensitive volume was saved into a data (.dat) text file.

4.3.8 Simulation time

For 8×10^8 incident gamma photons, it took approximately 70 hours for a single simulation to complete with the output being an absorbed dose to the sensitive volume.

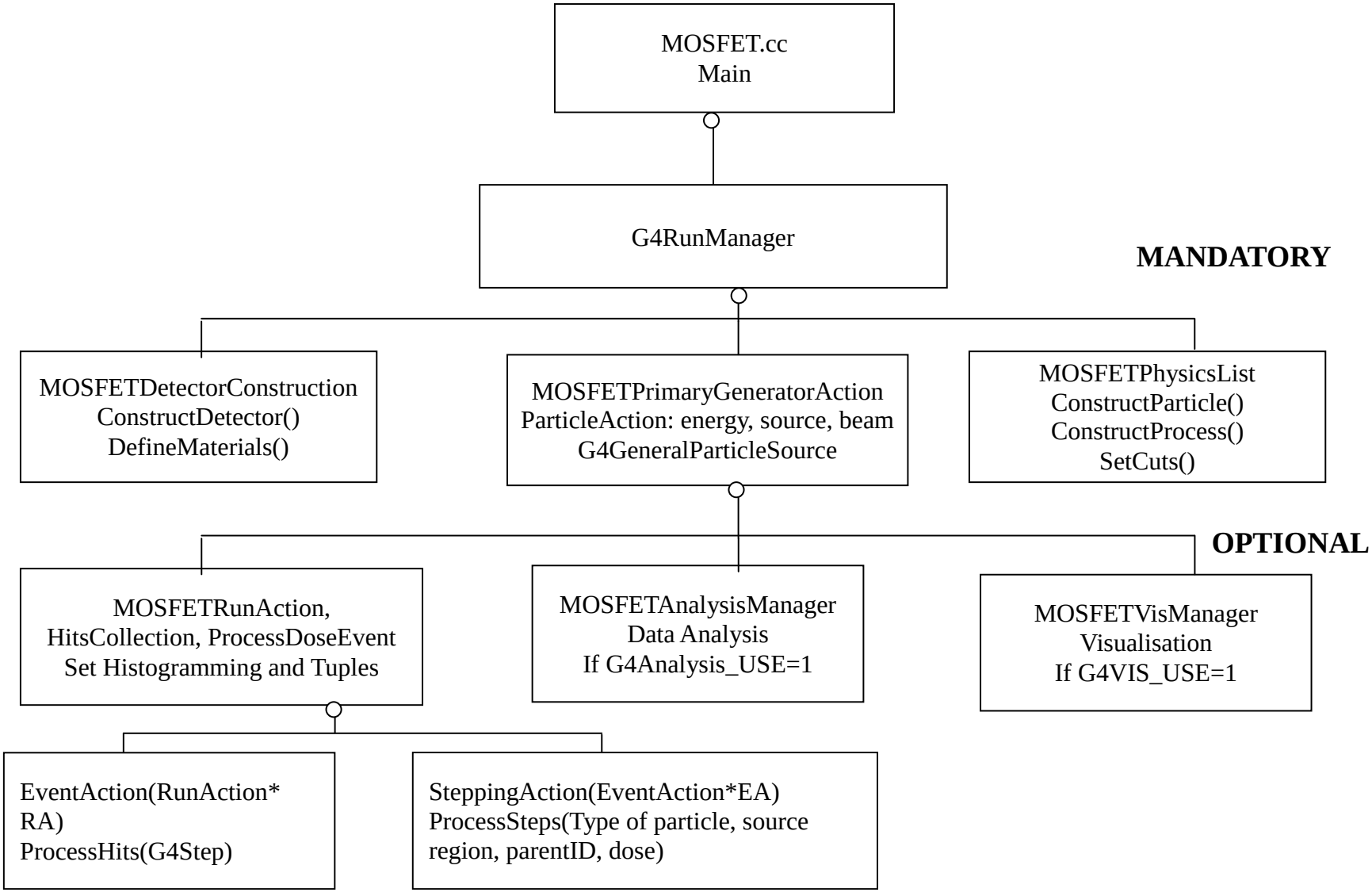

Figure 4.2: Hierarchical Class Diagram of the MOSFET GEANT4 application. The open circle on the lines represents a using relationship; the class at the circle end uses the adjoined category

4.4 Materials and Methods

4.4.1 Software generated x-ray spectra

XCOMP5R [180]is a software program that generates x-ray spectra for a user-specified tube potential (kVp), source-to-surface distance (SSD) and absorber thickness. Table 4.2 shows the details of the Gulmay D3300 superficial/orthovoltage unit used in this investigation. The mean effective energy of each spectral beam (column 2 of Table 4.2) was derived from the graphical interpolation of the relationship between HVL and mean effective energy [96]. Figure 4.3 shows a plot of the curves derived from experimental HVL measurements previously done by Johns and Cunningham [96] that relates the measured beam quality (HVL) to the mean effective energy of the beam.

The spectral files generated by XCOMP5R contained the energy and intensity of the photons that were subsequently input into GEANT4 to obtain the MOSFET device spectral energy response. Figure 4.4 shows the resulting generated x-ray spectra for tube potentials 100 kVp and 150 kVp. For the rest of the tube potentials, please refer to Appendix B. Since XCOMP5R only generates x-ray spectra for tube potentials up to 150 kVp, for beam energies larger than 150 kVp, the program SpekCalc[181] was applied. Spectra generated by XCOMP5R and SpekCalc were found to be similar for tube potentials under 150 kVp.

Table 4.2: Tube potential and filter combinations of the Gulmay D3300 orthovoltage unit used in this investigation.

Tube potential (kVp)	Effective energy (keV)	Added filter material and thickness	HVL
50	29.8	1.65 mm Al	1.27 mm Al
75	39.6	2.40 mm Al	2.23 mm Al
100	48.6	3.10 mm Al	3.43 mm Al
125	59.2	2.50 mm Al + 0.10 mm Cu	6.05 mm Al
150	71.9	1.50 mm Al + 0.35 mm Cu	0.63 mm Cu
200	95.9	1.0 mm Al + 0.9 mm Cu	1.43 mm Cu
250	120.3	1.5 mm Al + 0.5 mm Cu +	2.42 mm Cu

0.3 mm Sn

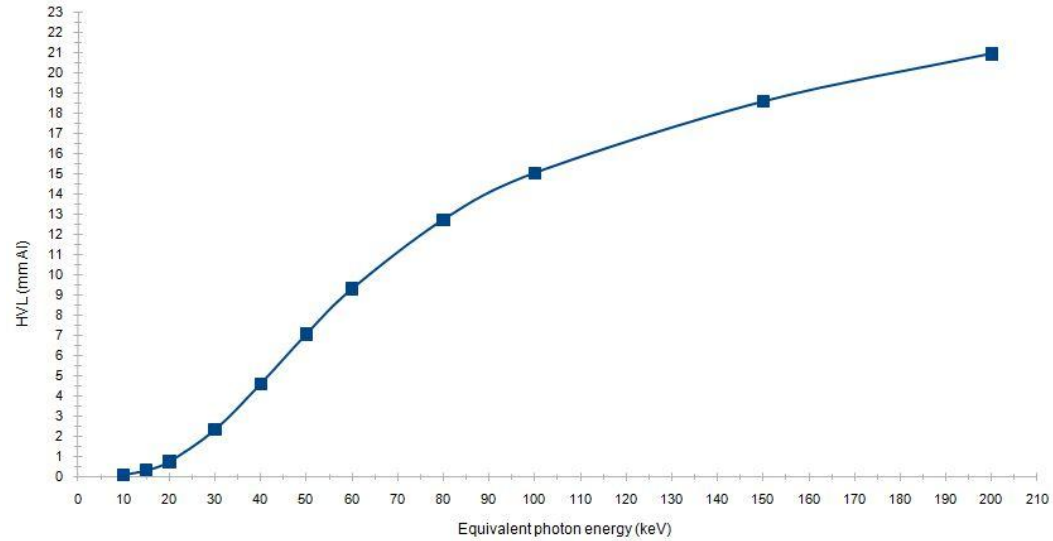

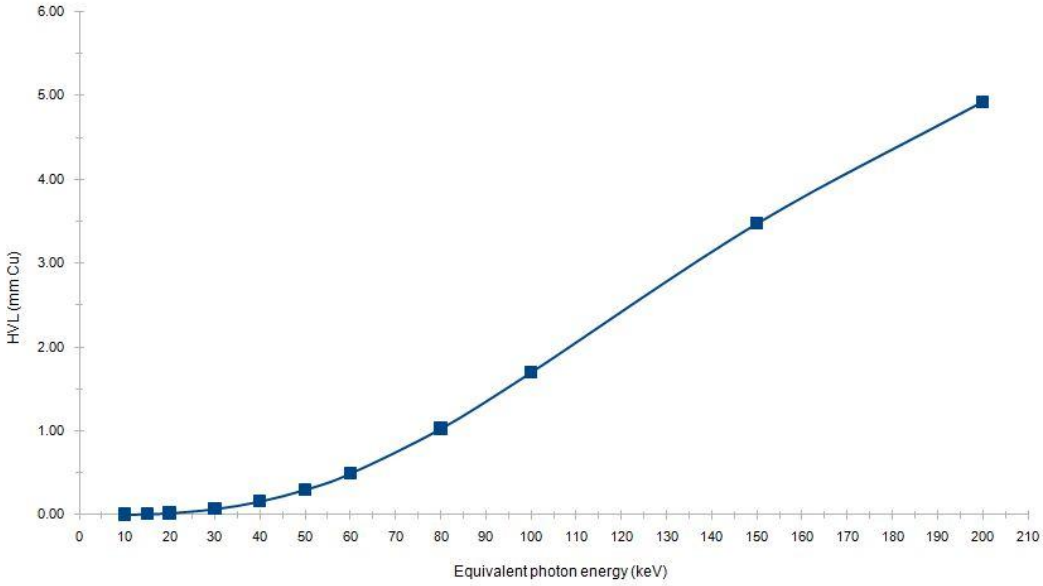

Figure 4.3: Graph showing the relationship between HVL and equivalent photon energy, calculated from the total attenuation coefficients by Johns and Cunningham [96] To obtain the equivalent photon energy of a known measured HVL from these graphs, the method of linear interpolation was used.

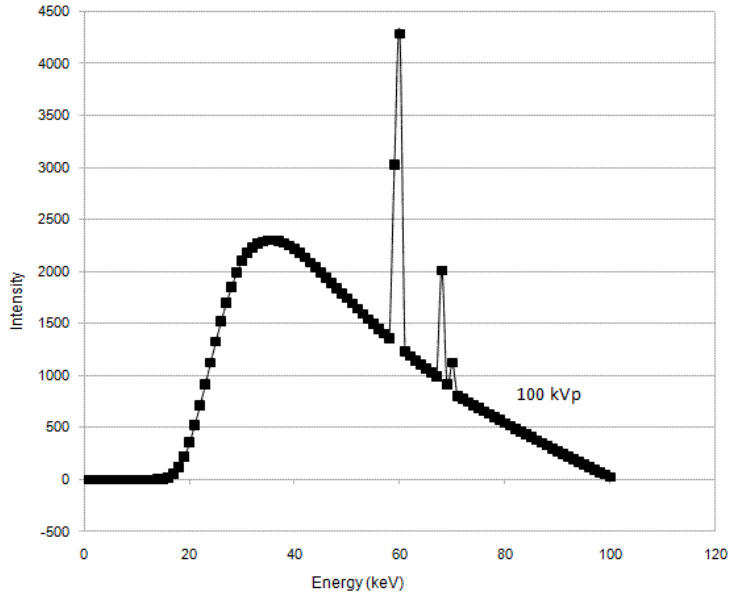

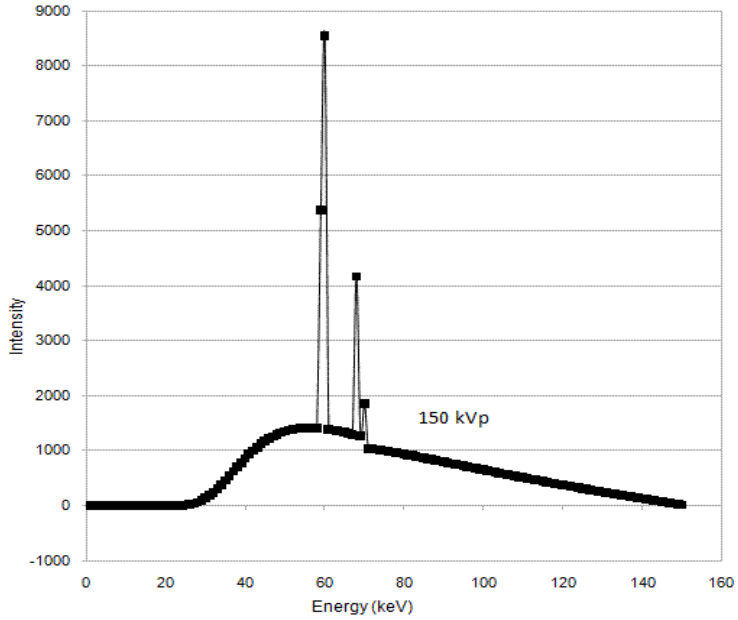

Figure 4.4: X-ray photon spectra produced by the Xcomp5r software for 50, 75, 100, 125, 150kVp and by the SpekCalc software for 200kVp and 250kVp with input machine parameters as specified in Table 4.1. Only the 100 and 150 kVp spectra are shown here. Binning of each datum point in the spectrum was set at 1 keV intervals. These photon spectra were input into the GEANT4 code. Appendix B shows the generated spectra at tube potentials of 50, 75, 100, 125, 150, 200, 250 kVp for the filter combinations listed in Table 4.2.

4.4.2 Geometrical description of the simulated MOSFET dosimeters

Two MOSFET dosimeter structures were geometrically modelled and simulated in this work; namely the MOSFET with epoxy bubble (conventional design) and the CMRP MOS*kin* with thin overlying polyamide film (new design). Table 4.3 shows the material specifications used in the simulated devices.

Table 4.3: Composition of materials in the simulated MOSFETs.

Material	**Density ($g\ cm^{-3}$)**	**Elemental composition (Mass %)**
Compound		
kapton	1.42 $g\ cm^{-3}$	C(69.1133), O(20.9235), N(7.3270), H(2.6368)
epoxy	1.3 $g\ cm^{-3}$	C (53.5360), H (13.1803), O (33.2836)
alumina	3.97 $g\ cm^{-3}$	Al (52.9251), O (47.0749)
silicon dioxide	2.32 $g\ cm^{-3}$	O (53.2565), Si (46.7435)
Element		
aluminum	2.699 $g\ cm^{-3}$	
silicon	2.33 $g\ cm^{-3}$	
copper	8.96 $g\ cm^{-3}$	

4.4.2.1 Simulated MOSFET with epoxy bubble

Figure 4.5 shows the cross sectional and top view of the conventional MOSFET with epoxy bubble, modeled after the structure of the typical Thomson-Nielson MOSFET [144,145].

The conventional MOSFET simulation model was modelled with base dimensions of 2.5 mm x 2.5 mm and an overall thickness of 1.25 mm. The MOSFET has a kapton layer of 0.25 mm thickness, and the 1 μm thick sensitive SiO_2 scoring layer was sandwiched between the 0.525 mm thick silicon substrate and epoxy bubble. The substrate is completely encapsulated in the hemispherical epoxy bubble.

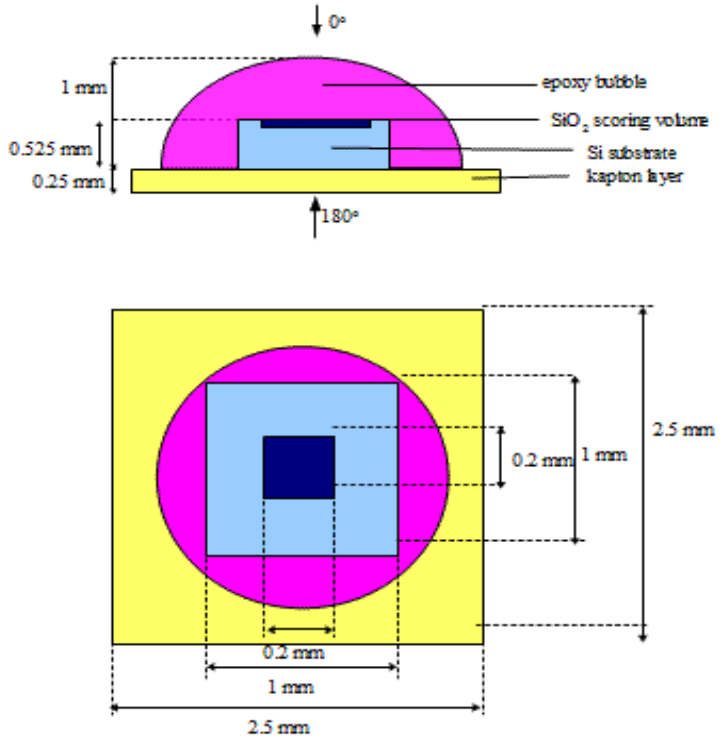

Figure 4.5 a) Cross sectional view of the simulated MOSFET structure with hemispherical epoxy bubble. The 0^o orientation of the MOSFET refers to the beam normally incident on the epoxy bubble, while the 180^o orientation refers to the beam normally incident on the flat kapton surface b) Top view of commercial MOSFET structure (not to-scale)

Figure 4.6 illustrates the simulated setup geometry of the MOSFET when placed on phantom surface. The beam is normally incident on the kapton surface as indicated by the directions of the arrows.

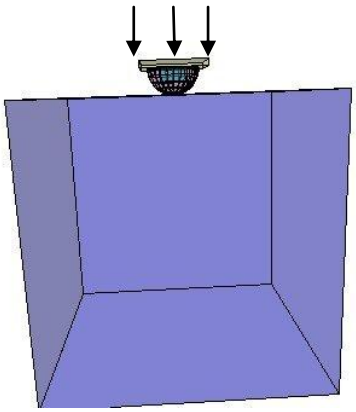

Figure 4.6: MOSFET setup geometry for an on-surface irradiation with the upside down MOSFET (i.e. at a 180^o orientation)

4.4.2.2 Simulated CMRP MOSkin

The CMRP MOS*kin* radiation dosimeter has base dimensions of 2.5 mm x 0.8 mm and has an overall thickness of 0.40 mm. The schematic of the MOS*kin* simulation model is illustrated in Figure 4.7. Its sensitive SiO_2 dose scoring volume is 1 μm thick, and is hermetically sealed in with the overlying kapton polyamide layer (with a reproducible thickness of 20 μm as illustrated) and sandwiched between the 0.374 mm thick silicon substrate. The silicon die is essentially a drop-well structure surrounded by tissue-equivalent kapton/epoxy.

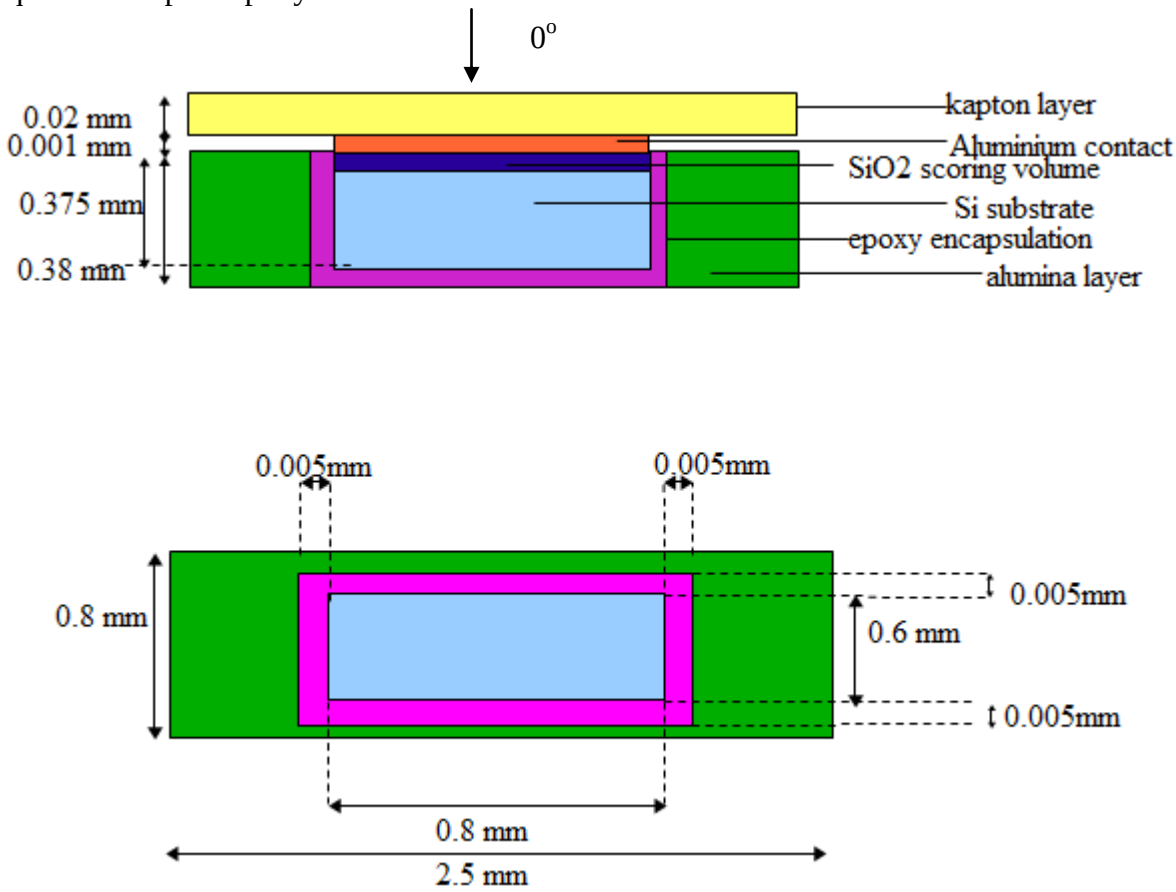

Figure 4.7: Cross sectional view of the MOS*kin* structure. The 0° orientation refers to the beam normally incident on the kapton polyamide surface of the MOS*kin*. b) Top view of MOS*kin* structure (not to-scale)

The primary difference in geometry between the conventional MOSFET and the MOS*kin* dosimeter is the encapsulation used. The conventional MOSFET uses a hemispherical epoxy bubble (with a radius of approximately 1 mm) which is not

reproducible, whereas the MOS*kin* encapsulation is essentially a highly reproducible, thin film of polyamide that hermetically seals and protects the sensitive volume of the MOS*kin*. The thickness of the polyamide film may be custom manufactured according to the clinical application of interest. For the measurement of skin dose, the polyamide film is set to be water equivalent depth (WED)70 µm thick, where 70 µm thickness is conventionally adopted as the depth of the skin according to ICRP recommendations [182]. Moreover, the MOSFET had high –Z wirebonding of a die to Cu leads on a kapton carrier this is not present in the MO*Skin.*

As illustrated in Figures 4.5 and 4.7, MOSFETs have an asymmetrical structure. Consequently, it is expected that they exhibit angular dependence, known as a measured change in detector response as a function of beam orientation, due to the different interaction coefficients and scattering behavior of the photon beam. To examine structural asymmetry, the angular response of the MOS*kin* was simulated in this work, and subsequently compared with current published literature on the angular response of the conventional MOSFET with epoxy bubble.

4.4.3 Dosimeter Response Factor

To assess the water equivalence of the MO*Skin*, we adopted the use of an energy dependence factor, the dosimeter response factor (DRF). The DRF at a known beam quality Q, DRF_Q, relates the ratio of the dose to the sensitive volume (SV) of the detector $D_{sv}(Q)$ to that of the dose to the medium in the absence of the detector $D_{med}(Q)$ at the same point of interest . That is,

$$DRF_Q = D_{sv}(Q)/D_{med}(Q) \qquad \text{(Eq. 4.4)}$$

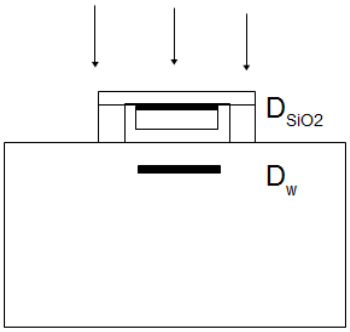

Figure 4.8: Diagram showing the use of the DRF at beam quality Q. With the MOS*kin*

positioned face-up on the surface of the water phantom and irradiated by an incident photon beam of beam quality Q, the DRF is defined as the ratio of the absorbed dose in the micron-thick SiO2 sensitive volume to the absorbed dose in the micron-thick water volume at 70 µm depth in the water phantom

Although the quantity DRF_Q is generally studied as a function of beam quality Q, DRF_Q also varies depending on the location (at different depths in a homogeneous water phantom, for example) in a particular beam quality Q [177]. At depth d in a water phantom with an incident beam quality Q, the DRF_Q is defined as:

$$DRF_Q(d) = D_{sv}(d, Q)/D_{water}(d, Q) \quad \text{(Eq. 4.5)}$$

4.5 Results and Discussion

4.5.1 Simulated energy response of the conventional MOSFET with epoxy bubble

Figure 4.9 shows the results of the simulated energy response of the MOSFET in free-air geometry (no backscatter) compared to that on a water phantom surface (with full backscatter). The curves are plotted alongside the ratio of the mass energy absorption curve of silicon-to-water in order to investigate the effect that device materials and geometry have on the detector energy response. In the presence of backscatter material, MOSFET energy response was larger than without backscatter material. There is a similar trend between the mass energy absorption curve of silicon-to-water and the MOSFET oriented upside down (i.e. in the 180^o orientation) showing that the response of the MOSFET is driven by secondary electrons from the silicon substrate immediately upstream to the scoring volume.

4.5.2 Simulated energy response of the MO*Skin*

Similarly, Figure 4.10 shows the energy response of the MO*Skin* in free-air geometry (no backscatter) and on a water phantom surface (with full backscatter). As is the case with the conventional MOSFET, there is a similar trend between the mass energy absorption curves of silicon-to-water with the MO*Skin* oriented upside down (i.e. in the 180^o orientation). Once again, this shows that the response of the MOS*kin* is very much driven by the secondary electrons from the silicon substrate immediately upstream to the scoring volume. It can also be seen that with backscatter material compared to

without backscatter, the upside down MOS*kin* shows a larger energy response.

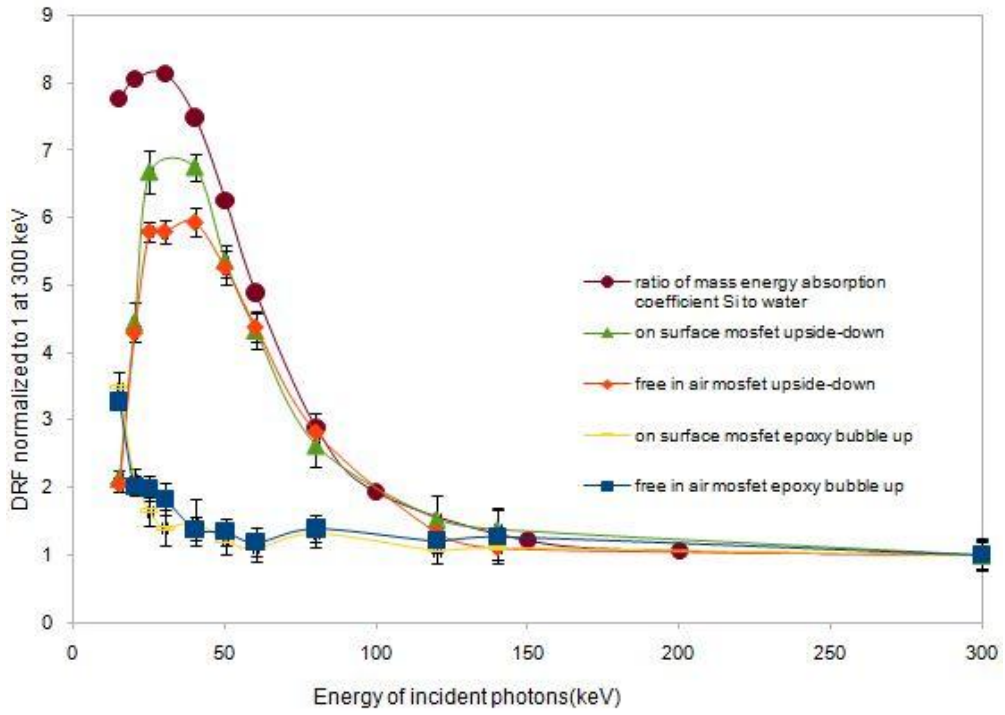

Figure 4.9: MOSFET energy response (DRF) for monoenergetic photon energies from 15 keV to 300 keV plotted alongside the mass energy absorption coefficient ratio of silicon to water.

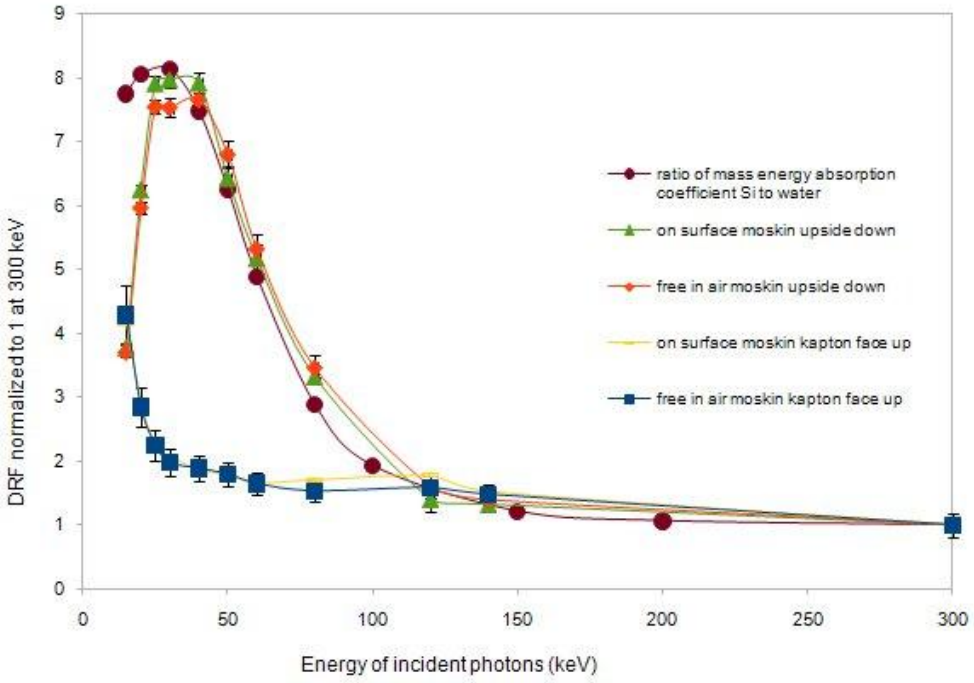

Figure 4.10: MOS*kin* energy response (DRF) for monoenergetic photon energies from 15 keV to 300 keV plotted alongside the mass anergy absorption coefficient ratio of silicon to water.

Table 4.4 summarizes the obtained simulation results. In this study, the simulation results with an ideal monoenergetic photon beam showed a maximum response of 3.3±10% (in air response) and 3.5±24% (on phantom surface) with the MOSFET with the epoxy bubble in the face-up orientation. With the MOSFET in the face down orientation, the maximum energy response factor of the MOSFET in air and on phantom surface was 5.9±20% and 6.7±20% at 40 keV respectively. A similar study by Wang et al. [144,145] performed in MCNP using monoenergetic photon beams showed a maximum response of up to 6.6 at 40 keV. This validates our MOSFET simulations in GEANT4.

The experimental work performed by Edwards et al (1997) [139] used quasi-monoenergetic beams which gave a maximum normalized energy response of 4.19±0.25 (MOSFET 1) and 4.44±0.26 (MOSFET 2) at a mean incident photon energy of 33 keV. As per manufacturer's data, the energy response was expected to be at a maximum of 4.4 for a mean incident x-ray energy of 45 keV compared to its response where the incident x-ray energy is greater than 200 keV [139]. For our simulations, the DRFs were normalized to that at 300 keV, since the energy response of the detector at 300 keV and 6 MV is nearly the same [117].

In addition, the experimental work done by Kron et al (1998) [142] it was found that the CMRP n-MOSFETs had a maximum response of 3.2 at 53 keV. A possible reason for the discrepancy between the experimentally reported results and the results of the simulations is likely due to the fact that the MOSFET dosimeter simulated model has not taken into account electron-hole recombination effects which is particularly significant at the low energies (i.e. the intrinsic energy dependence of the MOSFET), as previously discussed in section 4.1 and also due to different packaging. The metal substrate and the absence of any protective build up in the case of [138] results in the increase in response of the MOSFET for larger photon energies, due to backscattered electrons from the high Z metal substrate.

Figure 4.11 shows the effect of varying the thickness of the overlying polyamide kapton layer on the surface energy response of the MOS*kin*. Increasing the thickness of the polyamide film from 20 µm to 70 µm gave a two-fold improvement in energy response. This shows that by adjusting the thickness of the polyamide film, the surface energy response of the MOS*kin* can be optimised according to the clinical application of interest. With its near-flat energy response from 50 keV to 300 keV, it is clear that the MOS*kin* with its 70 µm overlying polyamide film is suitable for skin dosimetry in this energy range [183].

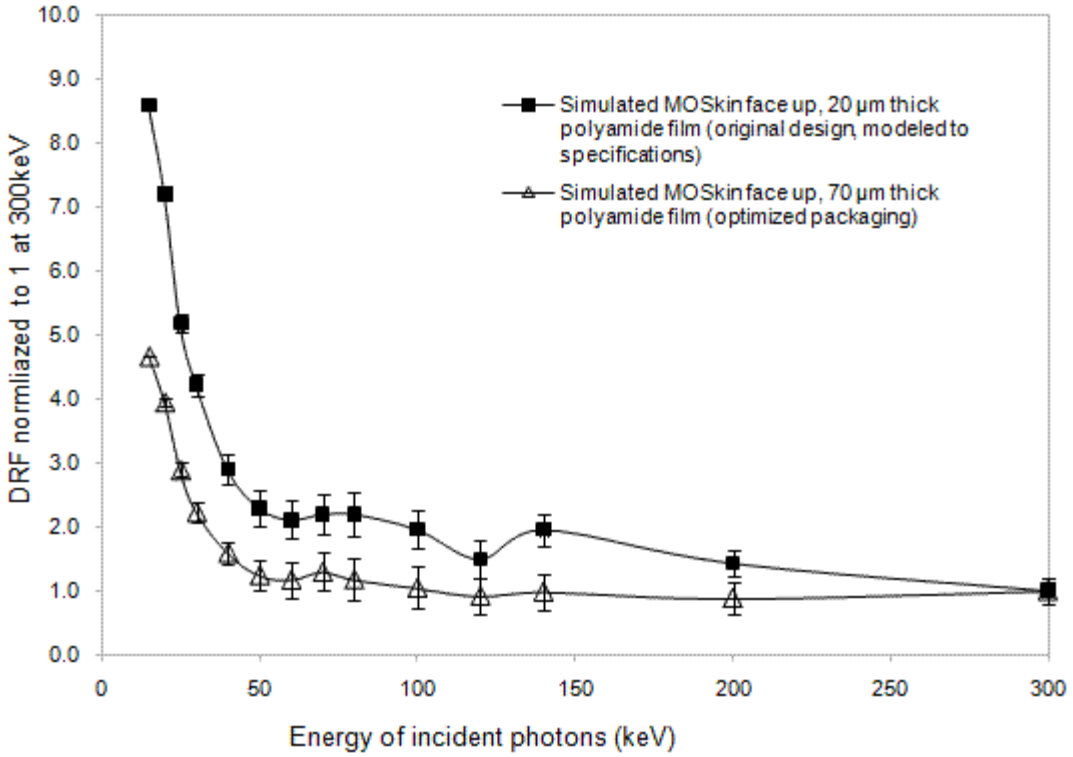

Figure 4.11: Monte Carlo simulated DRF with the faceup MOS*kin* on phantom surface. Different thicknesses of polyamide film were simulated; 20 µm polyamide film (♦) and 70 µm polyamide film (Δ).

Figure 4.12 shows the difference in surface energy response between the conventional MOSFET with epoxy bubble simulated by Wang *et al* [145]compared to that of the simulated CMRP MO*Skin* on the phantom surface. At low energies when used in the face-up orientation, the MO*Skin* demonstrates an improved energy response compared to the conventional MOSFET.

Table 4.4: Summary of the results of the maximum energy response factors in a monoenergetic photon beam, derived from this simulation study

3.3±10% at 15 keV (in air, face up) 5.9±20% at 40 keV (in air, face down)	MOSFET	ideal monoenergetic photon beam
3.5±24% at 15 keV(on phantom surface, face up) 6.7±20% at 40 keV (on phantom surface, face down)	MOSFET	ideal monoenergetic photon beam
4.3±4% at 15 keV (in air, face up) 7.7±17% at 40 keV (in air, face down)	MO*Skin* (CMRP)	ideal monoenergetic photon beam
4.2±5% at 15 keV(on phantom surface, face up) 7.9±15% at 40 keV (on phantom surface, face down)	MO*Skin* (CMRP)	ideal monoenergetic photon beam

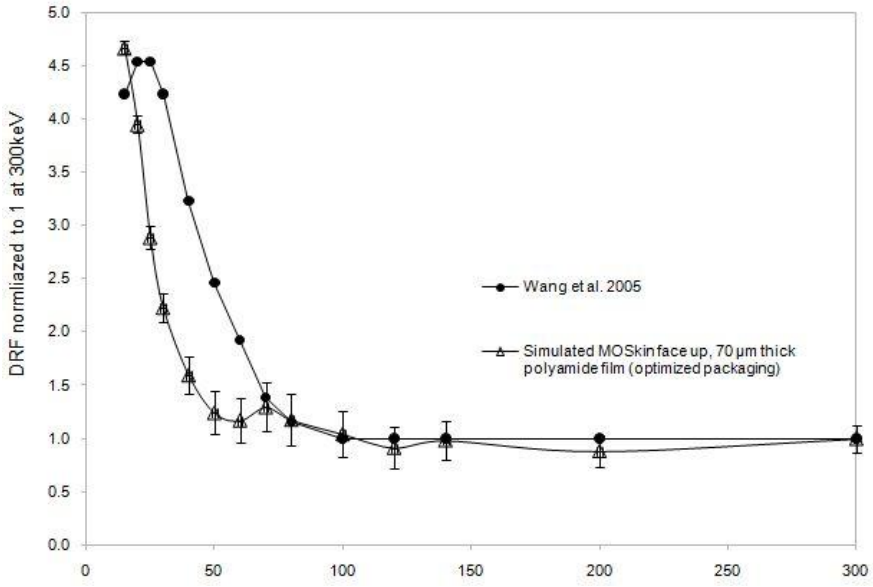

Figure 4.12: Comparison of the simulated energy response of the MOS*kin* with the simulated energy response of the conventional MOSFET with epoxy bubble.

Figure 4.13 compares the DRF obtained with monoenergetic x-ray photons with that of the spectral x-ray beam. In the energy range 50 keV upwards, there is a close match between the DRFs obtained with the simulated monoenergetic beams and spectral

beams; this verifies the validity of our simulated x-ray spectrum.

At photon energies lower than 50 keV, the DRF obtained with a spectral beam presented up to a 53% larger energy response compared to the monoenergetic x-ray beam. This is likely due to the compounding effect of the spectral x-rays.

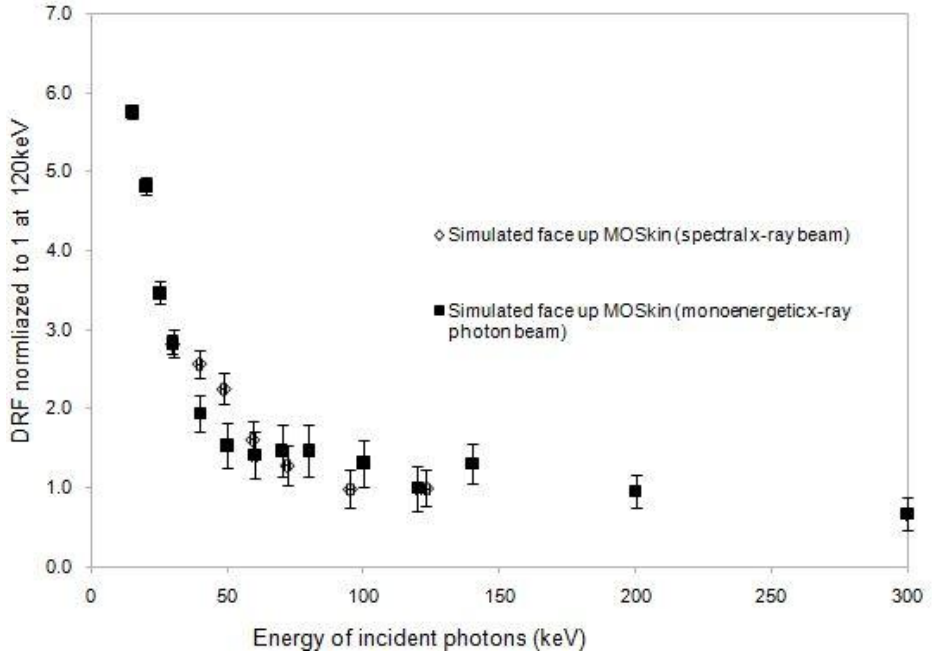

Figure 4.13: Comparison of the simulated energy response of the MOS*kin* in a monoenergetic beam and a spectral beam. Effective energy of the spectral beam was derived from the interpolation of values from the HVL curve in Appendix B.

4.5.3 Optimisation of MO*Skin* energy response with thin metallic foil

In order to achieve an energy optimised photon dosimeter (i.e. correction for the over-response of the MOSkin at low energies), the technique of low energy photon filtration was implemented in GEANT4 by means of the addition of a thin metallic foil above the sensitive volume of the MOSkin.

Through the method of iterative trial-and-error starting from the photon attenuation equation $I_1=I_oe^{-\mu t}$, an initial thickness of 35 µm of copper copper foil t_{cu} was determined. Monte Carlo simulations were run to fine tune the energy response of the MOS*kin*. It was found that using a single layer of metallic foil resulted in an overcorrection of response in most cases, which was less than ideal. The use of a composite metallic foil

resulted in an improved response compared to just a single layer of metallic foil. Figure 4.14 shows the improved MOS*kin* response with the composite copper-aluminium filter on the surface of the water phantom and Figure 4.15 shows the corresponding structure of the energy optimised MOS*kin*.

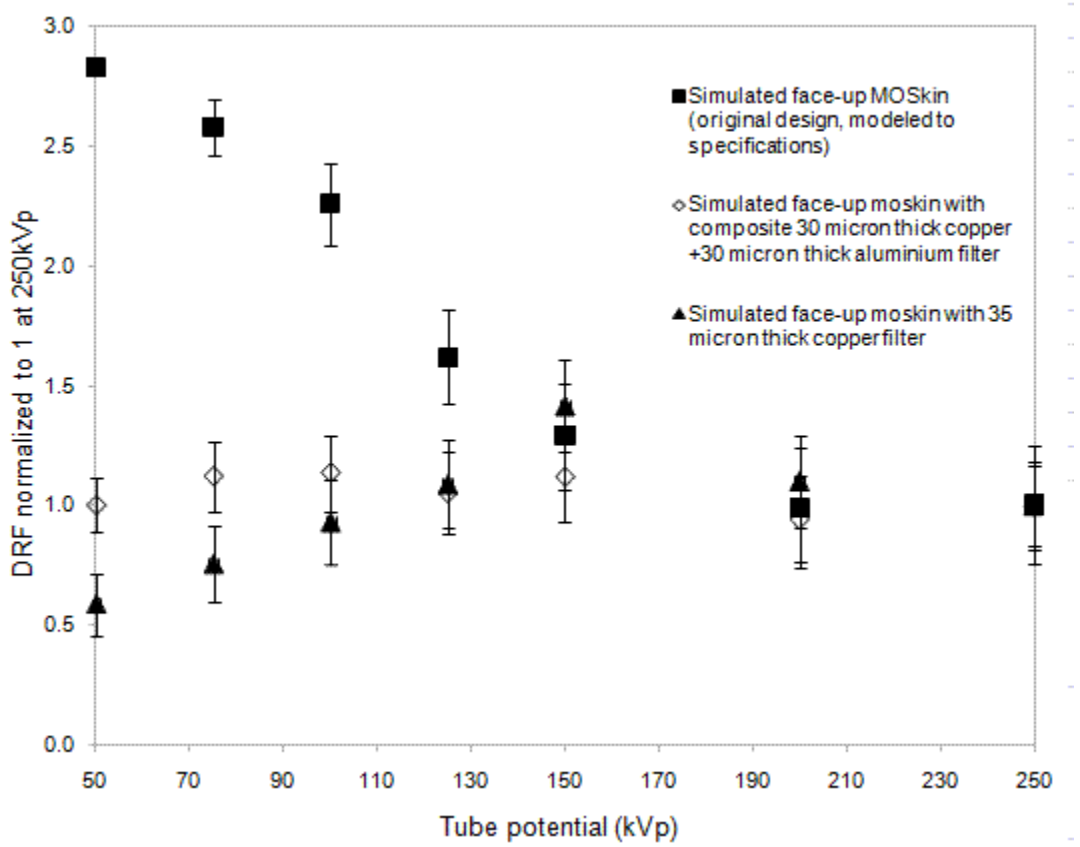

Figure 4.14: Comparison of the energy response of the face-up MOS*kin* (no metallic foil) with the energy-optimised MOS*kin* (with metallic foil) on the surface of the water phantom.

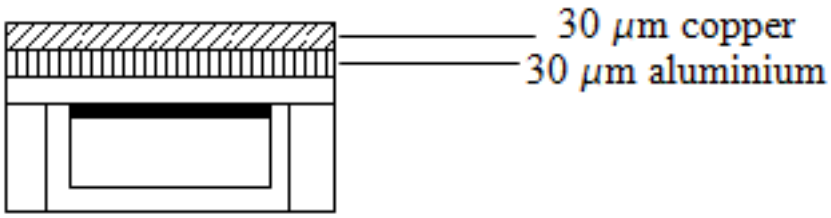

Figure 4.15: Schematic design of the energy-optimised MO*Skin* dosimeter, with the placement of a metallic filter, to correct the energy dependence of the MO*Skin* by flattening its dose response across a desired energy range.

4.5.4 Simulated depth dose response

Figure 4.16 shows the relative depth dose plots of the simulated MOS*kin* response at depth in water compared to that of the true simulated water response. For superficial beam qualities 50 kVp, 100 kVp and 150 kVp, the depth dose response was normalized to 1 at the surface of the water phantom (Figure 4.16 a, b, c) . For an orthovoltage energy of 250 kVp, the depth dose response was normalized to 1 at 2 cm depth in the water phantom (Figure 4.16 d).

For superficial photon beam qualities, there was a close correspondence between the simulated MOSkin depth dose response and that of the simulated water depth dose response at shallow depths under 2 cm. A maximum difference between the MOS*kin* and water scored depth dose response of 8 % at 20 mm depth was found for the 50 kVp spectrum, a 6% difference at 20 mm depth for the 100 kVp spectrum, and a 5% difference at 20 mm depth for the 150 kVp spectrum respectively. In general, beyond 20 mm water depth, the MOSkin generally under responds. This underresponse is attributed to increasing attenuation and out-of-field scatter of the primary photons in the water medium at deeper depths, thereby contributing less photon flux to the scoring volume of the MOS*kin*.

For the orthovoltage photon spectrum of 250 kVp, a maximum difference of 10% in depth dose response was found at the surface of the phantom where the depth of normalization was taken to be 20 mm depth in the phantom.

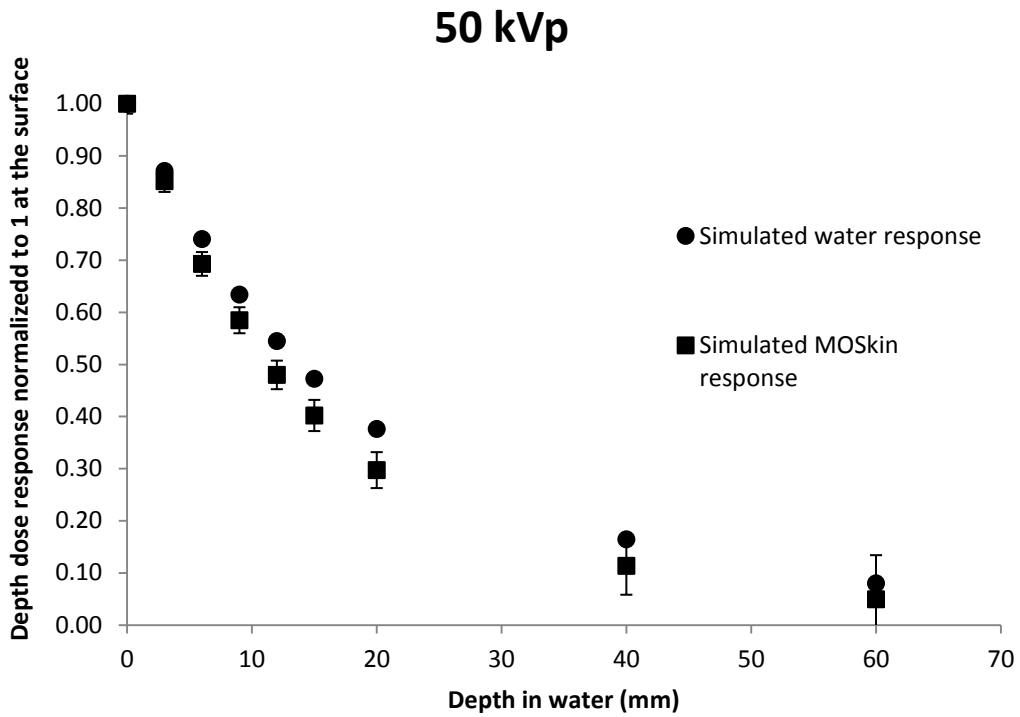
50 kVp
Depth dose response normalizedd to 1 at the surface
1.00
0.90
0.80
0.70
0.60
0.50
0.40
0.30
0.20
0.10
0.00
0
10
20
30
40
50
60
70
Depth in water (mm)
Simulated water response
Simulated MOSkin response

(a)

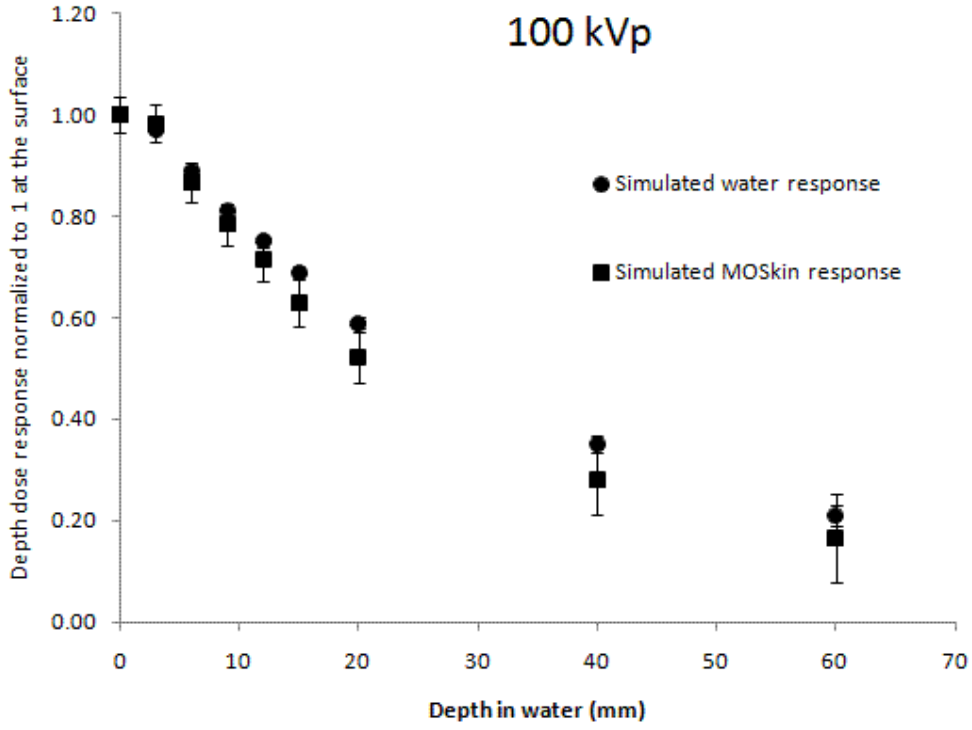
100 kVp
Depth dose response normalized to 1 at the surface
1.20
1.00
0.80
0.60
0.40
0.20
0.00
0
10
20
30
40
50
60
70
Depth in water (mm)
Simulated water response
Simulated MOSkin response

(b)

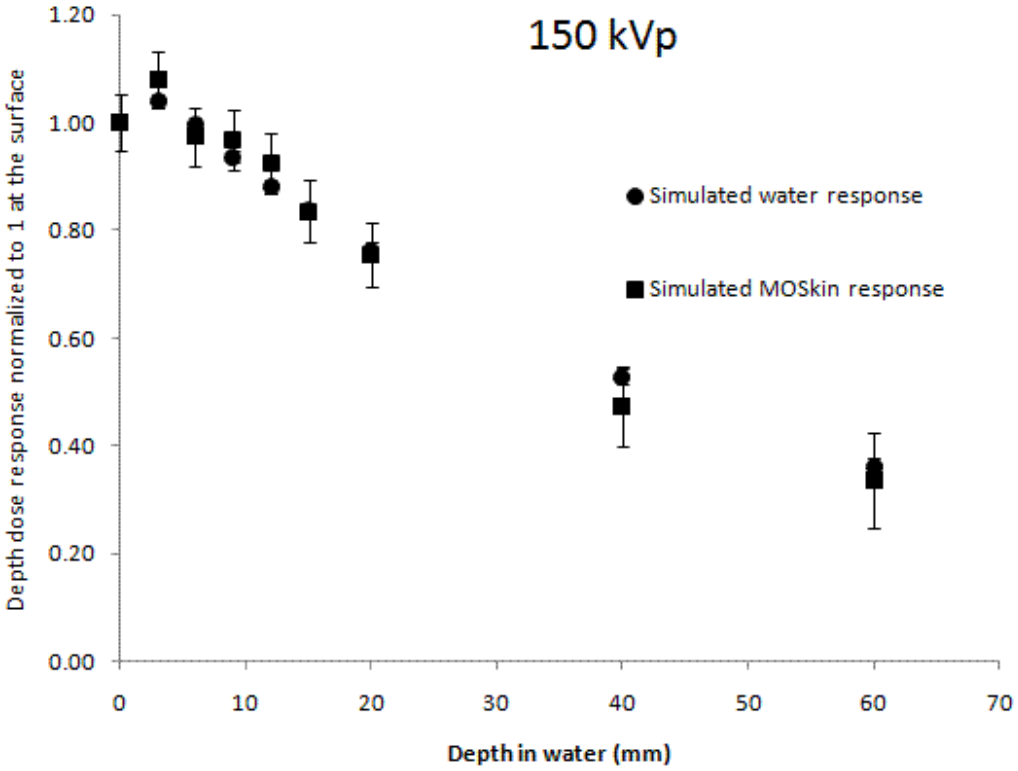

(c)

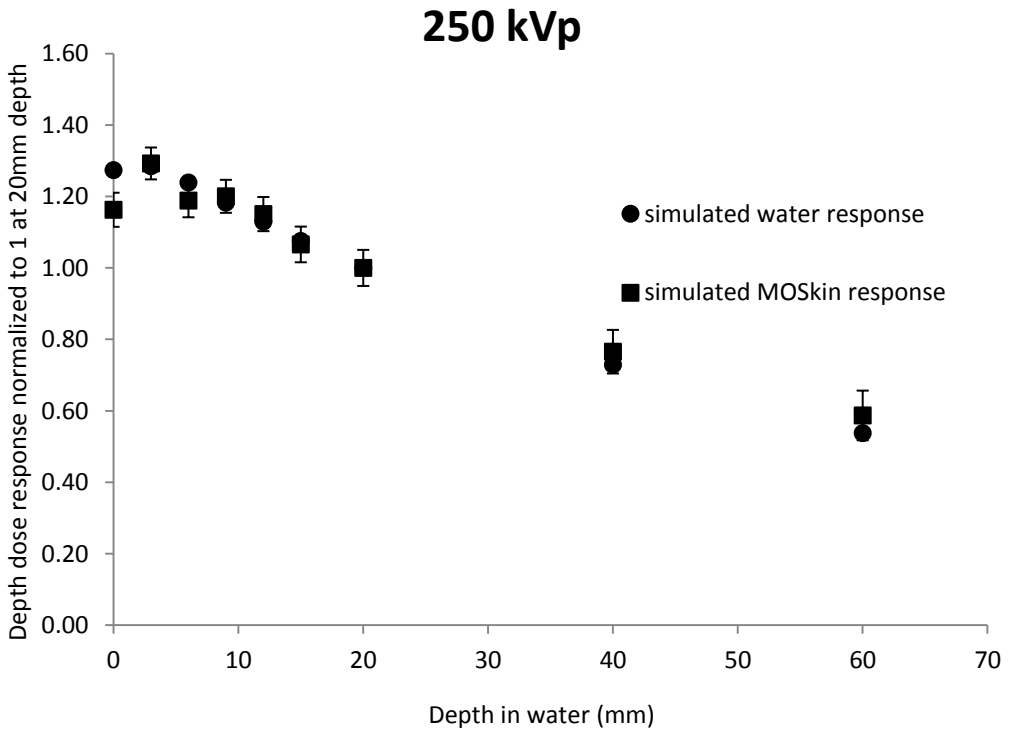

(d)

Figure 4.16: Depth dose response of the MOS*kin* dosimeter at various depths ranging from on surface (0 mm) to 60 mm depth in a 30 cm x 30 cm x 20cm homogeneous

water phantom for incident x-ray photon spectra (a) 50 kVp (b) 100 kVp (c) 150 kVp (d) 250 kVp. Responses were normalized to 1 at a depth of 20 mm in water.

4.5.5 Simulated angular response

The MOS*kin* is an asymmetrical device; scattering conditions and attenuation of photons are not equal for different directions of incidence. Consequently, it is expected to exhibit angular dependence, defined as a change in detector response as a function of beam orientation. For the MOS*kin* to be successfully applied in a multi-directional x-ray CT photon beam, its angular response was simulated. An ideal dosimeter would have zero angular dependence in a CT beam.

To investigate MOS*kin* angular response, the 50 kVp photon spectrum (low energy superficial beam) and the 200 kVp photon spectrum (orthovoltage beam) (Figure 4.17) were used as beam inputs in GEANT4. Air was chosen as the medium of interest to study the sole effect of structural geometry and materials on MOS*kin* angular response. A dual MOS*kin* configuration was also simulated which served as the simulation design control for this study. The dual MOS*kin* configuration consisted of 2 MOS*kin*s aligned polyamide kapton face- polyamide kapton face to each other; this negated the effect of angular response.

A maximum (worst-case) angular response of 6% and 8% was found for the 50 kVp (Figure 4.17 a) and 200 kVp photon spectrum respectively in the 180^{o} (face-down) orientation (Figure 4.17 b).

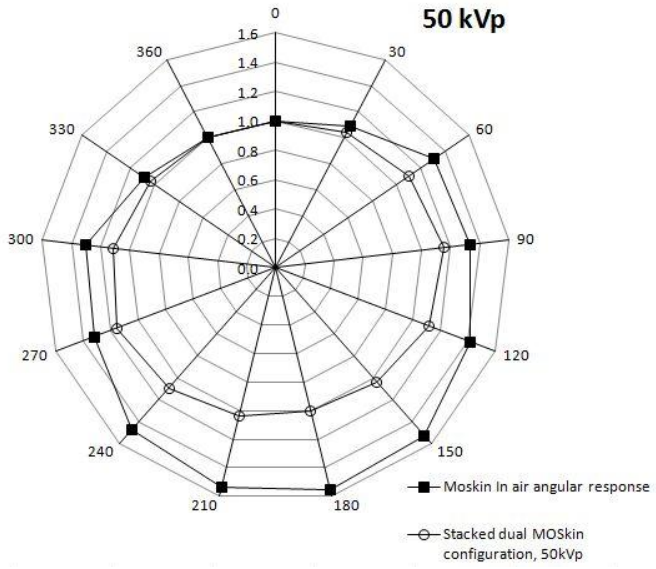

(a)

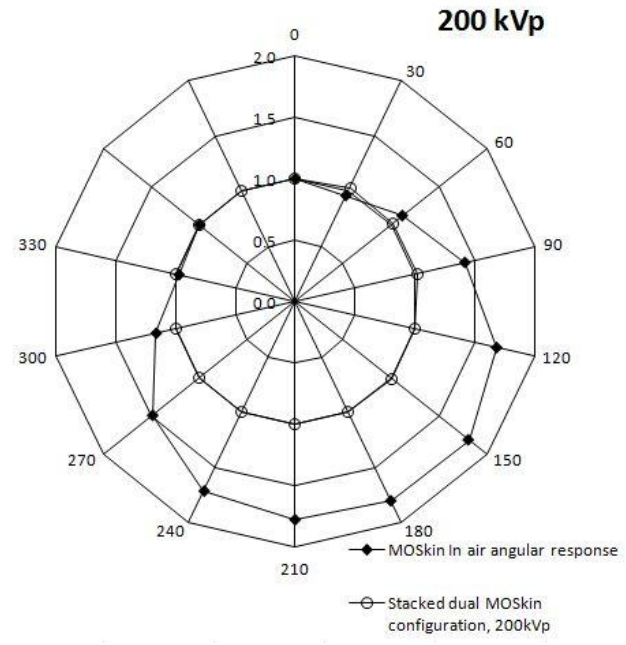

(b)

Figure 4.17: Simulated angular response of the MOSkin (a) 50 kVp (b) 200 kVp in free air geometry for single and dual MO*Skin* configurations.

4.6 Conclusions and Recommendations

This study has shown that the GEANT4 Monte Carlo Toolkit is a useful tool for studying the energy response of MOSFET radiation detectors. In particular, the GEANT4 Toolkit was used to model the materials and geometry of the MOS*kin*

dosimeter, and dosimeter energy response under different irradiation setups; in free- air (without backscatter), on phantom surface (with backscatter) in the 0^o and 180^o beam orientations, at various depths in a water phantom and the in-air angular response, was subsequently evaluated.

From the results of this simulation study, it was found that the MOS*kin* dosimeter with its polyamide kapton face up is the preferred orientation for cases in-air, on phantom surface and at water depth. Within the energy range 50 keV to 300 keV, it is proposed that the use of a composite metallic filter composed of a 30 μm thick copper and aluminium foil will achieve an improved energy response if the MOS*kin* is to be used as a skin dosimeter within this energy range. Beyond a depth of 2 cm, the MOS*kin* generally slightly underresponds compared to the simulated water dose for 50-250 kVp x-ray. Based on the results of this simulation, it is suggested that depth dose correction factors be implemented if the prototype MOS*kin* is used for the accurate measurement of phantom organ doses beyond the depth of 2 cm in clinical kilvoltage beams.

The maximum angular response of the MOS*kin* dosimeter in air was found to be 6% and 8% with the 50 kVp and 200 kVp x-ray spectra respectively. To correct for the angular response, a dual configuration MOS*kin* is proposed where the polyamide film of 2 MOS*kin*s face each other. Such a configuration negates the angular response of individual MOS*kin*s.

5 Experimental characterisation of the MO*Skin* radiation dosimeter at clinical kilovoltage photon energies

5.1 Introduction

The concept of a radiation-sensitive metal-oxide silicon field-effect transistor, the "RADFET" as coined by Hughes [184], was first initiated by Poch & Holmes-Siedle in 1968 [150,151,185]. The term RADFET has since been interchangeably referred to as MOS dosimeters and space-charge transducers. For the latter term, space-charge refers to the corresponding increase in space charge stored in the oxide as absorbed radiation dose increases. As previously described in Chapter 3, section 3.2, the principle of operation of the MOSFET radiation sensor is based on the generation of electron-hole pairs in the gate oxide of the MOSFET due to ionizing radiation. This results in a change of potential across the dielectric which can be measured.

The CMRP MOSkin radiation dosimeter with its novel packaging design is built upon MOSFET technology. The MOSkin has been successfully applied in several practical radiation therapy scenarios for skin dose measurements. These scenarios include high-dose rate (HDR) brachytherapy [156], helical tomotherapy in total scalp irradiation [157] and intensity modulated radiation therapy (IMRT) [112]. To date, the MOSkin dosimeter has not yet been characterised in a typical diagnostic kilovoltage energy x-ray beam at low doses. Prior to its clinical application in a diagnostic radiological beam, a comprehensive experimental characterisation of this radiation sensor is a necessary precursor to ensure accurate and reliable measurements.

The purpose of the following chapter therefore was to fully characterise the MO*Skin* dosimeter in the clinical kilovoltage photon energy range. This was achieved by performing a series of comprehensive radiological tests to elucidate the potential applications of the MO*Skin* dosimeter at clinical kilovoltage energies. These characterisation tests included the effect of varying gate voltage on surface dose measurements, MO*Skin* reproducibility and batch homogeneity, short term signal fading, dose linearity, the effect of accumulated dose on MO*Skin* sensitivity, energy dependence, angular dependence and depth dose water equivalence.

5.2 Materials

5.2.1 Source Beam

As detailed in Table 4.2 (Chapter 4), the Gulmay D3300 superficial/orthovoltage therapy unit provided the beam source for the following experimental characterisation work.

The x-ray tube target was a tungsten anode angled at 30^{o}, with an inherent 3 mm beryllium filtration. A 10 cm diameter open-ended applicator cone with a source-to-surface distance of 30 cm were used for 50, 75, 100, 125 and 150kVp irradiations, while a 10 cm diameter closed-ended applicator cone with a source-to-surface distance of 50 cm were used for 200 kVp to 250 kVp irradiations.

The nominal output for the Gulmay D3300 orthovoltage machine was calibrated to deliver 1 cGy MU^{-1} at D_{max} with D_{max} taken to be at the surface of the RMI 457 solid water phantom following the IPEMB code of practice as per biannual departmental quality assurance protocol [186]. A dose of 20 MU (20 cGy) was delivered at D_{max} (phantom surface).

5.2.2 Phantoms

The RMI 457 solid water phantom was previously evaluated to be water equivalent to within 1% uncertainty for kilovoltage beams [187,188] and low energy brachytherapy studies [187-189], thus meeting ICRU requirements [190]. Each solid water block had dimensions 30 cm x 30 cm and varying thickness of 0.1 cm, 0.2 cm, 0.5 cm, 1 cm, 2 cm, and 5 cm. Depending on the energy of interest, the appropriate backscatter thickness was selected. In particular, for the kilovoltage energy range of all of the measurements, we used a total backscatter thickness of 15 cm which was adequate to ensure full backscatter conditions.

A cylindrical polymethyl methacrylic (PMMA, ρ=1.2 g cm^{-3}) insert was custom designed and milled for this study. The insert was sliced into two halves in the longitudinal direction, with a trench running across the central axis for placement of the

MO*Skin* sensor embedded in a kapton strip. Figure 5.1 illustrates. This custom designed insert was milled in accordance with the dimensions of a typical Farmer ion chamber insert.

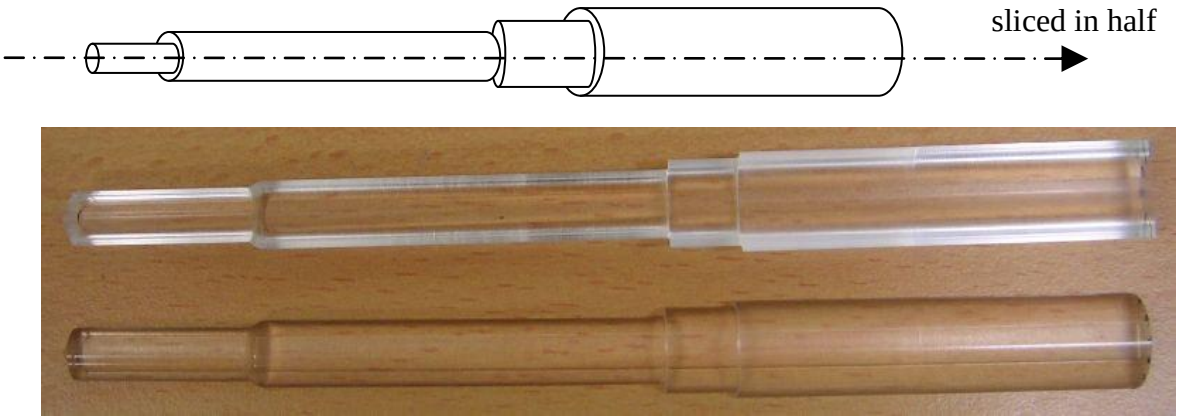

Figure 5.1: Custom manufactured cylindrical PMMA phantom insert for angular response characterisations

5.2.3 The MO*Skin* Dosimetry System

As photographed in Figure 5.2, the MOS*kin* detector is 30.0 cm long and 2.5 mm wide with an overall thickness of about 0.4 mm. On one end of the MOS*kin* detector lies the silicon radiation sensor, just 0.8 mm x 0.6 mm x 0.35 mm in size, with a submicron gate oxide thickness of 0.55 µm. On the other end of the MOS*kin* detector, is the connector pins leading to the cables for online readout with the MO*Skin* reader. Further structural and operational details of the MOS*kin* may be found in [112].

Figure 5.2: Photograph of the MO*Skin* dosimeter designed and developed by the Centre for Medical Radiation Physics (CMRP) at the University of Wollongong.

The threshold voltage, before and after irradiation, is proportional to the accumulated dose. The change in threshold voltage was measured with a custom-built portable, battery-powered MOS*kin* reader, the Clinical Semiconductor Dosimetry System (CSDS) designed by the CMRP at the University of Wollongong. Figure 5.3 illustrates. The CSDS reader allows up to 5 MOS*kin*s to be readout simultaneously. The reader works by applying a gate voltage of 15 V during irradiation to improve linearity of the

response and sensitivity of the MO*Skin.*

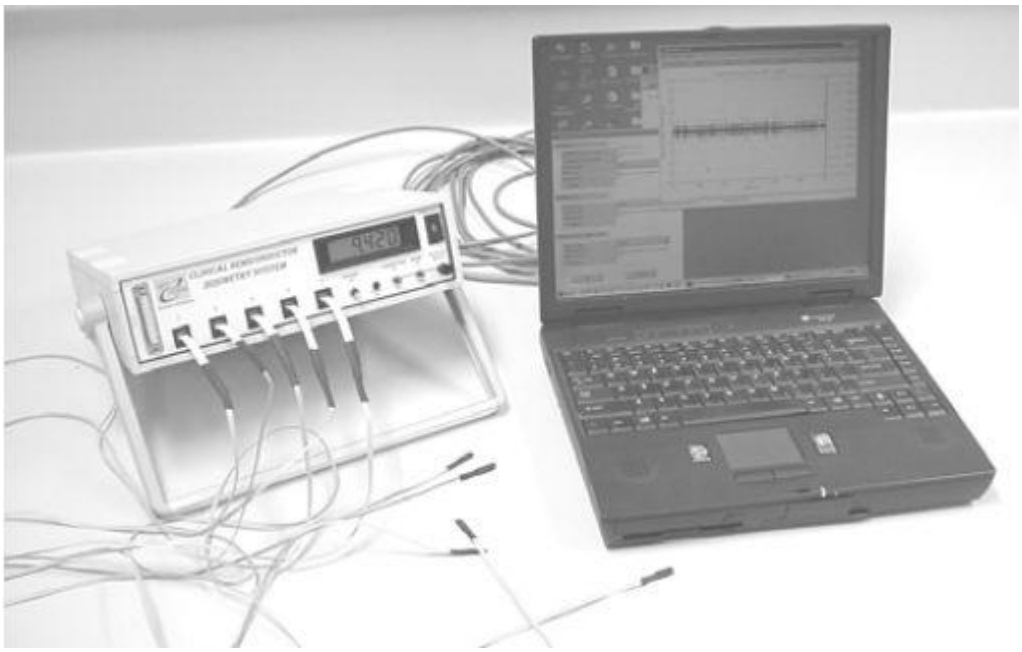

Figure 5.3: The Clinical Semiconductor Dosimetry System (CSDS) designed and developed by the Centre for Medical Radiation Physics (CMRP) at the University of Wollongong (Picture reproduced from [191])

5.2.4 Ionisation chambers

It has been shown that the use of parallel plate chambers is suitable for kilovoltage x-ray depth dose measurements [192,193]. The central axis depth dose profile obtained by the *MOSkin* was therefore compared with depth dose measurements obtained by the Markus parallel plate ionisation chamber (Model N23343, PTW-Frieburg, Germany) and the Attix plane-parallel ionisation chamber (Model 449, RMI, Middleton, WI). For the readout of deposited charge, each ionisation chamber was connected to a Farmer electrometer (Model 2570, NE Technology Ltd, Reading, UK).

5.3 Methods

5.3.1 Experimental setup for surface dose measurements

Figure 5.4 shows the experimental setup used for the *MOSkin* irradiations. To avoid measurement inconsistencies due to the heel effect, the *MOSkin* was aligned at the central beam axis in all cases.

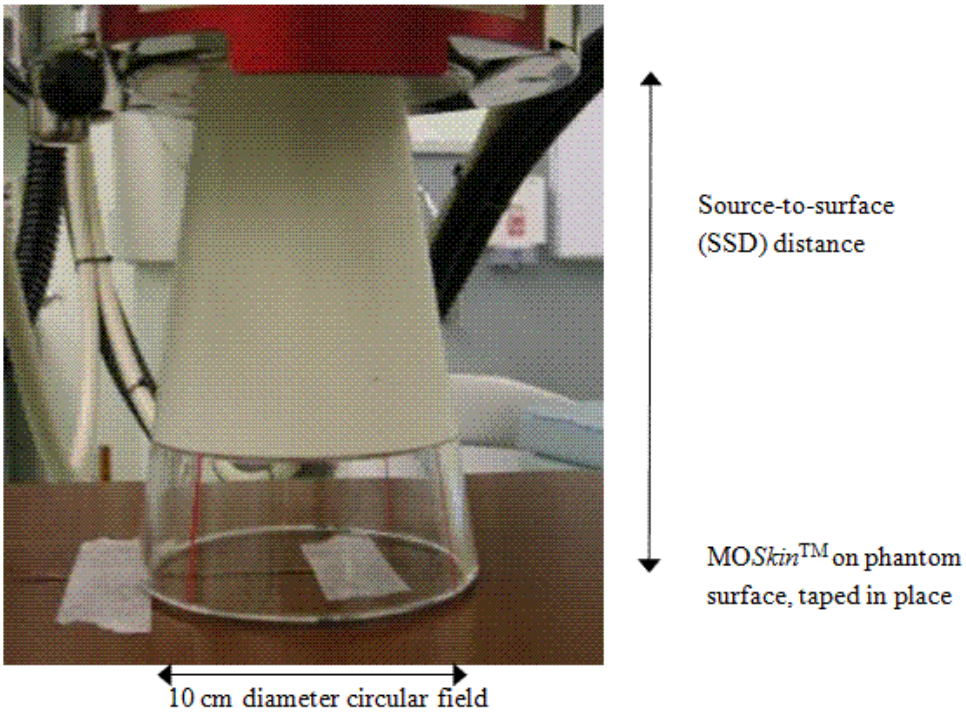

Figure 5.4: Experimental setup for the *MOSkin* placed on the surface of the 30 cm × 30 cm × 15 cm RMI 457 solid water phantom (Gammex RMI, Middleton, WI) during dose delivery at superficial and orthovoltage energies.

5.3.2 Effect of gate voltage on surface dose measurements

With the source and substrate terminals of the MOS*kin* grounded at a common potential, a gate bias was applied with respect to the drain terminal in order to investigate the effect of varying gate bias on MOS*kin* sensitivity.

For an applied tube potential of 150 kVp at a dose level of 20 cGy and a source-to-surface distance(SSD) of 30 cm, a known gate bias was applied to the MOS*kin* terminals by means of an external power supply during irradiation, and subsequently unplugged from the external power supply and readout with the CSDS. Each measurement was repeated thrice and the standard deviation calculated.

5.3.3 Individual Reproducibility and Batch Homogeneity

To investigate individual detector reproducibility, a single MOS*kin* detector on the surface of a solid water phantom was irradiated and readout for beam energies 50kVp, 100kVp and 150kVp at a dose level of 20 cGy. Measurements were repeated three

times and the standard deviation was calculated.

To investigate homogeneity across a batch of MO*Skins*, 4 MO*Skin* detectors were irradiated separately, with an applied dose of 20 cGy at 150 kVp tube potential.

5.3.4 Short-term Signal Fading

The fading test was conducted on a single MO*Skin* detector placed on the phantom surface at 150 kVp and a dose level of 20 cGy. After irradiation, the MO*Skin* detector was read out at 10 s intervals continuously over 240 s. The following equation illustrates how the percentage fading was calculated.

$$\% \text{ Fading} = \frac{|M_o - M_t| 100\%}{M_o}$$

where M_o and M_t are MO*Skin*™ measurements in mV, taken at $M_o = 0$ (immediate readout) and M_t (where $t \leq 240$ s) after irradiation.

5.3.5 Dose Linearity

With the MO*Skin* detector positioned at the beam central axis on the surface of the RMI 457 solid water phantom, doses from 2 cGy to 20 cGy at increments of 2 cGy were delivered for beam energies of 50 kVp, 100 kVp and 150 kVp to evaluate MO*Skin* linearity at these tube potentials.

5.3.6 MO*Skin* sensitivity change as a function of radiation history

With the MOS*kin* detector positioned at the beam central axis on the surface of the RMI 457 solid water phantom, the MOS*kin* was irradiated with a tube potential of 150 kVp at 50 cGy increments until it reached its maximum suggested accumulated dose (a change of 10 V in measured output which corresponded to a maximum accumulated dose of approximately 10 Gy).

As suggested by Lavallee et al. [146], sensitivity checks were conducted at 3 major checkpoints: start, mid-life (after an approximate 5 V change in measured output voltage) and end-life (after an approximate 10 V change in measured output) of the MO*Skin*. We made sure not to use the MO*Skin* dosimeter past its lifetime so as to avoid measurement inconsistencies associated with the creep-up effect [170] past an accumulated dose of 10 Gy.

5.3.7 Energy dependence

Energy dependence is broadly defined as the dependence of the dosimeter reading per unit of applied dose upon the incident photon energy E of the radiation beam.

The measured dosimeter response factor DRF(E) with the MOS*kin* on the surface of the phantom is defined as

$$DRF(E) = \frac{\Delta V_{th}(mV)}{D_{max}(cGy)} \qquad \text{(Eq. 2)}$$

where ΔV_{th} is the measured change in threshold voltage, which is directly proportional to the radiation dose absorbed in the SiO_2 (SV) of the *MOSkin* during irradiation. D_{max} is the dose delivered at the depth of maximum dose, defined in the IPEMB protocol [186], at the surface of the RMI 457 water phantom.

For comparability across the kilovoltage range of energies tested in this work, we normalized the DRF(E) to the end point DRF(250kVp) with the MOS*kin* positioned on the solid water phantom surface.

$$\text{Normalized DRF} = \frac{\text{DRF (E)}}{\text{DRF (250kVp)}}$$

5.3.8 Angular dependence

The angular dependence of the *MOSkin* was measured by rotating the PMMA phantom insert through increments of 30^o (as manually demarcated as shown in Figure 5.5) within the polystyrene block at 1 cm depth, giving a total of 11 measurements starting from 0^o and ending at 360^o (0^o). Each measurement was repeated twice.

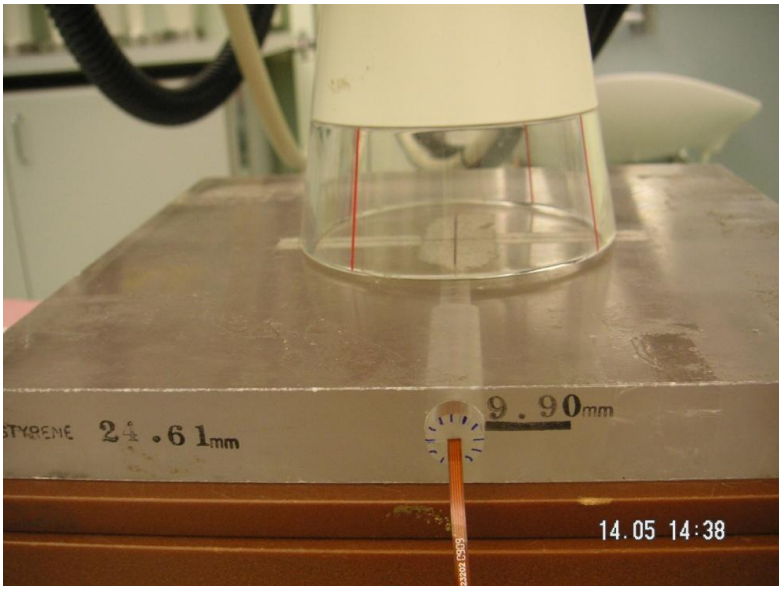

Figure 5.5: The custom manufactured phantom insert consisting of 2 longitudinally sliced PMMA halves were placed into the slot in the polystyrene phantom at a depth of 1 cm in polystyrene.

5.3.9 Depth dose water (tissue) equivalence

To assess if depth dose correction factors are needed for the MOS*kin* dosimeter at various depths in the water phantom, we measured the response of the MOS*kin* at increasing depths up to 60 mm starting at the surface of the water phantom for two beam qualities 100 kVp and 150 kVp.

The central axis depth dose profile obtained by the MOS*kin* measurements was compared with depth dose measurements obtained by the Markus parallel plate ionisation chamber (Model N23343, PTW-Frieburg, Germany) and the Attix plane-parallel ionisation chamber (Model 449, RMI, Middleton, WI). To measure the ionisation, each chamber was connected to a Farmer Dosemeter (Model 2570, NE Technology Ltd, Reading, UK).

5.4 Results and Discussion

5.4.1 Effect of gate voltage on surface dose measurements

Table 5.1 summarizes the results of varying gate voltage on MOSkin dose sensitivity. Without the use of an external power supply during irradiation, dose sensitivity was 6.7 mV/cGy. When a 30V gate bias was applied to the MOS*kin* during irradiation, MOS*kin*

dose sensitivity improved by 8% to 7.2 mV/cGy. Increasing the external bias supply further to 50 V during irradiation resulted in an overall 18% improvement in dose sensitivity to 7.9 mV/cGy. Where phantom measurements are concerned, the use of a high voltage power supply is not of major concern. However, at 50 V, the MOS*kin* should not be applied for in-vivo dosimetry (i.e. on the skin of real patients) due to patient safety considerations.

Table 5.1: Effect of different gate voltages on MOSkin Dose Sensitivity for a tube potential of 150 kVp and an applied dose of 20 cGy.

Applied gate voltage during irradiation (V)	Dose sensitivity (mV/cGy)	% improvement in dose sensitivity[a]
No external power supply	6.7	
30	7.2	8%
40	7.6	15%
50	7.9	18%

[a] % improvement in dose sensitivity= $\frac{Dose\ sensitivity_{applied\ gate\ bias} - Dose\ sensitivity_{no\ external\ power\ supply}}{Dose\ sensitivity_{no\ external\ power\ supply}}$ x100%

5.4.2 Individual Reproducibility and Batch Homogeneity

Measured reproducibility was under ± 5 % for the beam energies used in this study- 50kVp, 100kVp and 150kVp with an applied dose of 20 cGy (0.2 Gy). At 150 kVp, the reproducibility for 3 repeats was good with a coefficient of variation (COV) of 3.7%. Our reported findings are comparable with the error range of less than 8% for doses between 0.2 Gy and 1 Gy for the TN-502RDI MOSFET detectors with the standard bias sensitivity according to manufacturer's specifications [194].

At a tube potential of 150 kVp, the tested batch of MOS*kin*s demonstrated good homogeneity with an overall COV of 3.8%. This confirmed the excellent manufacturing reproducibility of the polyamide buildup layer and MO*Skin* chip.

5.4.3 Short-term Signal fading

Over a time interval of 240 s, the percentage fading of the MOS*kin* reading was less than 1%. This demonstrates that the MOS*kin*s are highly robust.

Our results are in good agreement a previous study done by Ehringfeld et al [194] for

MOSFETs irradiated at 150 kV at 200 cGy, considering that the dose levels at which our MOS*kin* detectors were irradiated was on an order of 10 times less than that of Ehringfeld's. They found that the MOSFET detector gave a maximum fading error of up to 1.7% within the first 15 minutes.

5.4.4 Dose Linearity

A linear dose response was observed for the 50 kVp, 100 kVp and the 150 kVp x-ray beam spectra as shown in Figure 5.6. The gradient of each plot gives the MOS*kin* sensitivity as follows: 10.6 mV/cGy, 9.4 mV/cGy and 6.7 mV/cGy for the 50 kVp, 100 kVp and 150 kVp x-ray beams respectively.

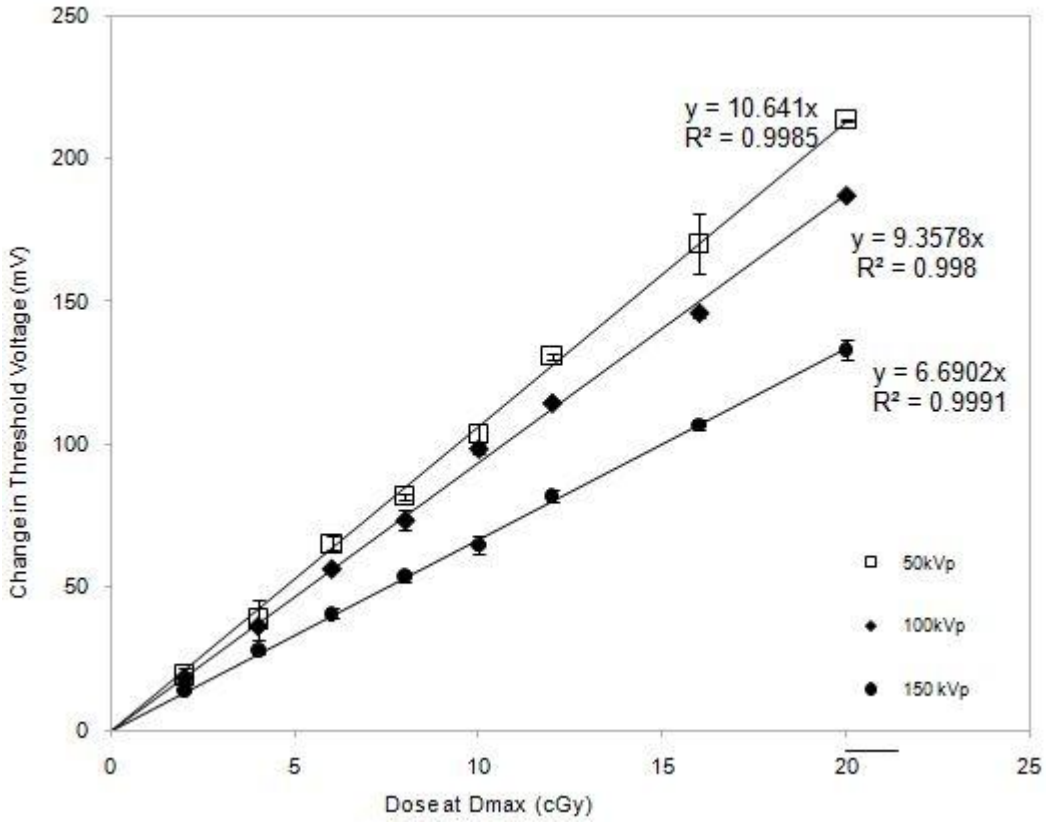

Figure 5.6: *MOSkin* surface dose linearity for 50 kVp, 100 kVp and 150 kVp beams.

5.4.5 Effect of accumulated dose on *MOSkin* sensitivity

MOSFET sensitivity is expected to decrease with integrated dose due to an accumulation of oxide and interface charges. This modifies the effective bias electric field across the sensitive volume [146]. As a result, fewer holes escape electron-hole recombination, resulting in fewer holes trapped at the interface.

For the MO*Skin* irradiated at a tube potential of 150 kVp, at the beginning of its lifetime, MO*Skin* sensitivity was 6.7 mV/cGy. At its mid-life, MO*Skin* sensitivity decreased by about 8% to 6.4 mV/cGy. At its end life, MO*Skin* sensitivity was found to be 6.10 mV/cGy, indicating a decrease from its initial sensitivity by 9%.

As MO*Skin* sensitivity is expected to decrease with accumulated dose, we recommend that re-calibration of the *MOSkin* dosimeter is performed for every 2.5 V increment [146] of measured output voltage. Alternatively, an energy correction function may be implemented, as previously suggested [113].

5.4.6 Energy Dependence

From Figure 5.7 it is seen that as beam quality decreases, on-surface MO*Skin* energy response increases, with a maximum energy response of 3.1 at 50 kVp. This is because most of the electrons that deposit energy at the sensitive volume are generated in silicon oxide and from the surrounding high atomic number silicon by the photoelectric effect, which is the dominant energy transfer mechanism at lower photon energies. The decrease of the response at 50kVp for the face down MO*Skin* is due to photon attenuation in silicon substrate while the increase of the relative response for x-rays above 130kVp is due to dose enhancement from electrons generated in the silicon substrate.

Individual MOSFETs are expected to have different measured DRFs due to the intrinsic energy dependence of the detector (such as recombination of electron-hole pairs) [178] as previously detailed in Chapter 4, Section 4.1. Chapter 3 provides a more extensive discussion of practical solid state physics. As GEANT4 modelling is exclusively a radiation transport modelling tool; it does not model such solid state physics. The modelling uncertainties would incorporate the range of DRFs that might be practically measured. This accounts for the 13% average difference between the predicted and measured DRFs in Table 5.2.

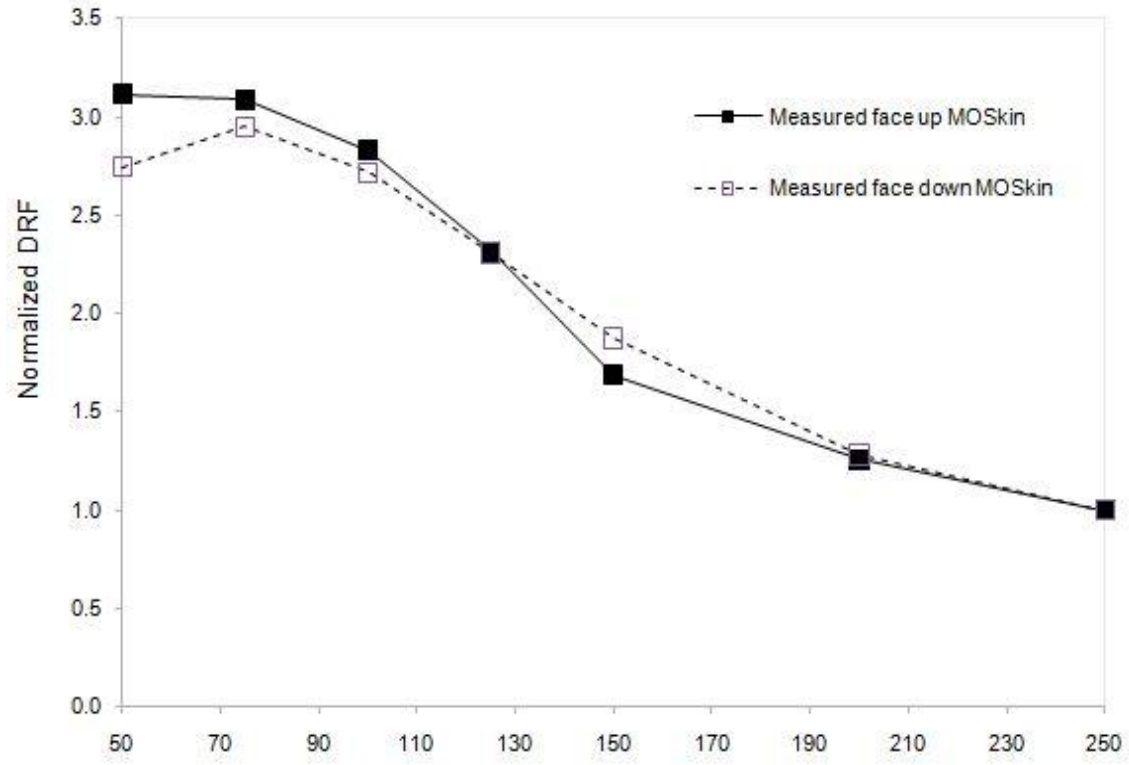

Figure 5.7: Measured *MOSkin* energy response normalized to 1 at 250kVp.

Table 5.2: Comparison of the Monte-Carlo predicted DRF with that of the measured DRFs. DRFs were normalized to 150 kVp.

	DRF					
Tube potential (kVp)	Measured by MOS*kin* 1	Measured by MOS*kin* 2	Monte Carlo Prediction	Min Difference (%)	Max Difference (%)	Mean Difference (%)
50	1.8 ± 0.1	1.8 ± 0.1	2.2 ± 0.3	18%	18%	18%
75	1.8 ± 0.1	1.7 ± 0.2	2.0 ± 0.4	10%	15%	13%
100	1.7 ± 0.1	1.6 ± 0.1	1.8 ± 0.4	6%	11%	8%
125	1.4 ± 0.1	1.3 ± 0.1	1.3 ± 0.3	0%	-8%	-4%
150	1.0 ± 0.1	1.0 ± 0.1	1.0 ± 0.3	NA	NA	NA
200	0.7 ± 0.0	0.7 ± 0.1	0.8 ± 0.2	13%	13%	13%
250	0.6 ± 0.0	0.5 ± 0.1	0.8 ± 0.2	25%	38%	31%

5.4.7 Angular Dependence

Angular response of the MO*Skin* dosimeter was within ± 3 % for the 100 kVp beam (Figure 5.8a). The maximum angular response was 8% for the 150 kVp beam (Figure

5.8b).

It can be seen that the face down orientation has a larger response compared to the face up orientation. This is due to the inherent design of the MO*Skin*; in the face down orientation, the response of the MO*Skin* is driven by the upstream silicon substrate, while in the face-up direction, MO*Skin* response is driven by the upstream polyamide layer with its sensitive volume having lower kerma.

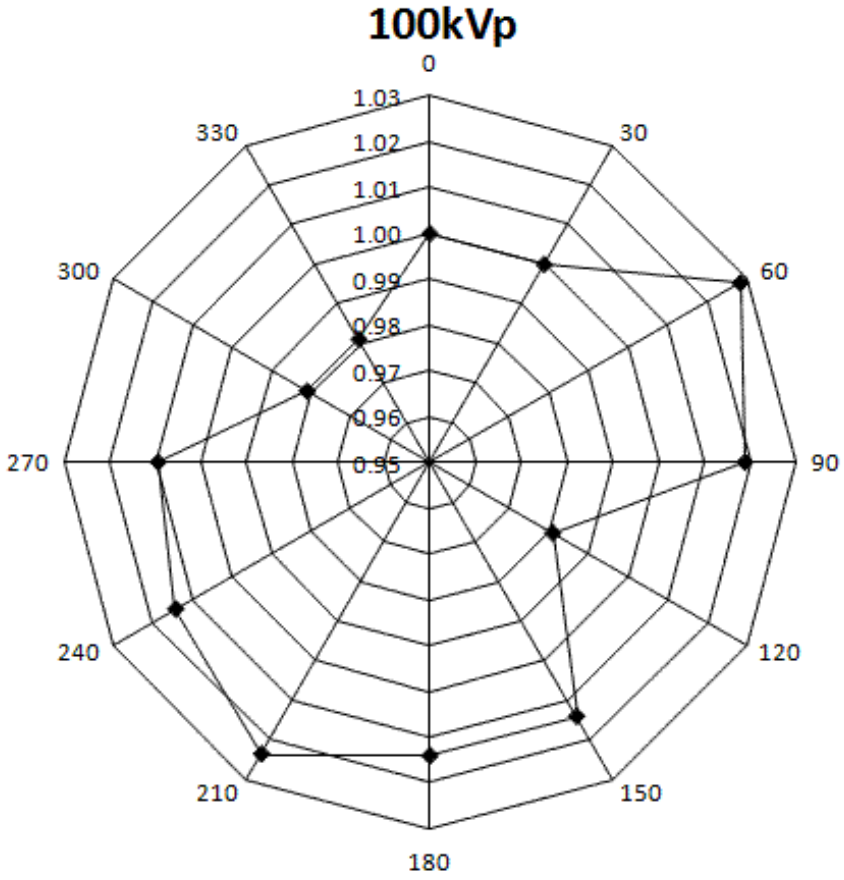

(a)

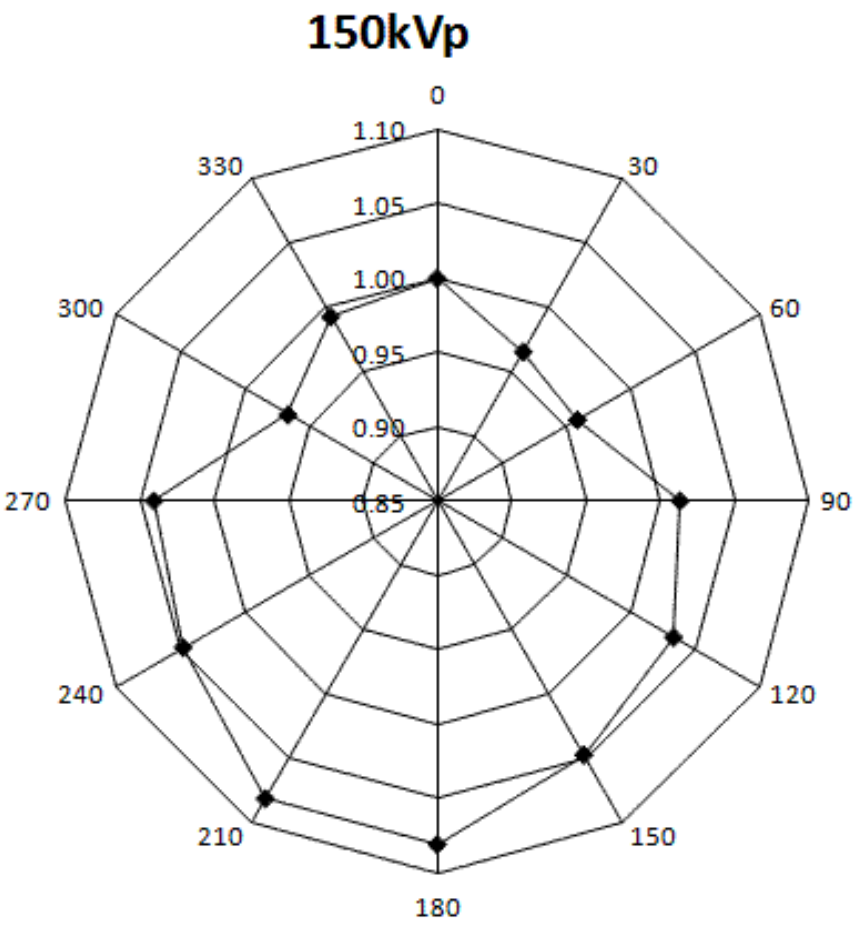

(b)

Figure 5.8: Angular response of the MO*Skin* with a (a) 100 kVp (b)150 kVp incident photon beam normalized to its response at 0^{o} (face up).

5.4.8 Depth dose water equivalence

For the 100 kVp beam, there was up to a 7 % agreement in depth dose response between the MO*Skin* dosimeter and both parallel-plate ionisation chambers at depths up to 60 mm (Figure 5.9a). With the 150 kVp beam, the agreement was 5 % between the *MOSkin* dosimeter and both parallel-plate ionisation chambers at water depths up to 60 mm (Figure 5.9b).

At larger depths, there is likely to be less lower energy photon flux that reaches the MO*Skin* due to the hardening of the photon spectra which may explain the larger

differences in response between the MO*Skin* and the ion chambers. At higher kilovoltage photon energies at larger depths, there is improved agreement between the MO*Skin* and the ion chambers due to the harder energy spectra.

The measured readings between the Attix chamber and the Markus chamber did not differ by more than 1% for all depths measured up to 60 mm.

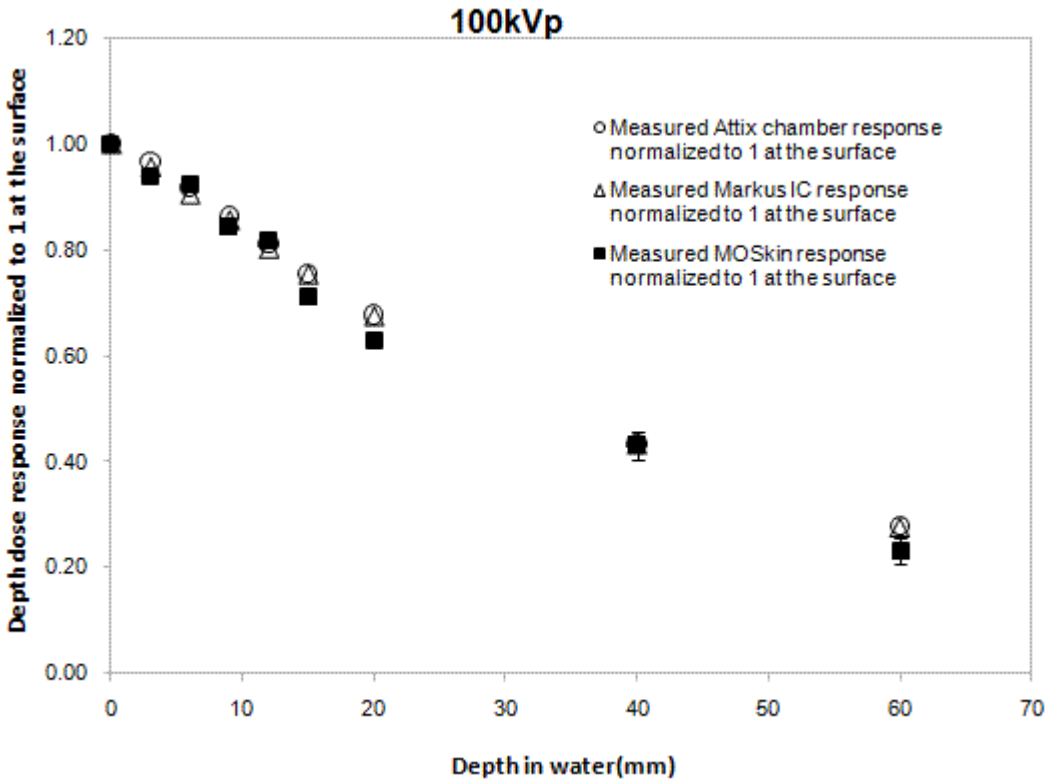

(a)

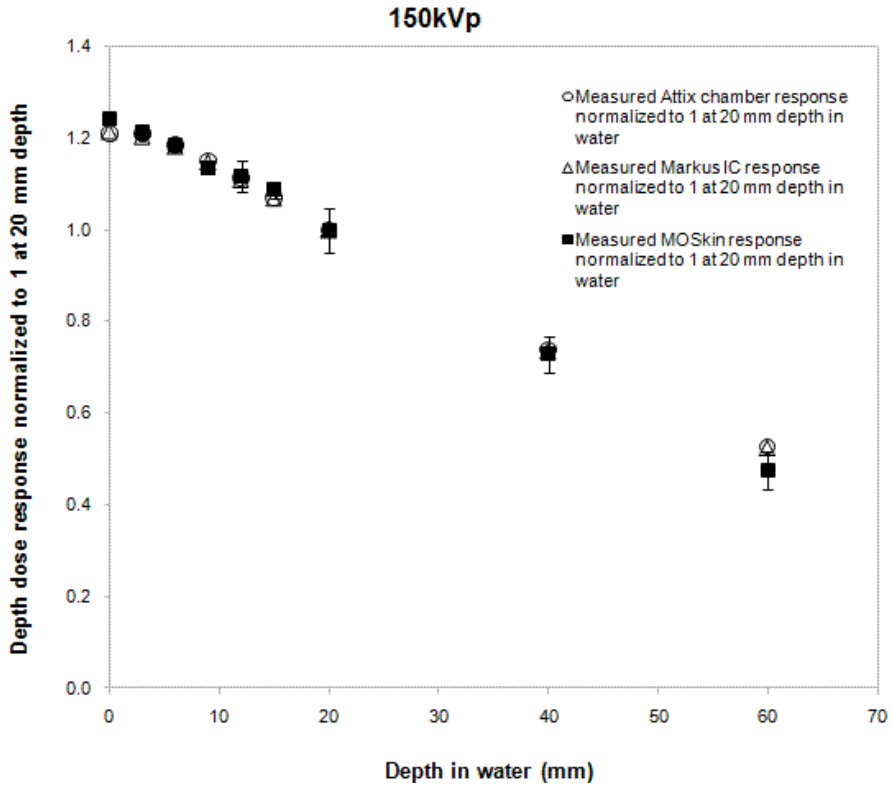

(b)

Figure 5.9: Measured depth dose response in RMI 457 solid water for the (a) 100 kVp beam (b) 150 kVp beam

Table 5.3 shows the comparison of results obtained from the GEANT4 simulated depth dose response factors and that obtained from experimental measurements with the MOS*kin* dosimeter. For the 100 kVp input spectrum (Table 5.3a), the maximum difference between the predicted Monte Carlo depth dose response factors was 15% at a water depth of 40 mm. An average difference of about 8% was obtained between measurements and simulations. For the 150 kVp input x-ray spectrum (Figure 5.3 b), the maximum difference between predictions and measurements was 12% at a water depth of 40 mm. An average difference of about 5% was obtained between the measurements and simulations for all other depths between 0 mm and 60 mm.

Table 5.3: Measured and predicted PDD (a) 100 kVp spectrum (b) 150 kVp spectrum

(a)

Depth in water (mm)	MOS*kin* measurement (%)	Monte Carlo Prediction (%)	Difference[a] (%)
0	100	100	0
3	94	98	-4
6	92	87	5
9	85	78	7
12	82	71	11
15	71	63	8
20	63	52	11
40	43	28	15
60	23	17	6

[a]% Difference = Measured PDD(%) - Simulated PDD(%)

(b)

Depth in water (mm)	MOS*kin* measurement (%)	Monte Carlo Prediction (%)	Difference[a] (%)
0	100	100	0
3	98	108	-10
6	95	97	-2
9	91	97	-6
12	90	92	-2
15	88	84	4
20	80	75	5
40	59	47	12
60	38	34	4

[a]% Difference = Measured PDD(%) - Simulated PDD(%)

5.5 Conclusions

This chapter reports on the characterisation of MO*Skin* behaviour at clinical kilovoltage energies with x-ray spectra generated from a superficial/orthovoltage therapy unit. For low doses < 20 cGy, we recommend individual MO*Skin* calibration. The MO*Skin* should be read out within the first 2 minutes after irradiation to minimize the effects of short-term signal fading. As sensitivity tends to decrease with accumulated dose, the MO*Skin* should be checked periodically (every 2.5 V increase in threshold voltage) for changes in sensitivity, and should not be used beyond its integrated dose lifetime of 10 Gy in kVp x-ray beams to ensure higher accuracy in dosimetric measurements.

As the MO*Skin* exhibits significant energy response particularly at low photon energies, it should be calibrated for the particular beam quality prior to use. Angular dependence of the MO*Skin* was found to be within ± 3% and 8% for the 100 kVp and 150 kVp photon beams respectively. Lastly, the results of our experimental measurements show that MO*Skin* dosimeter may be reliably applied for the assessment of point doses at depths up to 60 mm for a 150 kVp photon beam in RMI 457 solid water.

The results of this characterisation study show that the MO*Skin* demonstrates potential for application in a clinical x-ray CT beam due to its real time readout capability, ease of use and minimal angular dependence and reasonable sensitivity.

6 Multi-Slice Computed Tomography Dose Profile Assessment

6.1 Introduction

Multi-Slice Computed Tomography (MSCT) was first introduced by Elscint in 1992 with the creation of a dual-slice helical scanner, the world's first-ever multi-slice scanner [2]. Thereafter in 1998, several equipment manufacturers released the next generation of multi-slice CT scanners. It was also around this time that MOSFETs were recognised as a valuable dosimetric tool in megavoltage radiation therapy verification; however, MOSFET application in diagnostic radiology remained relatively unexplored until 1998 when they were first used in diagnostic radiology for patient skin dose measurement [148]. In 2003, the application of MOSFET technology was extended to CT dosimetry [51] in one of the first papers to explore the use of MOSFETs in CT.

As illustrated in Figure 6.1(b) compared to Figure 6.1(a), a quad-slice CT scanner allows the acquisition of 4 times the amount of data over the same scan time interval, in other words, increasing the speed of data collection by a factor of 4, compared to conventional single-slice helical scanners (Figure 6.1a). In addition, modern helical MSCT scanners have the capability of gantry rotation speeds of 2 revolutions per second, which is twice the speed of conventional single-section helical scanners. These 2 improvements combined, yield an 8-fold increase in scanning speed over conventional single-slice helical scanners. The only drawback, however, is that radiation dose is 30 to 50% greater with 4-slice MSCT compared to single slice helical CT scanners due to z-overscanning, positioning of the x-ray tube closer to the patient and increased scatter caused by the wider x-ray beam [195].

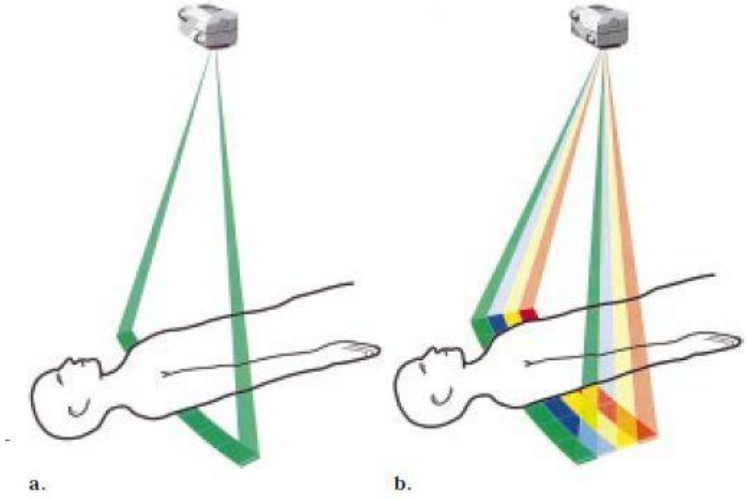

Figure 6.1: Oblique view of a CT gantry with an x-ray tube, an x-ray fan and detectors for (a) single slice CT scan (b) 4-slice CT scan (Reproduced from [2])

To put the imaging situation in perspective, the benefits of MSCT are well-recognised by clinicians. Firstly, MSCT offers higher spatial resolution along the z-axis, since scans can be performed with thinner sections. Secondly, MSCT offers improved temporal resolution and a reduction in motion artifacts since scanning can be performed at higher speeds. Thirdly, with its high speed scanning capabilities which permit fast multi-phasic scanning, MSCT technology allows the visualization of intravenously administered contrast material (such as iodine) thereby enhancing the contrast resolution in image acquisition. It is without a doubt therefore that, MSCT significantly increases the diagnostic accuracy of an imaging scan with its superior spatial, temporal and contrast resolution of output images. [2]

CT technology continues to evolve at this present day. It has been recognised by several medical physics practitioners that CT dosimetry is largely lagging behind current rapid advancements in CT technology. In particular, Geleijns et al [196] notes that the recent introduction of a 160 mm wide, 320 detector row, cone beam CT scanner (Toshiba Aquilion ONE) challenges existing CT dose metrics such as the most commonly known Computed Tomography Dose Index (CTDI) metric for evaluating scanner dose output. The standard cylindrical CT pencil ionisation chamber, traditionally used for the measurement of the $CTDI_{100}$, has an active length of merely 100 mm. Moreover, standard cylindrical head and body PMMA CT phantoms for evaluating beam output are

only 150 mm long. With its 160 mm beam width which exceeds the active length of the conventional pencil ion chamber and the length of the CT PMMA phantom, modern CT scanners such as the Toshiba Aquilion ONE certainly require a new kind of dosimetry.

With its real-time readout capability and high spatial and temporal resolution (0.2 mm and 0.1 s respectively), the Dose Magnifying Glass (DMG, Centre for Medical Radiation Physics, University of Wollongong, Australia) has previously been shown to be a novel quality assurance (QA) tool for intensity modulated radiotherapy (IMRT) [197] and stereotactic radiotherapy QA [198].

The objective of the following chapter is to jointly apply the MOS*kin* dosimeter and the DMG in the acquisition of diagnostic x-ray CT beam/dose profiles of a modern helical 16-slice MSCT scanner towards near-real-time CT quality assurance. A new type of film, the Gafchromic XR-QA2 film, was also evaluated in this study.

6.2 Materials

6.2.1 CT scanner

The CT system used was a 16-slice General Electric (GE) Discovery 670 NM/CT SPECT/CT scanner which allows general purpose nuclear imaging. Table 6.1 shows the scan parameters used for this work based upon commonly used clinical imaging parameters for diagnostic CT scans. For this work, we were primarily interested in studying the effect of varying axial beam collimations (1.25 mm, 5 mm, and 20 mm), helical pitch and the over-ranging phenomenon associated with the helical scan mode as compared to the axial scan mode, on the overall acquired dose profile. Beam profile data acquired by the DMG and point dose measurements with the MOS*kin* were compared with Gafchromic XR-QA2 film.

We varied scan mode in three ways; single rotation mode, axial scan mode and helical scan mode. In a single rotation scan, the tube is rotated around the gantry just once. In an axial scan, the couch is incrementally advanced each time the photon beam is emitted. In a helical scan, depending on the user-specified speed of rotation/pitch, the couch and tube move at the same time. The advantage of helical scanning is that it

allows for very fast data acquisitions at the expense of z-overscanning. For each setting, the operator console displays the corresponding $CTDI_{vol}$, DLP and dose efficiency values. These are shown in Table 6.1. Scanner console- displayed values are also indicated in this table. As noted by [199], typical CTDI values for diagnostic CT procedures are typically 60 mGy for adult head examinations. This is consistent with the clinical scanning protocols we selected in which 16 cm diameter PMMA cylindrical phantom (representing an adult head) was specified on the machine console for the purpose of machine calculated $CTDI_{vol}$.

Table 6.1: Scan parameters of this study with a typical clinical tube potential of 120 kVp tube current of 300 mAs and a total scan range of 120 mm.

Protocol #	Scan mode	Detector configuration	Nominal beam collimation (mm)	Scan length (mm)	pitch	$CTDI_{vol}$ (mGy)	DLP (mGy.cm)	Dose efficiency (%)
1	Single rotation	8 x 1.25 mm	10	8.75	-	69.89	69.89	78.41
2		8 x 2.5 mm	20	17.5	-	55.35	110.71	96.99
3	Axial[a]	2 x 0.625mm	1.25	29.375	-	142.56	427.69	41.87
4		4 x 1.25 mm	5	30	-	84.79	296.77	63.44
5		8 x 2.5 mm	20	30	-	55.35	221.41	96.99
6	Helical	8 x 2.5 mm	20	30	0.625	88.56	480.64	96.99
7					0.875	63.26	349.93	96.99
8					1.35	41.00	236.13	96.99

[a]Dose efficiency (z-axis geometric efficiency) increases with increasing beam collimation in axial scan mode. This is due to more of the x-ray beam width being seen by the active detectors for a larger nominal beam collimation.

6.2.2 Phantoms

Solid water phantom (RMI 457, Gammex) slabs of dimensions 30 cm x 30 cm x 1 cm were placed on the patient couch. A total thickness of 7 cm of solid water phantom slabs were placed below and above the DMG (the DMG itself is surrounded by a 1 cm thickness of solid water); creating a total phantom thickness of 16 cm approximating the thickness of a typical adult head or paediatric abdomen. Figure 6.6a shows the photograph of the experimental setup.

6.2.3 Dose Magnifying Glass (DMG) System

The silicon strip radiation detector DMG is an array of 128 phosphor implanted n^+ strips

on a p-type Si wafer, with a wafer thickness of 375 μm and a length of 25.4 mm; the DMG was so-named because of its ability to image radiation profiles at submillimetre spatial and subsecond temporal resolutions of 0.2 mm and 0.1 s respectively. The sensitive area of each n^+ strip (diode) is 20 x 2000 μm^2, with a detector-to-detector distance of 0.2 mm. Further details on its construction and associated electronics may be found in [197]. Figure 6.2 and 6.3 shows the DMG and the data acquisition and associated electronic control circuitry respectively. Both of these were placed within the CT scanner room during the CT scans.

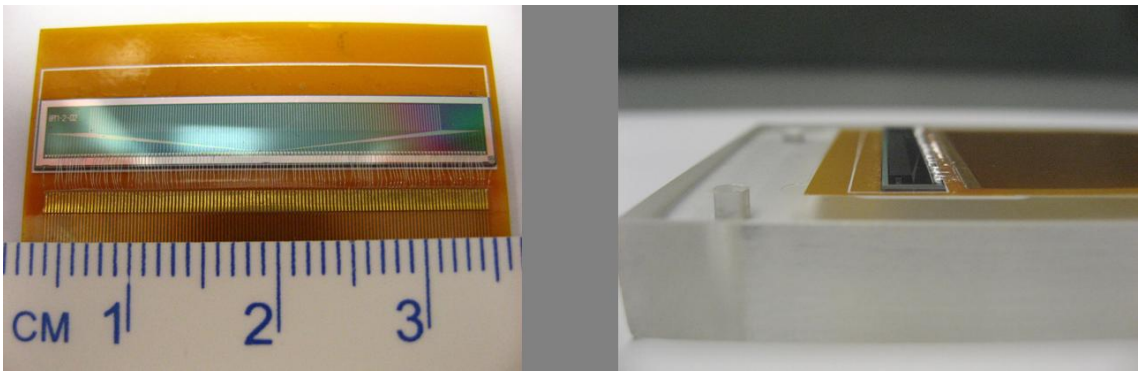

(a)

(b)

Figure 6.2: a) The CMRP Dose Magnifying Glass (DMG) mounted on a ceramic substrate. (Photograph reproduced from [197] (b) The isocentre of the sensitive detector is denoted by the intersection of the lines which corresponds approximately to channel 64 of the 128-channel DMG.

Figure 6.3: Control circuitry of the DMG system.

6.2.4 Gafchromic XR-QA2 film

Radiochromic film Gafchromic XR-QA2 (International Specialty Products, Wayne NJ, USA) lot number A10071002A, was used in this study. This model of self-developing radiochromic film has a high sensitivity to low doses in the dose range of 1 mGy to 200 mGy within an energy range of 20 kVp to 200 kVp. It has a high spatial resolution of 5000 dpi. [200].

The structure of this film is depicted in Figure 6.4. The active layer is 25 µm thick and is sandwiched between 97 µm thick polyester substrates (top and bottom face).

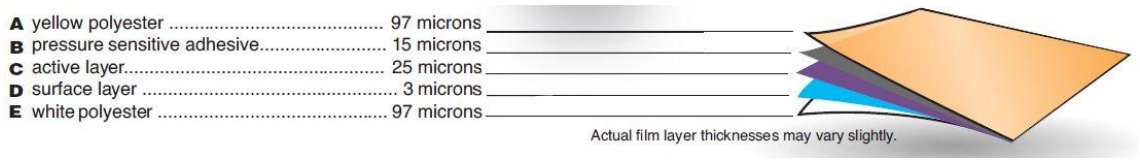

Figure 6.4: Structure of Gafchromic film, type XR-QA2 (Reproduced from [200])

There is currently no general consensus amongst published literature pertaining to the accuracy of this type of film for low dose measurements under 10 mGy. The issue with XR-QA2 film is that its sensitive layer is composed of high atomic number halides to increase photoelectric interaction at lower energy x-rays. As noted by [201], application of this type of film should be done with caution due to its tendency to over -respond at low x-ray energies. Brady *et al*. [202] verified the performance of this type of film for the measurement of organ doses with conventional thermoluminescent dosimetry (TLD) measurements and showed that after correction for angular dependence, this film

performed satisfactorily at low energies.

6.3 Methods

6.3.1 CT Beam Characterisation

Current commercially available CT systems have operating potentials of 120 to 140 kVp, with HVL values ranging from 4.5 to 10 mm of aluminum [203]. To determine the CT scanner HVL used in this study, the localization technique was adopted [203]. As previously found, the localization method was found to be accurate and reproducible, on the basis of comparison with the invasive technique (taken as the gold-standard for HVL measurements) [203]. The primary advantage of this localization technique for HVL determination is that the localization technique is a relatively straightforward procedure. It does not require service software intervention to stop the x-ray source rotation.

CT exposure was measured with an ionisation chamber, Compact chamber CC04 (IBA, Scanditronix Wellhofer) calibrated to a reference dosimeter traceable to the national primary standard (PTB). The ionisation chamber was connected to an electrometer model MAX-4001 (Standard Imaging, CMS Alphtech Sydney 2005). A copper HVL Attenuator set (RMI Model 116, Gammex RMI) was used to determine CT HVL.

In the localization technique for determining scanner HVL, the ionisation chamber was positioned in air at the scanner isocentre (Figure 6.7). Each localization scan was repeated 3 times in scout mode: 120 kVp, 300 mA and a scan length of 60 cm.

Figure 6.5: Photograph of the setup for the measurement of CT beam HVL with an ion chamber

6.3.2 Experimental Setup of the DMG data acquisition system

For data acquisitions with the DMG, Figures 6.6 and 6.7 show the DMG setup beam positioning with the aid of the lasers (detector at isocentre) and the overall experimental setup respectively.

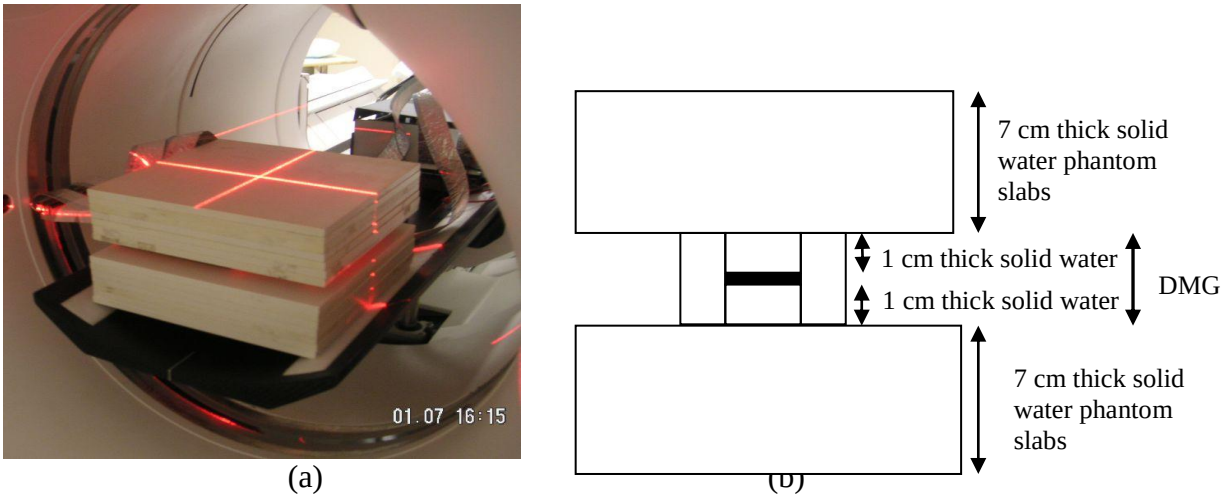

Figure 6.6: Experimental setup of the CMRP DMG system. a: Photograph showing the DMG aligned to the isocentre of the CT scanner using the laser positioning reference markers. b: Cross sectional profile (Not-to-scale). The sensitive detector array of the DMG is shaded in black for clarity.

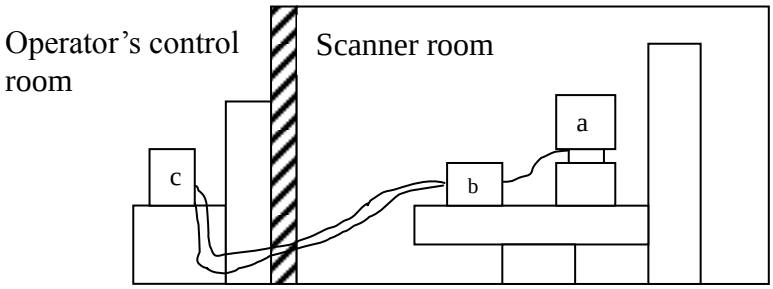

Figure 6.7: Schematic of the experimental setup a) solid water phantom and DMG positioned in the scanner room b) control circuitry with associated electronics positioned in the scanner room c) CPU for data acquisition at the operator's console for instantaneous data acquisition

6.3.3 Calibration of the dosimeters

6.3.3.1 The DMG System

Sensitivity mapping of the DMG system is essential prior to its clinical application to ensure measurement accuracy. To achieve a uniform detector response, a sensitivity map of all 128 channels of the DMG is necessary, since each channel of the DMG is coupled to individual charge amplifiers whose response may be different from each other.

For calibration of the DMG system, a CT detector configuration of 16 x 1.25 mm (nominal beam width of 20 mm) over a total scanning distance of 120 mm in axial mode was used. The CT tube potential was set at 120 kVp and tube current at 300 mAs.

A novel shift-and-irradiate method was developed with the objective of obtaining the sensitivity factor for each individual strip detector relative to the data in channel 64 (channel 64 was arbitrarily chosen since the position of channel 64 approximately corresponds to the beam isocentre).

A total of 12 CT axial scan acquisitions were obtained across the 120 mm scan distance; the scanner couch was shifted by 2 mm per irradiation. Each acquired 2 mm step dose profile was then smoothed and interpolated to a smaller step size of 0.2 mm, corresponding to the detector pitch. This represents the predicted dose profile, D_{fit}.

The detector sensitivity coefficient c for each strip i was then defined as a ratio of the measured dose value D_i to the predicted dose value D_{fit_i}.

$$\text{Sensitivity coefficient, } c_i = \frac{D_i}{D_{fit\_i}}$$

where index i represents the detector channel number.

The detector sensitivity factor was subsequently calculated as the ratio of the sensitivity coefficient c_i of the individual strip to the sensitivity coefficient of the centre strip c_o,

$$\text{Sensitivity factor, } s_i = \frac{c_i}{c_o}$$

Figure 6.8 illustrates the sensitivity factors obtained across the 128 channels of the DMG.

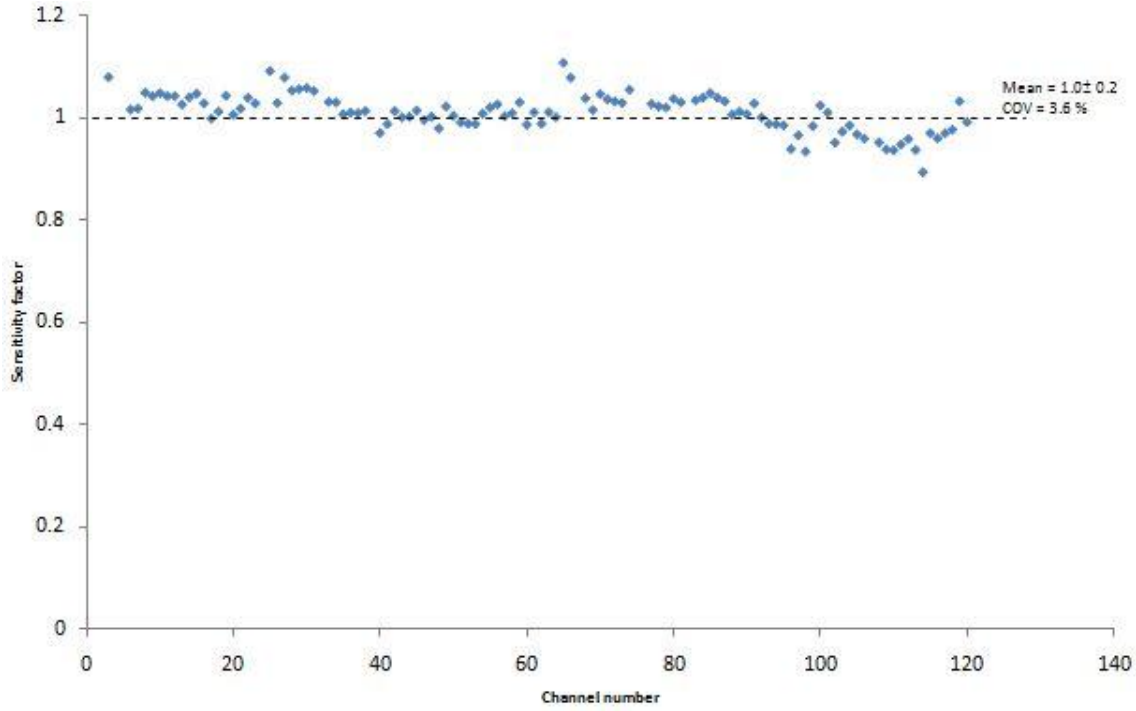

Figure 6.8: Sensitivity profile of the 25.4 mm length Dose Magnifying Glass (DMG) in a 120 kVp x-ray CT beam. Outlying points greater than 20% of the mean were not considered, indicating dead channels.

All subsequent measured values with the DMG were uniformity corrected based upon the above derived sensitivity factors.

6.3.3.2 Gafchromic XR-QA2 film

6.3.3.2.1 Film exposure

15 pieces of XR-QA2 film with dimensions 3 cm x 3 cm were cut from a 25.0 cm x 30.0 cm sheet of Gafchromic XR-QA2 film. As an added precaution, we ensured that the light-sensitive film pieces were only removed from their envelope during irradiation and readout scanning only.

The film pieces were irradiated at D_{max} taken to be at the surface of the solid water phantom at 15 dose levels from a dose range of 0 mGy to 200 mGy, at 10 mGy increments up to 100 mGy and at 20 mGy increments up to 200 mGy. Figure 6.9 shows

the various degrees of film darkening post-exposure at tube potential 150 kVp. Each irradiation was repeated twice with film pieces from the same batch to eliminate the possibility of random error.

To assess the energy dependence of the film, this same procedure was repeated at 100 kVp and 75 kVp.

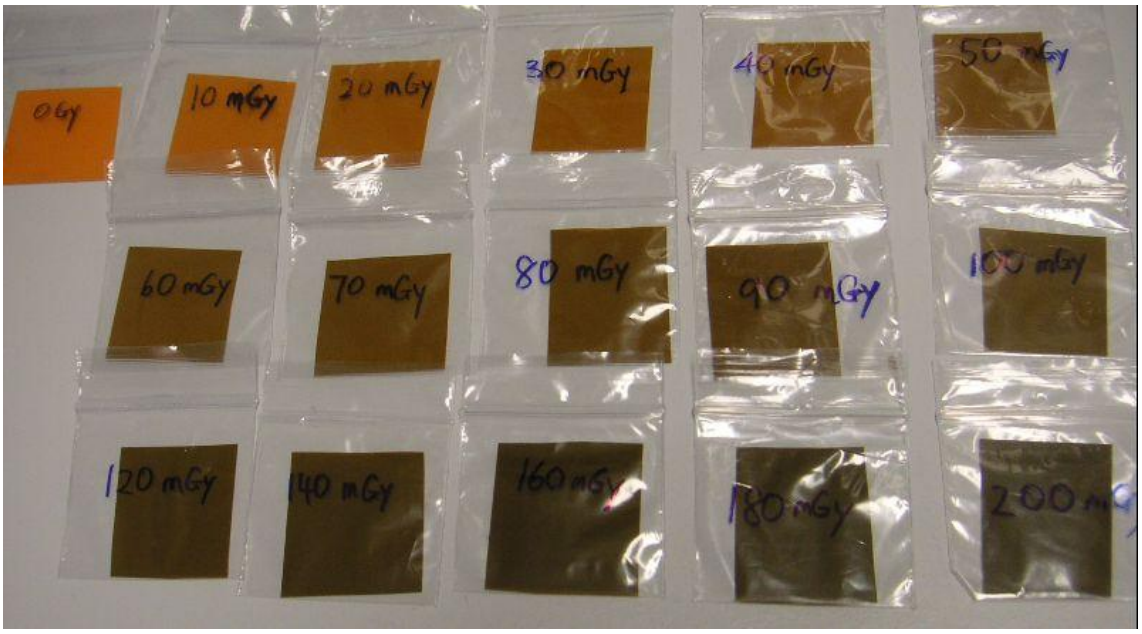

Figure 6.9: Each 3 cm x 3 cm Gafchromic XR-QA2 film piece was irradiated to a known dose using the Gulmay superficial orthovoltage unit.

6.3.3.2.2 Scan procedure and image processing

Exposed films were digitized with a scanner (Microtek ScanMaker i800, 9600 x 4800 DPI CCD, 48-bit color) at least 24 hours after x-ray irradiation. Each film sample was scanned before and after the exposure at the same position on the scanner bed to ensure readout measurement consistency. In addition, the scanner was allowed to warm up at least 10 minutes prior to its first scan.

The following scan protocol was applied: Reflective scan mode, RGB mode 48-bit color, resolution 300 dpi, 100% image scaling, with no color correction nor filters

applied. Each film piece was scanned three times to minimize scanner response variations and the scans were saved in the .tiff image file format.

The images obtained from film digitization were analyzed with ImageJ software (National Institutes of Health, MD, http://rsb.info.nih.gov/ij/) and Photoshop. For each film piece, a central region of interest (ROI) of 1 cm x 1 cm dimenstions was specified and analysed. The red channel was used for postprocessing since the red channel gives the largest response for this film with an absorption peak at 636 nm [199].

Figure 6.10 shows the calibration curve obtained at 150 kVp which relates the mean optical density of the exposed film with absorbed water dose. Figure 6.11 shows the energy dependence of the Gafchromic XR-QA2 film at 75 kVp, 100 kVp and 150 kVp respectively. Dose response of this type of film is largest in the dose range from 30 mGy to 120 mGy beyond which it largely saturates. At a dose level of 50 mGy, the difference in energy response was found to be up to 16% for the 100 kVp and the 150 kVp beams. This shows that calibration of this type of film is necessary for the particular x-ray energy spectra used for subsequent measurements.

From Figure 6.11, it can be seen that the observed film energy dependence (particularly at 100 kVp and 150 kVp) generally increases with decreasing dose levels. At a dose level of 20 mGy and 10 mGy, the difference in energy response between the 100 kVp and 150 kVp beam was 17% and 33% respectively.

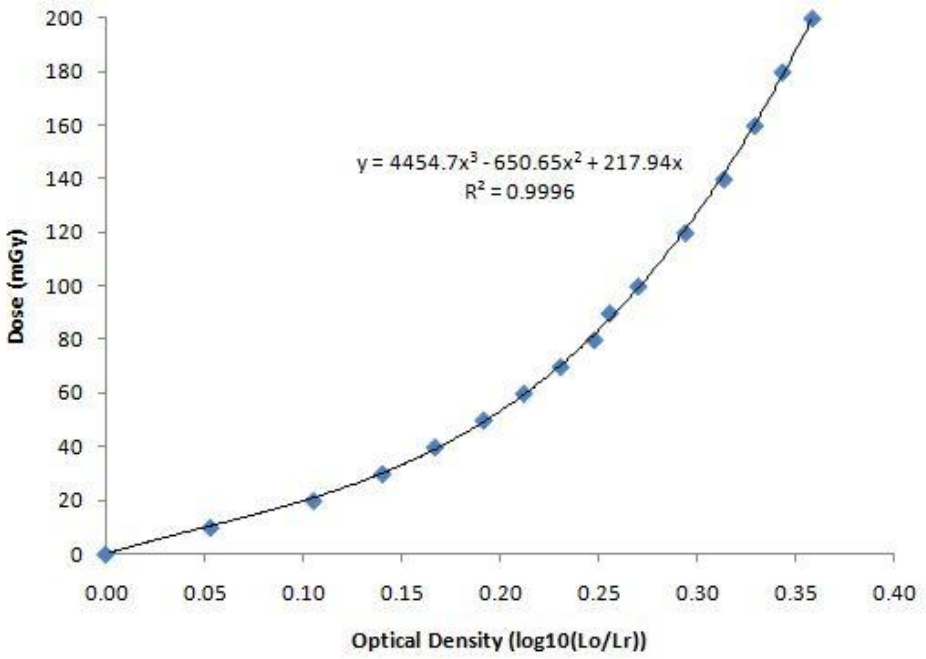

Figure 6.10: Calibration plot of Gafchromic XR-QA2 film at 150 kVp

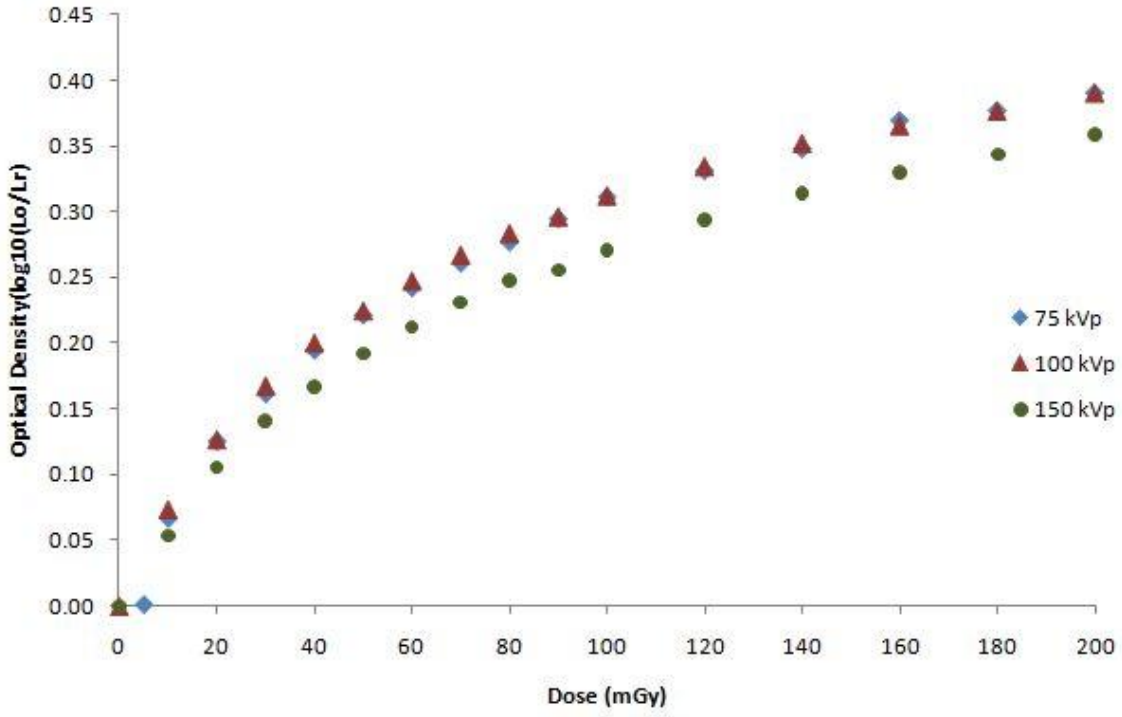

Figure 6.11: Energy response of Gafchromic XR-QA2 film at 75 kVp, 100 kVp and 150 kVp.

Figure 6.12 shows the depth dose characterisation plot of the film compared with that of the Markus ionisation chamber (gold-standard dosimeter) and the MOS*kin* with a surface delivered dose of 20 mGy. It can be seen from this figure that at a depth of 80 mm (the depth of interest as described in our experimental setup), the film has a depth dose over response of up to 30% compared to the ion chamber and the MOS*kin* dosimeter (which had a response within 2% of each other) at doses under 10 mGy . This shows that the MOS*kin* dosimeter may be reliably used at the lower depths, with a trade-off uncertainty of ±3 mGy at 20 mm depth.

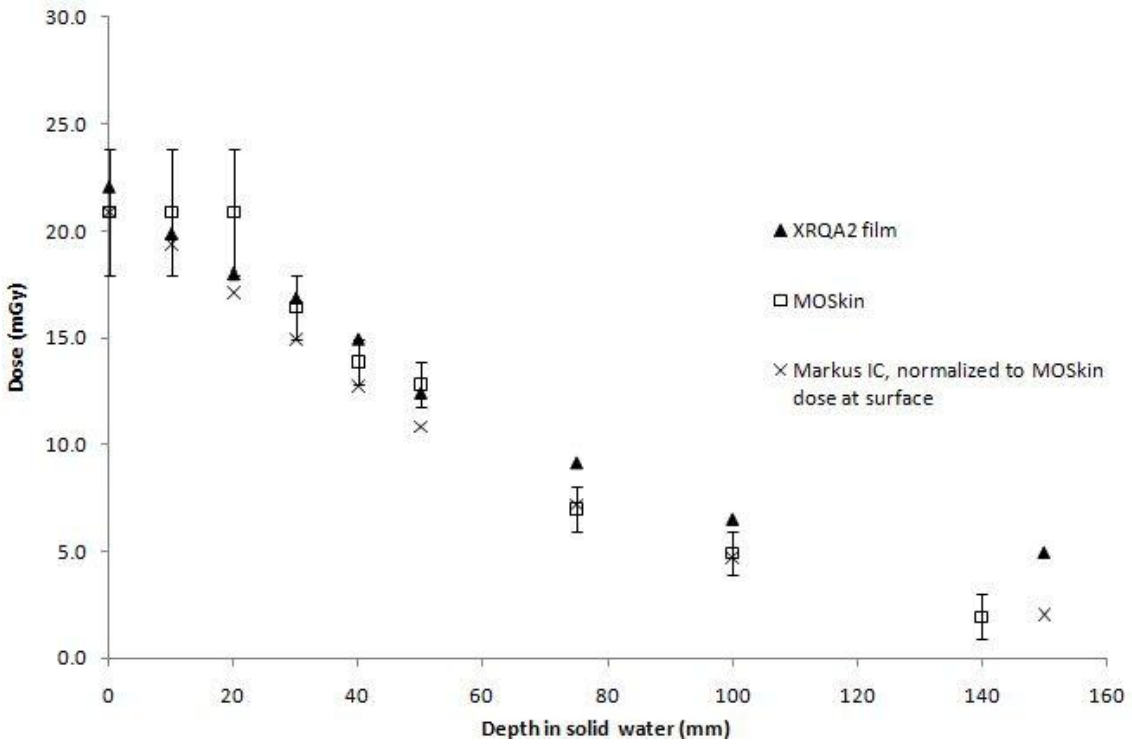

Figure 6.12: Low dose depth dose response of XR-QA2 film compared to the MOSkin dosimeter and Markus IC. 20 mGy was delivered on the phantom surface.

6.3.3.3 MOS*kin dosimeter*

From the direct measurement of CT HVL by the localization technique as described in section 6.3.1, the CT beam applied in this work was found to have a 0.8 mm Cu HVL at 120 kVp. To match as closely as possible the primary radiation beam quality of the CT

scanner, the MOS*kin*s were calibrated in a 150 kVp beam (with a HVL of 0.63 mm Cu) on the Gulmay D3300 unit (Table 4.2, Figure 4.3 respectively). For each individual MOS*kin*, a calibration factor (mV/cGy) was established and recorded for each irradiated beam quality.

6.3.4 CT Beam Profile Measurements

6.3.4.1 The DMG System

For each set of imaging protocols performed with the 25.4 mm length DMG, we moved the scanner couch 20 mm in the superior (caudal-cranial) direction for a total of 3 times, and repeated this in the inferior (supine) direction. As such, the overall beam profile was acquired over a total scan length of 120 mm. Using Microsoft Excel® software, the beam profile was reconstructed from the obtained scan acquisition series. Reconstruction of the beam profile was done in two steps, firstly, by translating data from the 128 channels across to the 25.4 mm length of the DMG, and secondly, by superimposing the scan profiles to obtain the final beam profile.

6.3.4.2 Radiochromic film

120 mm length strips of XR-QA2 radiochromic film were cut to shape and positioned at the scanner isocentre with the same experimental setup illustrated previously in Figure 6.6. Figure 6.13 shows a photograph of the exposed film irradiated under various scanning conditions in a CT beam, identified by the written numbers on the film's upper right hand corner to distinguish between the different CT scan protocols used.

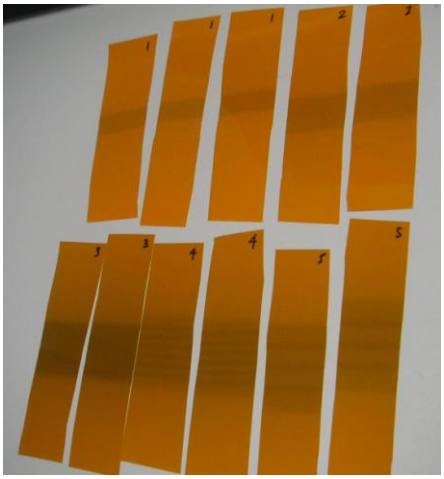

Figure 6.13: Gafchromic XR-QA2 film after CT irradiation

6.3.4.3 MOSkin dosimeter

For single tube rotation mode, point dose measurements were taken at intervals of 10 mm for a total of 5 points per scan. A single MOS*kin* measurement was taken at each position; each MOS*kin* measurement represents a snapshot of the dose value at a certain point in time.

For both axial and helical scans with the moving couch, a single point dose measurement was obtained with the sensitive detector volume positioned at CT isocentre throughout the scan. The single measured point dose represents the MSAD which includes the dose from scattered radiation from adjacent slices (as illustrated in Chapter 2, Figure 2.16).

6.4 Results and Discussion

6.4.1 Reproducibility of CT scans with the DMG

Figure 6.14 shows the readout reproducibility of the DMG for CT irradiations repeated 3 times. The COV was 7%; this uncertainty is attributed to reproducibility of the CT beam (up to 2%) and the reproducibility of the DMG readouts calibrated by the MO*Skin* dosimeter (up to 5%).

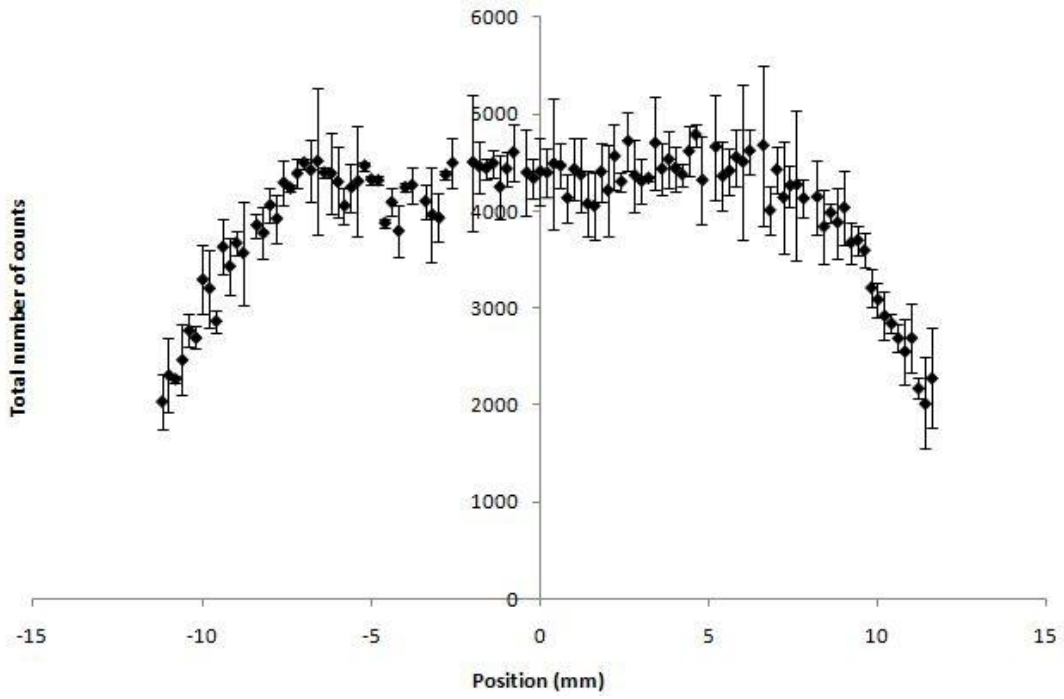

Figure 6.14: Reproducibility of CT beam measurements with the DMG. Measurements with the DMG were repeated three times in axial mode, nominal beam collimation=1.25 mm. The average COV across all channels was 7%. Maximum COV= 23%, Minimum COV=1%.

6.4.2 Beam Profile Assessment

As verified experimentally in Figure 6.12, MOS*kin* response at low doses under 10 mGy at 80 mm depth in solid water was shown to correspond closely to the values measured by the parallel plate ionisation chamber with 3% uncertainty. It follows that the MO*Skin* is a suitable dosimeter for the assessment of low doses below 20 mGy at a depth of 80 mm in the phantom, and was therefore adopted as the reference dosimeter in this work. The data acquired by the DMG (i.e. corrected total number of counts per channel) was subsequently normalised to the maximum MO*Skin* measured point dose at the scanner isocentre.

6.4.2.1 Single Tube Rotation

Figures 6.15 and 6.16 show the CT beam profiles for different nominal beam widths, in single tube rotation mode, with nominal beam widths set at 10 mm and 20 mm respectively. It can be seen from the figures that as the nominal beam collimation increases, dose profile widens. This is represented by the FWHM value which increases approximately two-fold as the nominal beam collimation increases two-fold.

The point dose measurement obtained with the MO*Skin* dosimeter and XR-QA2 film at CT beam isocentre increases with an increase in beam collimation. This is due to the greater contribution of scatter radiation to the central axis dose profile within the solid water phantom in the case of a larger beam collimation. At low doses of 10 mGy at depth in the phantom, MO*Skin* reproducibility was 3%.

There was a close agreement (less than 3% difference) between measured isocentre film dose and that of the DMG. However, an overall 15% and 32% difference in FWHM between film dose measurements and DMG measurements is noted for the 10 mm and 20 mm nominal beam collimation respectively (Figure 6.15 and 6.16). This over-

response is particularly obvious at the dose tails of the plotted beam profile where doses were below 10 mGy.

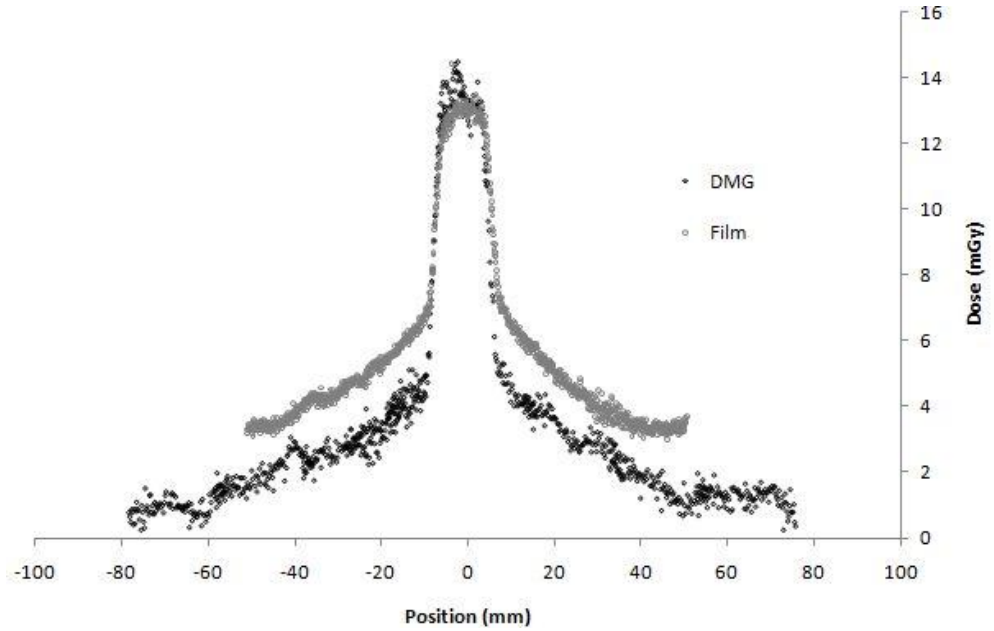

Figure 6.15: Single tube rotation with 10 mm nominal beam collimation. (Scan protocol 1, Table 6.1) FWHM (DMG) = 14.5 mm, FWHM (film) = 17.1 mm, % difference (Film-DMG) = 15%. MO*Skin* point dose measurement at CT beam isocentre = 13.0 mGy

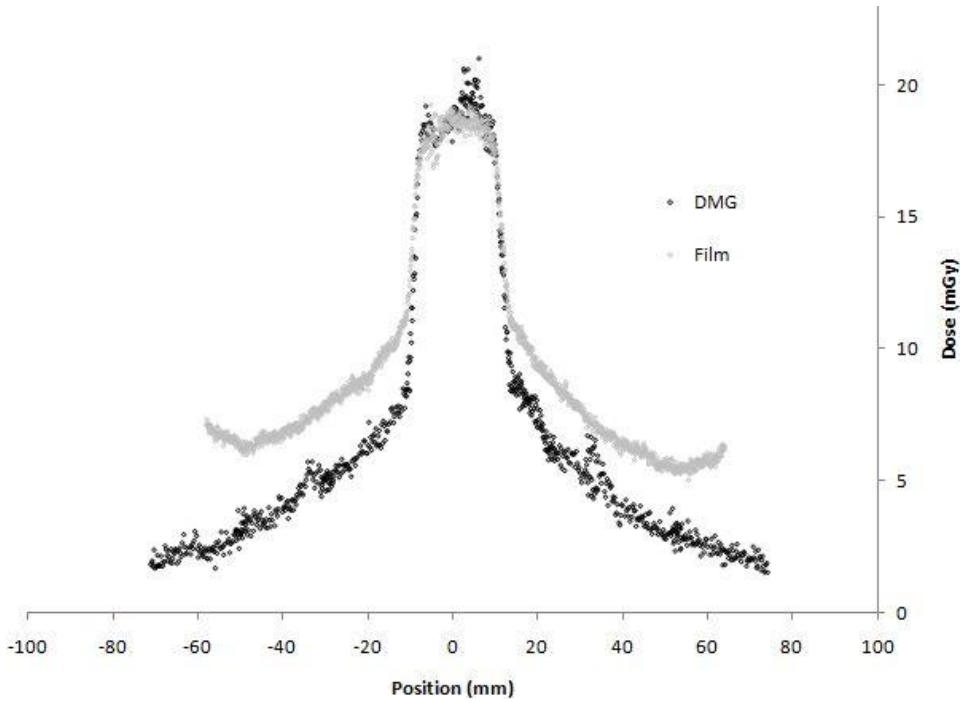

Figure 6.16: Single tube rotation with 20 mm nominal beam collimation (Scan protocol 2, Table 6.1) FWHM (DMG) = 22.6 mm, FWHM (film)= 33.3 mm, % difference (film-DMG)= 32%. MO*Skin* point dose measurement at CT beam isocentre=18.8 mGy

6.4.2.2 Axial scan mode

As with the single tube rotation scan mode, MOS*kin* point dose measurements with the axial mode obtained at scanner isocentre agreed well with film values to within 3% at scanner isocentre.

As expected, increasing the nominal beam collimation resulted in a larger measured beam width for all 3 axial scan protocols.

A single MOS*kin* point dose measurement was taken at the scanner isocentre at the end of each axial scan series. The point dose value measured by the MOS*kin* dosimeter at scanner isocentre agreed well with the absolute film measurement at scanner isocentre to within 3%.

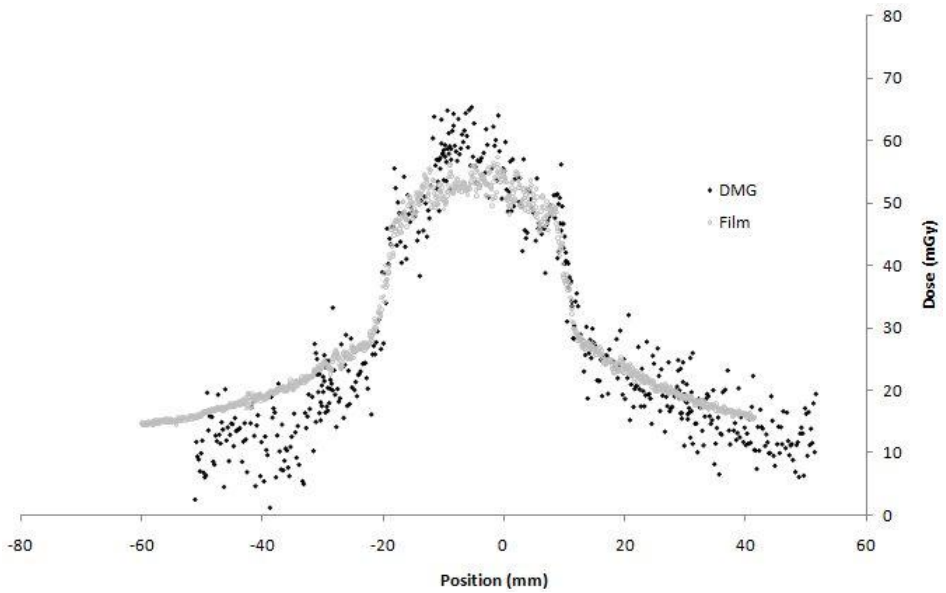

Figure 6.17: Axial scan mode with 1.25 mm nominal beam collimation (Scan protocol 3, Table 6.1). FWHM (DMG)=31.2 mm, FWHM (film)= 37.3 mm, % difference (film-DMG)= 16%. MOS*kin* point dose measurement at CT beam isocentre= 55.1 mGy

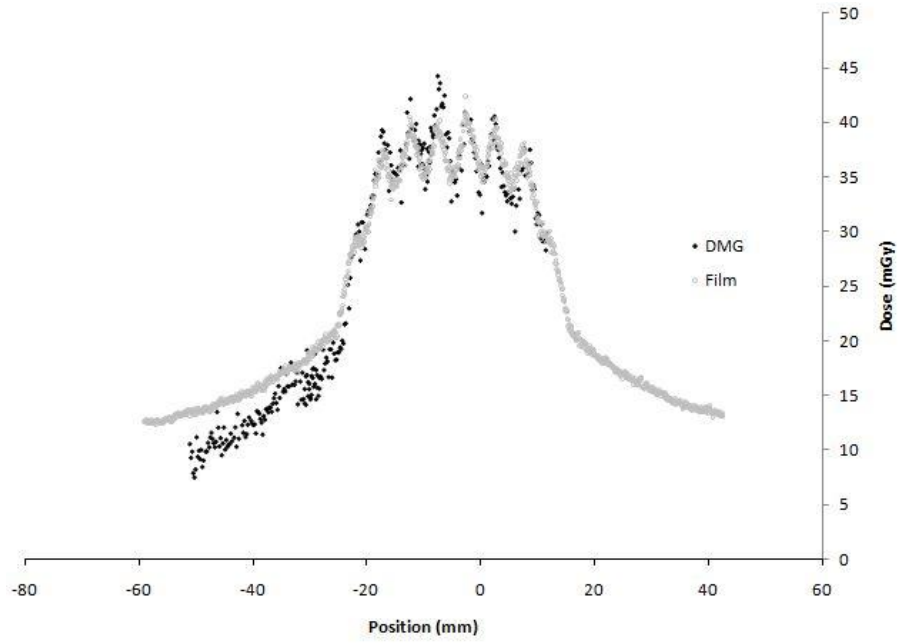

Figure 6.18: Axial scan mode with 5 mm beam collimation (Scan protocol 4, Table 6.1) FWHM (DMG)= 44.0mm, FWHM (film)=55.9 mm, % difference (film- DMG)= 21%. MO*Skin* point dose measurement at CT beam isocentre= 36.2 mGy

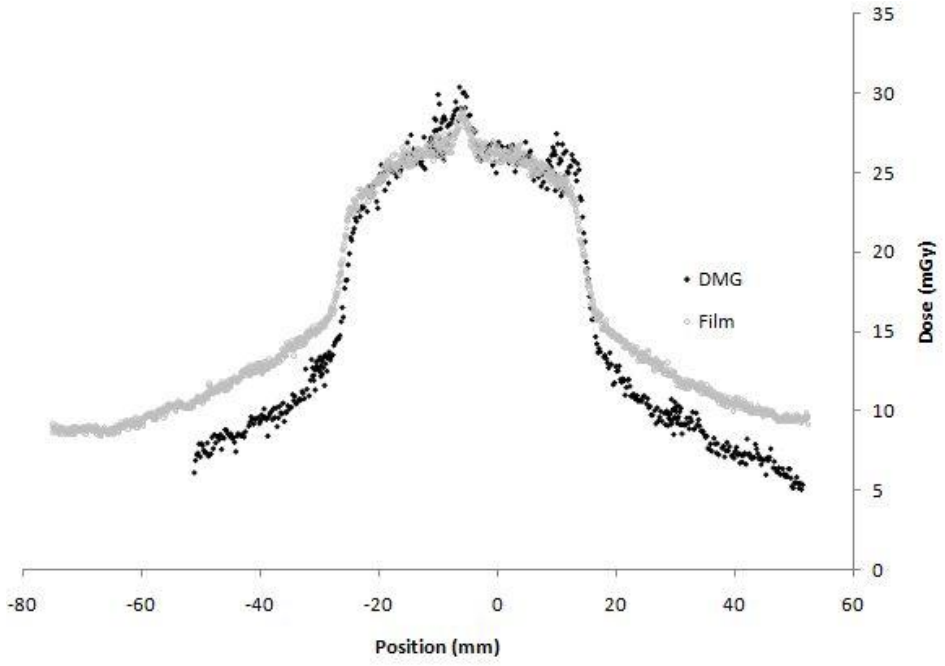

Figure 6.19: Axial scan mode with 20 mm beam collimation (Scan protocol 5, Table 6.1) FWHM (DMG)= 43.0 mm, FWHM (film)= 47.8 mm, % difference (film-DMG)=10.0%. MO*Skin* point dose measurement at CT beam isocentre= 30.4 mGy

6.4.2.3 Helical scan mode

In the helical scan mode, there is extra irradiation outside the imaged volume as additional information is required at the end of the planned image volume series to provide interpolation data for the first and the last images. For the same nominal beam width (i.e. 20 mm), it follows that a helical scan is expected to have a larger FWHM compared to that in axial mode due to this over ranging effect. Comparing Figure 6.20 (helical scan) and Figure 6.19 (axial scan) at the same nominal beam collimation of 20 mm, the measured FWHM for the helical scan was 1.5 times broader than that obtained for the axial scan as expected.

In helical scanning, as pitch increases from 0.625 to 1.35, the measured MSAD value represented by the MO*Skin* point dose measurement decreased as expected. The isocentre MO*Skin* point dose measurement was in agreement with the isocentre dose measured by the film to within 3% for all 3 helical scans at different pitches.

There was good agreement in beam profile measurements between the film and the DMG apart from the dose tails for measured doses under 10 mGy. In addition, there is the added uncertainty of DMG reproducibility in the CT beam, with a COV of up to 7% as discussed in section 6.4.1, which may well account for the different scatter contribution per scan volume.

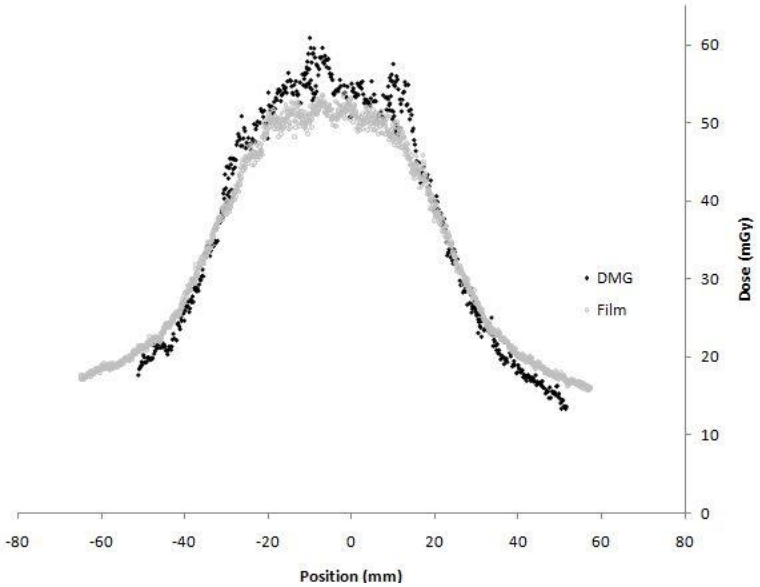

Figure 6.20: Helical scan mode at 20 mm nominal beam collimation, pitch 0.625 (Scan protocol 6, Table 6.1) FWHM (DMG)= 61.4 mm, FWHM (film)= 70.7 mm, % difference (film-DMG)=13.0%. MO*Skin* point dose measurement at CT beam isocentre = 55.1 mGy.

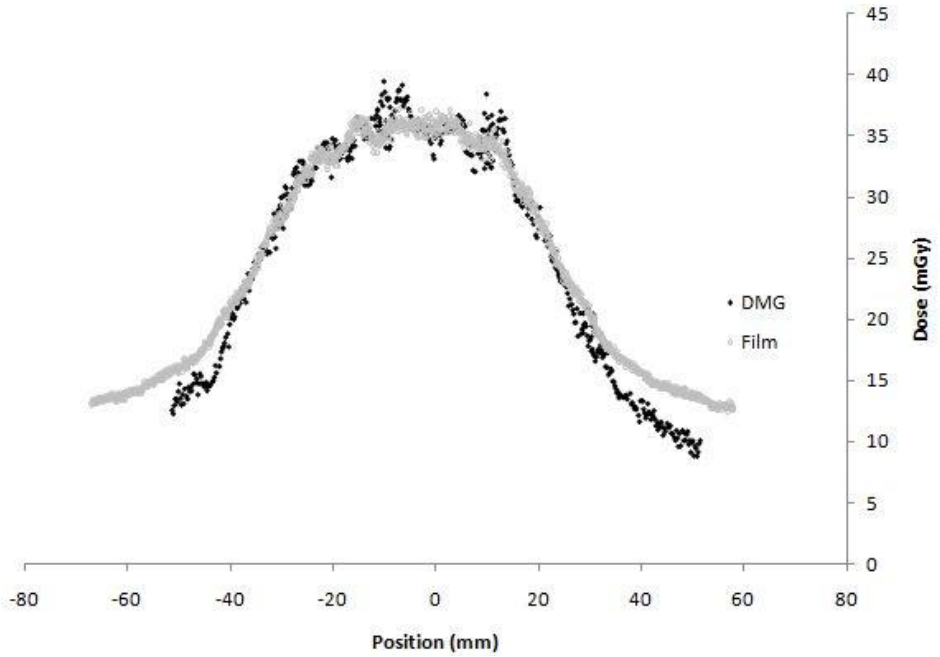

Figure 6.21: Helical scan mode at 20 mm nominal beam collimation, pitch 0.875 (Scan protocol 7, Table 6.1) FWHM (DMG)= 70.0 mm, FWHM (film)= 74.6 mm, % difference (film-DMG)=6.0%. MO*Skin* point dose measurement at CT beam isocentre= 34.8 mGy

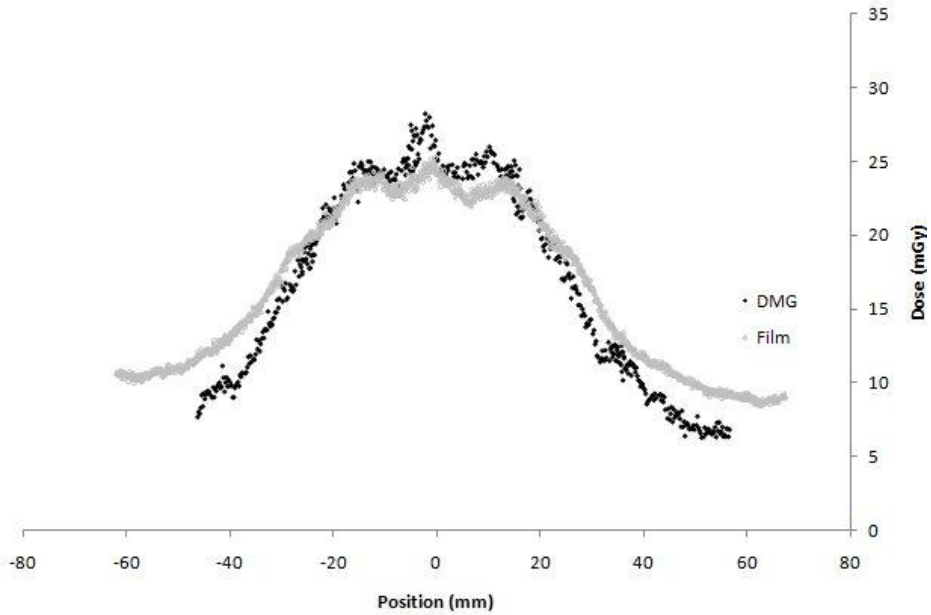

Figure 6.22: Helical scan mode at 20 mm nominal beam collimation, pitch 1.35 (Scan protocol 8, Table 6.1) FWHM (DMG)= 61.3 mm, FWHM (film)= 78.5 mm, %

difference (film-DMG)=22.0%. MOS*kin* point dose measurement at CT beam isocentre = 27.5 mGy

6.5 Conclusion

In this study, we have applied the CMRP Dose Magnifying Glass (DMG), in the measurement of the x-ray CT beam profile in 3 different scan modes, namely the single tube rotation mode, the axial scan mode and the helical scan mode. Data was acquired by the 128-channel, 25.4 mm length DMG in real-time, thus offering the potential for near-real time CT quality assurance data acquisitions.

A depth dose characterisation study with the ion chamber verified the accuracy and reproducibility of MO*Skin* measurements to 3% agreement at depth in solid water. Hence, the MOS*kin* dosimeter formed the basis for absolute dose calibrations of the DMG data acquisitions in this study. The DMG was found to be a useful tool for the assessment of beam dose profiles and should be considered in future applications in CT dosimetry quality assurance.

A new type of film known for its high sensitivity at low doses, the Gafchromic XR-QA2 film, was also evaluated for its capability as a point dosimeter to measure CT dose profile. The XR series of films has been known to exhibit significant energy response and relatively high uncertainties at low doses. Depth dose characterisation performed at low doses below 10 mGy showed that the QA2 film over-responded by up to 30% compared to the MO*Skin* dosimeter and the Markus parallel plate ionisation chamber. This over response of film particularly at low doses under 10 mGy may account for the differences of up to 30% (worst case scenario) in the plotted dose tails when compared with DMG measurements calibrated to the MO*Skin* dosimeter. For the accurate measurement of low doses under 10 mGy, it is imperative that this XR series of films be applied with caution.

7 Assessment of Breast Dose in Clinical MSCT Pulmonary Imaging with the MO*Skin* Radiation Dosimeter

7.1 Introduction

MSCT chest imaging has an important role in the diagnosis and management of patients with thoracic and pulmonary disease, including pulmonary thromboembolism [195]. During a thoracic CT scan where the actual scan organ of diagnostic interest may be the heart or the lungs, the female breasts are often inadvertently irradiated since they are located within the primary beam's field-of-view. Indeed, the breast is a tissue with high radiosensitivity, as identified by the ICRP with the newest assignments of tissue weighting factors; the breasts have recently been re-assigned a value of 0.12 (ICRP 103, 2007)[80] compared to the previous value of 0.05 (ICRP 60, 1991)[204].

For an average-sized woman, the typical absorbed breast dose received from a diagnostic chest x-ray CT is 20 to 50 mGy, approximately equivalent to the amount of absorbed radiation in 10 to 25 two-view mammographic examinations and in more than 100 x-ray chest radiographs [22]. This shows that CT dose risk is not trivial. It follows that where reasonably practicable, dose saving strategies such as tube current modulation (TCM) and the use of in-plane breast shields should be clinically implemented to reduce dose to radiosensitive superficial organs such as the breast, thyroid and eye lens, where the risk for cancer induction is higher than other less radiosensitive tissues in the body.

The aim of this chapter was firstly, to quantify the absorbed breast dose from clinical CT pulmonary embolus (PE) scans with the MO*Skin* dosimeter placed on the breast surface (for the measurement of breast skin dose) and at depth (deep dose; corresponding to the level on the phantom chest) in a thoracic anthropomorphic phantom. The second aim was to evaluate two dose reduction strategies; namely the effectiveness of in-plane breast shielding and the use of automatic tube current modulation (ATCM) in reducing dose to the breast. Finally, image quality analysis was also performed to assess the effect of these dose reduction strategies on diagnostic outcome (i.e. to determine if image quality in the imaged organs of interest such as the

heart and lung were compromised as a result of overall dose reduction).

7.2 Materials

7.2.1 The Alderson Radiation Therapy (ART) Anthropomorphic Phantom

The Alderson Radiation Therapy (ART) phantom is molded of tissue-equivalent material and follows the ICRU-44 standards in their design and construction. The phantom included bone, lung and soft tissue compositions. The male ART phantom represents a standard 175 cm tall, 73.5 kg adult male and the female ART phantom represents a standard 155 cm tall 50 kg adult female.

For this study, we used the standard adult ART phantom with attachable breasts (Figure 7.1). The ART phantom is composed of 2.5 cm thick contiguous axial sections. Each section is numbered for easy identification. Each section of the anthropomorphic phantom has multiple 5-mm diameter cylindrical through holes which are plugged with bone-equivalent, soft-tissue equivalent or lung-tissue equivalent pins depending on section location; each hole may in turn be replaced by TLD holder pins where an organ point dose measurement may be performed where needed.

For the measurement of superficial breast dose and deep breast dose, the MO*Skin* dosimeters were taped on the breast surface and chest wall directly under the breast as shown in Figure 7.1.

Figure 7.1: The chest anthropomorphic phantom showing one MO*Skin* on the

superficial surface of the breast representing superficial breast skin dose and another MO*Skin* at the base of the breast representing deep breast dose

7.2.2 The AttenuRad CT Breast Shield System

The AttenuRad CT Breast Shield System (F&L Medical Products, Vandergrift, PA) consists of a 1 mm thin single piece bismuth encased by a synthetic rubber covering that is mounted on an offset foam base (Figure 7.2). The function of the bismuth shield is to harden the beam's energy distribution by attenuating the superficial beam energies arising from soft radiation (Technical Note, F&L Medical Products, Vandergrift, PA). This is an improvement over conventional lead shields, where lead shields are known to completely absorb the radiation and possibly create metal artifacts which obscure essential anatomy [34].

For the breast attachments, we had a choice of 5 sizes with 200ml 400ml, 600 ml, 900 ml and 1200ml volumes representing female clothing size of cup A, B, C and D, DD respectively. The 200 ml smallest-sized breast was used for all our measurements; this breast size was most representative of young women under 30 years of age who have been found to be the group most at risk for radiation-induced breast carcinogenesis[205].

Figure 7.2: Bismuth breast shield placement (AttenuRad CT Breast Shield System, F&L Medical Products, Vandergrift, PA) for breast dose measurements

7.3 Methods

7.3.1 Scan protocols

Imaging protocols 1 to 4 as depicted in Table 7.1 show the typical clinical parameters used in routine pulmonary diagnosis.

7.3.1.1 Standard (reference) protocol

The standard protocol (scan protocol 1, Table 7.1) was performed at 120 kVp and a tube current of 360 mA with a rotation time of 0.5 s, and a pitch of 1.375. Slice collimation was 16 x 1.25 mm for a nominal beam width of 20 mm. This protocol was performed without dose saving features applied (i.e. neither automatic tube current modulation (ATCM) nor shielding applied). This protocol formed the basis of our reference scan (Table 7.1).

7.3.1.2 Automatic Tube Current Modulation (ATCM)

Smart mA (GE Medical) is an automatic tube current modulation (ATCM) dose saving feature that can be toggled on or off at the machine console depending on user requirements (scan protocol 2, Table 7.1).

In ATCM (with Smart mA toggled on), tube current is automatically adapted both along the z-axis (also known as z-axis modulation; with the aim of homogeneous image quality along the longitudinal axis) and the patient cross-section (known as angular modulation; where the tube current is adjusted based on attenuation for each projection angle around the patient. Projections with less attenuation will result in lower tube current). The initial scout acquisition provides the essential information for ATCM (Figure 7.7).

As a necessary precaution, it was essential to perform the scout acquisition prior to the placement of the bismuth shield on the anthropomorphic phantom, as presence of excess material (ie. lead or bismuth) in the initial scout scan would result in an unnecessary

overdosing to the patient thereafter.

7.3.1.3 Bismuth-shielding

For scan protocol 3, the bismuth breast shield was placed directly over the breasts of the anthropomorphic phantom to directly reduce in-plane breast dose (Table 7.1).

Table 7.1: Scan Parameters for CT Pulmonary Embolus (PE) imaging protocols

	Scan Protocol			
Imaging Parameters	**1 Reference**	**2 ATCM**	**3 Shield**	**4 ATCM and Shield**
Detector configuration (mm)	16 x 1.25			
Peak kV (kVp)	120			
Tube current (mA)	360			
Scan length (mm)	300			
Exposure time (s)	5.97			
Total scan time (s)	5.97			
Rotation time (s)	0.5			
Pitch factor	1.375			
Beam width (mm)	20.0			
Speed (mm/rot)	27.5			
$CTDI_{console}$ (mGy)[a]	12.11	6.57	12.11	6.57
$DLP_{console}$ (mGy.cm)[b]	397.57	205.25	397.57	205.25
Dose modulation	No	Yes	No	Yes
Breast shield used	No	No	Yes	Yes

[a]$CTDI_{console}$= value of CTDI displayed on the scanner console for a cylindrical PMMA phantom diameter of 32 cm.
[b]$DLP_{console}$= value of DLP displayed on the scanner console for a cylindrical PMMA phantom diameter of 32 cm.

7.3.2 Dosimetry

For each scan protocol, two MO*Skins* were positioned on the phantom, one to measure the superficial breast dose, and the other to measure the breast dose at depth (Figure 7.1). Each point dose measurement with the MO*Skin* dosimeter was repeated three times and the average reading was recorded.

Similarly, for each scan protocol, we placed 3 pieces of Gafchromic XR-QA2 film (cut

to shape 1 cm x 1 cm dimensions) directly over the breast and another 3 pieces of film on the chest wall directly under the breast. Film readings were similarly averaged for the evaluation of superficial breast dose and deep breast dose respectively. Each film piece was calibrated in a 150 kVp (0.63 mm Cu HVL) orthovoltage beam.

7.3.3 Quantitative image quality evaluation

For the objective evaluation of image quality, we adopted the use of noise (in Hounsfield units (HU)) as a measurement parameter. Noise as a measurement parameter has been shown by Vollmar and Kalender [206] to be especially suitable for the quantitative image quality evaluation of homogeneous phantoms.

For this research, we used a commercial PACS workstation for our image quality analysis. In particular, for the objective image quality analysis in the heart and breast region, the soft tissue window was displayed. Similarly, in the lung region, the lung window was selected as the display window of choice.

7.4 Results and Discussion

7.4.1 Evaluation of breast dose

Table 7.2 shows the measured superficial and deep breast dose results obtained by applying both the MO*Skin* dosimeter and the Gafchromic XR-QA2 film under 4 different scanning protocols; the reference protocol (scan protocol 1), the dose-modulated (ATCM) protocol (scan protocol 2), the protocol with the use of the in-plane breast shield without ATCM (scan protocol 3) and the protocol with both dose reduction strategies applied (scan protocol 4). Figure 7.3 and 7.4 is a graphical representation of the tabulated data from Table 7.2.

Table 7.2: Absorbed breast dose measured by the MOS*kin* dosimeter and Gafchromic XR-QA2 film

PE Scan Protocol #	**1 Without radiation protection**		**2 Dose modulation only**		**3 Shield only**		**4 Dose modulation and shield**	
	Skin	**Deep**	**Skin**	**Deep**	**Skin**	**Deep**	**Skin**	**Deep**
[a]Absorbed dose (MOSkin, mGy)	10.4±3.0	20.9±3.0	9.4±1.9	11.4±2.4	7.0±3.4	9.0±4.4	4.5±1.5	6.0±0.0
Absorbed dose (Film, mGy)	17.2±0.2	21.0±0.2	12.6±0.1	13.2±0.1	11.1±0.1	12.8±0.1	6.9±0.1	7.2±0.0
[b]Average breast dose (mGy)	17.4±2.1		11.7±1.1		10.0±2.0		6.2±0.4	

[a]Absorbed dose= $\frac{\text{MOSkin measurement (mV)}}{\text{Dose sensitivity calibration factor}(0.67\ \text{mV mGy}^{-1})}$

[b]Average breast dose = the average of the superficial (skin) and deep breast dose measured by both the MOSkin dosimeter and the film

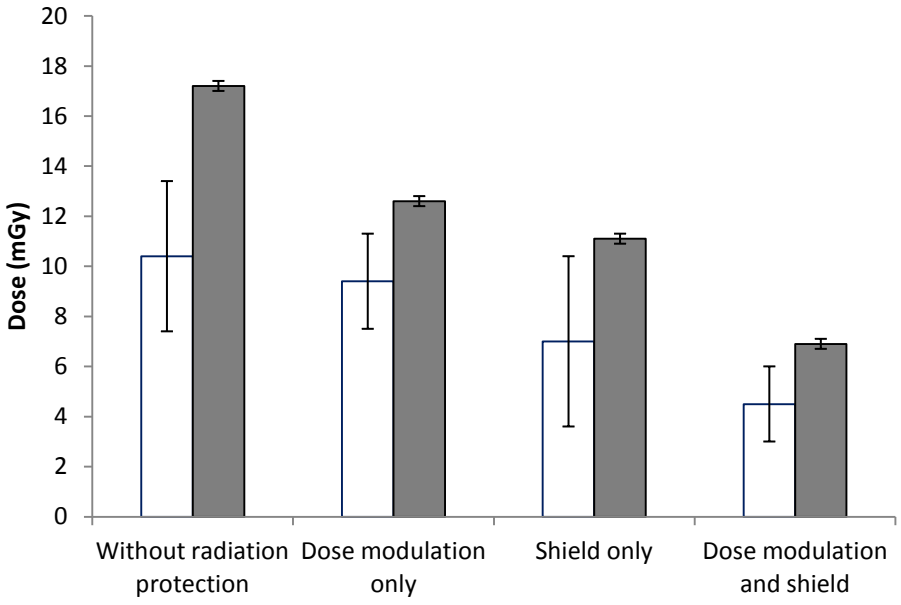

Figure 7.3: The effect of various dose reduction strategies on superficial breast dose measured by the MO*Skin* dosimeter (☐) and Gafchromic XR-QA2 film (■). Error bars show the range of point dose measurements obtained by both dosimeters.

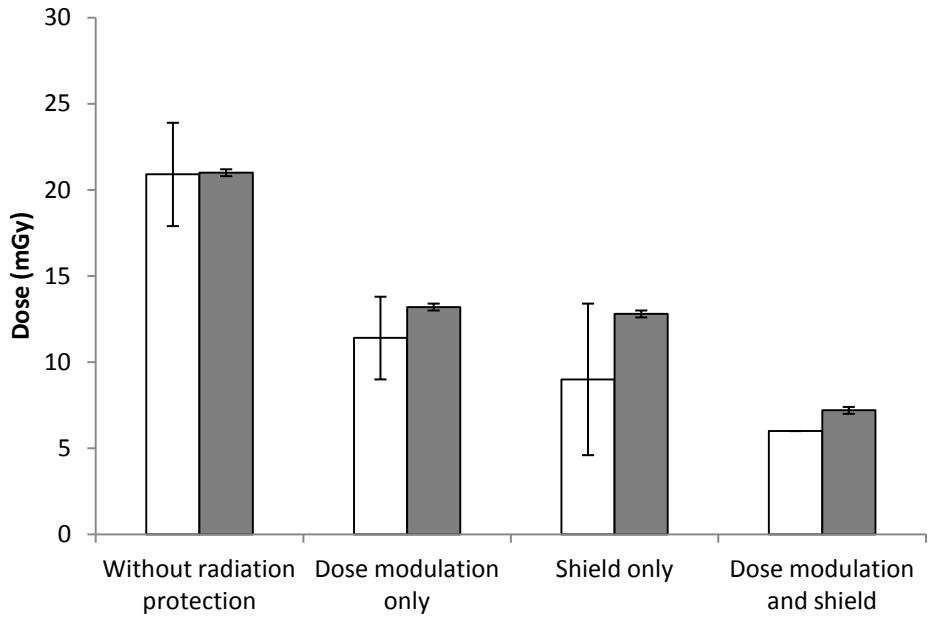

Figure 7.4: The effect of various dose reduction strategies on deep breast dose measured by the MOSkin dosimeter(☐) and Gafchromic XR-QA2 film(■). Error bars show the range of point dose measurements obtained by both dosimeter

The film dose measurements obtained in this study were consistently higher than MO*Skin* dose measurements by an average of 53% (4.1 mGy) and 20% (1.7 mGy) for superficial breast dose (Figure 7.3) and deep breast dose (Figure 7.4) measurements respectively. The consistently higher dose measurements recorded by the film may be attributed firstly, to the over-response of this particular type of film at low doses[201]; and secondly, to the larger WED of measurement for film (about 0.12 mm) in comparison with the MO*Skin* (0.07 mm). This difference as a result of different WED of dosimeters has similarly been previously reported for radiotherapy skin dosimetry studies of the breast, scalp and neck [112,157,207,208]. For the kilovoltage energies used in this study, it is expected that the WED effect is more pronounced due to the lower average energies in the kilovoltage field.

The larger spread of point dose measurements obtained by the MO*Skin* dosimeters would have been due to differences in the positioning of the x-ray tube start and end angle due to the CT helical beam not falling on the same position on the same point of the arc [51]. This is because each point dose measurement with the MO*Skin* dosimeter was repeated three times; 2 MO*Skin*s were used per CT run, one placed on the surface of the breast phantom and the other on the chest wall.

There was much less variation in the spread of point doses measured by the film pieces. This is due to a difference in experimental methodology used for film point dose acquisitions. Each point dose measurement with the film was obtained by 3 film pieces placed on the surface of the breast phantom and the other 3 film pieces on the chest wall at the same time. This shows that within the scan field of view, doses are uniform.

Figure 7.5 shows the reduction of average breast dose as a result of the application of dose reduction techniques. A 33% dose reduction was obtained with the use of ATCM only, a 43% dose reduction obtained with the use of bismuth shield only, and a breast dose saving of 64% was obtained with both dose reduction strategies applied.

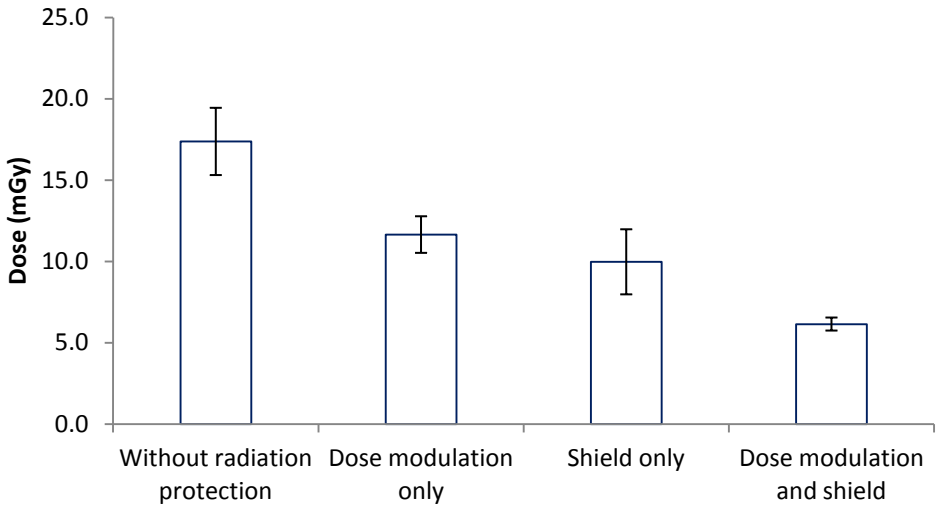

Figure 7.5: Average breast dose measured by both dosimeters in 4 different scan conditions. Error bars show the average spread of point dose measurements obtained by both dosimeters.

Our measured dose results were in excellent agreement with published data. Yilmaz et al [22] found that the use of bismuth breast shield when performing thoracic CT on a 16-slice CT scanner resulted in a 40% reduction of dose to patient breasts compared to our dose reduction findings in this study of 43% with the use of a breast shield in PE CT imaging.

Vollmar and Kalender [206] found a dose reduction of 42.8% in bismuth shielding and a 9.4% breast dose reduction when TCM was used. The authors' measured values compared well with our dose reduction findings of 43% (with bismuth shielding) and 9.6% (superficial breast dose) respectively.

Hurwitz et al [209] found that the use of ATCM and bismuth shields resulted in a 55% reduction in absorbed breast dose for adult PE scans on a 64 MSCT scanner, compared to our findings of 64% dose reduction with ATCM and bismuth shielding applied on a 16-slice MSCT scanner.

7.4.2 Quantitative image quality evaluation

Table 7.4 summarizes the image quality findings expressed in Hounsfeld units (HU) obtained for this study. It can be seen that the image quality values obtained in the ATCM only scan (protocol 2, Figure 7.8) compares well with that of the reference scan (protocol 1, Figure 7.6) with little to no deterioration in image noise. With the breast shield in place(Figure 7.9), image quality in the breast and heart region deteriorated by almost 32 times and 2 times respectively compared to that of the reference scan, while lung image quality deteriorated by 3%.

Table7.4: Image quality evaluation with circular regions of interest (ROI) for the heart region (37.291 cm^2), breast region (2.2365 cm^2) and lung region (21.263 cm^2). Each value was expressed as the mean ± sd corresponding to image quality ± noise.

Scan #	Image quality		
	Heart region (HU)	Breast region (HU)	Lung region
Reference scan (Protocol 1)	-7.05 ± 19.9	6.52 ± 9.0	-682.25 ± 59.9
ATCM scan (Protocol 2)	-6.96 ± 23.7	6.64 ± 13.6	-680.26 ± 62.2
Scan with bismuth shield (Protocol 3)	8.86 ± 25.6	208.08 ± 62.2	-664.69 ± 63.6

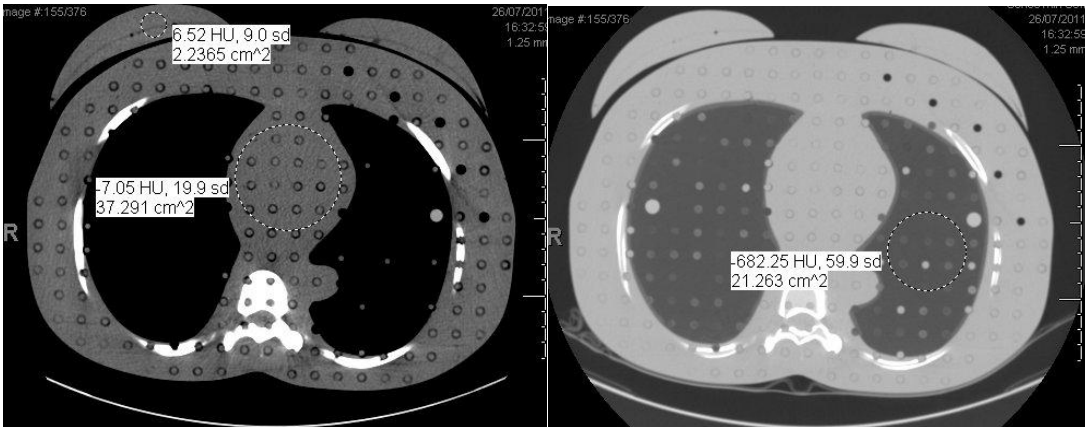

(a) (b)

Figure7.6: MSCT images obtained at the mid thoracic region (at slice location 23.6, image number 159 of 376) in the anthropomorphic phantom (a) soft tissue and (b) lung display windows at 120 kVp, 360 mA without ATCM nor bismuth shield. This formed the basis of our reference scan.

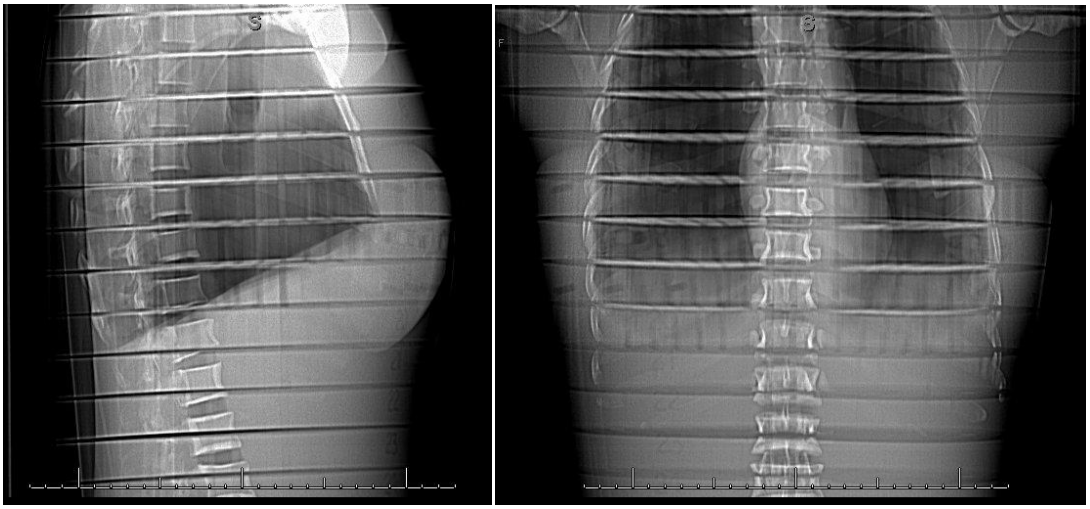

(a) (b)

Figure7.7: Lateral (a) and anterior (b) scout images acquired prior to the ATCM image acquisitions as a basis for z-axis and angular patient attenuation profile.

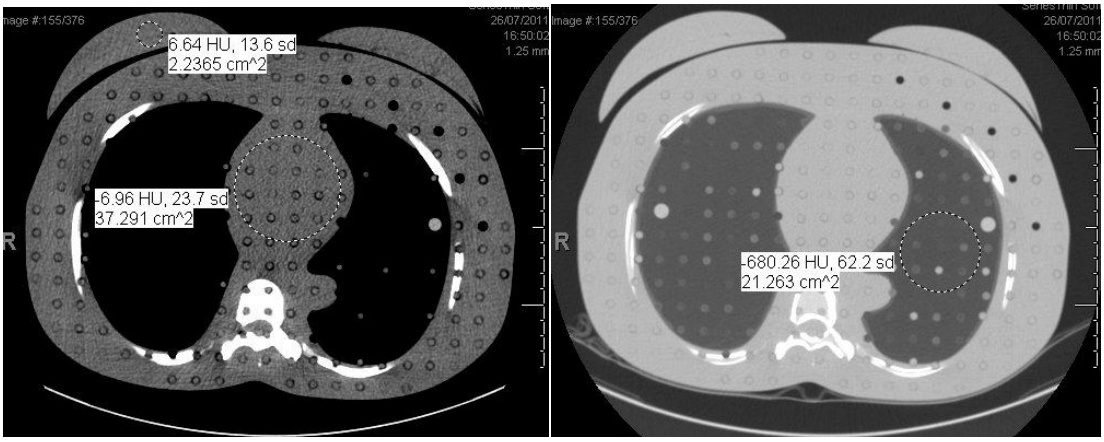

(a) (b)

Figure7.8: MSCT images obtained at the mid thoracic region (at slice location 23.6, image number 159 of 376) in the anthropomorphic phantom (a) soft tissue and (b) lung windows at 120 kVp, with ATCM applied (tube modulated current for this image was 100 mAs).

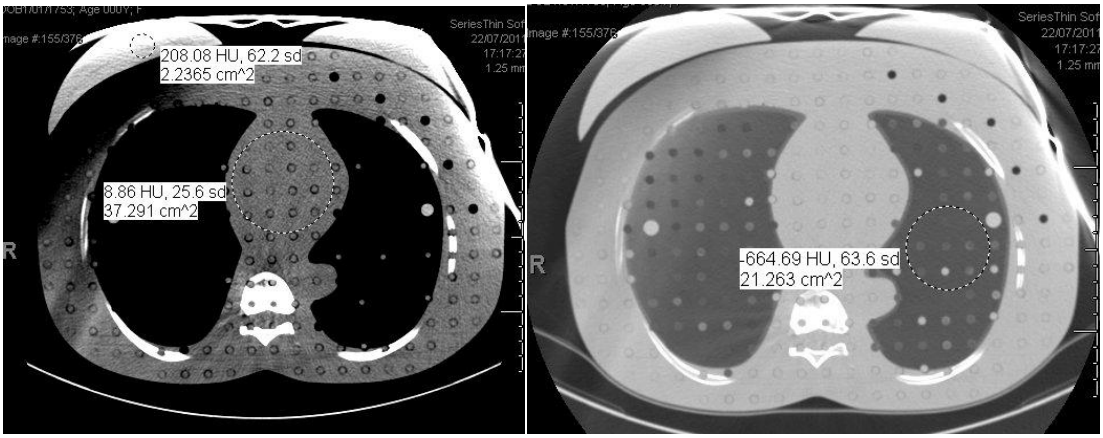

(a) (b)

Figure7.9: MSCT images obtained at the mid thoracic region (at slice location 23.6, image number 155 of 376) in the anthropomorphic phantom (a) soft tissue and (b) lung windows at 120 kVp at a fixed tube current of 360 mA, with the bismuth breast shield positioned directly over the breasts.

7.5 Conclusions

The PE scan protocol used in this experimental study reflects that currently used in clinical practice.

In this study, we have shown that if the imaged organ of interest is deep (ie. the lung for CT PE scanning), the use of the breast shield is recommended as there is a reduction of dose to the radiosensitive breast tissue with minimal loss of image quality. However, if the imaged organ of interest is superficial tissue such as the breast, alternative imaging modalities without the use of ionising radiation should be considered (MRI, ultrasound), since the benefit of CT imaging with the shield (a 32 fold and 2 fold increase in noise, for the superficial breast and heart tissue regions respectively) clearly outweighs the dose saving benefit (43% decrease in breast dose). In other words, in the case where the imaged organ of interest is superficial tissue, it is clear that use of the breast shield compromises image quality and should not be used.

Tube current modulation works by reducing the number of primary photons from the x-ray CT tube by adjusting the tube current according to individual patient attenuation. ATCM clearly offers the best possible solution for dose reduction as our study has shown; no significant deterioration in image quality was found.

In conclusion, when the radiosensitive breasts are within the irradiated field of view, automatic tube current modulation is the most effective strategy for image quality-dose optimisation in CT. Bismuth shielding should be judiciously applied and is not particularly recommended for use if the imaged structure of interest is superficial tissue as this study has shown.

8 Application of the MOS*kin* dosimeter in the assessment of effective dose in clinical MSCT scans

8.1 Introduction

In CT QA assessment, CTDI and DLP are reference quantities used for the development and optimisation of CT imaging protocols. As the dose expressed by these dose indices is in relation to standard-sized cylindrical PMMA phantoms, they do not give a direct assessment of individual absorbed patient dose. For this, direct organ dose measurements in a tissue-equivalent anthropomorphic phantom provide a more realistic assessment of patient dose and associated cancer risk. This knowledge in turn provides a practical basis for the optimisation of patient protection in radiology.

The clinical implementation of individualised patient dosimetry is an attractive option for 21st century radiology and beyond, as the world becomes increasingly vigilant of the risks associated with high dose CT imaging scans. As reported by Rehani et al[87], the use of an individualised patient electronic smart card to monitor lifetime cumulative radiation dose is possibly the next leap forward in radiological dose monitoring, considering the fact that several countries in Europe already have in place electronic health record systems. Measurements of patient organ doses have been successfully performed by various researchers by means of conventional TLDs [22] [28]. But clearly, a real-time readout system presents a more attractive individual patient dose monitoring option [51,54,56]. For this, a dosimeter such as the MO*Skin* dosimeter, based upon MOSFET technology, presents a potentially viable real-time tool for the measurement of patient skin dose and for organ dose measurements in a phantom.

The primary aim of this chapter was to perform direct organ point dose measurements with the MO*Skin* dosimeter. Organ point dose measurements obtained with the MO*Skin* dosimeter were then compared against measurements obtained with the Gafchromic

XR-QA2 film. By applying the most recent ICRP 103 tissue weighting factors to our measured organ doses, the effective dose for 2 common clinical MSCT imaging protocols, namely the renal calculus diagnostic CT imaging scan and the pulmonary embolus diagnostic CT imaging scan were subsequently calculated. The measured derived effective dose was then evaluated against gold-standard Monte Carlo calculations performed in a mathematical phantom with NRPB-SR250 datasets.

8.2 Materials and Methods

8.2.1 MSCT scanner and anthropomorphic phantom inserts

Knowledge of CT scanner HVL provided the primary basis onto which our radiation detectors were calibrated. The dosimeters were calibrated in a 150 kVp (HVL=0.63 mm Cu) orthovoltage beam on the Gulmay D3300 unit whose effective energy of 71.9 keV most closely corresponded to the 71 keV effective energy of the 16-slice GE Discovery 670 NM/CT SPECT/CT scanner with an applied 120 kVp tube potential and a measured HVL of 0.8 mm Cu.

To measure point organ doses, custom-milled individual solid water holders (2.5 cm length and 0.5 cm diameter) were inserted into the anthropomorphic phantom at known depths of interest. Figure 8.1 shows a cross-sectional schematic of the custom-milled solid water holder with a 1.5 cm length insert, specifically designed to accommodate the MO*Skin* dosimeter or film.

Figure 8.2 shows the same holder placed into the slot of the anthropomorphic phantom for the assessment of organ point dose at a known depth of interest for a known slab. Unused slots of the phantom were filled with tissue equivalent plugs.

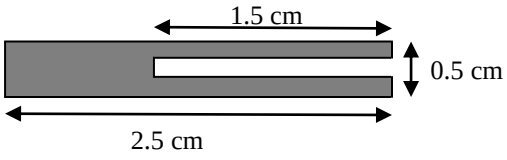

Figure 8.1: Schematic of the custom-milled solid water holder designed to fit into the anthropomorphic phantom for dosimeter point organ dose assessment

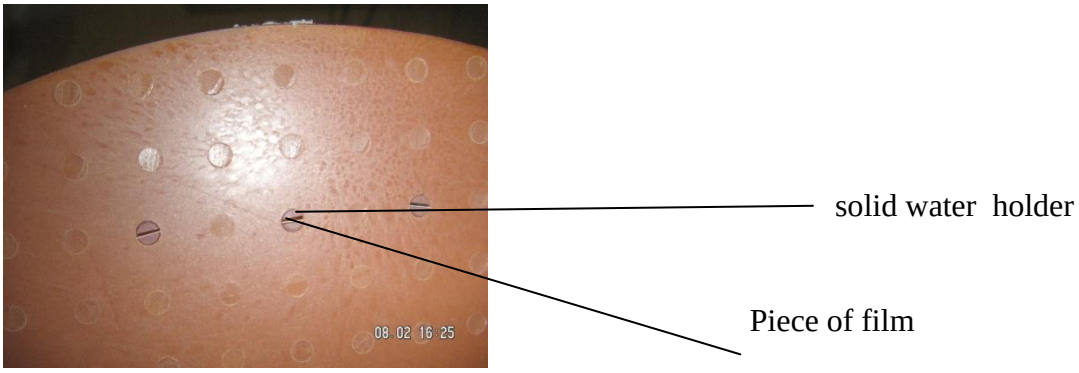

Figure 8.2: Photograph of a single slab of the anthropomorphic phantom with a piece of Gafchromic film placed in the custom made solid water holder

8.2.2 Dosimeters

Gafchromic film

Strips of Gafchromic XR-QA2 film (dimensions 1.5 cm x 0.5 cm) were cut from a standard sized film sheet. XR-QA2 film was calibrated on the solid water phantom surface; a dose calibration plot was obtained to relate the optical density of the exposed films to the applied dose as previously plotted in Figure 6.10.

MO*Skin dosimeter*

Each MOS*kin* dosimeter was assigned an individual calibration factor expressed in units of mV/cGy. As MO*Skin* calibration factors vary as a function of tube potential (due to MO*Skin* energy dependence), it was essential to establish unique calibration factors at the CT beam energy of interest. For the 150 kVp orthovoltage calibration beam across 3 separate MO*Skins* from the same batch, a calibration factor of 0.67 ± 0.02 mV/mGy was found.

Figure 8.3 shows the schematic of the experimental setup; illustrating how dosimeters were applied in the measurement of phantom CT organ dose.

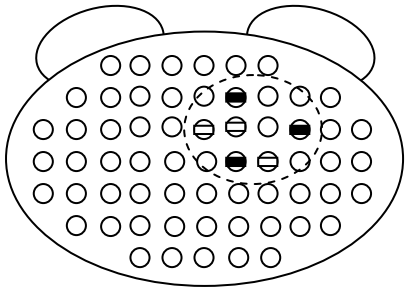

Figure 8.3: Application of the MOS*kin* (■) and film (☐) dosimeters for CT organ point dose measurement in the anthropomorphic phantom. The dotted line demarcates the anatomical position of the heart.

Figure 8.4 shows the depth dose characterisation plot of the MO*Skin* dosimeter and the XR-QA2 film with a delivered dose of 100 mGy at solid water phantom surface, closely matching each other in depth dose response down to 20 mGy at 10 cm solid water phantom depth. Both dosimeters were referenced to the Markus ion chamber taken as the gold-standard depth dose dosimeter.

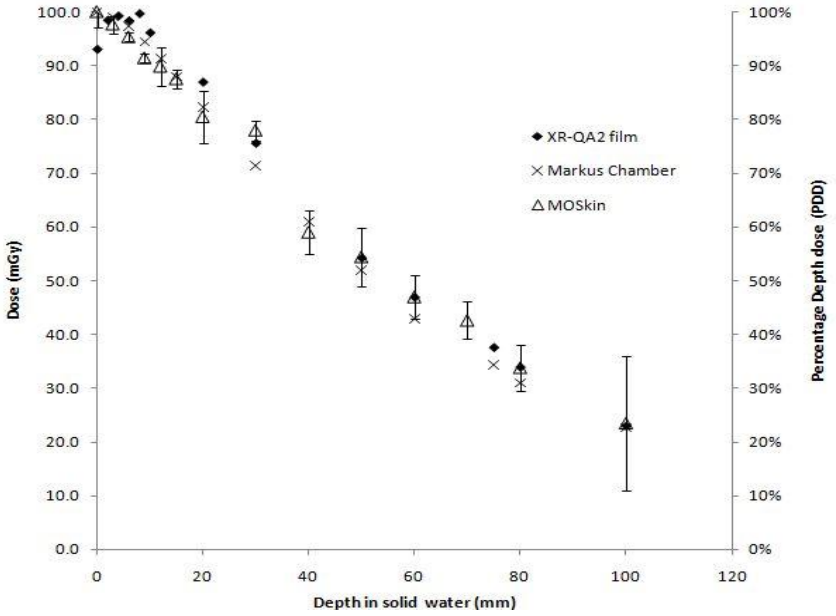

Figure 8.4: Characterisation of the depth dose response of the MOSkin dosimeter and film with 10 cGy (100 mGy) delivered dose to the surface of the phantom

8.2.3 MSCT Scan protocols

The CT imaging parameters of the scans that were performed in this study are listed in Table 8.1.

Table 8.1: Imaging parameters for 16-slice MDCT of the abdominal-pelvic region for a renal calculus protocol; and of the chest for a pulmonary embolus (PE) protocol

	Protocol name	
Imaging Parameters	Renal Calculus	PE
Tube potential (kVp)	120	120
Fixed mAs	150	360
Effective mAs[a]	54.5	130.9
Table movement (mm rot^{-1})	27.5	27.5
Pitch	1.375	1.375
Detector configuration	16 x 1.25	16 x 1.25
Beam width (mm)	20.0	20.0
Planned scan length (mm)	250	300
Exposed scan length (mm)	278	328
Coverage time (s)	5.05	5.97
$CTDI_{vol}$ (mGy)[b]	5.10	12.11
DLP[b] (mGy cm)	141.62	397.57

[a]Effective mAs=$\frac{\text{Average tube current x rotation time}}{\text{Pitch factor}}$

[b] $CTDI_{vol}$ and DLP as displayed on the operator console was based on a PMMA cylindrical body phantomwith a diameter of 32 cm

The scan range in the renal calculus abdominal-pelvic CT scan was from the upper region of the diaphragm to the pubic symphasis, corresponding to slab numbers 25 to 34 of the anthropomorphic phantom and a prescribed scan length of 250 mm. The scan range in the pulmonary embolus chest CT scan was from the upper end of the lung apex to the lower region of the diaphragm, corresponding to slab numbers 10 to 21 of the anthropomorphic phantom corresponding to a prescribed scan length of 300 mm. (Figure 8.5)

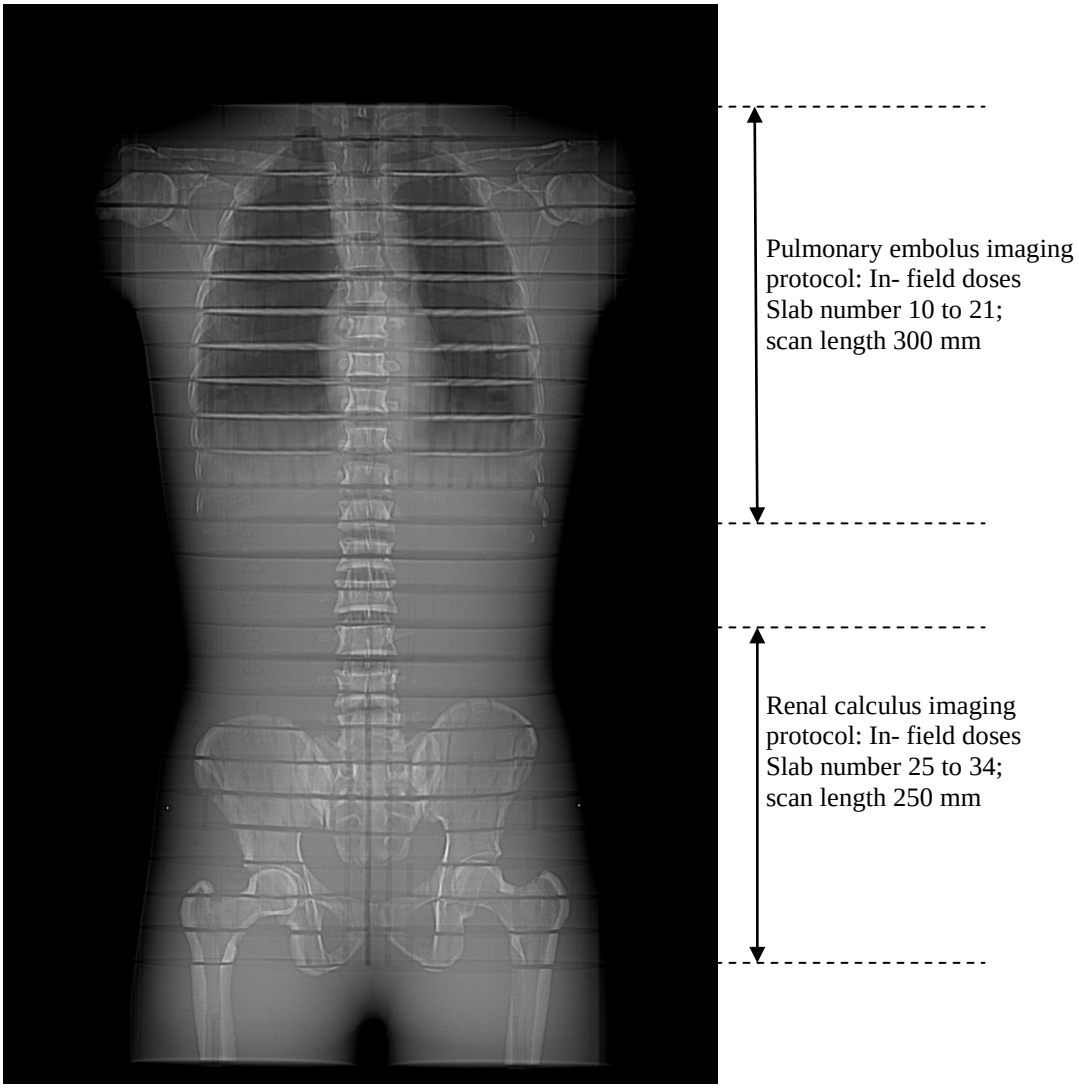

Figure 8.5: Scout scan (120 kVp, 10 mA) of the tissue-equivalent anthromorphic phantom used in this study. The total scan range of this phantom was 800.7 mm. Slab numbers 10 to 34 are depicted as shown. Each slab is 25 mm.

For both scans, a headless phantom was used. As such, doses to the brain, eye lens, and salivary glands were not measured. It is reasonable to assume that absorbed organ doses to the head are negligible for both abdominal-pelvic region scans and chest region scans as the distances from the primary beam to these organs is more than 8 cm. This assumption has similarly been adopted by [54]. Moreover, preliminary measurements in this study indicated that out-of-field doses, particularly for dose measurements beyond the boundaries of the scan field of view (more than a distance of 50 mm equivalent to 2 slab lengths), exceed the low dose detection threshold of both dosimeters and cannot be measured.

Within the same organ, the detectors were randomly placed throughout the organ, at the same specified depth. In the scan field-of-view, with the exception of the remainder organs, each recorded organ point dose measurement was the average of 3 individual dosimeter readings. For measurement of dose to the remaining organs, each point dose measurement was taken by a single dosimeter placed in the centroid of the organ.

For the measurement of out-of-field doses (i.e. at the scan boundaries), to overcome the low dose detection threshold of the dosimeters used, the technical parameters of the imaging protocols was scaled up. In the low-dose renal calculus protocol, we doubled the tube current and scanned 3 times before taking a dose measurement. The cumulative dose measured was then scaled down by a factor of 6, to determine dose in a single phasic MSCT scan. In the case of the pulmonary embolus protocol, we scanned 4 times before taking a dose measurement. The cumulative dose was then scaled down by a factor of 4 to determine single phasic MSCT scan dose.

8.2.4 NRPB-SR250 ImPACT CT Patient Dosimetry Calculator

The ImPACT CT Patient Dosimetry Calculator (Version 1.0.4) Excel spreadsheet provides a convenient user interface for calculating patient organ and effective doses from a wide range of current MSCT scanners. This software incorporates data from the NRPB Monte Carlo dose datasets [65] and normalized dose data from the SR250 report.

The scanner-specific technical parameters required for software input were namely, the CT tube potential (kV), start position, end position and the acquisition parameters (which included the tube current in mA, rotation time, spiral pitch and beam width) (See Appendix D for further details). Amongst the CT scanners available for selection on the spreadsheet, the GE Lightspeed 16 was chosen as most representative of our actual applied protocols on the clinical 16-slice GE Discovery 670 NM/CT SPECT/CT scanner; the software-computed $CTDI_{vol}$ and DLP matched what was displayed on our actual CT scanner console. This provided verification of correct data input [210].

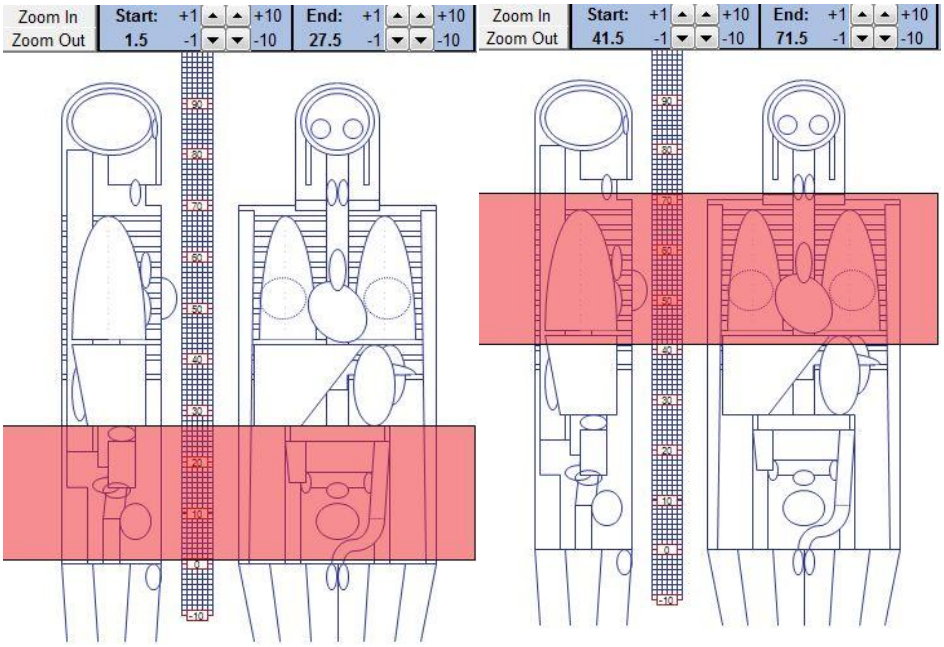

Figure 8.6: The mathematical software model applied in the NRPB-SR250 CT Dosimetry calculator used for the computation of effective dose. A scan range of 260 mm and 300 mm was specified in the renal calculus scan (shown on left) and the pulmonary embolus scan (shown on right) respectively.

Figure 8.6 shows the mathematical software phantom used in the NRPB SR250 software for the computation of effective dose. The mathematical model was essentially a hermaphrodite patient with geometrically defined organs and tissues. This phantom consisted of 208 contiguous slabs each of 5 mm thickness.

The effective doses derived as a result of the software simulations on this mathematical phantom formed the basis for our gold-standard dose values, for the comparison of derived effective doses from our measurements done with film and the MO*Skin* detector.

8.2.5 Calculation of Effective dose

Effective dose is essentially a summation of organ doses multiplied by individual tissue weighting factors as described in Chapter 1, Section 1.4. For this study, we used the following equation to derive effective dose E.

$$E = \sum_{T} w_T \cdot H_T$$

where w_T is the tissue weighting factor and H_T is the equivalent organ dose multiplied by the radiation weighting factor of 1 for x-rays.

The alternative way of calculating effective dose was to multiply the DLP value as displayed on the CT scanner console by a known k- coefficient previously established by the EC2004[211].

8.3 Results and Discussion

8.3.1 Measured organ doses

The measured organ doses were tabulated in Table 8.2 and 8.3, and illustrated in Figures 8.7 and 8.8 for the renal calculus and pulmonary MSCT scan protocols respectively.

Organs in the imaged field of view were in the dose range 4.7 to 9.5 mGy and 16.2 to 27.4 mGy for the renal calculus (RC) and pulmonary embolus (PE) CT scan protocols respectively. Within the imaged field of view, point doses obtained with the MOS*kin* dosimeter and film compared favourably to within 20% of each other, with the exception of measured average point breast dose (up to 40% difference for the PE protocol) and measured bone surface dose (up to 37% difference for the RC protocol).

This difference may be explained by the electronic disequilibrium created by the presence of the air-tissue interface and bone-tissue interface for the assessment of breast dose and bone surface dose respectively.

For doses outside the imaged field of view, particularly at the boundaries of the scan field of view (within 5 mm of the specified scan field), doses recorded by both dosimeters differed by up to 33% for both imaging protocols. Due to the different scattering angles of the incident beam path (the start and stop positions of the rotating CT tube source are different and cannot be controlled for repeated measurements), dose measurements by both dosimeters are bound to differ.

Table 8.2: Comparison of CT anthropomorphic phantom organ point dose measurements between the MO*Skin* and Gafchromic XR-QA2 radiochromic film for the renal calculus scan. Organ locations were derived from references [51,212]. The primary scan field ranged from slab 25 to 34.

Organ (slab number, depth in mm)	ICRP 60 w_T	ICRP103 w_T	MO*Skin* point dose measurement (mGy)	Film point dose measurement (mGy)	Percentage difference (%)[1]
Lung (S13,122)	0.12	0.12	ND[2]	ND	-
Breast[3](S18, 15)	0.05	0.12	ND	ND	-
Oesophagus (S10, 20)	0.05	0.04	ND	ND	-
Liver (S20, 33)	0.05	0.04	ND	ND	-
Stomach (S22, 43)	0.12	0.12	ND	ND	-
Colon (S28, 68)	0.12	0.12	9.0 ± 1.5	8.0 ± 2.1	11
Ovaries (S31, 117)	0.20	0.08	8.0 ± 1.0	7.8 ± 2.0	2.5
Bladder (S31, 44)	0.05	0.04	8.0 ± 1.0	9.5 ± 1.0	-19
Bone surface (S29, 135)	0.01	0.01	7.5 ± 1.5	4.7 ± 0.8	37
Red bone marrow, pelvis (S30, 100)	0.12	0.12	5.0 ± 0.5	5.5 ± 0.8	-10
Skin (S30, surface)	0.01	0.01	8.1 ± 0.4	7.6 ± 1.1	6
Remainder organs, ICRP 60, w_T=0.05					
Thymus (S14, 20)			ND	ND	-
Spleen (S23, 150)			2.7	3.6	-33
Adrenals (S22, 100)			ND	ND	-
Kidney (S23, 120)			2.7	3.4	-26
Pancreas (S23, 50)			3.3	3.0	9
Small intestine (S23, 80)			2.7	3.4	-26
Uterus (S31, 125)			5.7	5.9	-4
Remainder organs, ICRP 103, w_T=0.12					
Adrenals (S22, 100)			ND	ND	-
Gall bladder (S21, 70)			ND	ND	-
Heart (S16, 30)			ND	ND	-
Kidney (S23, 120)			2.7	3.4	-26

Pancreas (S23, 50)	3.3	3.0	9
Small intestine (S23, 80)	2.7	3.4	26
Spleen (S23, 150)	2.7	3.6	-33
Thymus (S14, 20)	ND	ND	
Uterus (S31, 125)	5.7	5.9	-4

[1]Percentage difference = (MOS*kin* measurement- Film measurement)/MOS*kin* measurement x 100%
[2]ND= Doses were Not Detectable as they were below the low dose detection threshold of both dosimeters, < 2 mGy
[3]Breast dose refers to the average of the surface and chest point dose measurements

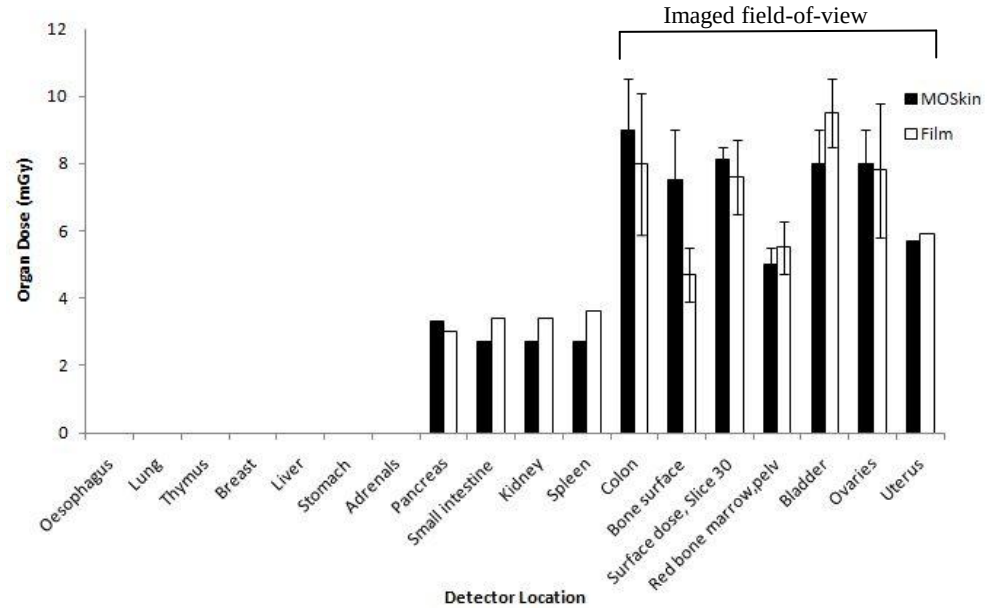

(a)

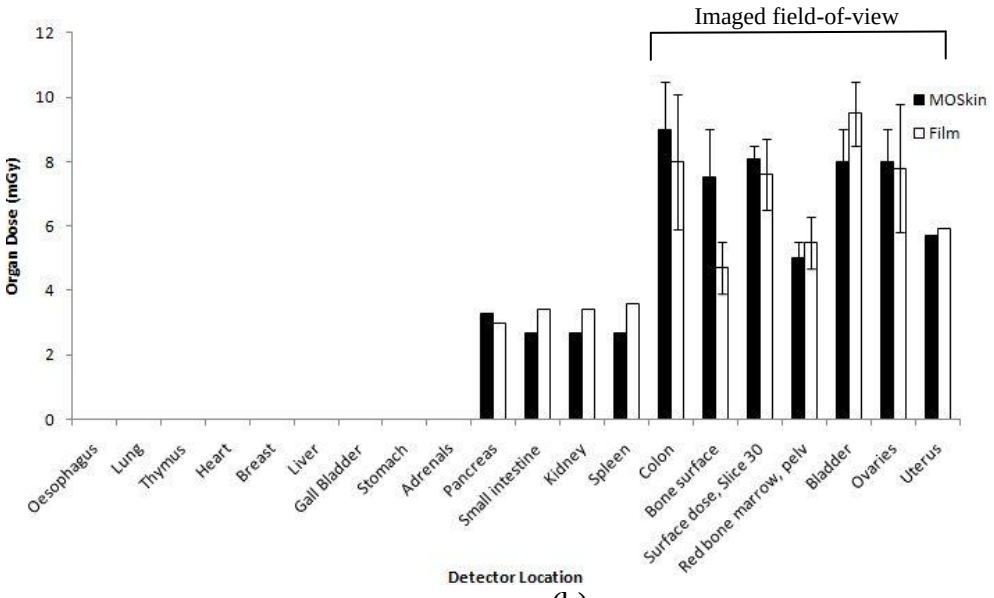

(b)

Figure 8.7: Renal calculus CT imaging scan. Point organ dose measurements obtained with the MOS*kin* dosimeter and Gafchromic XR-QA2 film (a) 18 organ locations of interest as specified in ICRP 60 (b) 20 organ locations of interest as specified in ICRP 103. Error bars refer to the range of doses obtained with 3 individual point dosimeter readouts.

Table 8.3: Comparison of CT anthropomorphic phantom organ point dose measurements between the MOS*kin* and Gafchromic XR-QA2 radiochromic film for the pulmonary embolus scan. Organ locations were derived from references [51,212]. The primary scan field ranged from slab number 10 to 21.

Organ (section number, depth in mm)	ICRP 60 w_T	ICRP103 w_T	MOS*kin* point dose measurement (mGy)	Film point dose measurement (mGy)	Percentage difference [1](%)
Lung (S13,122)	0.12	0.12	18.6 ± 1.7	21.3 ± 2.2	-15
Breast[3] (S18, 15)	0.05	0.12	16.2 ± 3.8	22.6 ± 3.7	-40
Thyroid (S10, 10)	0.05	0.04	24.3 ± 5.2	25.4 ± 7.6	-5
Oesophagus (S10, 20)	0.05	0.04	25.0 ± 0.0	24.9 ± 4.8	0
Liver (S20, 33)	0.05	0.04	19.7 ± 0.3	21.8 ± 3.5	-11
Stomach (S22, 43)	0.12	0.12	10.8 ± 1.8	8.6 ± 1.2	20
Colon (S28, 68)	0.12	0.12	ND	ND	-
Ovaries (S31,117)	0.20	0.08	ND	ND	-
Bladder (S31, 44)	0.05	0.04	ND	ND	-
Bone surface (S29, 135)	0.01	0.01	ND	ND	-
Red bone marrow (S22, 130)	0.12	0.12	6.2 ± 0.5	6.8 ± 0.8	-10
Skin (S16, surface)	0.01	0.01	22.4 ± 5.1	21.7 ± 3.9	3
Remainder organs, ICRP 60, w_T=0.05					
Thymus (S14,20)			27.4	27.1	1
Spleen (S23, 150)			4.0	5.2	-30
Adrenals (S22, 100)			7.1	8.2	-16
Kidney (S23, 120)			5.5	5.7	-4
Pancreas (S23, 50)			4.2	4.8	-14

Small intestine (S23, 80)	4.8	4.7	2
Uterus (S31, 125)	ND	ND	-
Remainder organs, ICRP 103, w_T=0.12			
Adrenals (S22, 100)	7.1	8.2	-16
Gall bladder (S21, 70)	14.9	15.2	-2
Heart (S16,30)	22.4	21.9	2
Kidney (S23, 120)	5.5	5.7	-4
Pancreas (S23, 50)	4.2	4.8	-14
Small intestine (S23, 80)	4.8	4.7	2
Spleen (S23, 150)	4.0	5.2	-30
Thymus (S14, 20)	27.4	27.1	1
Uterus (S31, 125)	ND	ND	

[1]Percentage difference = (MOS*kin* measurement- Film measurement)/MOS*kin* measurement x 100%
[2]ND= Doses were Not Detectable as they were below the low dose detection threshold of both dosimeters, < 2 mGy
[3]Breast dose refers to the average of the surface and chest point dose measurements

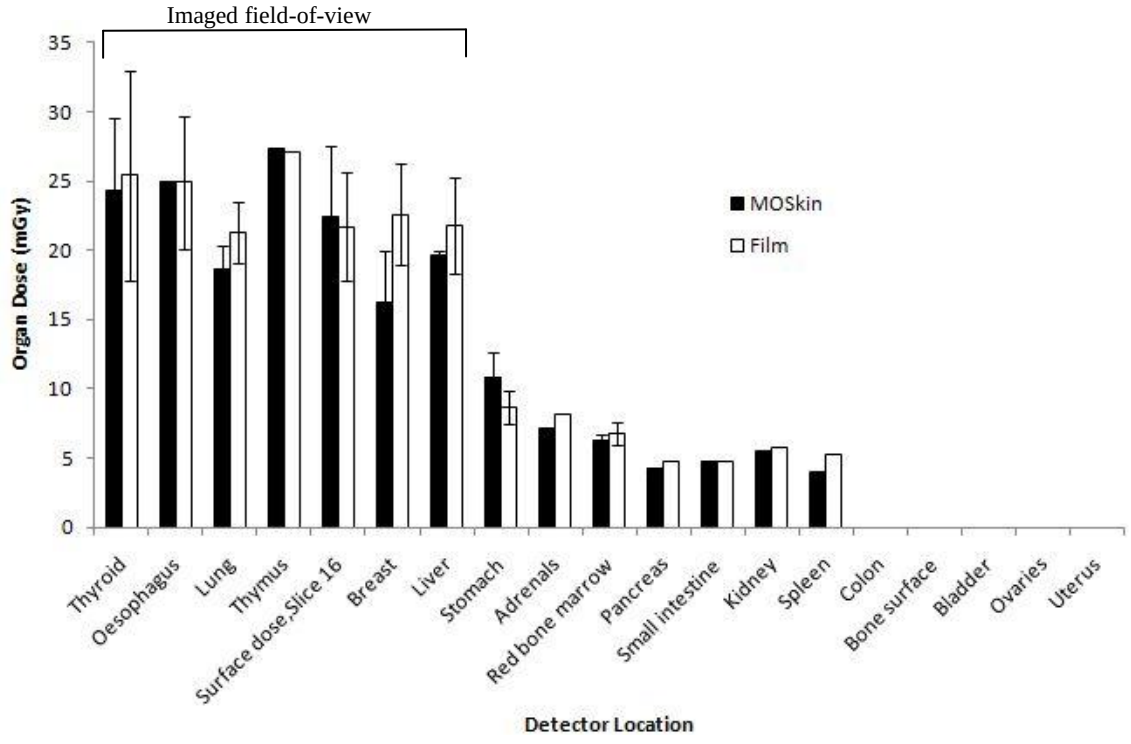

(a)

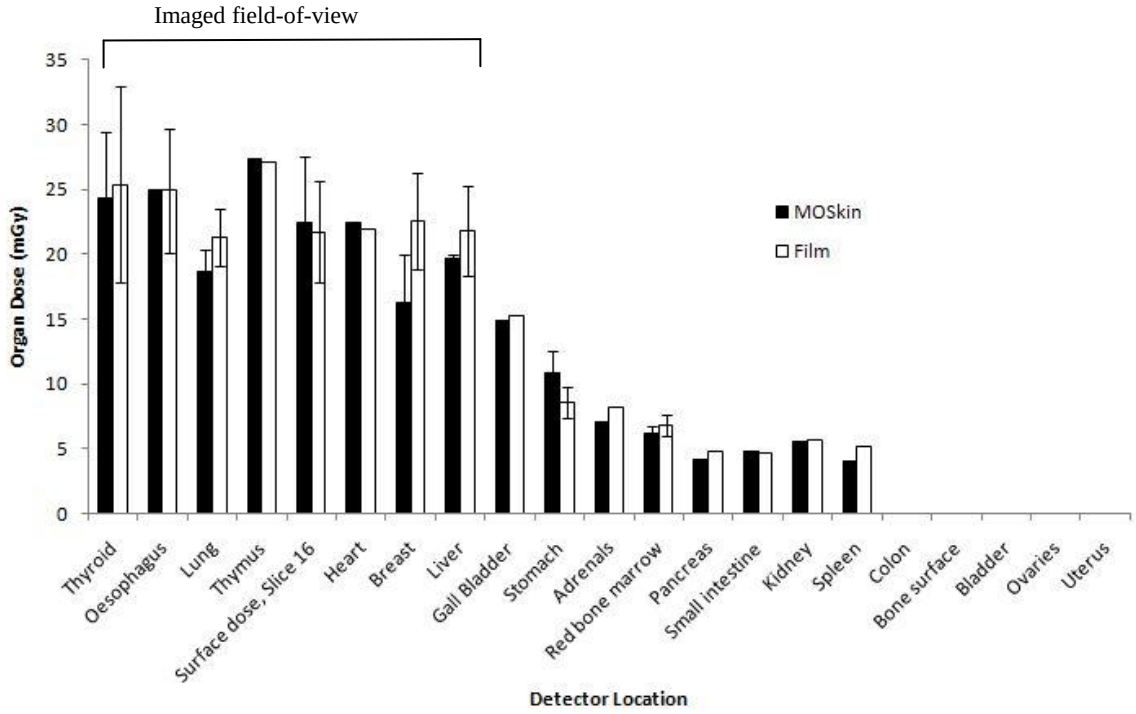

(b)

Figure 8.8: Pulmonary embolus CT imaging scan. Point organ dose measurements obtained with the MOSkin dosimeter and Gafchromic XQ-QA2 film (a) 19 organs of interest, ICRP 60 (b) 21 organs of interest, ICRP 103. Error bars refer to the range of doses obtained with 3 individual point dosimeter readouts.

8.3.2 Evaluation of Effective Dose

Effective dose estimates were calculated by 3 different methods, namely by applying known k-coefficients to the console DLP, using the NRPB-SR250 Monte Carlo derived datasets on a mathematical phantom and by applying ICRP recommended tissue weighting factors to our directly measured organ point doses. The derived effective doses E_{DLP}, E_{MC} and E_{MOSkin}, E_{Film} are shown in Table 8.4 and illustrated in Figure 8.9 for both the renal calculus MSCT scan and the pulmonary embolus MSCT scan.

Table 8.4: Comparison of effective dose calculated by direct and indirect means

	Direct measurements		Indirect means	
Protocol Name	E_{MOSkin} (mSv)	E_{Film} (mSv)	E_{MC} (mSv)	E_{DLP} (mSv)*
Renal calculus	4.0 (ICRP 60) 3.2 (ICRP 103)	4.0 (ICRP 60) 3.2 (ICRP 103)	2.4 (ICRP 60) 2.0 (ICRP 103)	2.1 (EC 2004) 2.7 (ICRP 103)
Pulmonary embolus	9.2 (ICRP 60) 10.6(ICRP 103)	9.8 (ICRP 60) 11.6 (ICRP 103)	6.3 (ICRP 60) 7.5 (ICRP 103)	5.6 (EC 2004) 9.5 (ICRP 103)

*Conversion factors from DLP to effective dose.
[1]ICRP 103 Adult abdominopelvic region, k coefficient= 0.019 mSv mGy^{-1} cm^{-1}
[2]EC 2004 Adult abdominopelvic region, k coefficient=0.015 mSv mGy^{-1} cm^{-1}[211]

[3]ICRP 103 Adult chest region, k coefficient = 0.024 mSv mGy^{-1} cm^{-1}
[4]EC 2004 Adult chest region, k coefficient = 0.014 mSv mGy^{-1} cm^{-1}[211]

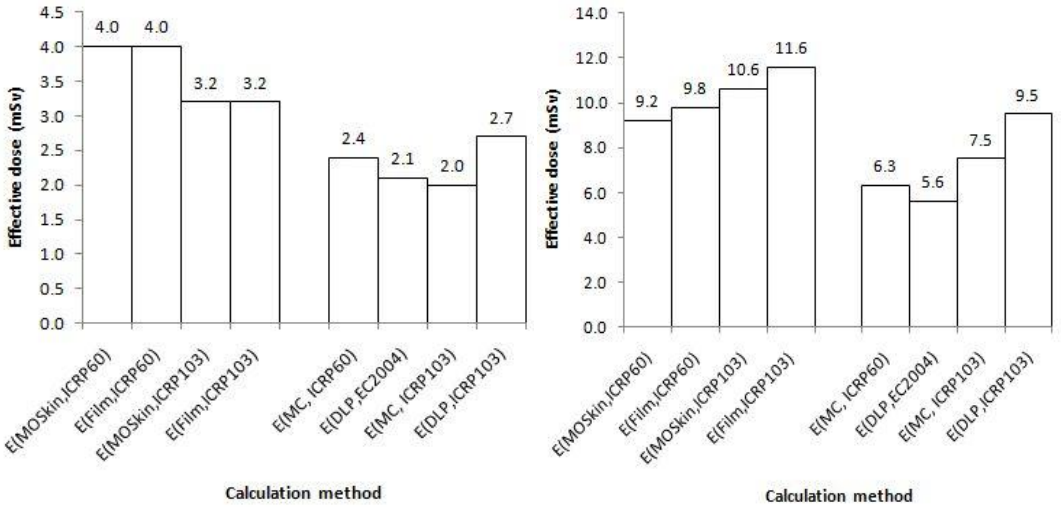

(a) (b)

Figure 8.9: Comparison of effective dose (E) estimates by 3 methods for the (a) renal calculus (b) pulmonary embolus protocol

For both protocols, the derived effective dose E from MO*Skin* and film point dose organ measurements agreed to within ±10% of each other (PE protocol). There was full agreement in the derived effective dose E for MO*Skin* and film organ dose measurements in the RC protocol. This shows that the MO*Skin* and film dosimeters may be used interchangeably in the measurement of point organ doses in anthropomorphic tissue equivalent phantoms with advantage of the MO*Skin* for real time dosimetry. The values of E_{MC} and E_{DLP} under-estimated derived E from measured doses, as expected, due to different phantoms used.

For the RC imaging protocol where the primary imaged field-of-view includes the gonads, there was a -20% difference in derived effective dose E_{103} and E_{60} as a result of the application of ICRP 103 tissue weighting factors (T_w) and ICRP 60 T_w to the various organs of interest. This decrease in value of effective dose, E_{103} is primarily due to the recent decrease in the assigned T_w for gonadal tissue (ovaries in our female anthropomorphic phantom) from 0.20 in ICRP 60 to 0.08 in ICRP 103.

Similarly for the PE protocol where the primary imaged field-of-view includes the female breasts, a +17% difference in E_{103} and E_{60} was due to the recent increase in the assigned T_w of the radiosensitive breast from 0.05 (ICRP 60) to 0.12 (ICRP 103).

The calculated values of both E_{DLP} and E_{MC} were up to 1.9 mSv (62%) and 4.2 mSv (55%) lower than the effective doses E_{60} and E_{103} derived from direct organ point dose measurements with both dosimeters (Figure 8.9) for the RC and PE imaging protocols respectively. This apparent disparity in the derived E values from measurements versus calculations is hardly surprising; given that firstly, the k- conversion coefficient applied is based on data averaged over many scanners, and not specific to this particular scanner model as used in our work. Secondly, different phantoms were used; for our direct organ dose measurements we used a physical anthropomorphic phantom whose organ size and positions would have differed to some extent from that of the geometrical software phantom applied in the NRPB-SR250 data sets.

Moreover, Martin 2007[213] has previously postulated that the inherent uncertainties in estimating relative doses using measured organ doses in an anthropormorphic phantom to a reference patient to be about ±40%. On this basis, the differences in derived values of effective dose E are trivial, mostly because our calculated values were on the same order of magnitude as the measured values.

Finally, the study performed by Hurwitz et al [23] on a 16-slice MSCT scanner (Lightspeed, GE) provides good verification for the effective dose values derived from our study. Their clinical scan protocols were similar to the scan protocols used in our study. They found that the effective dose E_{60} for the renal calculus protocol was 4.5 ± 0.45 mSv in their study, compared to 4.0 mSv obtained in our study. For the pulmonary embolus MSCT protocol, they obtained an E_{60} value of 14.4 ± 2.1 mSv compared to 9.2 mSv in our PE study. As further validation of our organ-based E values, Martin [214] reported that the representative effective doses for medical adult CT scans done in UK hospitals were in the range 5-7 and 5-8 mSv for the chest and abdomen-pelvic region respectively. McCollough consolidated effective doses from previous literature and

found that the effective doses for the chest and abdomen-pelvic region were 5-8 mSv and 8-14 mSv respectively. Our E_{60} and E_{103} values were on the same order of magnitude as expected of these examinations.

8.4 Conclusions

This chapter reports on the application of the MO*Skin* dosimeter and the Gafchromic XR-QA2 film in the direct measurement of absorbed organ point doses in a tissue-equivalent anthropomorphic phantom. Effective doses were derived from the measured organ point doses on 2 commonly applied clinical imaging protocols, namely the renal calculus (RC) protocol and the pulmonary embolus (PE) protocol, on a modern clinical diagnostic 16-slice General Electric MSCT scanner.

Application of the more recent ICRP 103 tissue weighting factors compared to that of the ICRP 60 tissue weighting factors resulted in a difference in the derived effective dose by up to 0.8 mSv (-20%) in the renal calculus protocol and up to 1.8 mSv (18%) in the pulmonary embolus protocol. This may be explained by the reduced radiosensitivity of the gonads and the increased radiosensitivity of breast tissue in the RC and PE imaging protocol respectively, expressed as a difference in the assigned tissue weighting factors of the ICRP 103 and ICRP 60 reports respectively.

Effective doses derived from the Gafchromic XR-QA2 film and the MO*Skin* dosimeter organ point dose measurements were found to agree within 10% of each other, showing that both this type of film and the MO*Skin* dosimeter may be used interchangeably in the assessment of point organ doses in tissue-equivalent phantoms. The MOS*kin* dosimeter, however, presents a major advantage over film due to its real-time readout capability.

Effective doses derived in this research study compared favorably (ie. within the same order of magnitude) with that from existing literature for both CT scan protocols tested. Differences in MSCT scanner design combined with differences in the choice of technical scan parameters made it difficult to truly compare doses across a large body of published literature. However, the doses obtained in this research are helpful for future

scanner protocol optimisation for this particular CT scanner model as well as for the estimation of stochastic health risk to CT patients after taking into account patient specific age-, gender and body habitus.

9 Overall Findings and Conclusions

The MO*Skin* radiation dosimeter is a radiation detector designed at the Centre for Medical Radiation Physics (CMRP), University of Wollongong, Australia. The MO*Skin* detector has a reproducible 70 μm thick tissue-equivalent build up layer which makes this radiation dosimeter suitable for radiological skin dose assessment at the ICRP recommended skin depth of 70 μm. Moreover, its small size and its radiolucence at kilovoltage energies makes this dosimeter suitable for organ dose assessment since its presence does not interfere with diagnostic image quality.

The main purpose of this thesis was to characterise MO*Skin* response at kilovoltage energies by means of Monte Carlo simulations and practical experiments, and subsequently apply the MO*Skin* dosimeter to CT quality assurance and organ point dose measurements.

From the results of our simulation studies in Chapter 4, it was found that the addition of a composite metallic filter resulted in a nearly flat MO*Skin* energy response; an improvement by a factor of up to 2.5 in the photon energy range of 30 keV to 120 keV. It was also found that by increasing the thickness of the overlying polyamide layer of the MO*Skin* dosimeter from an original 20 μm manufacturing thickness to a 70 μm thickness, the energy response of the MO*Skin* dosimeter improved by up to two-fold at low energies of 50 keV. In addition, the MO*Skin* dosimeter was found to be water equivalent at depths up to 60 mm in the solid water phantom for the incident 50 kVp, 100 kVp, 150 kVp and 250 kVp x-ray photon spectra. Within the same spectral energy range, maximum angular response was found to be 8% in the upside-down (180^{o}) worst-case orientation.

From the results of our experimental characterisations in Chapter 5, it was found that with an applied dose of 20 cGy at a tube potential of 150 kVp (0.63 mm Cu HVL), the use of an additional 50 V bias supply resulted in an improvement in MOS*kin* dose sensitivity of 18%, i.e. from 6.7 mV/cGy to 7.9 mV/cGy. MO*Skin* reproducibility was

within ±5% with a coefficient of variation (COV) of 3.7% and batch homogeneity was good with an overall COV of 3.8%. Signal fading was found to be less than 1% over a post-irradiation time interval of 4 minutes that is long enough for real time readout or reasonable delay in readout after irradiation in the clinical scenario. MO*Skin* response was linear with dose; depending on the applied tube potential, the MOS*kin* sensitivity (expressed as the surface dose response factor) decreased with an increase in applied tube potential from 10.6 mV/cGy to 6.7 mV/cGy for applied tube potentials of 50 kVp, 100 kVp and 150 kVp. Throughout dosimeter lifetime (determined to be 10 Gy for kVp diagnostic x-ray case) with accumulated dose, MO*Skin* sensitivity decreased by up to 13% from its initial sensitivity at a tube potential of 150 kVp. For subsequent experimental measurements with the MOS*kin* dosimeter, we recommend that the MO*Skin* dosimeter is re-calibrated for every 2.5 V increase in threshold voltage. MO*Skin* surface energy response was found to vary by as much as a factor of 3 across a tube potential of 50 kVp to 250 kVp. This indicates that MO*Skin* calibrations should be done at a specified beam quality if the MO*Skin* dosimeter is to be accurately applied in clinical dose measurements. Angular response of the MO*Skin* dosimeter was measured to be ± 8% for the 150 kVp photon beam. The MOSkin was also found to be water equivalent at depths up to 60 mm; its depth dose response agreed with the gold-standard Markus ionisation chamber to within 5% for the 150 kVp beam. The results of the depth dose Monte Carlo simulations and the experimental measurements agreed well with each other; average agreement was about 5% at an applied tube potential of 150 kVp.

Chapter 6 demonstrated the application of the Dose Magnifying Glass (DMG) with the MO*Skin* dosimeter in the acquisition of CT dose profiles in a General Electric (GE) clinical diagnostic 16-slice MSCT scanner for 3 CT scan modes; namely single tube rotation, axial and helical mode. The results of this study showed that beam collimation, selected scan mode and helical pitch had a direct effect on the obtained dose profiles. As beam collimation increased, the FWHM measured by the DMG and Gafchromic XR-QA 2 film increased as expected. For a constant collimation, the helical mode compared to the axial mode had a larger FWHM attributed to the larger scatter due to the over-ranging effect associated with the helical scan mode. It was seen

that the MSAD value decreased as pitch increased. Film- and MO*Skin*- acquired dose profiles were generally in good agreement with each other, except at the dose tails where film tended to over-respond by up to 30% for doses less than 10 mGy. The novel combined use of the MO*Skin* dosimeter and DMG presents a future possible solution to the assessment of wider CT cone beam profiles, to overcome the limitation of currently used CT pencil ion chamber dosimeters with their 100 mm length. In addition, the DMG is capable of measuring CTDI and DLP in real time simultaneously with high spatial resolution. Based on the results of this study, a DMG with length 100 mm is recommended for development at CMRP. This will avoid translation of the 25.4 mm length of the current DMG along the scan FOV, resulting in an improved tool for CT QA.

Chapter 7 applied the MO*Skin* dosimeter to radiation protection in chest imaging. As radiosensitive female breast tissue is inadvertently irradiated during chest pulmonary embolus diagnostic scans, implementation of radiation protection measures is necessary. The MO*Skin* dosimeter was applied in the verification of breast tissue point doses to assess the use of automatic tube current modulation and the effect of bismuth shields in breast dose savings. We found from our dosimeter measurements that the use of automatic tube current modulation (ATCM) and breast shields resulted in an average breast dose reduction of 33% and 43% respectively. The combined use of ATCM and breast shields resulted in overall breast dose savings of 64% with no detriment to lung (deeper tissue) image quality.

Chapter 8 applied the MO*Skin* to the measurement of individual organ point doses within a tissue-equivalent anthropomorphic phantom for 2 typical clinical MSCT diagnostic imaging examinations, namely the renal calculus and the pulmonary embolus CT scans. Film measurements agreed with MO*Skin* measurements to within 20% for measured point doses throughout the imaged field-of-view. The results of the derived effective dose obtained from direct organ dose measurements with the MO*Skin* compared very well with existing effective dose values for similar scan protocols published in previous literature.

In conclusion, the successful application of the MO*Skin* in our experimental measurements shows that the MO*Skin* radiation dosimeter is a flexible and robust measurement tool for real-time dose measurements in diagnostic CT following its characterisation. With its real-time readout capabilities, the MO*Skin* dosimeter was shown to be a practical dosimetry tool for the assessment of dose profiles in diagnostic x-ray CT beams towards future CT quality assurance in wide beams and for the measurement of point organ doses in CT scans.

References

1. Angel E, Wellnitz C, Goodsitt M, DeMarco J, Cagnon C, Ghatali M, Cody D, Stevens D, McCollough C, Primak A and McNitt-Gray M, 2007, Radiation dose from MDCT using Monte Carlo simulations: estimating fetal dose due to pulmonary embolism scans accounting for overscan. *Proc. SPIE* 6510.

2. Rydberg J, 2000, Multisection CT: Scanning Techniques and Clinical Applications. *Radiographics* 20 (6), 1787-806.

3. Lewis M, 2005. Radiation dose issues in multi-slice CT scanning: ImPACT technology update No. 3. In. Medicines and Healthcare Products Regulatory Agency.

4. Wallace AB, 2010, The implementation of diagnostic reference levels to Australian radiology practice. *Journal of Medical Imaging and Radiation Oncology* 54, 465-71.

5. UK HPA, 2011. *Scale of UK exposure to X-rays revealed*. Available at: http://www.hpa.org.uk/webw/HPAweb&HPAwebStandard/HPAweb_C/1287147994040?p=1287147958032. Last Accessed: 21 Jan 2011

6. Mettler F, Bhargavan M, Faulkner K, Gilley D, Gray J, Ibbott G, Lipoti J, Mahesh M, McCrohan J, Stabin M, Thomadsen B and Yoshizumi T, 2009, Radiologic and Nuclear Medicine Studies in the United States and Worldwide: Frequency, Radiation Dose, and Comparison with Other Radiation Sources 1950–2007. *Radiology* 253 (2), 520-31.

7. United Nations Scientific Committee on the Effects of Atomic Radiation, 2008, *UNSCEAR Report: Sources and Effects of Ionizing Radiation:Volume 1: Sources-Report to the General Assembly Scientific Annexes A and B*. New York, United Nations.

8. Hall E and Brenner D, 2008, Cancer risks from diagnostic radiology. *Br J Radiol* 81 (965), 362-78.

9. Hricak H, Brenner D, Adelstein S, Frush D, Hall E, Howell R, McCollough C, Mettler F, Pearce M, Suleiman O, Thrall J and Wagner L, 2011, Managing Radiation Use in Medical Imaging: A Multifaceted Challenge. *Radiology* 258 (3), 889-905.

10. Brenner D and Hall E, 2007, Computed Tomography — An Increasing Source of Radiation Exposure. *The New England Journal of Medicine* 357 (22), 2277-84.

11. Brenner DJ, Doll R, Goodhead DT, Hall EJ, Land CE, Little JB, Lubin JH, Preston DL, Preston RJ, Puskin JS, Ron E, Sachs RK, Samet JM, Setlow RB and Zaider M, 2005, Cancer risks attributable to low doses of ionizing radiation: Assessing what we really know. *Proceedings of the National Academy of Sciences of the United States of America* 100 (24), 13761-66.

12. Mettler FA, Huda W, Yoshizumi TT and Mahesh M, 2008, Effective Doses in Radiology and Diagnostic Nuclear Medicine: A Catalog. *Radiology* 248 (1), 254-63.

13. Lewis MA and Edyvean S, 2005, Patient dose reduction in CT *British Journal of Radiology* 78, 880-83.

14. Angel E, Yaghmai N, Jude C, DeMarco J, Cagnon C, Goldin J, Primak A, Stevens D, Cody D, McCollough C and McNitt-Gray M, 2009, Monte Carlo simulations to assess the effects of tube current modulation on breast dose for multidetector CT. *Physics in Medicine and Biology* 54 (3), 497-511.

15. McCollough CH, 2010. *Image Wisely: Diagnostic Reference Levels*. Available at: http://www.imagewisely.org/~/media/ImageWisely%20Files/Medical%20Physicist%20Articles/IW%20McCullough%20Diagnostic%20Reference%20Levels.pdf. Last Accessed: 28 Feb 2011

16. Australian Radiation Protection and Nuclear Safety Agency, *Current Australian National Diagnostic Reference Levels for MDCT*. Available at: http://www.arpansa.gov.au/services/ndrl/current.cfm Last Accessed: 11 Aug 2013

17. Hayton A, Wallace A, Marks P, Edmonds K, Tingey D and P J, 2013, Australian diagnostic reference levels for multi detector computed tomography. *Austral. Phys. Eng. Sci. Med.* 36 (1), 19-26.

18. Frush D, 2004, Computed tomography and radiation: understanding the issues. *Journal of the American College of Radiology* 1 (2), 113-19.

19. Yoshizumi TT and Nelson RC, 2003, Radiation Issues with Multidetector Row Helical CT. *Critical Reviews in Computed Tomography* 44 (2), 95-117.

20. Einstein A, Henzlova M and Rajagopalan S, 2007, Radiation dose to the breast and estimated breast cancer risk in women from 64-slice CT coronary angiography: insights from the Biological Effects of Ionizing Radiation (BEIR) VII report. *Journal of Nuclear Cardiology* 14 (2), S59.

21. Dong S, Chu T, Lee J, Lan G, Wu T, Yeh Y and Hwang J, 2002, Estimation of mean-glandular dose from monitoring breast entrance skin air kerma using a high sensitivity metal oxide semiconductor field effect transistor (MOSFET) dosimeter system in mammography. *Applied Radiation and Isotopes* 57 (6), 791-99.

22. Yilmaz M, Albayram S, Yaşar D, Ozer H, Adaletli I, Selçuk D, Akman C and Altuğ A, 2007, Female breast radiation exposure during thorax multidetector computed tomography and the effectiveness of bismuth breast shield to reduce breast radiation dose. *J Comput Assist Tomogr* 31 (1), 138-42.

23. Hurwitz LM, Yoshizumi TT, Reiman RE, Paulson EK, Frush DP, Nguyen GT, Toncheva GI and Goodman PC, 2006, Radiation Dose to the Female Breast from 16-MDCT Body Protocols. *AJR* 186, 1718-22.

24. Sechopoulos I, Vedantham S, Suryanarayanan S, D'Orsi C and Karellas A, 2008,

Monte Carlo and Phantom Study of the Radiation Dose to the Body from Dedicated CT of the Breast. *Radiology* 247 (1), 98-105.

25. Angel E, Wellnitz C, Goodsitt M, Yaghmai N, DeMarco J, Cagnon C, Sayre J, Cody D, Stevens D, Primak A, McCollough C and McNitt-Gray M, 2008, Radiation Dose to the Fetus for Pregnant Patients Undergoing Multidetector CT Imaging: Monte Carlo Simulations Estimating Fetal Dose for a Range of Gestational Age and Patient Size. *Radiology* 249 (1), 220-27.

26. Brenner DJ, Elliston CD, Hall EJ and Berdon WE, 2001, Estimated Risks of Radiation induced fatal cancer from Pediatric CT. *AJR* 176, 289-96.

27. Sessions J, Roshau J, Tressler M, Hintenlang D, Arreola M, Williams J, Bouchet L and Bolch W, 2002, Comparisons of point and average organ dose within an anthropomorphic physical phantom and a computational model of the newborn patient. *Medical Physics* 29 (6), 1080.

28. McDermott A, White A, Mc-Nitt-Gray M, Angel E and Cody D, 2009, Pediatric organ dose measurements in axial and helical multislice CT. *Medical Physics* 36 (5), 1494.

29. Kleinerman R, 2006, Cancer risks following diagnostic and therapeutic radiation exposure in children. *Pediatric Radiology* 36 (0), 121-25.

30. Slovis TL, 2002, The ALARA Concept in Pediatric CT: Myth or Reality. *Radiology* 223, 5-6.

31. Colombo P, Pedroli G, Nicoloso M, Re S, Valvassori L and Vanzulli A, 2004, Evaluation of the efficacy of a bismuth shield during CT examinations. *Radiol Med* 108 (5-6), 560-8.

32. Mukundan S, Wang P, Frush D, Yoshizumi T, Marcus J, Kloeblen E and Moore M, 2007, MOSFET Dosimetry for Radiation Dose Assessment of Bismuth Shielding of the Eye in Children. *Am. J. Roentgenol.* 188 (6), 1648-50.

33. Perisinakis K, Raissaki M, Theocharopoulos N, Damilakis J and Gourtsoyiannis N, 2005, Reduction of eye lens radiation dose by orbital bismuth shielding in pediatric patients undergoing CT of the head: a Monte Carlo study. *Med Phys* 32 (4), 1024-30.

34. Curtis J, 2010, Computed tomography shielding methods: a literature review. *Radiol Technol* 81 (5), 428-36.

35. Gu J, Bednarz B, Caracappa P and Xu X, 2009, The development, validation and application of a multi-detector CT (MDCT) scanner model for assessing organ doses to the pregnant patient and the fetus using Monte Carlo simulations. *Physics in Medicine and Biology* 54 (9), 2699-717.

36. Kim S, Yoshizumi TT, Toncheva G, Frush D and Yin F-F, 2010, Estimation of

absorbed doses from paediatric cone-beam CT scans: MOSFET measurements and Monte Carlo simulations. *Radiat Prot Dosim* 138 (3), 257-63.

37. U.S-Food-and-Drug-Administration, 2010. *Safety Investigation of CT Brain Perfusion Scans: Update 11/9/2010*. Available at: http://www.fda.gov/MedicalDevices/Safety/AlertsandNotices/ucm185898.htm. Last Accessed: 28 Feb 2011

38. Bogdanich W, 2009. *Radiation Overdoses Point Up Dangers of CT Scans*. Available at: http://www.nytimes.com/2009/10/16/us/16radiation.html. Last Accessed: 23 Aug 2010

39. Cancer Council Australia, *Facts and Figures- Cancer in Australia*. Available at: http://www.cancer.org.au/aboutcancer/FactsFigures.htm. Last Accessed: 21 Nov 2011

40. Berrington de Gonzalez A and Darby S, 2004, Risk of cancer from diagnostic x-rays: estimates for the UK and 14 other countries. *Lancet* 263, 345-51.

41. Board on Radiation Effects Research, 2006, *Health risks from exposure to low levels of ionizing radiation: BEIR VII phase 2*. National Academies Press, Washington, DC.

42. Geleijns J and Wondergem J, 2005, X-ray imaging and the skin: radiation biology, patient dosimetry and observed effects. *Radiat Prot Dosimetry* 114 (1-3), 121-25.

43. National.Cancer.Institute, 2010. *Genetics of Skin Cancer*. Available at: http://www.cancer.gov/cancertopics/pdq/genetics/skin/HealthProfessional/page2 Last Accessed: 28 Feb 2011

44. Charles M, 2004, The skin in radiological protection--recent advances and residual unresolved issues. *Radiat Prot Dosim* 109 (4), 323-30.

45. Allisy-Roberts P and Williams J, 2008, *Farr's Physics for Medical Imaging*. Elsevier Ltd, PA, USA.

46. Scholz M, 2006. Dose Response of Biological Systems to Low- and High-LET Radiation. In: Horowitz Y (Ed.), Microdosimetric Response of Physical and Biological Systems to Low- and High-LET Radiations. Elsevier, Oxford, UK.

47. McCollough CH, Christner JA and Kofler JM, 2010, How Effective is Effective Dose as a Predictor of Radiation Risk? *AJR* 194, 890-6.

48. Bauhs J, Vrieze T, Primak A, Bruesewitz M and McCollough C, 2008, CT Dosimetry: Comparison of Measurement Techniques and Devices. *Radiographics* 28 (1), 245-53.

49. Brisse HJ, Robilliard M, Savignoni A, Pierrat N, Gaboriaud G, Rycke YD, Neuenschwander S, Aubert B and Rosenwald J-C, 2009, Assessment of organ absorbed

doses and estimation of effective doses from pediatric anthropomorphic phantom measurements for multidetector row CT with and without automatic exposure control. *Health Physics* 97 (4), 303-14.

50. Cohnen M, Poll LW, Puettmann C, Ewen K, Saleh A and Mödder U, 2003, Effective doses in standard protocols for multi-slice CT scanning. *European Radiology* 13, 1148-53.

51. Yoshizumi T, Goodman P, Frush D, Nguyen G, Toncheva G, Sarder M and Barnes L, 2007, Validation of Metal Oxide Semiconductor Field Effect Transistor Technology for Organ Dose Assessment During CT: Comparison with Thermoluminescent Dosimetry. *Am. J. Roentgenol.* 188 (5), 1332-36.

52. Lee R, Thomas K, Connolly B, Falkiner M and Gordon C, 2009, Effective dose estimation for pediatric voiding cystourethrography using an anthropomorphic phantom set and metal oxide semiconductor field-effect transistor (MOSFET) technology. *Pediatric Radiology* 39 (6), 608-15.

53. Hurwitz L, Reiman R, Yoshizumi T, Goodman P, Toncheva G, Nguyen G and Lowry C, 2007, Radiation dose from contemporary cardiothoracic multidetector CT protocols with an anthropomorphic female phantom: implications for cancer induction. *Radiology* 245 (3), 742-50.

54. Fujii K, Aoyama T, Yamauchi-Kawaura C, Koyama S, Yamauchi M, Ko S, Akahane K and Nishizawa K, 2009, Radiation dose evaluation in 64-slice CT examinations with adult and paediatric anthropomorphic phantoms. *British Journal of Radiology* 82, 1010-18.

55. Aoyama T, Koyama S and Kawaura C, 2002, An in-phantom dosimetry system using pin silicon photodiode radiation sensors for measuring organ doses in x-ray CT and other diagnostic radiology. *Medical physics* 29 (7), 1504-10.

56. Kawaura C, Aoyama T, Koyama S, Achiwa M and Mori M, 2006, Organ and effective dose evaluation in diagnostic radiology based on in-phantom dose measurements with novel photodiode-dosemeters. *Radiat Prot Dosimetry* 118 (4), 421-30.

57. Li X, Samei E, Segars WP, Sturgeon GM, Colsher JG, Toncheva G, Yoshizumi TT and Frush DP, 2011, Patient-specific radiation dose and cancer risk estimation in CT: Part I. Development and validation of a Monte Carlo program. *Medical Physics* 38 (1).

58. Li X, Samei E, Segars WP, Sturgeon GM, Colsher JG, Toncheva G, Yoshizumi TT and Frush DP, 2011, Patient-specific radiation dose and cancer risk estimation in CT: Part II. Application to patients. *Medical Physics* 38 (1).

59. DeMarco J, Cagnon C, Cody D, Stevens D, McCollough C, Zankl M, Angel E and McNitt-Gray M, 2007, Estimating radiation doses from multidetector CT using Monte Carlo simulations: effects of different size voxelized patient models on magnitudes of

organ and effective dose. *Physics in Medicine and Biology* 52 (9), 2583-97.

60. Jarry G, DeMarco J, Beifuss U, Cagnon C and McNitt-Gray M, 2003, A Monte Carlo-based method to estimate radiation dose from spiral CT: from phantom testing to patient-specific models. *Physics in medicine and biology* 48 (16), 2645-63.

61. DeMarco J, Cagnon C, Cody D, Stevens D, McCollough C, O'Daniel J and McNitt-Gray M, 2005, A Monte Carlo based method to estimate radiation dose from multidetector CT (MDCT): cylindrical and anthropomorphic phantoms. *Physics in Medicine and Biology* 50 (17), 3989-4004.

62. International_Commission_on_Radiological_Protection, 1977, *Recommendations of the International Commission on Radiological Protection: ICRP Publication no. 26*. Pergamon Press, Oxford, UK.

63. ICRP, 1991, 1990 recommendations of the International Commission on Radiological Protection. *Ann ICRP; 21; publication no. 60*.

64. ICRP, 2007, 2007 recommendations of the International Commission on Radiological Protection. *Ann ICRP; 37; publication no. 103*.

65. Jones DG and Shrimpton PC, *NRPB-SR250: Normalised Organ Doses for X-Ray Computed Tomography Calculated Using Monte Carlo Techniques*. Available at: http://www.hpa.org.uk/Publications/Radiation/Software/softwareNRPBSR250NormalisedOrganDosesforXRay/. Last Accessed: 3 Mar 2011

66. Petoussi-Henss N, Zankl M, Fill U and Regulla D, 2001, The GSF family of voxel phantoms. *Physics in Medicine and Biology* 47 (1).

67. Zaidi H and Ay M, 2007, Current status and new horizons in Monte Carlo simulation of X-ray CT scanners. *Medical and Biological Engineering and Computing* 45 (9), 809-17.

68. Zhang D, Zankl M, DeMarco JJ, Cagnon CH, Angel E, Turner AC and McNitt-Gray MF, 2009, Reducing radiation dose to selected organs by selecting the tube start angle in MDCT helical scans: A Monte Carlo based study. *Medical Physics* 36 (12), 5654-64.

69. Rodrigues P, 2004, Application of GEANT4 radiation transport toolkit to dose calculations in anthropomorphic phantoms. *Applied Radiation and Isotopes* 61 (6), 1451-61.

70. International Atomic Energy Agency, 2007. Technical Reports Series no. 457 Dosimetry in Diagnostic Radiology: An International Code of Practice. In, Vienna.

71. Frush D and Yoshizumi T, 2006, Conventional and CT angiography in children: dosimetry and dose comparisons. *Pediatric Radiology* 36 (0), 154-58.

72. Jessen K, Shrimpton P, Geleijns J, Panzer W and Tosi G, 1999, Dosimetry for optimisation of patient protection in computed tomography. *Appl Radiat Isot* 50, 165-72.

73. Committee to Assess Health Risks from Exposure to Low Levels of Ionizing Radiation NRC, 2006, *Health Risks from Exposure to Low Levels of Ionizing Radiation: BEIR VII Phase 2*. The National Academies Press, Washington D.C.

74. Mosman KL, 2007, *Radiation Risks in Perspective*. Taylor & Francis, FL, USA.

75. Mothersill C and Seymour C, 2004, Radiation-induced bystander effects and adaptive responses?the Yin and Yang of low dose radiobiology? *Mutation Research/Fundamental and Molecular Mechanisms of Mutagenesis* 568 (1), 121-28.

76. Einstein A, Henzlova M and Rajagopalan S, 2007, Estimating risk of cancer associated with radiation exposure from 64-slice computed tomography coronary angiography. *JAMA : the journal of the American Medical Association* 298 (3), 317-23.

77. Abadi S, Mehrez H, Ursani A, Parker M and Paul N, 2011, Direct Quantification of Breast Dose During Coronary CT Angiography and Evaluation of Dose Reduction Strategies. *Medical Physics and Informatics* 196, 152-8.

78. Schonfeld S, Lee C and Gonzalez ABd, 2011, Medical Exposure to Radiation and Thyroid Cancer. *Clinical Oncology*.

79. Cardis E, Vrijheid M, Blettner M, Gilbert E, Hakama M, Hill C, et al., 2007, The 15-Country Collaborative Study of Cancer Risk Among Radiation Workers in the Nuclear Industry: estimates of radiation related cancer risks. *Radiation Research* 167 (4), 396-416.

80. International_Commission_on_Radiological_Protection, 2007, Recommendations of the International Commission on Radiological Protection: Publication no. 103. *Ann ICRP 2007* 37.

81. Brenner D, 1999, Does fractionation decrease the risk of breast cancer induced by low LET radiation? *Radiation Research* 151 (2), 225-9.

82. Preston D, Ron E, Tokuoka S, Funamoto S, Nishi N, Soda M, Mabuchi K and Kodama K, 2007, Solid cancer incidence in atomic bomb survivors: 1958-1998. *Radiation Research* 168 (1), 1-64.

83. Mazonakis M, Tzedakis A, Damilakis J and Gourtsoyiannis N, 2007, Thyroid dose from common head and neck CT examinations in children: is there an excess risk for thyroid cancer induction? *Eur Radiol* 17, 1352-57.

84. ICRP, 2002, *Managing patient dose in computed tomography ICRP Publication 87*. Elsevier Science, Oxford, UK.

85. Pearce MS, Salotti JA, Little MP, McHugh K, Lee C, Kim KP, Howe NL, Ronckers CM, Rajaraman P, Sir Craft AW, Parker L and Berrington de González A, 2012, Radiation exposure from CT scans in childhood and subsequent risk of leukaemia and brain tumours: a retrospective cohort study. *Lancet* 380 (9840), 499-505.

86. Mathews JD, Forsythe AV, Brady Z, Butler MW, Goergen SK, Byrnes GB, Giles GG, Wallace AB, Anderson PR, Guiver TA, McGale P, Cain TM, Dowty JG, Bickerstaffe AC and Darby SC, 2013, Cancer risk in 680 000 people exposed to computed tomography scans in childhood or adolescence: data linkage study of 11 million Australians. *BMJ* 346.

87. Rehani MM, *Smart Protection*. Available at: http://www.iaea.org/Publications/Magazines/Bulletin/Bull502/50205813137.html. Last Accessed: 21 Mar 2011

88. Currie B, 2009, Determining superficial dosimetry for the internal canthus from the Monte Carlo simulation of kV photon and MeV electron beams. *Austral Phys Eng Sci Med* 32 (2), 68-80.

89. Tobias J and Hochhauser D, 2010, *Cancer and its management*. John Wiley and Sons.

90. Panizzon RG, 2006. Basal Cell and Squamous Cell Carcinoma-Radiotherapeutic Approaches. In, Basel, Karger, pp. 38-49.

91. Amdur RJ, Kalbaugh KJ, Ewald LM, Parsons GT, Mendenhall WM, J.Bova F and Million RR, 1992, Radiation therapy for skin cancer near the eye: kilovoltage x-rays versus electrons. *International Journal of Radiation Oncology Biology and Physics* 23, 769-79.

92. Sabol J and Weng P-s, 1995, *Introduction to Radiation Protection Dosimetry*. World Scientific Co. Pte. Ltd., Singapore.

93. Turner JE, 2007, *Atoms, Radiation and Radiation Protection*. Wiley-VCH, Verlag GmbH & Co. KGaA, Weinheim.

94. Attix F, 1986, *Introduction to radiological physics and radiation dosimetry*. John Wiley & Sons, Inc., Germany.

95. Mobit P, Mayles P and Nahum A, 1996, The quality dependence of LiF TLD in megavoltage photon beams: Monte Carlo simulation and experiments. *Physics in Medicine and Biology* 41 (3), 387-98.

96. Johns HE and Cunningham JR, 1983, *The Physics of Radiology*. Charles C Thomas, Springfield, Illinois, USA.

97. Shope T, Gagne R and Johnson G, 1981, A Method for Describing the Doses Delivered by Transmission X-ray Computed Tomography *Medical Physics* 8, 488-95.

98. Nakonechny K, Fallone B and Rathee S, 2005, Novel methods of measuring single scan dose profiles and cumulative dose in CT. *Medical Physics* 32 (1), 98-109.

99. Zhou H and Boone J, 2008, Monte Carlo evaluation of CTDI in infinitely long cylinders of water, polyethylene and PMMA with diameters from 10mm to 500mm. *Medical Physics* 35 (6), 2424.

100. International Electrotechnical Commission, 2002, *International Standard IEC 60601-2-44 Edition 2.1, Medical electrical equipment – Part 2-44: Particular requirements for the safety of X-ray equipment for computed tomography*.

101. Hoeschen C, Regulla D, Zankl M, Schlattl H and Brix G, 2009. Radiation Exposure and Protection in Multislice CT. In: Reiser M, Becker C, Nikolaou K, Glazer G (Eds.), Multislice CT. Berlin, Heidelberg.

102. Dixon R, 2003, A new look at CT dose measurement: Beyond CTDI. *Medical Physics* 30 (6), 1272-80.

103. Brenner DJ and McCollough CH, 2006, Point/Counterpoint: It is time to retire the computed tomography dose index (CTDI) for CT quality assurance and dose optimization. *Medical Physics* 33 (5), 1189-91.

104. International Atomic Energy Agency, Division of Human Health and Dosimetry and Medical Radiation Physics, 2007. *Radiation Oncology Physics Handbook*. Available at: http://www-naweb.iaea.org/nahu/dmrp/syllabus.shtm. Last Accessed: 19 Apr 2011

105. Gregory K, Bibbo G and Pattison J, 2005, A Standard Approach to Measurement Uncertainties for Scientists and Engineers in Medicine. *Australasian Physical & Engineering Sciences in Medicine* 28 (2), 131-39.

106. Jones A, Pazik F, Hintenlang D and Bolch W, 2005, MOSFET dosimeter depth-dose measurements in heterogeneous tissue-equivalent phantoms at diagnostic energies. *Medical Physics* 32 (10), 3209-13.

107. Eklund K and Ahnesjö A, 2009, Modeling silicon diode energy response factors for use in therapeutic photon beams. *Phys Med Biol* 54 (20), 6135-50.

108. Griessbach I, Lapp M, Bohsung J, Gademann G and Harder D, 2005, Dosimetric characteristics of a new unshielded silicon diode and its application in clinical photon and electron beams. *Med Phys* 32 (12), 3750-4.

109. Yin Z, Hugtenburg R and Beddoe A, 2004, Response corrections for solid-state detectors in megavoltage photon dosimetry. *Phys Med Biol* 49 (16), 3691-702.

110. Saini AS and Zhu TC, 2007, Energy dependence of commercially available diode detectors for in-vivo dosimetry. *Medical Physics* 34 (5), 1704-11.

111. Jursinic P, 2009, Angular dependence of dose sensitivity of surface diodes. *Medical Physics* 36 (6), 2165.

112. Qi Z, Deng X, Huang S, Zhang L, He Z, Li A, Kwan I, Lerch M, Cutajar D, Metcalfe P and Rosenfeld A, 2009, In vivo verification of superficial dose for head and neck treatments using intensity-modulated techniques. *Medical Physics* 36 (1), 59-70.

113. Cheung T, Butson MJ and Yu PKN, 2009, Energy dependence corrections to MOSFET dosimetric sensitivity. *Austral. Phys. Eng. Sci. Med.* 32 (1), 16-20.

114. Roshau J and Hintenlang D, 2003, Characterization of the Angular response of an "isotropic" MOSFET dosimeter. *Health Physics* 84 (3), 376-79.

115. Mobit PN and Kron T, 2006. Applications of Thermoluminscent Dosimeters in Medicine. In: Horowitz Y (Ed.), Microdosimetric Response of Physical and Biological Systems to Low- and High-LET Radiations. Elsevier, Oxford, UK.

116. Davis S, Ross C, Mobit P, Van der Zwan L, Chase W and Shortt K, 2003, The response of LiF thermoluminescence dosemeters to photon beams in the energy range from 30 kV x rays to Co-60 gamma rays. *Radiation protection dosimetry* 106 (1), 33-43.

117. Butson MJ, Yu PKN, Cheung T and Alnawaf H, 2010, Energy response of the new EBT2 radiochromic film to x-ray radiation. *Radiation Measurements* 45, 836-39.

118. Butson MJ, Cheung T and Yu P, 2006, Weak energy dependence of EBT gafchromic film dose response in the 50 kVp–10MVp X-ray range. *Applied Radiation and Isotopes* 64 (1), 60-2.

119. Fletcher CL and Mills JA, 2008, An assessment of GafChromic film for measuring 50 kV and 100 kV percentage depth dose curves. *Phys. Med. Biol.* 53, 209-18.

120. Chiu-Tsao S-T, Ho Y, Shankar R, Wang L and Harrison L, 2005, Energy dependence of response of new high sensitivity radiochromic films for megavoltage and kilovoltage radiation energies. *Med Phys* 32 (11), 3350.

121. Rampado O, Garelli E, Deagostini S and Ropolo R, 2006, Dose and energy dependence of response of Gafchromic XR-QA film for kilovoltage x-ray beams. *Physics in Medicine and Biology* 51 (11), 2871-81.

122. Yukihara EG, Ruan C, Gasparian P, Clouse WJ, Kalavagunta C and Ahmad S, 2009, An optically stimulated luminescence system to measure dose profiles in x-ray computed tomography. *Phys. Med. Biol.* 54, 6337-52.

123. Reft CS, 2009, The energy dependence and dose response of a commercial optically stimulated luminescent detector for kilovoltage photon, megavoltage photon, and electron, proton, and carbon beams. *Medical Physics* 36 (5), 1690-99.

124. Yukihara E and McKeever S, 2008, Optically stimulated luminescence (OSL) dosimetry in medicine. *Physics in Medicine and Biology* 53, R351-79.

125. Agyingi E, Mobit P and Sandison G, 2005, Energy response of an Aluminium Oxide detector in kilovoltage and megavoltage photon beams: An EGSnrc Monte Carlo Simulation Study. *Radiat Prot Dosimetry* 118 (1), nci329-31.

126. Glennie D, Connolly B and Gordon C, 2008, Entrance skin dose measured with MOSFETs in children undergoing interventional radiology procedures. *Pediatric Radiology* 38 (11), 1180-87.

127. Meyer P, Regal R, Jung M, Siffert P, Mertz L and Constantinesco A, 2001, Feasibility of a semiconductor dosimeter to monitor skin dose in interventional radiology. *Medical Physics* 28 (10), 2002.

128. Thierry-Chef I, Simon S and Miller D, 2006, Radiation dose and cancer risk among pediatric patients undergoing interventional neuroradiology procedures. *Pediatric Radiology* 36 (0), 159-62.

129. *Unfors Instruments- Patient Skin Dose measurements in fluoro and CT*. Available at: http://www.unfors.com/products.php?catid=74. Last Accessed: 25 Mar 2011

130. Vano E, Ubeda C, Leyton F, Miranda P and Gonzalez L, 2009, Staff Radiation Doses in Interventional Cardiology: Correlation With Patient Exposure. *Pediatric Cardiology* 30 (4), 409-13.

131. Best Medical Canada Ltd, 2007-2011. *Best Medical Canada- MOSFET dosimetry*. Available at: http://www.mosfet.ca/products/dosimeters.htm. Last Accessed: 30 Mar 2011

132. Landauer Inc, 2008. *Landauer OSL dosimetry*. Available at: http://www.osldosimetry.com/applications/medical.asp. Last Accessed: 30 Mar 2011

133. Al-Senan R, Hatab M and Mueller D, 2010, SU-GG-I-66: Measuring Thyroid Dose for a Multi-Slice CT Scanner with OSL, TLD, and ImPACT in an Anthropomorphic Phantom and Teenage Patients. *Medical Physics* 37 (6), 3116.

134. Lu Z, So J, Dutta A and Nickoloff E, 2010, SU-GG-I-07: Monitoring Radiation Dose in Cerebral CT Perfusion Exams *Medical Physics* 37, 3102.

135. RTI Electronics, *CT Dose Profiler*. Available at: http://www.rti.se/products/accessories/ct-dose-profiler/. Last Accessed: 31 Mar 2011

136. L. Herrnsdorfa, M. Björka, Cederquista B, Mattssonb CG, Thungströmb G and Fröjdhb C, 2009, Point dose profile measurements using solid-state detectors in characterization of Computed Tomography systems *Nuclear Instruments and Methods in Physics Research Section A: Accelerators, Spectrometers, Detectors and Associated Equipment* 607 (1), 223-25.

137. Bower MW and Hintenlang DE, 1998, The Characterization of a commercial MOSFET dosimeter system for use in diagnostic x-ray. *Health Physics* 75 (2), 197-204.

138. Pomije B, Huh C, Tressler M, Hintenlang D and Bolch W, 2001, Comparison of Angular free-in-air and Tissue Equivalent phantom response measurements in p-MOSFET dosimeters. *Health Physics* 80 (5), 497???505.

139. Edwards CR, Green S, Palethorpe JE and Mountford PJ, 1997, The response of a MOSFET, p-type semiconductor and LiF TLD to quasi-monoenergetic x-rays. *Phys. Med. Biol.* 42, 2383-91.

140. Dong S, Chu T, Lan G, Wu T, Lin Y and Lee J, 2002, Characterization of high-sensitivity metal oxide semiconductor field effect transistor dosimeters system and LiF:Mg,Cu,P thermoluminescence dosimeters for use in diagnostic radiology. *Appl Radiat Isot.* 57 (6), 883-91.

141. Benevides LA and Hintenlang DE, 2006, Characterization of metal oxide semiconductor field effect transistor dosimeters for application in clinical mammography. *Medical Physics* 33 (2), 514-20.

142. Kron T, Duggan L, Smith T, Rosenfeld A, Butson M, Kaplan G, Howlett S and Hyodo K, 1998, Dose response of various radiation detectors to synchrotron radiation. *Phys. Med. Biol.* 43, 3235-59.

143. Wang B, Kim CH and Xu XG, 2003, Monte Carlo modeling of the MOSFET dosimeter and its application. *Trans. Am. Nucl. Soc.* 88, 218-20.

144. Wang B, Kim CH and Xu XG, 2004, Monte Carlo modeling of a high-sensitivity MOSFET dosimeter for low- and medium-energy photon sources. *Med Phys.* 31 (5), 1003-08.

145. Wang B, Xu XG and Kim CH, 2005, Monte Carlo study of MOSFET dosemeter characteristics: dose dependence on photon energy, direction and dosemeter composition. *Radiat. Prot. Dosim.* 113 (1), 40-46.

146. Lavallee M-C, Gingras L and Beaulieu L, 2006, Energy and integrated dose dependence of MOSFET dosimeter sensitivity for irradiation energies between 30kV and Co-60. *Medical Physics* 33 (10), 3683.

147. Gladstone DJ, Lu XQ, Humm JL, Bowman HF and Chin LM, 1994, A miniature MOSFET radiation dosimeter probe *Med. Phys. 21, 1721* 21 (11), 1721-28.

148. Peet DJ and Pryor MD, 1999, Evaluation of a MOSFET radiation sensor for the measurement of entrance surface dose in diagnostic radiology. *British Journal of Radiology* 72, 562-68.

149. Cheung T, Butson MJ and Yu PKN, 2003, MOSFET dosimetry in-vivo at

superficial and orthovoltage x-ray energies. *Austral. Phys. Eng. Sci. Med.* 24 (2), 81-83.

150. Holmes-Siedle A, 1974, The space charge dosimeter. *Nucl. Instrum. Methods* 121, 169-79.

151. Rosenfeld A, 2007, Electronic dosimetry in radiation therapy. *Radiation Measurements* 41, S134-53.

152. Freeman R and Holmes-Siedle A, 1978, A simple model for predicting radiation effects in MOS devices. *IEEE Trans. Nucl. Sci.* NS-25-6, 1216-25.

153. Ravotti F, M G, Rosenfeld AB, Lerch MLF, Holmes-Siedle A and Sarrabayrouse G, 2007, Radiation monitoring in mixed environments in CERN: from the IRRAD6 facility to the LHC experiments. *IEEE Trans. Nucl. Sci.* 54, 1170-77.

154. Rosenfeld AB, Carolan MG, Kaplan GI, J.Allen B and Khivrich VI, 1995, MOSFET Dosimeters: The Role of Encapsulation on Dosimetric Characteristics in Mixed Gamma-Neutron and Megavoltage X-ray Fields. *IEEE Trans. Nucl. Sci* 42 (6), 1870-77.

155. Qi ZY, Deng XW, Huang SM, Lu J, Lerch MLF, Cutajar D and Rosenfeld AB, 2007, Verification of the plan dosimetry for high dose rate brachytherapy using metal oxide semiconductor field effect transistor detectors. *Med Phys* 34, 2007-13.

156. Kwan IS, Wilkinson D, Cutajar D, Lerch M, Rosenfeld A, Howie A, Bucci J, Chin Y and Perevertaylo VL, 2009, The effect of rectal heterogeneity on wall dose in high dose rate brachytherapy. *Med Phys* 36 (1), 224-32.

157. Hardcastle N, Soisson E, Metcalfe P, Rosenfeld A and Tome W, 2008, Dosimetric verification of helical tomotherapy for total scalp irradiation. *Medical physics* 35 (11), 5061-68.

158. Zilio Vr, Joneja O, Popowski Y, Rosenfeld A and Chawla R, 2006, Absolute depth-dose-rate measurements for an Ir192 HDR brachytherapy source in water using MOSFET detectors. *Medical Physics* 33 (6), 1532.

159. Verhaegen F, Lemire M, Hallil A and Hegyi G, 2008, Surface dosimetry in a CT scanner using MOSFET detectors and Monte Carlo simulations. *Journal of Physics: Conference Series* 102 (1), 012026.

160. Sarrabayrouse G and Siskos S, 2002, Radiation dose measurment using MOSFETs. *Instrumentation & Measurement Magazine, IEEE* 1 (2), 26-34.

161. Desendorfer PV and Ma TP, 1989, *Effect of Radiation on MOS*. Wiley, NY.

162. Soubra M, Cygler J and Mackay G, 1994, Evaluation of a dual bias dual metal oxide-silicon semiconductor field effect transistor detector as radiation dosimeter. *Medical physics* 21 (4), 567-72.

163. Ensell G, Holmes-Siedle A and Adams L, 1988, Thick oxide pMOSFET dosimeters for high energy radiation. *Nucl. Instrum. Methods A* 269, 655-58.

164. P.G. Litovchenko, L.I. Barabash, A.B. Rosenfeld, V.I. Khivrich, O.S. Zinets, V.I. Kuts, I.A. Marusan, V.I. Petrov, G.F. Sluchenkov, G.N. Koval, V.I. Fominych, L.F. Belovodskiy, Dumik AI and Kiblik VY, 1990, MOS structure for emergency gamma and proton dosimetry. *Radiat. Prot. Dosim.* 33, 179-82.

165. Marre D and Marinello G, 2004, Comparison of p-type commercial electron diodes for in vivo dosimetry. *Medical Physics* 31 (1), 50-56.

166. Bower MW and Hintenlang DE, 1998, The characterization of a commercial MOSFET dosimeter system for use in diagnostic x ray. *Health Physics* 75, 197-204.

167. Lemire M, 2006. Accurate Surface Dose Measurements in CT Examinations using High Sensitivity MOSFET Dosimeters Calibrated by Monte Carlo Simulations. In, Medical Physics Unit. McGill University, Montreal, Quebec, Canada.

168. Rosenfeld AB, Lerch MLF, Kron T, Brauer-Krisch E, Bravin A, Holmes-Siedle A and Allen BJ, 2001, Feasibility study of online high-spatial-resolution MOSFET dosimetry in static and pulsed x-ray radiation fields. *IEEE Trans. Nucl. Sci.* 48 (6), 2061-68.

169. Ristic G, 2009, Thermal and UV annealing of irradiated pMOS dosimetric transistors. *Journal of Physics D: Applied Physics* 42 (13), 1-12.

170. Ramani R, Russell S and O'Brien P, 1997, Clinical dosimetry using MOSFETs. *International Journal of Radiation Oncology Biology Physics*, 959-64.

171. Buehler MG, Blaes BR, Soli GA and Tardio GR, 1993, On-chip p-MOSFET Dosimetry. *IEEE Trans. Nucl.Sci.* NS-40, 1442–9.

172. Cheung T, Butson M and Yu P, 2004, Effects of temperature variation on MOSFET dosimetry. *Phys Med Biol* 49 (13), N191-N96.

173. Brucker GJ, Kronenberg S and Gentner F, 1995, Effects of package geometry, materials, and die design on energy dependence of pMOS dosimeters. *IEEE Trans. Nucl. Sci.* 42 (1), 33-40.

174. Long DM, Millward DG and Wallace J, 1982, Dose Enhancement Effects in Semiconductor Devices. *IEEE Trans. Nucl. Sci.* 29 (6), 1980-84.

175. Savic Z, Stankovic S, Kovacevic M and Petrovic M, 1996, Energy Dependence of pMOS Dosemeters. *Radiat. Prot. Dosim.* 64, 205-11.

176. Rozenfeld AB, 2008 Radiation Sensor and Dosimeter (MOSkin) PCT/AU2008/000788 PCT/AU2008/000788 Australia.

177. Sutherland J and Rogers D, 2010, Monte Carlo calculated absorbed-dose energy dependence of EBT and EBT2 film. *Medical Physics* 37 (3), 1110-6.

178. Nunn A, Davis S, Micka J and DeWerd L, 2008, LiF:Mg,Ti TLD response as a function of photon energy for moderately filtered x-ray spectra in the range of 20-250 kVp relative to Co-60. *Medical Physics* 35 (5), 1859.

179. Geant4 Collaboration, 2010. *Geant4 User's Guide for Application Developers* Available at: http://geant4.web.cern.ch/geant4/UserDocumentation/UsersGuides/ForApplicationDeveloper/html/index.html. Last Accessed: 09 Feb 2011

180. Nowotny R and Hvfer A, 1985. Ein Programm fur die Berechnung von diagnostischen Roentgenspektren. In, Fortschr Roentgenstr. pp. 685-89.

181. Poludniowski G, Landry G, DeBlois F, Evans P and Verhaegen F, 2009, SpekCalc: a program to calculate photon spectra from tungsten anode x-ray tubes. *Physics in Medicine and Biology* 54 (19), N433-N38.

182. ICRP, 1991, The Biological Basis for Dose Limitation in the Skin (ICRP Publication 59). *Ann. ICRP* 22 (2).

183. Lian CPL, Othman MAR, Cutajar D, Butson M, Guatelli S and Rosenfeld AB, 2011, Monte Carlo study of the energy response and depth dose water equivalence of the MOSkin radiation dosimeter at clinical kilovoltage photon energies. *Australasian Physical & Engineering Sciences in Medicine* 34 (2), 273-79.

184. Hughes RC, 1985, Theory of response of radiation sensing field-effect transistors in zero-bias operation. *Journal of Applied Physics* 60 (3), 1216-7.

185. Holmes-Siedle A and Adams L, 1986, RADFET: A review of the use of metal-oxide-silicon devices as integrating dosimeters. *Int J Radiat Applications and Instrumentation. Part C. Radiation Physics and Chemistry* 28 (2), 235-44.

186. Klevenhagen, Aukett R, Harrison R, Moretti C, Nahum A and Rosser K, 1996, The IPEMB code of practice for the determination of absorbed dose for x-rays below 300 kV generating potential (0.035 mm Al - 4 mm Cu HVL; 10 - 300 kV generating potential). *Physics in Medicine and Biology* 41 (12), 2605-25.

187. Healy B, Gibbs A, Murry R, Prunster J and Nitschke K, 2005, Output factor measurements for a kilovoltage x-ray therapy unit. *Australasian Physical and Engineering Sciences in Medicine* 28 (2), 115-21.

188. Hill R, Holloway L and Baldock C, 2005, A dosimetric evaluation of water equivalent phantoms for kilovoltage x-ray beams. *Physics in Medicine and Biology* 50 (21), N331-N44.

189. Reniers B, Verhaegen F and Vynckier S, 2004, The radial dose function of low-energy brachytherapy seeds in different solid phantoms: comparison between calculations with the EGSnrc and MCNP4C Monte Carlo codes and measurements. *Physics in Medicine and Biology* 49 (8), 1569-82.

190. Hill R, Brown S and Baldok C, 2008, Evaluation of the water equivalence of solid phantoms using gamma ray transmission measurements. *Radiation Measurements* 43, 1258-64.

191. Rosenfeld AB, 2007. Electronic Dosimetry based on Solid State Detectors. 3rd Solid State Dosimetry Summer School, July 4-7 2007.

192. Hill R, Mo Z, Haque M and Baldock C, 2009, An evaluation of ionization chambers for the relative dosimetry of kilovoltage x-ray beams. *Medical Physics* 36 (9), 3971-81.

193. Li X, Ma C and Salhani D, 1997, Measurement of percentage depth dose and lateral beam profile for kilovoltage x-ray therapy beams *Phys Med Biol* 42 (12), 2561-8.

194. Ehringfeld C, Schmid S, Poljanc K, Kirisits C, Aiginger H and Georg D, 2005, Application of commercial MOSFET detectors for in vivo dosimetry in the therapeutic x-ray range from 80 kV to 250 kV. *Physics in Medicine and Biology* 50 (2), 289-303.

195. Parker MS, Hui FK, Camacho MA, Chung JK, Broga DW and Sethi NN, 2005, Female Breast Radiation Exposure During CT Pulmonary Angiography. *American Journal of Roentgenology* 185, 1228-33.

196. Geleijns J, Artells MS, Bruin PWd, Mather R, Muramatsu Y and McNitt-Gray MF, 2009, Computed tomography dose assessment for a 160 mm wide, 320 detector row, cone beam CT scanner. *Physics in Medicine and Biology* 54 (3141-59).

197. Wong JHD, Carolan M, Lerch MLF, Petasecca M, Khanna S, Perevertaylo VL, Metcalfe P and Rosenfeld AB, 2010, A silicon strip detector dose magnifying glass for IMRT dosimetry. *Med Phys* 37 (2), 427-39.

198. Wong JHD, Knittel T, Downes S, Carolan M, Lerch MLF, Petasecca M, Perevertaylo VL, Metcalfe P, Jackson M and Rosenfeld AB, 2011, The use of a silicon strip detector dose magnifying glass in stereotactic radiotherapy QA and dosimetry. *Med Phys* 38 (3), 1226-38.

199. Rampado O, Garelli E and Ropolo R, 2009, Computed tomography dose measurements with radiochromic films and a flatbed scanner. *Med Phys* 37 (1), 189-96.

200. International Specialty Products, *Product Specification Sheet- Gafchromic XR Series*. Available at: http://www.gafchromic.com/. Last Accessed: 01 Sept 2011

201. Ebert M, Asad A and Siddiqui S, 2009, Suitability of radiochromic films for dosimetry of low energy x-rays. *Journal of Applied Clinical Medical Physics* 10 (4),

232-40.

202. Brady S, Yoshizumi T, Toncheva G and Frush D, 2010, Implementation of radiochromic film dosimetry protocol for volumetric dose assessments to various organs during diagnostic CT procedures. *Med Phys* 37 (9), 4782-92.

203. Kruger RL, McCollough CH and Zink FE, 2000, Measurement of half-value layer in x-ray CT: A comparison of two noninvasive techniques. *Med Phys* 27 (8), 1915-19.

204. International_Commission_on_Radiological_Protection, 1991, Recommendations of the International Commission on Radiological Protection: Publication no. 60. *Ann ICRP 1991* 21.

205. Anouk P, Nadine A, Douglas FE, Ausrele K, Elisabeth C, Catherine Ns, et al., 2012, Exposure to diagnostic radiation and risk of breast cancer among carriers of BRCA1/2 mutations: retrospective cohort study (GENE-RAD-RISK). *BMJ* 345.

206. Vollmar SV and Kalender WA, 2008, Reduction of dose to the female breast in thoracic CT: a comparison of standard-protocol, bismuth-shielded, partial and tube-current-modulated CT examinations. *European Radiology* 18, 1674-82.

207. Alexandra Quinn, Lois Holloway, Dean Cutajar, Nicholas Hardcastle, Anatoly Rosenfeld and Metcalfe P, 2011, Megavoltage cone beam CT near surface dose measurements: potential implications for breast radiotherapy. *Med Phys* 38, 6222-27.

208. Andrew Kelly, Nicholas Hardcastle, Peter Metcalfe, Dean Cutajar, Alexandra Quinn, Kerwyn Foo, Michael Cardoso, Sheree Barlin and Rosenfeld A, 2011, Surface dosimetry for breast radiotherapy in the presence of immobilisation cast material. *Phys Med Biol* 56, 1001-13.

209. Hurwitz LM, Yoshizumi TT, Goodman PC, Nelson RC, Toncheva G, Nguyen GB, Lowry C and Anderson-Evans C, 2009, Radiation Dose Savings for Adult Pulmonary Embolus 64-MDCT Using Bismuth Breast Shields, Lower Peak Kilovoltage, and Automatic Tube Current Modulation. *American Journal of Roentgenology* 192, 244-53.

210. Christner JA, Kofler JM and H.McCollough C, 2010, Estimating Effective Dose for CT Using Dose–Length Product Compared With Using Organ Doses: Consequences of Adopting International Commission on Radiological Protection Publication 103 or Dual-Energy Scanning. *American Journal of Roentgenology* 194, 881-89.

211. Shrimpton P, 2004, Assessment of patient dose in CT. *EUR. European guidelines for multislice computed tomography funded by the European Commission 2004: contract number FIGMCT2000-20078-CT-TIP. Luxembourg, Luxembourg: European Commission, 2004: Appendix C*.

212. Kieffer SA and Heitzman ER, 1979, *An Atlas of Cross-Sectional Anatomy: Computed Tomography, Ultrasound, Radiography, Gross Anatomy*.

213. Martin C, 2007, Effective dose: how should it be applied to medical exposures? *Br J Radiol* 80, 639-47.

214. Martin C, 2008, Radiation Dosimetry for Diagnostic Medical Exposures. *Radiation Protection Dosimetry* 128 (4), 389-412.

Appendix A: Source Code for the computational model of the MOS*kin*

This appendix contains the source code for the MOS*kin* dosimeter for the essential classes of this software application.

main.cc

```
#include "G4RunManager.hh"
#include "DetectorConstruction.hh"
#include "PhysicsList.hh"
#include "PrimaryGeneratorAction.hh"
#include "G4UIterminal.hh"
#include "G4UItcsh.hh"
#include "G4VisExecutive.hh"
#include "RunAction.hh"

/*the main function*/
int main(int argc, char** argv){

  //construct the default run manager
  G4int seed=41;

  if(argc>=2){
     G4String Arg = argv[1];
     if((Arg != "vis.mac") & (Arg != "vis2.mac"))
       {
         G4String Number = Arg;
         seed = atoi(Number);
       }else if((Arg == "vis.mac") | (Arg == "vis2.mac")){
       seed = time(0);
     }
   }else if(argc==1){
     seed = time(0);
   }

   CLHEP::HepRandom::setTheEngine(new CLHEP::RanecuEngine);
   CLHEP::HepRandom :: setTheSeed(seed);
   G4cout<<"The seed has been set to: "<< seed <<G4endl;


     G4RunManager* rm = new G4RunManager();

 // set mandatory user initialization classes
     DetectorConstruction* detector = new DetectorConstruction();
     rm->SetUserInitialization(detector);
     G4VUserPhysicsList* physics = new PhysicsList();
     rm->SetUserInitialization(physics);
```

```
   rm->Initialize();

//set mandatory user action class
   G4VUserPrimaryGeneratorAction* pga = new PrimaryGeneratorAction();
   rm->SetUserAction(pga);

//set optional user action classes
   G4UserRunAction* ra = new RunAction(detector);
   rm->SetUserAction(ra);

//construct visualization manager
  G4UImanager * UI = G4UImanager::GetUIpointer();

//set visualization
   G4VisManager* visManager = new G4VisExecutive();
   visManager->Initialize();

//if only 1 command line argument, run in interactive mode
   if(argc == 1){
      G4UIsession* session = new G4UIterminal(new G4UItcsh);
      UI->ApplyCommand("/control/execute vis.mac");
      session->SessionStart();
      delete session;
   } else {

//if more than 1 command line argument, run in batch mode
      G4String command = "/control/execute ";//create first part of command
      G4String fileName = argv[1];//second part is the file name that was typ\
ed at the command line
      UI->ApplyCommand(command+fileName);//join the two and pass to the UI ma\
nager for interpretation
   }

/*the memory that was dynamically allocated for the run manager must be freed*/
   delete rm;

   return 0;
}
```

DetectorConstruction.cc

```
//preprocessor directive to include header file with class declarations
#include "DetectorConstruction.hh"
#include "globals.hh"
#include "G4Element.hh"
#include "G4Material.hh"
#include "G4PVPlacement.hh"
#include "G4LogicalVolume.hh"
#include "G4Box.hh"
#include "G4Sphere.hh"
#include "G4Orb.hh"
#include "G4Colour.hh"
#include "G4VisAttributes.hh"
#include "G4ThreeVector.hh"
#include "G4Transform3D.hh"
#include "G4Region.hh"
#include "G4ProductionCuts.hh"
//for sensitive detector definition
#include "SensitiveDetector.hh"
#include "G4SDManager.hh"

//NIST manager
#include "G4NistManager.hh"

//for geometry definition
#include "G4SubtractionSolid.hh"

//constructor / destructor do nothing
DetectorConstruction::DetectorConstruction(){
}

DetectorConstruction::~DetectorConstruction(){
}

G4VPhysicalVolume* DetectorConstruction::Construct(){
  G4Colour  white   (1.0, 1.0, 1.0);
  G4Colour  grey    (0.5, 0.5, 0.5);
  G4Colour  lgrey   (.75, .75, .75);
  G4Colour  red     (1.0, 0.0, 0.0);
  G4Colour  blue    (0.0, 0.0, 1.0);
  G4Colour  cyan    (0.0, 1.0, 1.0);
  G4Colour  magenta (1.0, 0.0, 1.0);
  G4Colour  yellow  (1.0, 1.0, 0.0);
  G4Colour  lblue   (0.20, .50, .85);

//define hydrogen
  G4double A = 1.01 * g/mole;
  G4double Z = 1;
```

```
  G4Element* elH = new G4Element ("Hydrogen", "H", Z, A);

  //define oxygen
  A = 16.0 * g/mole;
  Z = 8;
  G4Element* elO = new G4Element ("Oxygen", "O", Z, A);

  //define nitrogen
  A = 14.0 * g/mole;
  Z = 7;
  G4Element* elN = new G4Element("Nitrogen", "N", Z, A);

//define carbon
  A= 12.011 * g/mole;
  Z= 6;
  G4Element* elC = new G4Element("Carbon", "C", Z, A);

  //define aluminium
  A=26.981538 * g/mole;
  Z=13;
  G4Element*elAl=new G4Element("Aluminium","Al", Z, A);

  //now define a G4Material object called 'water', assign it the attributes of \
water
  //constructor of the G4Material class requires arguments: string containing n\
ame of material, density, number of elements
  G4Material* water = new G4Material("water", 1.0 * g/cm3, 2);
  //now call a method of the G4Material class to add an element to this materia\
l
  water->AddElement(elH,2);
  water->AddElement(elO,1);

  /*now we define air for the world volume*/
  G4Material* air = new G4Material("dry air", 1.20*mg/cm3, 2);
  //specify the percentage (by mass) composition
  air->AddElement(elN, 75*perCent);
  air->AddElement(elO, 25*perCent);

  //define kapton
  G4Material* kapton= new G4Material("kapton", 1.42*g/cm3, 4);
  kapton->AddElement(elH,02.6368*perCent);
  kapton->AddElement(elC,69.1133*perCent);
  kapton->AddElement(elN,07.3270*perCent);
  kapton->AddElement(elO,20.9235*perCent);

  //define epoxy
  G4Material* epoxy = new G4Material("epoxy",1.3*g/cm3, 3);
  epoxy->AddElement(elH, 44);
```

```
   epoxy->AddElement(elC, 15);
   epoxy->AddElement(elO, 7);

 //define alumina
   G4Material* alumina=new G4Material("alumina", 3.97*g/cm3,2);
   alumina->AddElement(elO,47.0749*perCent);
   alumina->AddElement(elAl,52.9251*perCent);

   //define silicon dioxide, Si, Al, Au, Ni from NIST
   G4NistManager* man = G4NistManager::Instance();
   G4Material* SiO2  = man->FindOrBuildMaterial("G4_SILICON_DIOXIDE");
   G4Material* Si  = man->FindOrBuildMaterial("G4_Si");
   G4Material * Cu = man-> FindOrBuildMaterial("G4_Cu");
   G4Material* Al  = man->FindOrBuildMaterial("G4_Al");

   /*the volumes: */

   G4double world_dimx = 40 * cm;
   G4double world_dimy = 40 * cm;
   G4double world_dimz = 30 * cm;

   //solid volume defines the shape and size (dimensions)
   G4Box* world = new G4Box("world_box", world_dimx/2, world_dimy/2,
world_dimz/\
 2);

   //logical volume: has a solid volume as a member, a material
   G4LogicalVolume* logical_world = new G4LogicalVolume(world, air, "world_log",\
  0,0,0);

   //physical volume: G4PVPlacement class, no rotation;at (0,0,0);its logical vo\
 lume;its name;its mothervol;no boolean ops;no magnetic field
   G4VPhysicalVolume* physical_world = new
G4PVPlacement(0,G4ThreeVector(),logic\
 al_world, "world_phys", 0, false, 0);

   //set the visualisation attributes of the world volume
   logical_world->SetVisAttributes(G4VisAttributes::Invisible);

 //-----------------WATER PHANTOM-----------------

   G4double phantom_x = 30 * cm;
   G4double phantom_y = 30 * cm;
   G4double phantom_z = 20 * cm;

   //solid volume defines the shape and size (dimensions)
   G4Box* phantom = new G4Box("phantom_box", phantom_x/2, phantom_y/2,
phantom_z\
```

```
 /2);

   //logical volume: has a solid volume as a member, a material
   G4LogicalVolume* logical_phantom = new G4LogicalVolume(phantom, water,
"phantom_log", 0,0,0);

 //physical volume: G4PVPlacement class, no rotation;at (0,0,0);its logical vo\
 lume;its name;its mothervol;no boolean ops;no magnetic field
   G4VPhysicalVolume* physical_phantom = new
G4PVPlacement(0,G4ThreeVector(0,0,0\
 ),logical_phantom, "phantom_phys", logical_world, false, 0);

   //set the visualisation attributes of the world volume
   logical_phantom->SetVisAttributes(G4VisAttributes(blue));

     //container

  G4double container_x = 20 * cm;
  G4double container_y = 20 * cm;
  G4double container_z = 3 * cm;

 //solid volume defines the shape and size (dimensions)
  G4Box* container = new G4Box("container_box", container_x/2, container_y/2, co\
 ntainer_z/2);

   //logical volume: has a solid volume as a member, a material
  G4LogicalVolume* logical_container = new G4LogicalVolume(container, water, "co\
 ntainer_log", 0,0,0);

   //physical volume: G4PVPlacement class, no rotation;at (0,0,0);its logical vo\
 lume;its name;its mothervol;no boolean ops;no magnetic field
  G4VPhysicalVolume* physical_container = new
G4PVPlacement(0,G4ThreeVector(0,0,\
 8.5* cm),logical_container, "container_phys", logical_phantom, false, 0);

   //set the visualisation attributes of the world volume
   logical_container->SetVisAttributes(G4VisAttributes(blue));


   //===Base layer kapton contact====\
  G4double basecontactlayer_dimx = 2.5 * mm;
   G4double basecontactlayer_dimy = 0.8 * mm;
   G4double basecontactlayer_dimz = 0.02 * mm;

   /*place a base contact layer below substrate*/
   G4Box* basecontactlayer = new G4Box("basecontactlayer_box", basecontactlayer_\
 dimx/2, basecontactlayer_dimy/2, basecontactlayer_dimz/2);
   //argument list for constructor: solid volume, material, name, ???
```

```
   G4LogicalVolume* logical_basecontactlayer = new G4LogicalVolume(basecontactla\
  yer, kapton, "basecontactlayer_log", 0,0,0);
    //argument list for the G4PVPlacement constructor: rotation matrix, position,\
   logical volume, name, mother logical volumer, boolean, copy number
   G4VPhysicalVolume* physical_basecontactlayer = new G4PVPlacement(0,
G4ThreeVe\
  ctor(0.*mm,0.*mm,100.391*mm), logical_basecontactlayer, "basecontactlayer_phys"\
  , logical_world, false, 0);

    //set the visualisation attributes of the gold base contact-blue
    logical_basecontactlayer->SetVisAttributes(G4VisAttributes(G4Colour(yellow)))\
  ;

  //=======Al contact============
    G4double metalcontactlayer_dimx = 0.8 * mm;
    G4double metalcontactlayer_dimy = 0.6 * mm;
    G4double metalcontactlayer_dimz = 0.001 * mm;

    /*place a base contact layer below substrate*/
    G4Box* metalcontactlayer = new G4Box("metalcontactlayer_box",
metalcontactlayer_dimx/2, metalcontactlayer_dimy/2, metalcontactlayer_dimz/2);
    //argument list for constructor: solid volume, material, name, ???
    G4LogicalVolume* logical_metalcontactlayer = new
G4LogicalVolume(metalcontactlayer, Al, "metalcontactlayer_log", 0,0,0);
    //argument list for the G4PVPlacement constructor: rotation matrix, position,\
   logical volume, name, mother logical volumer, boolean, copy number
    G4VPhysicalVolume* physical_metalcontactlayer = new G4PVPlacement(0,
G4ThreeVector(0.*mm,0.*mm,100.3805*mm), logical_metalcontactlayer,
"metalcontactlayer_phys", logical_world, false, 0);

  //set the visualisation attributes of the gold base contact-blue
    logical_metalcontactlayer->SetVisAttributes(G4VisAttributes(G4Colour(white)))
  ;
    //=Alumina (encap/packaging) layer===========
    G4double encap1_dimx = 2.5 * mm;
    G4double encap1_dimy = 0.8 * mm;
    G4double encap1_dimz = 0.38 * mm;

    G4Box* encap1 = new G4Box("encap1_box", encap1_dimx/2, encap1_dimy/2,
encap1_dimz/2);
    //argument list for constructor: solid volume, material, name, ???
    G4LogicalVolume* logical_encap1 = new G4LogicalVolume(encap1, kapton,
"encap1_log", 0,0,0);
    //argument list for the G4PVPlacement constructor: rotation matrix, position,logical
volume, name, mother logical volumer, boolean, copy number
    G4VPhysicalVolume* physical_encap1 = new G4PVPlacement(0,
G4ThreeVector(0.*mm,0.*mm,100.19*mm), logical_encap1, "encap1_phys",
logical_world, false, 0);
```

```
  //set the visualisation attributes of the substrate-grey
    logical_encap1->SetVisAttributes(G4VisAttributes(G4Colour(lblue)));

    //==Epoxy volume=====
    G4double epoxyshell_dimx = 0.81 * mm;
    G4double epoxyshell_dimy = 0.61 * mm;
    G4double epoxyshell_dimz = 0.38 * mm;

    //place a epoxy layer on top of sensitive layer
    G4Box* epoxyshell = new G4Box("epoxyshell_box", epoxyshell_dimx/2,
epoxyshell_dimy/2, epoxyshell_dimz/2);
    //argument list for constructor: solid volume, material, name, ???
    G4LogicalVolume* logical_epoxyshell = new G4LogicalVolume(epoxyshell, epoxy,
"epoxyshell_log", 0,0,0);
    //argument list for the G4PVPlacement constructor: rotation matrix, position,\
   logical volume, name, mother logical volumer, boolean, copy number
    G4VPhysicalVolume* physical_epoxyshell = new G4PVPlacement(0,
G4ThreeVector(0*mm,0*mm,0*mm), logical_epoxyshell, "epoxyshell_phys",
logical_encap1, false, 0);

    //set the visualisation attributes of the epoxy- magenta
    logical_epoxyshell->SetVisAttributes(G4VisAttributes(G4Colour(magenta)));

    //==Si substrate layer======
```

```
  G4double substrate_dimx = 0.8 * mm;
    G4double substrate_dimy = 0.6 * mm;
    G4double substrate_dimz = 0.35 * mm;

    /*place a Si substrate in the middle of this volume*/
    G4Box* substrate = new G4Box("substrate_box", substrate_dimx/2, substrate_dim\
  y/2, substrate_dimz/2);
    //argument list for constructor: solid volume, material, name, ???
  G4LogicalVolume* logical_substrate = new G4LogicalVolume(substrate, Si, "subs\
  trate_log", 0,0,0);
    //argument list for the G4PVPlacement constructor: rotation matrix, position,\
   logical volume, name, mother logical volumer, boolean, copy number
    G4VPhysicalVolume* physical_substrate = new G4PVPlacement(0,
G4ThreeVector(0.*mm,0.*mm,0.015*mm), logical_substrate, "substrate_phys",
logical_epoxyshell, false, 0);

    //set the visualisation attributes of the substrate-grey
    logical_substrate->SetVisAttributes(G4VisAttributes(G4Colour(cyan)));


    //===SiO2 scoring layer==========
    G4double scoring_dimx = 0.8 * mm;
    G4double scoring_dimy = 0.6 * mm;
```

```
  G4double scoring_dimz = 1 * um;

  /*now make the SiO2 layer the scoring layer*/
G4Box* scoring = new G4Box("scoring_box", scoring_dimx/2, scoring_dimy/2, sco\
ring_dimz/2);
  //argument list for constructor: solid volume, material, name, ???
  G4LogicalVolume* logical_scoring = new G4LogicalVolume(scoring, SiO2, "scorin\
g_log", 0,0,0);
  //assign scoring volume mass
  ScoringVolumeMass = logical_scoring->GetMass();

  //create SensitiveDetector object
  SensitiveDetector* SD = new SensitiveDetector("SD");
  //get pointer to the sensitive detector manager: this class is used by G4RunM\
anager to see which sensitive detectors there are
  G4SDManager* SDman = G4SDManager::GetSDMpointer();
  //pass to manager
  SDman->AddNewDetector(SD);

  //now we pass the sensitive detector pointer to the logical volume of our sco\
ring volume
  logical_scoring->SetSensitiveDetector(SD);

 //argument list for the G4PVPlacement constructor: rotation matrix, position,\
  logical volume, name, mother logical volumer, boolean, copy number
  G4VPhysicalVolume* physical_scoring = new G4PVPlacement(0,
G4ThreeVector(0*mm,0*mm,0.1745*mm), logical_scoring, "scoring_phys",
logical_substrate, false, 0);

  //set the visualisation attributes of the scoring volume-blue
  logical_scoring->SetVisAttributes(G4VisAttributes(G4Colour(white)));

   G4Region* containerregion = new G4Region("container_log");
   logical_container->SetRegion(containerregion);
   containerregion->AddRootLogicalVolume(logical_container);

    G4Region* phantomregion = new G4Region("phantom_log");
    logical_phantom->SetRegion(phantomregion);
    phantomregion->AddRootLogicalVolume(logical_phantom);

 G4Region* basecontactlayerregion = new G4Region("basecontactlayer_log");
    logical_basecontactlayer->SetRegion(basecontactlayerregion);
    basecontactlayerregion->AddRootLogicalVolume(logical_basecontactlayer);

    G4Region* metalcontactlayerregion = new G4Region("metalcontactlayer_log");
    logical_metalcontactlayer->SetRegion(metalcontactlayerregion);
    metalcontactlayerregion->AddRootLogicalVolume(logical_metalcontactlayer);
```

```
    G4Region* encap1region = new G4Region("encap1_log");
    logical_encap1->SetRegion(encap1region);
    encap1region->AddRootLogicalVolume(logical_encap1);

  G4Region* epoxyshellregion = new G4Region("epoxyshell_log");
    logical_epoxyshell->SetRegion(epoxyshellregion);
    epoxyshellregion->AddRootLogicalVolume(logical_epoxyshell);

    G4Region* substrateregion = new G4Region("substrate_log");
    logical_substrate->SetRegion(substrateregion);
    substrateregion->AddRootLogicalVolume(logical_substrate);

    G4Region* scoringregion = new G4Region("scoring_log");
    logical_scoring->SetRegion(scoringregion);
    scoringregion->AddRootLogicalVolume(logical_scoring);

    return physical_world;

  }
```

PhysicsList.cc

```
#include "PhysicsList.hh"

#include "G4ParticleDefinition.hh"
#include "G4ProcessManager.hh"
#include "G4ProcessVector.hh"
#include "G4ios.hh"
#include "G4Region.hh"
#include "G4RegionStore.hh"
#include "G4ProductionCuts.hh"
#include "globals.hh"

PhysicsList::PhysicsList():  G4VUserPhysicsList()
{
  //  SetVerboseLevel(1);

defaultCutValue = 0.1 * um;
}

PhysicsList::~PhysicsList()
[142]

#include "G4Gamma.hh"
#include "G4Electron.hh"
#include "G4Geantino.hh"
#include "G4Positron.hh"

void PhysicsList::ConstructParticle()
{
  G4Geantino::GeantinoDefinition();
  G4Gamma::GammaDefinition();
G4Electron::ElectronDefinition();
  G4Positron::PositronDefinition();
}

//physics processes to be used in the simulation

//photon interactions
#include "G4LowEnergyPhotoElectric.hh"
#include "G4LowEnergyCompton.hh"
#include "G4LowEnergyRayleigh.hh"
#include "G4LowEnergyGammaConversion.hh"

//electron interactions
#include "G4LowEnergyBremsstrahlung.hh"
#include "G4LowEnergyIonisation.hh"
#include "G4MultipleScattering.hh"
```

```
//positron interaction
#include "G4eIonisation.hh"
#include "G4eBremsstrahlung.hh"
#include "G4eplusAnnihilation.hh"

void PhysicsList::ConstructProcess()
{
  AddTransportation();

  theParticleIterator->reset();
  while((*theParticleIterator)()){

    //for photons

    G4ParticleDefinition* ParDef = theParticleIterator->value();
    G4ProcessManager* PManager = ParDef->GetProcessManager();
    G4String ParName = ParDef->GetParticleName();

    if(ParName == "gamma"){
      //model the photo electric and compton interaction

      G4LowEnergyPhotoElectric* LEPE = new G4LowEnergyPhotoElectric();
      PManager->AddDiscreteProcess(LEPE);

//
      G4LowEnergyCompton* LEC = new G4LowEnergyCompton();
      PManager->AddDiscreteProcess(LEC);

      //
      G4LowEnergyRayleigh* LER = new G4LowEnergyRayleigh();
      PManager->AddDiscreteProcess(LER);

      //
      G4LowEnergyGammaConversion* LEGC = new
G4LowEnergyGammaConversion();
      PManager->AddDiscreteProcess(LEGC);

    }else if(ParName == "e-") {
//for electron
      //model the electron process
      G4LowEnergyIonisation* LEI = new G4LowEnergyIonisation();
      G4LowEnergyBremsstrahlung* LEB = new G4LowEnergyBremsstrahlung();
      G4MultipleScattering* MScatter = new G4MultipleScattering();

      //add these process to the process manager
      PManager->AddProcess(MScatter, -1, 1, 1);
      PManager->AddProcess(LEI, -1, 2, 2);
```

```
      PManager->AddProcess(LEB, -1, -1, 3);

    }else if(ParName == "e+") {
      //for positron
      G4MultipleScattering* epMScatter = new G4MultipleScattering();
      G4eIonisation* epIon = new G4eIonisation();
      G4eBremsstrahlung* epBrem = new G4eBremsstrahlung();
      G4eplusAnnihilation* epAnn = new G4eplusAnnihilation();

      PManager->AddProcess(epMScatter, -1, 1, 1);
      PManager->AddProcess(epIon, -1, 2, 2);
      PManager->AddProcess(epBrem, -1, -1, 3);
      PManager->AddProcess(epAnn, 0, -1, 4);

    }

  }

 }

 void PhysicsList::SetCuts(){
 //
    SetCutsWithDefault();

 //Production thresholds for detector regions
 G4Region*
containerregion=G4RegionStore::GetInstance()>GetRegion("container_log");
 G4ProductionCuts* containercuts=new G4ProductionCuts;
 containercuts->SetProductionCut(1*cm,G4ProductionCuts::GetIndex("gamma"));
containercuts->SetProductionCut(8*um,G4ProductionCuts::GetIndex("e-"));
containercuts->SetProductionCut(8*um,G4ProductionCuts::GetIndex("e+"));
containerregion->SetProductionCuts(containercuts);

G4Region*
phantomregion=G4RegionStore::GetInstance()>GetRegion("phantom_log");
G4ProductionCuts* phantomcuts=new G4ProductionCuts;
 phantomcuts->SetProductionCut(1*cm,G4ProductionCuts::GetIndex("gamma"));
 phantomcuts->SetProductionCut(1*cm,G4ProductionCuts::GetIndex("e-"));
 phantomcuts->SetProductionCut(1*cm,G4ProductionCuts::GetIndex("e+"));
phantomregion->SetProductionCuts(phantomcuts);

G4Region*
basecontactlayerregion=G4RegionStore::GetInstance()>GetRegion("basecontactlayer_l
og");
G4ProductionCuts* basecontactlayercuts=new G4ProductionCuts;
basecontactlayercuts->SetProductionCut(0.1*um);
basecontactlayerregion->SetProductionCuts(basecontactlayercuts);
```

```
G4Region*
metalcontactlayerregion=G4RegionStore::GetInstance()>GetRegion("metalcontactlayer
_log");
G4ProductionCuts* metalcontactlayercuts=new G4ProductionCuts;
metalcontactlayercuts->SetProductionCut(0.1*um);
metalcontactlayerregion->SetProductionCuts(metalcontactlayercuts);

G4Region* encap1region=G4RegionStore::GetInstance()->GetRegion("encap1_log");
G4ProductionCuts* encap1cuts=new G4ProductionCuts;
encap1cuts->SetProductionCut(0.1*um);
encap1region->SetProductionCuts(encap1cuts);

G4Region*
epoxyshellregion=G4RegionStore::GetInstance()>GetRegion("epoxyshell_log");
G4ProductionCuts* epoxyshellcuts=new G4ProductionCuts;
epoxyshellcuts->SetProductionCut(0.1*um);
 epoxyshellregion->SetProductionCuts(epoxyshellcuts);

G4Region* substrateregion=G4RegionStore::GetInstance()->GetRegion("substrate_lo\
g");
G4ProductionCuts* substratecuts=new G4ProductionCuts;
substratecuts->SetProductionCut(0.1*um);
substrateregion->SetProductionCuts(substratecuts);

G4Region* scoringregion=G4RegionStore::GetInstance()->GetRegion("scoring_log");
G4ProductionCuts* scoringcuts=new G4ProductionCuts;
scoringcuts->SetProductionCut(0.1*um);
scoringregion->SetProductionCuts(scoringcuts);

}
```

PrimaryGeneratorAction.cc

```
#include "PrimaryGeneratorAction.hh"

//include class definition for the particle gun
#include "G4Event.hh"
#include "G4GeneralParticleSource.hh"
#include "G4ParticleTable.hh"
#include "G4ParticleDefinition.hh"
#include "globals.hh"

//include header file for particle
#include "G4Gamma.hh"

#include "Randomize.hh"

PrimaryGeneratorAction::PrimaryGeneratorAction(){

  //we need to use dynamic memory allocation for the G4ParticleGun object
  gun = new G4GeneralParticleSource();

}

PrimaryGeneratorAction::~PrimaryGeneratorAction(){
  //free the dynamically allocated memory
  delete gun;

}


//this method will be called by the RunManager at the beginning of each particl\
e history
void PrimaryGeneratorAction::GeneratePrimaries(G4Event* anEvent){

  gun->GeneratePrimaryVertex(anEvent);

}
```

RunAction.cc

```
#include "RunAction.hh"
#include "G4Run.hh"
#include "DetectorConstruction.hh"

RunAction::RunAction(DetectorConstruction* DC){
   Dose = 0;
   DoseSquared = 0;

//take the DetectorConstruction pointer given when this object is created (in m\
ain) and copy to local member
   myDC = DC;

//define string variable to store filename
   G4String Filename = "/home/cheryl/results/msm5_50.dat";

// at the moment run action only has one output file, it will either print out \
dose deposition, OR photon spectrum for particles entering SV from world
  outfile.open(Filename);
}

RunAction::~RunAction(){

//close the output file when this class is destroyed
   outfile.close();

}

void RunAction::BeginOfRunAction(const G4Run* aRun){

//initialise the dose and dose squared for this run
   Dose = 0;
   DoseSquared = 0;

}


//this will be called each time there is a primary that deposits energy in our \
readout geometry. Called by SensitiveDetector class

void RunAction::ProcessDoseEvent(const G4double DosePerEvent){
/*here we receive the dose deposited for a single event, add to accumulative depth dose
and the accumulated dose per primary squared*/

//increment the dose deposited in this  box
   Dose += DosePerEvent;
```

```
//increment the sum of the dose in this box squared
   DoseSquared += pow(DosePerEvent,2);

}

//task to be carried out at the end of the run
void RunAction::EndOfRunAction(const G4Run* aRun){
//
   //get the number of primary particles being simulated for this run
   G4double NumberOfEvents = aRun->GetNumberOfEventToBeProcessed();

//first, calculation average energy deposition per event along with errors

//average energy deposition
   G4double AverageEnergy = Dose/NumberOfEvents;
//calculate the average dose squared in this grid box
   G4double AverageEnergySquared = DoseSquared / NumberOfEvents;


//calculate the square of the average dose
   G4double SquaredAverageEnergy = pow(AverageEnergy, 2);
//calculate the standard deviation in the average dose squared
   G4double StandardDeviation = sqrt(AverageEnergySquared - SquaredAverageEner\
gy);
//calculate the standard error in the average dose estimate, 95% confidence lim\
its
   G4double EnergyError = 2 * StandardDeviation / sqrt(G4double(NumberOfEvents\
));

//second, calculate the average Dose (in joules) per event along with error est\
imate


//convert energy deposition from MeV to joules
   G4double EnergyInJoules = AverageEnergy / joule;

//get the mass of the scoring volume
   G4double MassInKilos = myDC->GetScoringVolumeMass() / kg;
   // G4cout << "MassInKilos " << MassInKilos << G4endl;
   //
   G4double AbsorbedDose = EnergyInJoules / MassInKilos; // joule per kilo

//calculate Dose error from energy deposition error

G4double DoseError = EnergyError / joule / MassInKilos;


/*print message to screen*/
```

```
   G4cout << "****************************************" << G4endl;
   G4cout << "*  Dose (Gy)    Error (Gy)            *" << G4endl;
   G4cout << "****************************************" << G4endl;
//print the result to screen
   G4cout << AbsorbedDose << " " << DoseError <<  G4endl;

//if the output file exists, print the result to it
   if(outfile)
      outfile << AbsorbedDose << " " << DoseError << G4endl;
}
```

SensitiveDetector.cc

```
#include "SensitiveDetector.hh"
#include "G4Step.hh"

#include "G4HCofThisEvent.hh"
#include "G4TouchableHistory.hh"

#include "RunAction.hh"
#include "G4RunManager.hh"


SensitiveDetector::SensitiveDetector(G4String name) : G4VSensitiveDetector(name\
){

}

SensitiveDetector::~SensitiveDetector(){}



/*This method is invoked at the beginning of each event. The argument of this m\
ethod is an object of the G4HCofThisEvent class. Hits collections, where hits p\
roduced in this particular event are stored, can be associated to the G4HCofThi\
sEvent object in this method. The hits collections associated with the G4HCofTh\
isEvent  object during this method can be used for ``during the event processin\
g" digitization.*/
void SensitiveDetector::Initialize(G4HCofThisEvent* HCE){

   Dose = 0;

}

G4bool SensitiveDetector::ProcessHits(G4Step* theStep, G4TouchableHistory*){

// if we are tallying the dose, increment event wide dose with dose for this st\
ep

      const G4double edep = theStep->GetTotalEnergyDeposit();

//if there was any energy deposition, accumulate the dose for this event
      if(edep > 0){
         Dose += edep;
      }

  return true;

}
```

```
void SensitiveDetector::EndOfEvent(G4HCofThisEvent*)
{
//if the dose for this event is non zero
      if(Dose > 0){
         //apparently so, so we pass the dose for this event to the method of the run aciton
that accumulates dose per event
         RunAction* myRunAction = (RunAction*)(G4RunManager::GetRunManager()\
->GetUserRunAction());
//
         if(myRunAction)
            myRunAction->ProcessDoseEvent(Dose);
      }
}
```

Appendix B: X-ray spectra generated by XCOMP5R and SpekCalc at beam qualities 50 kVp to 250 kVp

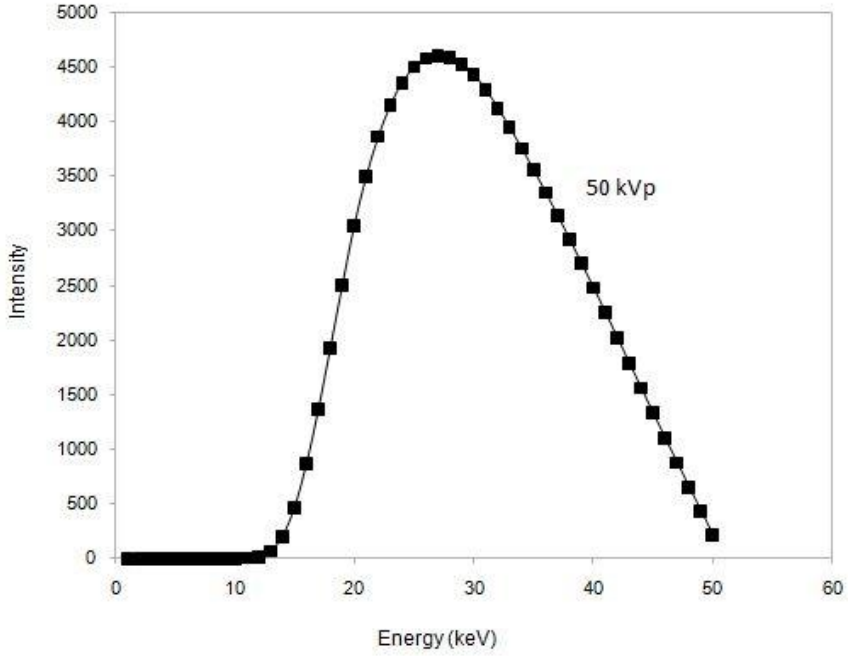

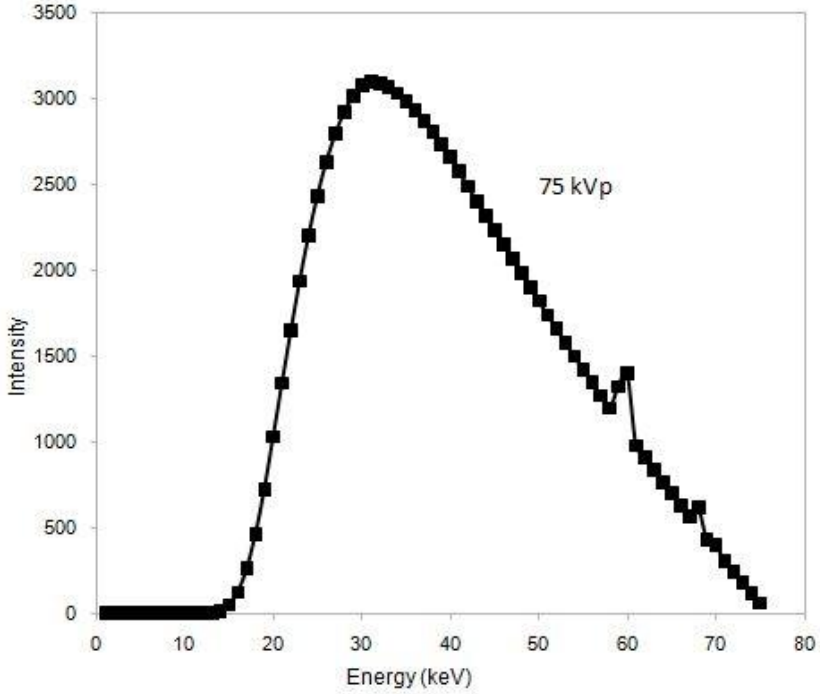

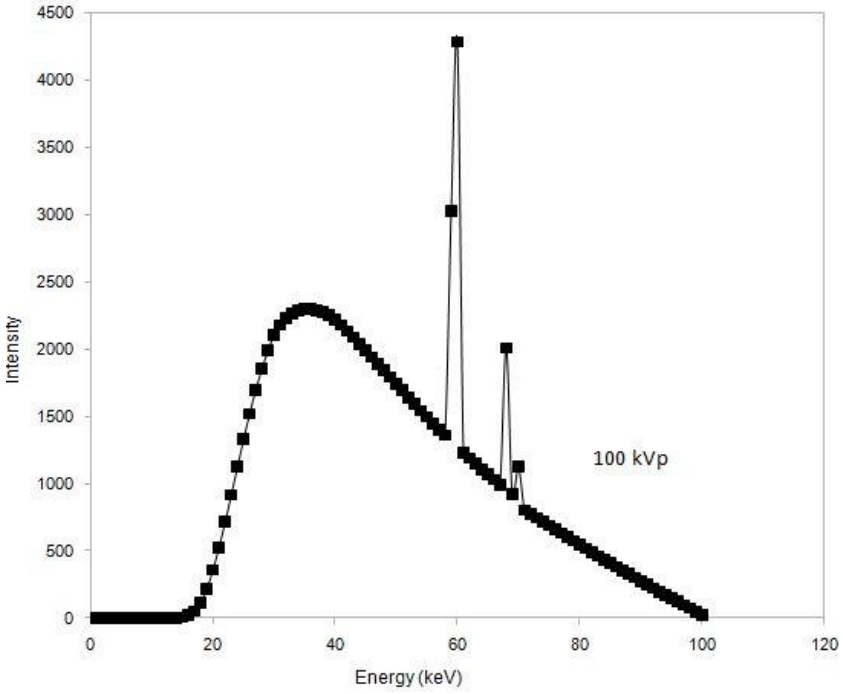
4500
4000
3500
3000
2500
2000
1500
1000
500
0
Intensity
0
20
40
60
80
100
120
Energy (keV)
100 kVp

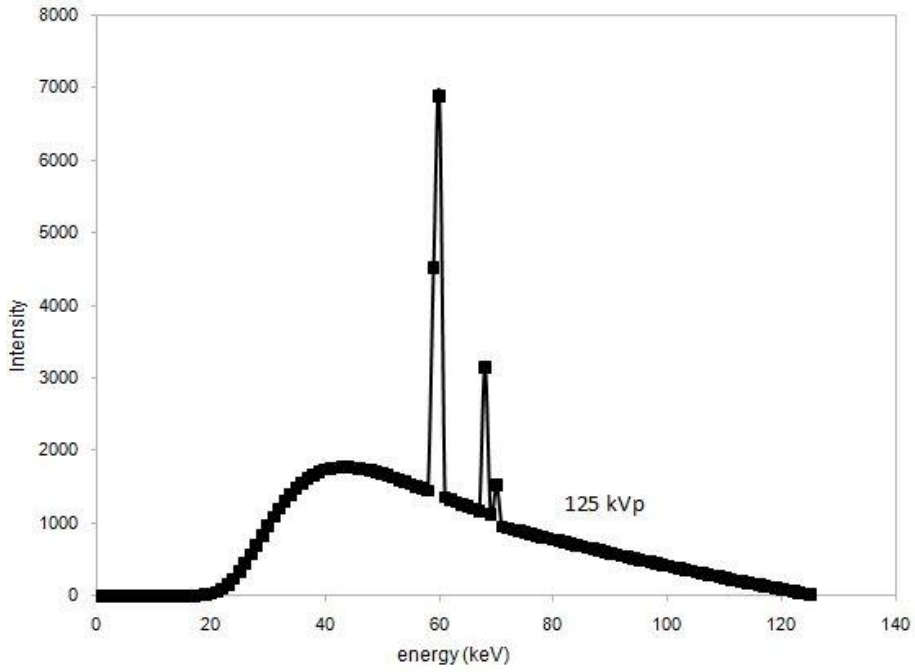
8000
7000
6000
5000
4000
3000
2000
1000
0
Intensity
0
20
40
60
80
100
120
140
energy (keV)
125 kVp

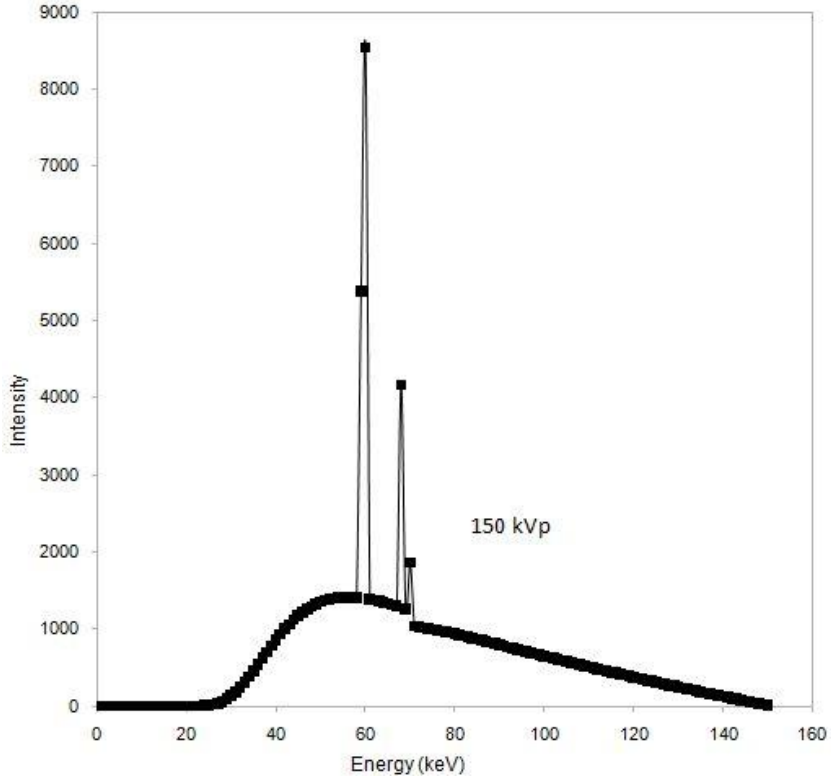
9000
8000
7000
6000
5000
4000
3000
2000
1000
0
Intensity
150 kVp
0
20
40
60
80
100
120
140
160
Energy (keV)

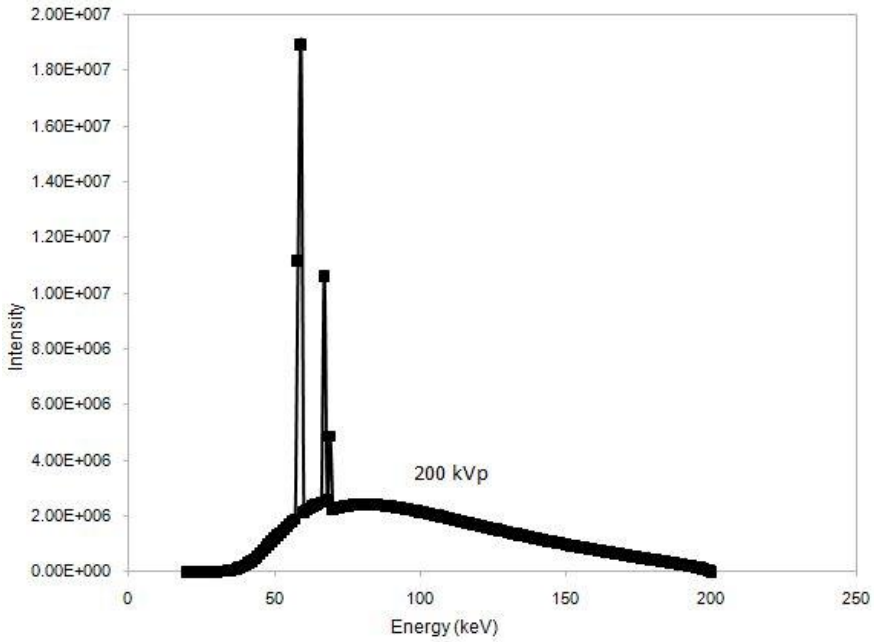
2.00E+007
1.80E+007
1.60E+007
1.40E+007
1.20E+007
1.00E+007
8.00E+006
6.00E+006
4.00E+006
2.00E+006
0.00E+000
Intensity
200 kVp
0
50
100
150
200
250
Energy (keV)

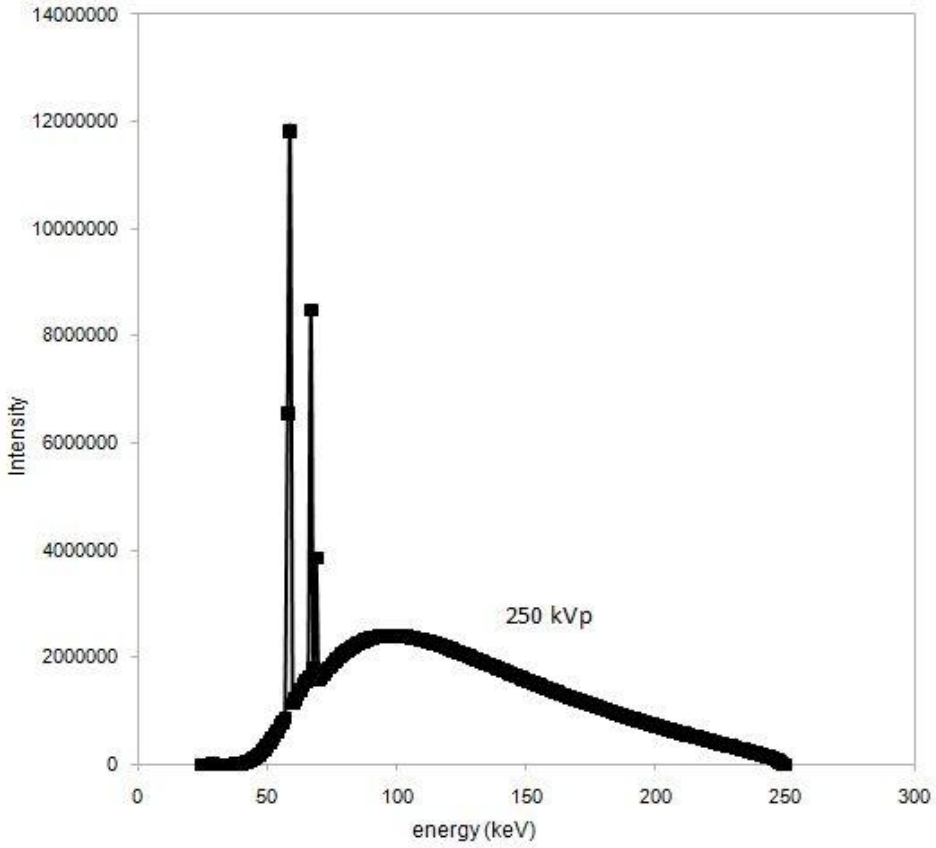
14000000
12000000
10000000
8000000
6000000
4000000
2000000
0
Intensity
0
50
100
150
200
250
300
energy (keV)
250 kVp

Appendix C: Calibration and Measurement Protocols for the application of radiation dosimeters in clinical kilovoltage x-ray photon beams

Dosimetry with radiation detectors such as the MOSkin and radiochromic film is a 2-step process. The first procedure involves detector calibration; during which the detector is irradiated to known doses to plot a calibration curve which essentially relates dose absorbed to a known property of the dosimeter (threshold voltage change in the MOS*kin* and change in optical density for the film). The second step involves measurement of the unknown dose using the calibration curve obtained in the previous process.

MOS*kin*

MOS*kin* Calibration Protocol in a clinical kilovoltage therapy beam

1. With a pre-selected tube potential and filtration, deliver a known dose at D_{max} of the solid water phantom surface.
2. The change in threshold voltage of the MOSkin dosimeter placed at D_{max} gives the dose sensitivity factor, otherwise known as the calibration factor in mV/cGy.
3. The MOSkin dosimeter should be re-calibrated as in steps 1 and 2, for every 2.5 V increase in accumulated voltage.

MOS*kin* Measurement and Readout Protocol

To ensure optimal measurements with the MOS*kin*,

1. Expose MOS*kins*
2. 30 seconds wait
3. Read and record MOS*kin* measurement
4. 30 seconds stabilization period
5. Repeat steps 1 to 4 for all subsequent exposures

Radiochromic Film Calibration Protocol on the Gulmay D3300 superficial/orthovoltage therapy unit

Film preparation and handling precautions

- Avoid getting fingerprints or scratching the film as this contributes to measurement inaccuracy. Use clean gloves when handling films.
- Mark pieces with numbers on top right hand corner of film and symbol 'Δ' on the top left hand corner of the film
- Prescan the film to determine film uniformity
- Note face-up and face-down orientation when handling films and be consistent throughout

Calibration Protocol
Exposure of radiochromic films to known doses from 0 mGy to 200 mGy (XR-QA2)

1. Irradiate each numbered film piece at beam isocentre.

   Example film numbering and preparation:

Tube potential 150 kVp Date of irradiation: Start time of irradiation: End time of irradiation: Lot number:				Tube potential 100 kVp Date of irradiation: Start time of irradiation: End time of irradiation: Lot number:			
Film number	Dose (cGy)	Film number	Dose (cGy)	Film number	Dose (cGy)	Film number	Dose (cGy)
1		13		25		37	
2		14		26		38	
3		15		27		39	
4		16		28		40	
5		17		29		41	
6		18		30		42	
7		19		31		43	
8		20		32		44	
9		21		33		45	
10		22		34		46	
11		23		35		47	
12		24		36		48	

2. Repeat irradiations at a different tube potential to verify the energy independence of film

Appendix D: NRPB-SR250 Calculation of Effective Dose

ImPACT CT Patient Dosimetry Calculator
Version 1.0.4 27/05/2011

Scanner Model:		
Manufacturer:	GE	
Scanner:	GE LightSpeed 16	
kV:	120	
Scan Region:	Body	
Data Set	MCSET12	
Current Data	MCSET12	
Scan range		
Start Position	1.5	cm
End Position	27.5	cm

Organ weighting scheme	ICRP 60

Acquisition Parameters:		
Tube current	150	mA
Rotation time	0.5	s
Spiral pitch	1.375	
mAs / Rotation	75	mAs
Effective mAs	54.54545	mAs
Collimation	20	mm
Rel. CTDI 0.856073	0.86	at selected collimation
CTDI (air) 25.115	25.1	mGy/100mAs
CTDI (soft tissue)	26.9	mGy/100mAs
$_nCTDI_w$ 9.9093	9.9	mGy/100mAs

$CTDI_w$	7.4	mGy
$CTDI_{vol}$	5.4	mGy
DLP	141	mGy.cm

Organ	w_T	H_T (mGy)	$w_T.H_T$
Gonads	0.2	3.9	0.78
Bone Marrow	0.12	2.1	0.25
Colon	0.12	6	0.73
Lung	0.12	0.038	0.0046
Stomach	0.12	0.83	0.099
Bladder	0.05	7.6	0.38
Breast	0.05	0.02	0.00098
Liver	0.05	0.55	0.027
Oesophagus (Thymus)	0.05	0.0093	0.00046
Thyroid	0.05	0.0012	0.000058
Skin	0.01	1.4	0.014
Bone Surface	0.01	2.2	0.022
Not Applicable	0	0	0
Not Applicable	0	0	0
Remainder	0.05	2	0.1
Not Applicable	0	0	0
Total Effective Dose (mSv)			2.4

Remainder Organs	H_T (mGy)
Adrenals	0.2
Small Intestine	6.4
Kidney	0.98
Pancreas	0.43
Spleen	0.41
Thymus	0.0093
Uterus	7.4
Muscle	2
Brain	0.000053
Not Applicable	N/A
Not Applicable	N/A
Not Applicable	N/A
Not Applicable	N/A

Other organs of Interest	H_T (mGy)
Eye lenses	0
Testes	1
Ovaries	6.7
Uterus	7.4
Prostate	7.6

Scan Description / Comments	

Software-input technical and acquisition CT parameters for the renal calculus protocol for the calculation of effective dose based on ICRP 60 tissue weighting factors

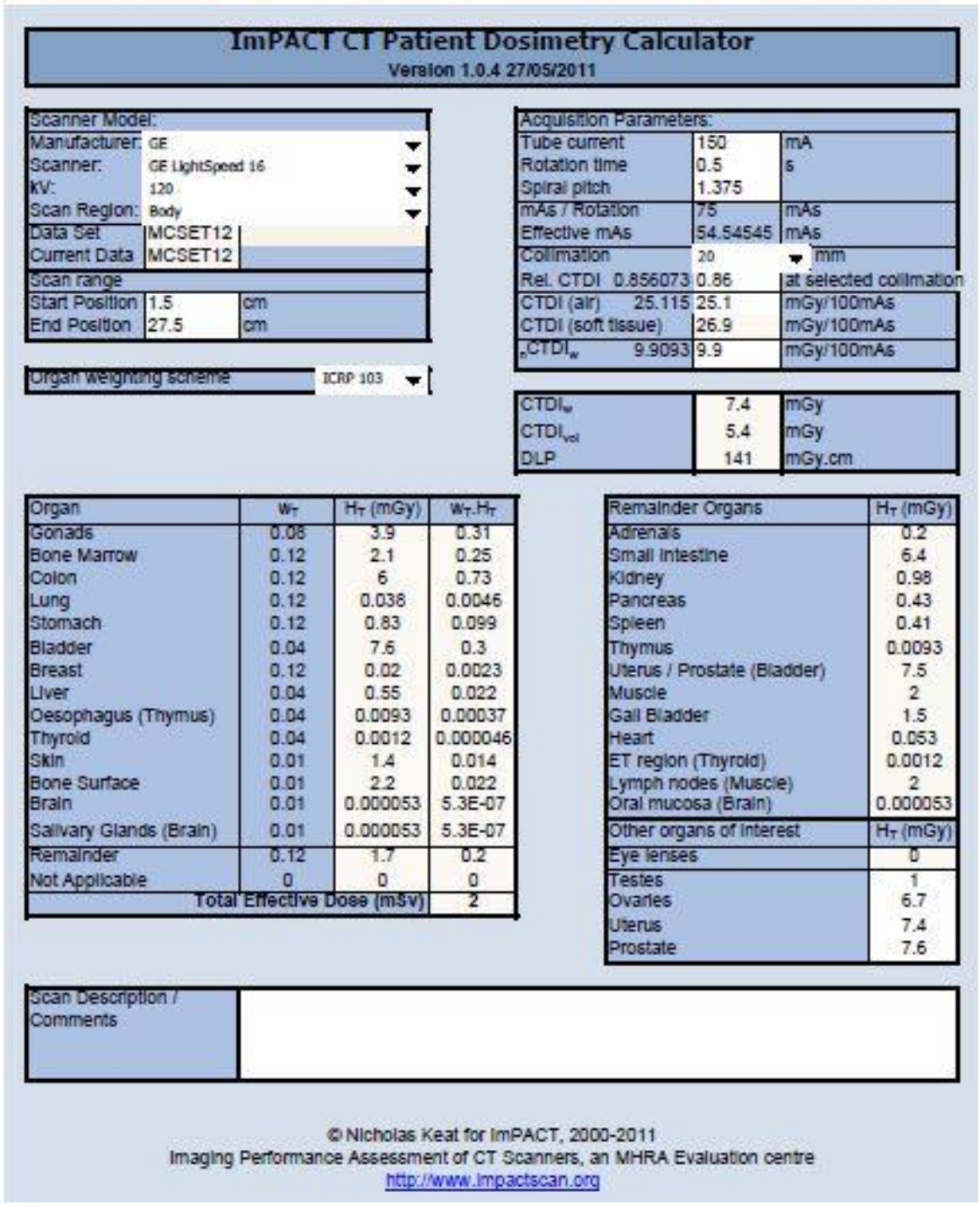

ImPACT CT Patient Dosimetry Calculator
Version 1.0.4 27/05/2011

Scanner Model:		
Manufacturer:	GE	
Scanner:	GE LightSpeed 16	
kV:	120	
Scan Region:	Body	
Data Set	MCSET12	
Current Data	MCSET12	
Scan range		
Start Position	1.5	cm
End Position	27.5	cm

Acquisition Parameters:		
Tube current	150	mA
Rotation time	0.5	s
Spiral pitch	1.375	
mAs / Rotation	75	mAs
Effective mAs	54.54545	mAs
Collimation	20	mm
Rel. CTDI 0.856073	0.86	at selected collimation
CTDI (air) 25.115	25.1	mGy/100mAs
CTDI (soft tissue)	26.9	mGy/100mAs
$_nCTDI_w$ 9.9093	9.9	mGy/100mAs

Organ weighting scheme: ICRP 103

$CTDI_w$	7.4	mGy
$CTDI_{vol}$	5.4	mGy
DLP	141	mGy.cm

Organ	w_T	H_T (mGy)	$w_T.H_T$
Gonads	0.08	3.9	0.31
Bone Marrow	0.12	2.1	0.25
Colon	0.12	6	0.73
Lung	0.12	0.038	0.0046
Stomach	0.12	0.83	0.099
Bladder	0.04	7.6	0.3
Breast	0.12	0.02	0.0023
Liver	0.04	0.55	0.022
Oesophagus (Thymus)	0.04	0.0093	0.00037
Thyroid	0.04	0.0012	0.000046
Skin	0.01	1.4	0.014
Bone Surface	0.01	2.2	0.022
Brain	0.01	0.000053	5.3E-07
Salivary Glands (Brain)	0.01	0.000053	5.3E-07
Remainder	0.12	1.7	0.2
Not Applicable	0	0	0
Total Effective Dose (mSv)			2

Remainder Organs	H_T (mGy)
Adrenals	0.2
Small Intestine	6.4
Kidney	0.98
Pancreas	0.43
Spleen	0.41
Thymus	0.0093
Uterus / Prostate (Bladder)	7.5
Muscle	2
Gall Bladder	1.5
Heart	0.053
ET region (Thyroid)	0.0012
Lymph nodes (Muscle)	2
Oral mucosa (Brain)	0.000053

Other organs of interest	H_T (mGy)
Eye lenses	0
Testes	1
Ovaries	6.7
Uterus	7.4
Prostate	7.6

Scan Description / Comments

Software-input technical and acquisition CT parameters for the renal calculus protocol for the calculation of effective dose based on ICRP 103 tissue weighting factors

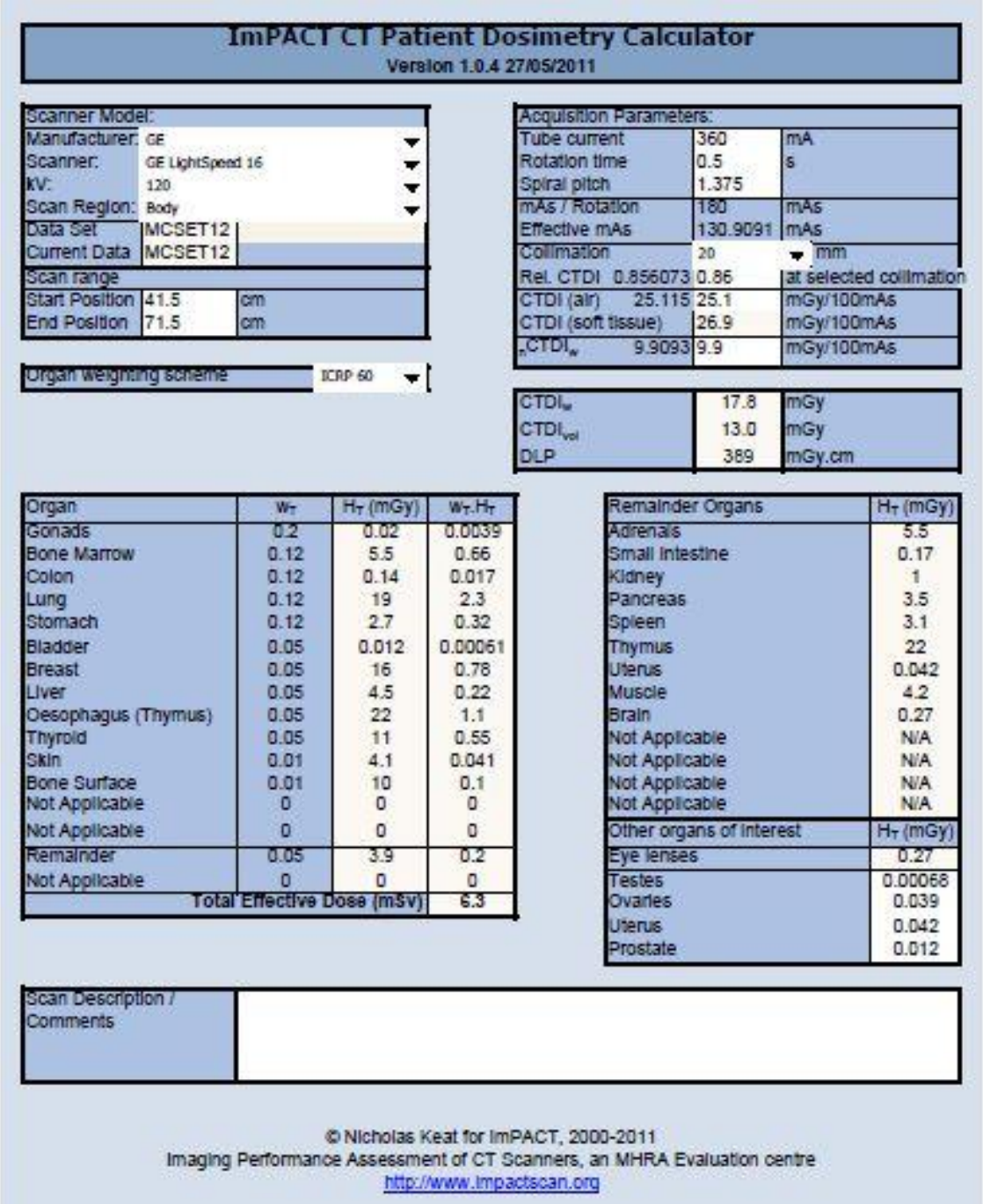

ImPACT CT Patient Dosimetry Calculator
Version 1.0.4 27/05/2011

Scanner Model:		
Manufacturer:	GE	
Scanner:	GE LightSpeed 16	
kV:	120	
Scan Region:	Body	
Data Set	MCSET12	
Current Data	MCSET12	
Scan range		
Start Position	41.5	cm
End Position	71.5	cm

Acquisition Parameters:		
Tube current	360	mA
Rotation time	0.5	s
Spiral pitch	1.375	
mAs / Rotation	180	mAs
Effective mAs	130.9091	mAs
Collimation	20	mm
Rel. CTDI 0.856073	0.86	at selected collimation
CTDI (air) 25.115	25.1	mGy/100mAs
CTDI (soft tissue)	26.9	mGy/100mAs
$_nCTDI_w$ 9.9093	9.9	mGy/100mAs

Organ Weighting Scheme: ICRP 60

$CTDI_w$	17.8	mGy
$CTDI_{vol}$	13.0	mGy
DLP	389	mGy.cm

Organ	w_T	H_T (mGy)	$w_T.H_T$
Gonads	0.2	0.02	0.0039
Bone Marrow	0.12	5.5	0.66
Colon	0.12	0.14	0.017
Lung	0.12	19	2.3
Stomach	0.12	2.7	0.32
Bladder	0.05	0.012	0.00061
Breast	0.05	16	0.78
Liver	0.05	4.5	0.22
Oesophagus (Thymus)	0.05	22	1.1
Thyroid	0.05	11	0.55
Skin	0.01	4.1	0.041
Bone Surface	0.01	10	0.1
Not Applicable	0	0	0
Not Applicable	0	0	0
Remainder	0.05	3.9	0.2
Not Applicable	0	0	0
Total Effective Dose (mSv)			6.3

Remainder Organs	H_T (mGy)
Adrenals	5.5
Small Intestine	0.17
Kidney	1
Pancreas	3.5
Spleen	3.1
Thymus	22
Uterus	0.042
Muscle	4.2
Brain	0.27
Not Applicable	N/A
Not Applicable	N/A
Not Applicable	N/A
Not Applicable	N/A

Other organs of interest	H_T (mGy)
Eye lenses	0.27
Testes	0.00068
Ovaries	0.039
Uterus	0.042
Prostate	0.012

Scan Description / Comments

Imaging Performance Assessment of CT Scanners, an MHRA Evaluation centre
http://www.impactscan.org

Software-input technical and acquisition CT parameters for the pulmonary embolus protocol for the calculation of effective dose based on ICRP 60 tissue weighting factors

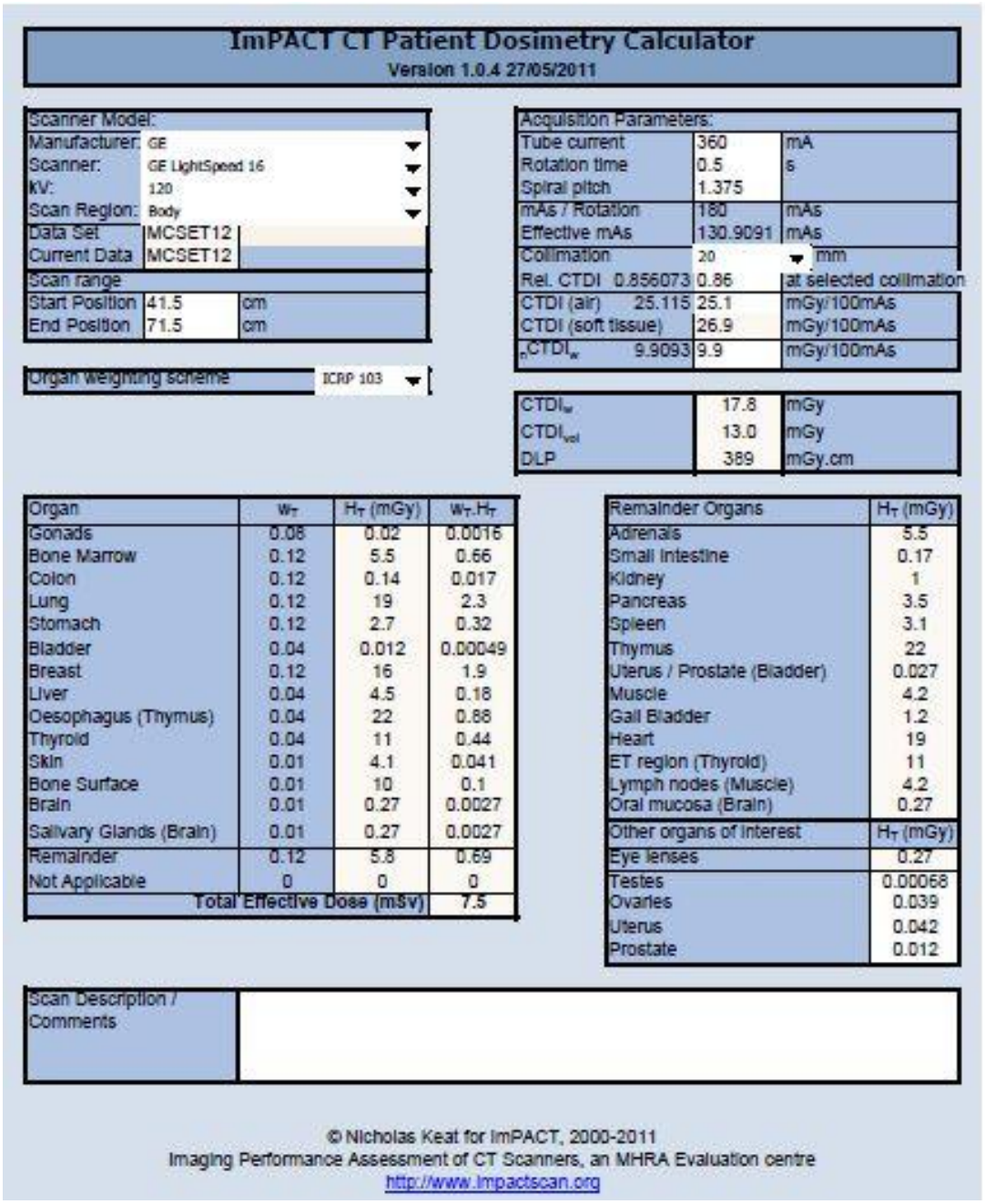

ImPACT CT Patient Dosimetry Calculator
Version 1.0.4 27/05/2011

Scanner Model:		
Manufacturer:	GE	
Scanner:	GE LightSpeed 16	
kV:	120	
Scan Region:	Body	
Data Set	MCSET12	
Current Data	MCSET12	
Scan range		
Start Position	41.5	cm
End Position	71.5	cm

Acquisition Parameters:		
Tube current	360	mA
Rotation time	0.5	s
Spiral pitch	1.375	
mAs / Rotation	180	mAs
Effective mAs	130.9091	mAs
Collimation	20	mm
Rel. CTDI 0.856073	0.86	at selected collimation
CTDI (air) 25.115	25.1	mGy/100mAs
CTDI (soft tissue)	26.9	mGy/100mAs
$_nCTDI_w$ 9.9093	9.9	mGy/100mAs

Organ weighting scheme: ICRP 103

$CTDI_w$	17.8	mGy
$CTDI_{vol}$	13.0	mGy
DLP	389	mGy.cm

Organ	w_T	H_T (mGy)	$w_T.H_T$
Gonads	0.08	0.02	0.0016
Bone Marrow	0.12	5.5	0.66
Colon	0.12	0.14	0.017
Lung	0.12	19	2.3
Stomach	0.12	2.7	0.32
Bladder	0.04	0.012	0.00049
Breast	0.12	16	1.9
Liver	0.04	4.5	0.18
Oesophagus (Thymus)	0.04	22	0.88
Thyroid	0.04	11	0.44
Skin	0.01	4.1	0.041
Bone Surface	0.01	10	0.1
Brain	0.01	0.27	0.0027
Salivary Glands (Brain)	0.01	0.27	0.0027
Remainder	0.12	5.8	0.69
Not Applicable	0	0	0
Total Effective Dose (mSv)			7.5

Remainder Organs	H_T (mGy)
Adrenals	5.5
Small Intestine	0.17
Kidney	1
Pancreas	3.5
Spleen	3.1
Thymus	22
Uterus / Prostate (Bladder)	0.027
Muscle	4.2
Gall Bladder	1.2
Heart	19
ET region (Thyroid)	11
Lymph nodes (Muscle)	4.2
Oral mucosa (Brain)	0.27

Other organs of interest	H_T (mGy)
Eye lenses	0.27
Testes	0.00068
Ovaries	0.039
Uterus	0.042
Prostate	0.012

Scan Description / Comments

Software-input technical and acquisition CT parameters for the pulmonary embolus protocol for the calculation of effective dose based on ICRP103 tissue weighting factors